UNIVERSITY OF SÃO PAULO
SÃO CARLOS SCHOOL OF ENGINEERING

Erivelto dos Santos Filho

Evaluation of flow-induced noise, structure vibration, and flow morphology of R134a flowing through a thermostatic expansion valve

São Carlos

2022

Erivelto dos Santos Filho

Evaluation of flow-induced noise, structure vibration, and flow morphology of R134a flowing through a thermostatic expansion valve

Thesis (Doctorate) presented to the Graduate Program in Mechanical Engineering of São Carlos School of Engineering, University of São Paulo, Brazil to obtain the degree of Doctor of Science.

Concentration area: Thermal and Fluid Science

Supervisor: Prof. Gherhardt Ribatski

VERSÃO CORRIGIDA

São Carlos

2022

S856m

dos Santos Filho, Erivelto

Evaluation of flow-induced noise, structure vibration, and flow morphology of R134a flowing through a thermostatic expansion valve / Erivelto dos Santos Filho; advisor Gherhardt Ribatski. – Sao Carlos, 2022.

Tese (Doutorado) - Programa de Pós-graduação em Engenharia Mecânica e área de concentração em Térmica e Fluidos – São Carlos School of Engineering, University of São Paulo, 2022.

1. Thermal and Fluid Science. 2. Refrigerant flow-induced noise. 3. Refrigeration. 4. Thermostatic expansion valve. 5. Two-phase flow. 6. Air-conditioning. I. Ribatski, advisor Gherhardt. II. Titulo.

FOLHA DE JULGAMENTO

Candidato: Engenheiro **ERIVELTO DOS SANTOS FILHO.**

Título da tese: "Avaliação do ruído induzido pelo escoamento, vibração da estrutura e morfologia do R134a através de uma válvula de expansão termostática".

Data da defesa: 12/12/2022.

Comissão Julgadora	**Resultado**
Prof. Titular **Gherhardt Ribatski** **(Orientador)** (Escola de Engenharia de São Carlos – EESC/USP)	APROVADO
Prof. Dr. **Alberto Hernandez Neto** (Escola Politécnica/EP-USP)	APROVADO
Profa. Dra. **Elaine Maria Cardoso** (Universidade Estadual Paulista "Júlio de Mesquita Filho"/UNESP-Ilha Solteira)	APROVADO
Prof. Associado **Leopoldo Pisanelli Rodrigues de Oliveira** (Escola de Engenharia de São Carlos – EESC/USP)	APROVADO
Prof. Dr. **Luiz Machado** (Universidade Federal de Minas Gerais/UFMG)	APROVADO

Coordenador do Programa de Pós-Graduação em Engenharia Mecânica:
Prof. Associado **Adriano Almeida Gonçalves Siqueira**

Presidente da Comissão de Pós-Graduação:
Prof. Titular **Murilo Araujo Romero**

The present Thesis is dedicated to my beloved parents, for their love, endless support, encouragement, and wisdom advices.

ACKNOWLEDGEMENTS

I would like to acknowledge the financial support provided by CAPES (Coordination for the Improvement of Higher Education Personnel) - Financial Code - 001, CNPq (National Council for Scientific and Technological Development) under process number of 141946/2017-2, and the infrastructure and personnel provided by the University of São Paulo. Also, I would like to express my sincere gratitude to be part of the Heat Transfer Research Group at EESC/USP since 2014 and for the friendship developed during these years: André, Andres, Alex, Alexandre, Bianca, Daiane, Daniel, Débora, Douglas, Francisco, Gabriel, Guilherme, Gustavo, Hugo, Maurício, Tiago, Valter, and Victor. The technical support and the test bench development by Mr. José Roberto Bogoni and the automation of the test bench and the software acquisition development by Eng. Jorge Nicolau are deeply recognized. I also would like to thank Prof. Leopoldo P. R. de Oliveira for always being present and sharing his knowledge of acoustic fundamentals in this interdisciplinary research. Foremost, I shall thank my advisor, Prof. Gherhardt Ribatski for the opportunity, expertise, assistance, guidance, and patience throughout this thesis. Without his help, this work would not have been possible.

Behind this entire journey, I would thank my parents for their love and endless support. My parents Erivelto dos Santos and Renata do Carmo provided me all the opportunities, experiences, and wisdom advices encouraging me as I grew up. I could not ask for better parents. I also would like to express my gratitude for my beloved girlfriend Jakeline Ferreira for the support during this journey.

ABSTRACT

DOS SANTOS FILHO, E. **Evaluation of flow-induced noise, structure vibration, and flow morphology of R134a flowing through a thermostatic expansion valve**. 2022. 179p. Thesis (Doctor of Science) - São Carlos School of Engineering, University of São Paulo, São Carlos, 2022.

The flow-induced noise in refrigerators, vending machines, and air-conditionings deserves attention since residential/commercial environments provide good acoustic propagation conditions. As additional constraints, the expansion device is usually located in the indoor unit, deteriorating the silent environment and leading to unwanted and annoying noise to the customer. Up to the present date, a limited but increasing number of studies have explored the outcome of flow-induced noise in expansion devices such as capillary tubes, short-orifice tubes, thermostatic, and electronic expansion valves. The number of studies concerning flow-induced noise in thermostatic expansion valves are even more scarce. As novelty, the current doctoral thesis aims to fill a gap in the literature by experimentally evaluating the two-phase flow morphology upstream and downstream the flow restriction, structure vibration, and external and internal flow-induced noise of R134a flowing through a commercial thermostatic expansion valve. Results were obtained for a borosilicate test section with an internal diameter of 10.12 mm for mass flow rate from 0.02 to 0.04 kg/s (mass velocity from 4583 to 36701 kg/(m^2s)), saturation pressure and temperature upstream of the expansion valve from 7.7 to 10.2 bar and from 30 to 40ºC, respectively, expanding into a low-pressure reservoir at 4.1 bar and saturation temperature of 10ºC for inlet liquid subcooled degree from -15ºC up to vapor qualities of 15% and outlet vapor qualities ranging from 8 to 34 %. This study was carried out for a commercial expansion valve with outlet orifice diameter of 2.52 mm and aperture varying from 7 to 100%. Images of the flow morphology upstream and downstream of the expansion valve were obtained and correlated with the flow-induced noise and test section structure acceleration. Isolated bubbles, coalescing bubbles, churn, and annular flow patterns were observed in the images recorded upstream the expansion valve. Downstream of the valve, the flow morphology displayed a chaotic behavior due to the fluid flashing process, therefore it was not possible to classify the flow according to well-known flow patterns as defined in the literature. In addition, the velocity of the jets exiting the expansion valve orifice was estimated along the visualization section. The flashing jet was characterized as a wave of liquid followed by dispersed bubbles. The jets exhibited an approximately constant velocity of 20 m/s for subcooled liquid upstream of the valve, regardless of the experimental condition. As the subcooled liquid evolves into two-phase flow at the valve inlet, the jet velocity increases abruptly. On the other hand, under annular flow conditions at the valve inlet, the jet velocity remains approximately constant independently of the experimental condition. In addition, the jet velocity decreases as it flows along the visualization section. Jet frequencies observed at 48 and 96 Hz were similar to the values found for the external noise. The total sound pressure level of the external noise and the structure acceleration exhibited

similar trends with increasing the vapor quality at the valve inlet. Moreover, superior structure acceleration and external and internal noise were found for isolated bubbles at the valve inlet. The frequency spectrum behavior of the external noise and acceleration of the test section were almost similar, while the noise evaluated at the valve decreases asymptotically with increasing frequency. Finally, the parametric analysis revealed that the external noise and acceleration of the structure are directly related to the flow pattern, jet velocity, and vapor quality; however, a noise dependence of the mass flow and pressure drop across the expansion device was not found. Furthermore, no parametric effect of the measured and estimated variables on the internal flow-induced noise was identified. Besides, statistically it was not found effect of the inlet/outlet vapor quality, mass flow rate, external noise, test section acceleration, pressure drop, and jet velocity on the internal noise.

Keywords: Refrigerant flow-induced noise. Refrigeration. Thermostatic expansion valve. Two-phase flow. Air-conditioning.

RESUMO

DOS SANTOS FILHO, E. **Avaliação do ruído induzido pelo escoamento, vibração da estrutura e morfologia do R134a através de uma válvula de expansão termostática**. 2022. 179p. Tese (Doutorado) - Escola de Engenharia de São Carlos, Universidade de São Paulo, São Carlos, 2024.

O ruído induzido pelo escoamento em refrigeradores e sistemas de condicionamento de ar merecem atenção, pois ambientes residenciais/comerciais proporcionam condições adequadas para propagação sonora. Dispositivos de expansão são normalmente posicionados no interior das residências, deteriorando o silêncio do ambiente e resultando em ruídos indesejados e incômodos ao usuário. Até o presente momento, um número crescente de estudos, porém limitado, exploraram o ruído induzido pelo escoamento em dispositivos de expansão, como tubos capilares, tubos de orifício, válvulas de expansão termostáticas e eletrônicas. O número de estudos abrangendo o ruído induzido pelo escoamento em uma válvula de expansão termostática é ainda mais escasso. Neste contexto, a presente tese de doutorado apresenta uma avaliação experimental inédita da morfologia do escoamento bifásico a montante e jusante do orifício de expansão, vibração da estrutura e do ruído interno e externo induzido pelo escoamento de R134a através de uma válvula de expansão termostática com características comercial. Os resultados foram obtidos para uma seção de teste de borossilicato com um diâmetro interno de 10,12 mm, vazão mássica de 0,02 a 0,04 kg/s (velocidade mássica de 4583 a 36701 kg/(m^2s)), pressão e temperatura de saturação a montante da válvula de expansão de 7,7 a 10,2 bar e 30 a 40ºC respectivamente, expandindo em um reservatório a pressão e temperatura de saturação de de 4,1 bar e 10ºC, respectivamente. Os testes foram executados para líquido subresfriado de até -15ºC até títulos de vapor de 15% a montante da válvula expandindo para títulos de vapor de 8 a 34 %. Imagens da morfologia do escoamento a montante e a jusante da válvula de expansão foram obtidas e correlacionadas com o ruído induzido pelo escoamento e a aceleração da seção de testes. Os padrões de bolhas isoladas, bolhas coalescentes, agitante e anular foram observadas nas imagens registradas a montante da válvula de expansão. A jusante da válvula, a morfologia do escoamento mostrou-se caótica devido ao processo de evaporação do fluido, não podendo ser classificada de acordo com os padrões de escoamento previamente definidos na literatura. Além disso, foi estimada a velocidade dos jatos partindo do orifício da válvula de expansão ao longo da seção de visualização. Os jatos foram caracterizados como frentes de líquido seguidas por bolhas dispersas. Os jatos exibiram velocidades aproximadamente constantes de 20 m/s para líquido sub-resfriado a montante da válvula, independentemente da condição experimental. A transição de líquido subresfriado para escoamento bifásico na entrada da válvula resultou em um aumento abrupto na velocidade do jato. Por outro lado, com o estabelecimento do padrão anular na entrada da válvula, a velocidade do jato manteve-se aproximadamente constante independente da condição experimental. Além disso, a velocidade do jato diminui ao longo da

seção de visualização. As frequências de jato observadas em 48 e 96 Hz foram semelhantes às frequencias encontradas no ruído externo. A avaliação do ruído externo e da aceleração da seção de testes apresentaram tendências semelhantes com incremento do título de vapor. Além disso, observou-se elevados ruído externo, interno e vibrações da seção de testes para a presença de bolhas isoladas na entrada da válvula. O espectro de frequência apresentou comportamento semelhante para o ruído externo e aceleração da seção de testes, enquanto o ruído interno apresentou comportamento distinto. Por fim, a análise paramétrica revelou que o ruído externo e a aceleração da seção de testes estão diretamente relacionados ao padrão do escoamento, velocidade do jato e título de vapor; no entanto, são independentes do fluxo mássico e da diferença de pressão através do dispositivo de expansão. Além disso, estatisticamente não foi encontrado efeito do título de vapor de entrada/saída, vazão mássica, ruído externo, aceleração da seção de teste, queda de pressão e velocidade do jato sobre o ruído interno.

Palavras-chave: Ruído induzido pelo escoamento. Refrigeração. Válvula de expansão termostática. Escoamento bifásico. Ar-condicionado.

LIST OF FIGURES

LIST OF TABLES

LIST OF SYMBOLS

Nomenclature

a	Wall length in the x-axis direction [m]
A	Area [m^2]
b	Wall length on the y-axis direction [m]
B	Bending stiffness per unit length [Nm]
c	Speed of sound [m/s]
c_l	Longitudinal wave speed [m/s]
c_p	Specific heat at constant pressure [J/kgK]
c_v	Specific heat at constant volume [J/kgK]
D	Diameter [m]
E	Young's modulus [Pa]
f	Friction factor [–]
$\dot{f}$	Frequency [Hz]
$\dot{f}_c$	Critical frequency [Hz]
G	Mass velocity [kg/m^2s]
$\dot{G}$	Dimensionless rectangular plate frequency coefficient [–]
h	Heat transfer coefficient [W/m^2K]; Wall thickness [m]
H	Dimensionless rectangular plate frequency coefficient [–]
i	Enthalpy [kJ/kg]
I	Sound intensity [W/m^2]
I_L	Sound intensity level [dB]
j	Imaginary unity [–]
J	Dimensionless rectangular plate frequency coefficient [–]
k	Thermal conductivity [W/mK] Polytropic index [–]

K	Bulk modulus [Pa]
l	Length of the bubble from center to the end of the one side [m]
L	Length [m]
L_B	Length from center of the bubble to the center of the liquid column [m]
L_P	Sound pressure level [dB]
m	Mass per unit area [kg/m^2]
$\dot{m}$	Mass flow rate [kg/s]
M	Molar mass [g/mol]
p	Pressure [Pa]
Q	Heat [W]
r	Radius [m]
R	Universal gas constant [J/molK]
R_0	Sound reduction index [dB]
R_d	Sound reduction index for a diffuse field [dB]
t	Time [s]
T	Temperature [K]
x	Vapor quality [–]
z	Coordinate along tube axis [m]
Z_g	Surface impedance [Pas/m]
Z_0	Air impedance [Pas/m]

Greek Symbol

α	Void fraction [–]
β	Contact angle [Degree]
Δp	Pressure drop [Pa]
ΔT	Mean logarithm temperature difference [C]

ε	Surface roughness [m]
η	Loss factor [–]
Θ	Angle [Degree]
$\varkappa$	Wave number [m^{-1}]
λ	Wavelength [m]
μ	Dynamic viscosity [N/m^2s]
ν	Poisson's ratio [–]
ξ	Wavenumber ratio [–]
ρ	Specific weight [kg/m^3]
σ	Radiation factor [–]
Γ	Pearson's correlation coefficient [–]
τ	Transmission factor [–]
ω	Angular frequency [radians/s]
Π	Sound power [W]

Subscripts

0	Initial condition
air	Referent to air medium
accel	Accelerational
b	Bubble
c	Channel
fric	Friction
g	Gas
grav	Gravitational
hs	Heater section
i	Index

in	Inlet
int	Internal
l	Liquid
lg	Difference from liquid to gas properties
lo	Liquid only
loss	Refereed to heat losses
max	Maximum
n	Natural
o	Orifice
out	Outlet
p	Plate
ref	Reference
room	Ambient
sat	Saturation (Thermodynamic)
sub	Subcooled
rms	Root-mean-square
ts	Test section
x	X-axis direction
y	Y-axis direction
z	Z-axis direction
2φ	Two-phase

Dimensionless numbers

$Nu = \frac{hD}{k}$	Nusselt number
$Re = \frac{\rho v d}{\mu}$	Reynolds number

Acronyms

CB	Coalescence bubble
EEV	Electronic expansion valve
HCC	Honeycomb cylinder
IB	Isolated bubble
PCC	Pearson's correlation coefficient
PMD	Porous metal disc
PWM	Pulse with modulation
ROI	Region of interest
SC	Subcooled
SPL	Sound pressure level
TSPL	Total sound pressure level
TXV	Thermostatic expansion valve
WSS	Within-cluster sum of squares

CONTENTS

1 INTRODUCTION

Designing expansion devices with low refrigerant induced noise is still a great challenge, since this kind of noise occurs irregularly during the thermodynamic cycle. Noise in household refrigeration system can be from the compressor and ventilators, but also can be from the induced noise of the refrigerant flowing in the pipes and the expansion device. The expansion devices induce mechanical vibration as combination of shear, turbulence and/or shock wave interaction during the expansion process (REETHOF, 1977). This mechanical vibrations may propagate through the components being able to produce resonance, and also propagates as sound waves through the air, reaching the human ear (SINGH et al., 1999).

The noise emission of household refrigerators deserves attention because residential environment provides suitable conditions for acoustic propagation (JEON; YOU; CHANG, 2007). For conventional air-conditioning with high cooling capacity, the expansion device is usually disposed in the indoor unit, deteriorating the indoor silent environment (HIRAKUNI et al., 2004). Flow-induced noise is unwanted and sometimes annoying, which increases the costs associated with service call and also affects the consumer perspective of the product and the manufacturer. According to Soeta and Shimokura (2017), the flow-induced noise in electronic expansion valve (EEV) is the main cause of annoyance to machine operators and customers.

The human sound perception of sound quality is not only represented by sound pressure level (SPL) (LIU; DONG; ZHAO, 2017; ZWICKER; FASTL, 2013), but also by the customer psychological feelings of the noise (SUN et al., 2017). Therefore, to improve the sound quality, studies have been conducted on the use of objective psychoacoustics metrics such as A-weighted sound pressure level, loudness, sharpness, and fluctuation strength (ZHAO; WU, 2020), jury tests (TUZE; K; M, 2020) that directly access the subjective perception of humans and correlations of both (BAARS; LENZI; NUNES, 2002) as the former provides a straightforward objective tool, while the latter requires time, statistical data processing, and ethical aspects due to the involvement of humans for the data acquisition. Liu, Dong and Zhao (2017) pointed out that the loudness and sharpness were proved effective in sound quality evaluation of air-conditioning noise. Moreover, Boabaid Neto et al. (2014) suggested that the acoustic excitation at the expansion device outlet is high enough to induce significant vibration at the evaporator, which may reduce the component lifetime. In this context, Han et al. (2009) pointed out that the noise at the evaporator inlet is the highest sound level among the equipments of the refrigeration system.

The flow-induced noise by refrigerant has not been extensively studied, but only as a subject of interest for troubling shooting of refrigerator and air-conditioning units (AOYAMA et al., 2006; UMEDA, 1994; HAN et al., 2009). The most effective and least expensive way to reduce unwanted noise is to reduce the noise at the source (ASHRAE, 2013). It is worth mentioning that modification to the pipe layout, outlet capillary geometry and introduction of

artefacts to change the flow pattern at the expansion device are passive and permanent ways to reduce the flow-induced noise at low-cost.

ASHRAE (2013) recommends design guidelines for HVAC background noise in a guest room should be from 25 to 35 dB, houses from 30 to 35 dB, schools from 25 to 30 dB, libraries 30 dB, hospitals and clinics from 30 to 35 dB, and offices from 25 to 40 dB. The studies in the literature concerning the evaluation of external and internal flow-induced noise of expansion devices exhibit values from 17 to 55 dB and from 117 to 153 dB, respectively. Table 1 illustrates examples of decibel levels and the human reaction.

Table 1 – Typical Sound Pressures Levels (SPL).

Source	SPL (dB)	Subjective reaction
Military jet takeoff	140	Extreme danger
Artillery fire	130	Threshold of pain
Automobile horn	100	Very loud
Accelerating diesel truck	80	Loud
Normal conversation	60	Moderate
Quiet residential area	40	Quiet
Whispered conversation	30	
Buzzing insect	20	Perceptible

Source: ASHRAE (2013)

The expansion devices can be divided in two classes: the constant (capillary tube and short-tube orifice) and the variable restriction types (electric and thermostatic expansion valves). Capillary tubes are narrow and long tubes with diameter ranging from 0.5 to 3 mm and length from 1.0 to 6.0 m. It is a low-cost device with no moving parts; hence it does not require maintenance. Additionally, the cooling capacity is affected by the capillary length (SARAVANAN; LAL; SELVAM, 2020). Due to its structural characteristic, it cannot be adjusted to changes in the flow conditions and the flashing process due to daily and seasonal variations in ambient temperature and load. Capillary tubes are commonly found in household refrigeration systems.

In the last two decades, the short orifice tube has been widely employed as an expansion device in residential and automotive air-conditioning (SHAH, 2009). According to Fang (2001), the short tube orifice employed in small residential air conditioners are manufactured with small bore hollow brass ingots with lengths ranging from 10 to 13 mm and length/diameter ratios ranging from 3 to 20, while the diameter and length/diameter of short tube orifices for automotive application are 1 to 2 mm and 21 to 35 mm length/diameter ratios. Although the capillary and short tube orifice geometrical designs are simple, the two-phase flow phenomenon inside them is complex (NILPUENG; WONGWISES, 2012; Boabaid Neto et al., 2018). Experimental results indicate that chocked and metastable flow phenomena occur in these devices under normal operational conditions in air-conditioning and heat pumps (AARON; DOMANSKI, 1990; KIM; O'NEAL, 1995; LIU et al., 2004). According to Nilpueng and Wongwises (2012), the short

orifice tube has the benefice of low starting compressor torque, however it is only suitable for one operating condition, usually presenting metastable flow and chocked flow at the outlet (Simões-Moreira and Bullard, 2003). Therefore, the evaluation of flow pattern and its correlation to the flow-induced noise in theses expansion devices are difficult tasks.

The thermostatic expansion valve (TXV) is a device capable of controlling the refrigerant flow, maintaining nearly constant superheat temperature at the exit of evaporator, protecting the compressor from damage. Any oscillation at the refrigeration system load is adjusted by changing the valve aperture, which is controlled by the evaporator outlet temperature. Electronic expansion valves are similar to the TXV, however the aperture in these devices is regulated by a pulse with modulation (PWM) providing more precise control of the refrigerant flow rate. The expansion valves are commonly found in refrigeration systems with higher load capacity as heat pumps, chillers, air-conditioning, and ice and vending machines. Figure 1 illustrates expansion devices and their applicability.

Figure 1 – Expansion devices and their characteristic applications.

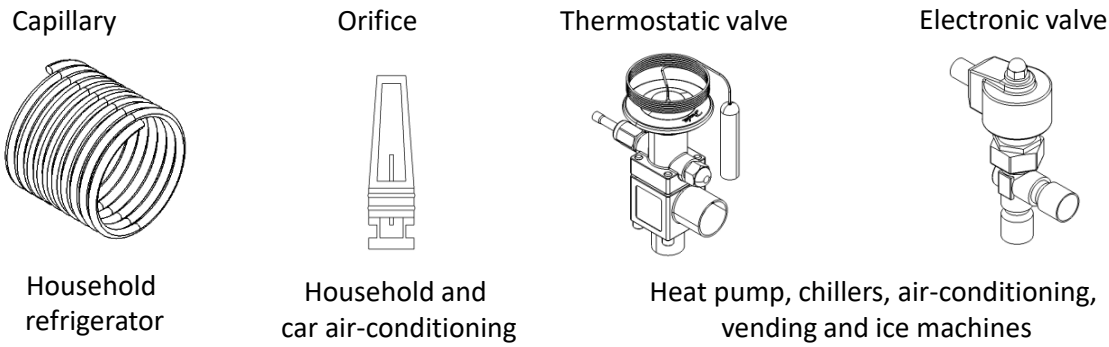

Source: Author

The previous studies in literature concerning refrigerant flow-induced noise have attempted to investigate the relationship between the noise and the following parameters: flow orientation, flow patterns, mass velocities, in/outlet vapor qualities, in/outlet temperature and pressure, capillary diameter and length, capillary outlet geometry, valve aperture, and the effect of a porous midia on the flow pattern for different fluids. Han, Jeong and Kim (2011) suggested that the noise is strongly related to the flow patterns, since the acoustic characteristic of the flow is directly associated to the size and shape of the bubble. Under conditions that the bubbles assume long shape, such as slug flow the produced noise is higher than for the others flow patterns, such as annular and stratified flows (HAN; JEONG; KIM, 2011). Recently, Kim et al. (2019) pointed out that to avoid noise generation, the tube should be placed horizontally, and the mass flux should be increased to generate annular flow. However, in the refrigeration machines design, the increase in the inlet vapor quality at the expansion device leads to a reduction in the refrigeration capacity.

With the focus on reduce the SPL in capillary tubes, Xia et al. (2014) employed a numerical simulation to determine the turbulent kinetic flow energy during the transition from capillary outlet to evaporator inlet for distinct outlet capillary geometry. These authors were able to experimentally reduce the noise of the cooling system only by adjusting capillary outlet geometry for the lowest turbulent kinetic flow energy.

Boabaid Neto et al. (2018) claim that the inner diameter of the capillary is the main parameter that affects the noise performance of the system, once it is related to the vortex formation in the filter-dryer, which directly affects the flow pattern. On the other hand, Ruebeling and Grohmann (2020) pointed out that the SPL increases as the outlet vapor quality increases, regardless the flow pattern. Moreover, Tannert and Hesse (2016) and Apaydin and Heperkan (2016) pointed out that the fluid along the capillary tube is under several complex phenomena such as metastable flow (CHEN, 1997). In addition to this, the condensation of the vapor bubbles within the capillary tube flow can also be a source of anomalous noise (MCLEVIGE; MILLER, 2001; HARTMANN; MELO, 2013). Furthermore, it is well known that an intense acoustic excitation is promoted by the jet formed at the outlet of the capillary tube (LIGHTHILL, 1963; REETHOF, 1978).

Additionally, Koberstein et al. (2015) identified that even the suction pilot length and its joint geometry with the TXV may result in a unwanted noise. As a passive approach to reduce the noise, Hirakuni et al. (2004) came up with porous pieces of metal positioned directly at the EEV inlet and outlet in order to change the flow pattern from slug to bubbly flow, reducing the noise level up to 13 dB. According to these authors, the pressure fluctuation at the inlet of EEV without the porous material is related to the distinct velocity of the gas and the liquid phase passing through the pressure sensor of the EEV, which induces vibration.

The two-phase flow-induced noise phenomena has not yet been fully understood and the discrepancies in literature among the results obtained by independent laboratories make difficult to perform systematic comparison among different studies. In fact, there is a reduced number of studies in literature concerning the noise during expansion process in a expansion valve, and most of the studies does not provide all the information about how the experiments were conducted. Therefore, additional research is still needed to better understanding the effects of the operational conditions on the level of the flow-induced noise and to compare the results under similar experimental conditions among independent laboratories.

In this context, the present study aims to contribute to the knowledge concerning the acoustic characteristics of internal and external flow-induced noise and structure acceleration in a thermostatic expansion device. The experiments were performed for R134a flowing through the flow restriction region of a commercial expansion valve assembled between two borosilicate glass tubes with I.D. of 10.12 mm vertically displayed. Moreover, the glass tube allows the investigation of the flow morphology upstream and along the expansion process, which has no precedent in the literature as far as the present author knows. Therefore, as a novelty, this study

fills a gap in the literature by evaluating the in/outlet TXV flow pattern, internal and external flow-induced noise, and structure acceleration. A parametric analysis was also performed in order to better understand the effect of the fluid inlet subcooling degree, vapor quality, flow pattern, mass flow rate, pressure drop, and jet velocity on the internal and external flow-induced noise and the structure acceleration.

1.1 Study objectives

The main objective of this study is to characterize the flow pattern and inlet subcooling degree/vapor quality upstream of the TXV and cross-correlate them to the internal and external flow-induced noise, and fluid-structure acceleration. Moreover, this study aims to investigate the parametric effect of the inlet subcooling degree/vapor quality, pressure drop, and mass flow rate on the jet velocity along the visualization section downstream the TXV. Based on the noise and structure acceleration measured along the time it is possible to investigate the frequency spectrum analysis to identify potential peaks of excitation and its coherence signal.

1.2 Document organization

The present document is organized according to the following chapters:

- Chapter 2: a literature review on acoustic characteristics of two-phase flow in pipes and flow-induce noise in expansion devices such as capillary tube, short-orifice tube, thermal and electrical expansion valve is presented. In this analysis, focus is given on performing comparative and relative analyses among the experimental studies regarding the parametric effect of vapor quality, mass velocity, pressure drop, flow pattern, and expansion device characteristic on the flow-induced noise.

- Chapter 3: a detailed description of the experimental apparatus designed and built to conduct the experimental work and to study the flow-induced noise through a TXV is provided.

- Chapter 4: in this chapter, the data regression procedure, the experimental uncertainty, and the experimental procedure are detailed. It is also presented the validation of the experimental apparatus. At the end of this chapter, the experimental matrix of the database obtained in this study is presented.

- Chapter 5: the experimental results for flow morphology, outlet TXV jet velocity, internal and external flow-induced noise, and structure acceleration are presented. Moreover, a parametric analysis of the data is performed and the main trends are identified. Focus is given on identifying the phenomenological aspects of the flow-induced noise by cross-

correlating the structure acceleration, external and internal noise signals, inlet flow pattern, and vapor quality.

- Chapter 6: in this chapter, the main conclusions drawn from the experimental results obtained in this study and recommendations for future investigations are outlined.

This document also counts with the following appendix

- Appendix A: the fundamental parameters of two-phase flow are presented, followed by a brief description of gas-liquid flow patterns. Then, the fundamentals of acoustic and definitions of the sound transmission parameters are described. It also presents predictive methods for sound transmission loss for isotropic materials based on a single layer element.
- Appendix B: detailed description of the procedure adopted for the calibration of the temperature measurements.
- Appendix C: detailed description of the procedure adopted for errors to the estimated parameters.

2 LITERATURE REVIEW

The subjects covered in this chapter are the theoretical natural frequency models of bubbles with spherical and cylindrical shapes and flow-induced noise in capillary tubes, short-orifice tubes, thermal and electric expansion valves. Then the discussion proceeds with a presentation of the effects of the main parameters on the flow-induced noise such as outlet capillary geometry, capillary inner diameter and length, flow orientation, outlet vapor quality, mass velocity, pressure drop, in/outlet flow pattern, evaporation temperature, and refrigeration cycle operational conditions. At the end of the chapter, the main conclusions based on the analysis of the literature are presented and a contextualization of the current study is provided.

2.1 Characteristics noise of in-tube two-phase flows

Bubbles behave as a non-linear oscillator, and their mathematical dynamic modeling can be quite complicated. Figure 2 illustrates geometrical boundary conditions adopted in the literature (MINNAERT, 1933; DEVIN, 1961; BLUE, 1967; HAN; JEONG; KIM, 2011) in the development of theoretical models for the natural frequency of bubbles.

Figure 2 – Geometrical boundary conditions from literature for modelling the natural frequency of a gas bubble: a) Minnaert (1933), b) Devin (1961), c) Blue (1967) and d) Han, Jeong and Kim (2011).

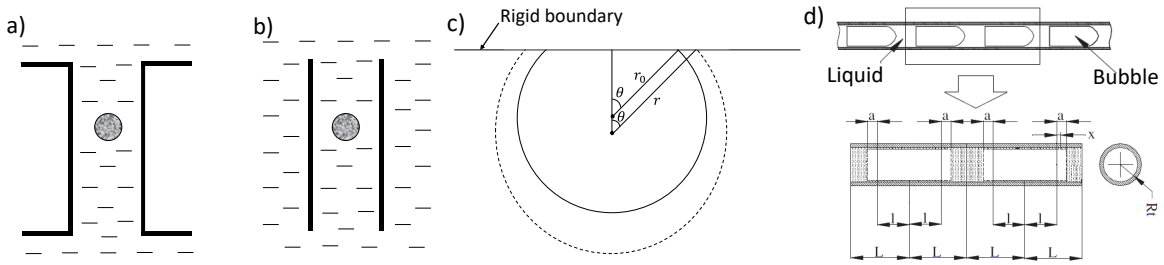

Source: Adapted by author from Minnaert (1933), Devin (1961), Blue (1967) and Han, Jeong and Kim (2011).

Minnaert (1933) proposed a model for the acoustic characteristic of a freely rising bubble in an infinite liquid medium (Fig. 2a). In his model, the theoretical estimation of the natural frequency of the bubble was derived from the first law of thermodynamics. He expressed the potential energy as adiabatic compression accumulated until the moment that the bubble volume is reduced to its minimum, as equal to the water's kinetic energy surrounding the bubble at the moment when half of the expansion has taken place, which corresponds to the equilibrium state of the bubble. It was assumed that the bubble periodically vibrates in a radial direction maintaining its spherical shape under adiabatic gas compression. Minnaert (1933) conducted

experiments for bubbles of air, hydrogen, and butane with diameters ranging from 3 to 6 mm rising in water in order to validate the accuracy of its model. The natural frequency of a bubble according to his model, is given as follows:

$$f_n = \frac{1}{2\pi r_b}\sqrt{\frac{3kp}{\rho_l}} \tag{2.1}$$

in which f_n is the resonance frequency, r_b the bubble radius, p the liquid pressure, and k is the specific heat ratio of the gas. Gases with approximate specific heat ratio would return similar results for the natural frequency since this is the only gas property included in his model. This model neglects the effects of energy dissipation due to viscosity effects. This model could predict experimental data of the natural frequency of air hydrogen and butane bubbles, with diameters from 3 to 6 mm rising in water, even though it does not accomplish the liquid downward movement and the energy dissipation due to viscosity effects (MINNAERT, 1933).

The natural frequency of bubble confined in a channel (Fig. 2b) is described in a brief unpublished report by Devin (1961). For configurations characterized by tube radius much larger than the bubble, as should be the case of a bubble entrained in a macroscopic flow, the model proposed by Minnaert (1933) can be employed as an approximation. Devin (1961) performed experiments for bubbles generated from a needle placed at the center of a vertical open tube with negligible tube wall thickness immersed in an unbounded liquid. In his model, the natural frequency is given as follows:

$$f_n = f_0\sqrt{\left[1 + \frac{2r}{r_c}\left(\frac{L/2 + 1.22r_c}{r_c} - 1.108\right)\right]^{-1}} \tag{2.2}$$

in which f_0 is the natural frequency of a bubble in an infinity liquid determined according to Minnaert (1933) model, r_c is the radius of the channel, and L is the tube length. The term in brackets is greater than one, therefore the natural frequency proposed by Devin (1961) presents lower resonance frequency than those predicted by Minnaert (1933). The value 1.22 comes from the assumption that bubble is geometrically located at the midpoint of the tube.

Blue (1967) developed a theoretical model for the resonant frequency of a bubble attached to a rigid infinite plane, taking into consideration the contact angle of the bubble resting against the plane. Due to the buoyancy force, the bubble will be slightly flattened against the boundary (Fig. 2c). However, the author assumed that bubble shape would be retained during resonance; hence the contact angle β will remain unaltered. The natural frequency equation was derived from energy equation assuming adiabatic conditions and neglecting surface tension and viscosity. In his model, the natural frequency of the bubble is given by the following equation:

$$f_n = \frac{1}{2\pi r_0}\sqrt{\frac{3kp}{\rho_l(1+\cos\beta)}} \tag{2.3}$$

where r_0 is the initial bubble radius. Thus, a bubble contacting a rigid boundary will present inferior resonant frequency than the model proposed by Minnaert (1933), since this model differs

from Eq. 1 by 1/(1+cosβ), with β ranging from 0 to 90°. In fact, Blue (1967) performed an experiment and compared the present theoretical model against the proposed models of Minnaert (1933). For the resonance bubble frequency of 33 kHz and 36 kHz, Blue (1967) evaluated experimentally a bubble radius of 76 and 67 μm, and his model predicted a radius of 77 and 71 μm, while Minnaert (1933) model over predicted the Blue (1967) results, finding a radius of 99 and 91 μm, respectively.

Han, Jeong and Kim (2011) developed a theoretical model for natural frequency for intermittent flow pattern based on the energy conservation considering a single bubble. These authors assumed the bubble as cylindrical-shaped with both ends as flat surfaces as illustrated in Fig. 2d. From Fig. 2d, a is the amplitude of displacement of oscillating bubble, l is the bubble length from center to the end of one side, L_B is the length from the center of the bubble to the center of the liquid column, and X is the axial bubble displacement. In this model, the authors have assumed that the bubble only oscillates in axial direction because the movement on radial direction is restrained by the channel wall. According to their model the natural frequency of the bubble is given by the following equation:

$$f_n = \frac{1}{2\pi l}\sqrt{\frac{kp}{\rho_l(L_B/l - 1)}} \tag{2.4}$$

From Eq. 2.4, it is possible to infer that the noise from slug flow is strongly dependent of the frequency of the bubble. The model proposed by Han, Jeong and Kim (2011) is based on the following assumptions: (i) axial bubble displacement is negligible compared to the distance from bubble center to its end, (ii) liquid backflow is ignored, (iii) energy losses due to non-linear effects such as viscosity and thermal conduction are ignored, and (iv) friction does not affect the resonance frequency of the bubble, however reduces its oscillation amplitude. The reduction of the amplitude oscillation implies on bubble energy losses once the amplitude displacement is directly related to the bubble potential energy. According to Oguz and Prosperetti (1998), the acoustic losses are predominant for bubbles with a radius larger than several millimeters, while the viscous dissipation becomes significant for bubbles smaller than 10 μm. It is also important to highlight that on practical applications, the slug flow pattern does not occur symmetrically distributed on the cross-sectional area and with bubbles of same size, and it also, frequently, exhibits small bubbles attached to vapor phase tail as already registered in the literature (REVELLIN; THOME, 2007; REVELLIN et al., 2006; ONG; THOME, 2011; TIBIRIÇÁ; RIBATSKI, 2014; TIBIRIÇÁ; CZELUSNIAK; RIBATSKI, 2015; WANG; CHENG; BERGLES, 2008).

Figure 3 shows the comparison between the predictive methods for the natural frequency and the experimental data of slug bubbles from Han, Jeong and Kim (2011) for adiabatic flow in a channel with 10 mm diameter employing R600a as test fluid. In order to employ the natural frequency model of Minnaert (1933), Han, Jeong and Kim (2011) considered a possible equivalent radius of a sphere with the same volume as the experimental cylindrical bubble. As depicted in Fig. 3, such approximation resulted in a much higher natural frequency prediction.

The prediction method from Devin (1961) estimated the frequency from 170.0 to 775.5 Hz, over predicting parcel of the experimental results. He assumed that bubble holds a diameter inferior to the tube, which is unsuitable for evaluating the natural frequency of slug flow. The model proposed by Han, Jeong and Kim (2011) estimated the slug natural frequency from 133.9 to 501.0 Hz, showing a reasonable agreement with the experimental results. It is also possible to notice that the natural frequency of long-cylindrical shaped bubble is lower than a spherical bubble rising in infinite liquid with same volume. This behavior is related to the superior length l when compared to a spherical bubble radius r_b.

Figure 3 – Comparison of natural frequency predictive methods (DEVIN, 1961; MINNAERT, 1933; HAN; JEONG; KIM, 2011) and Han, Jeong and Kim (2011) experimental results.

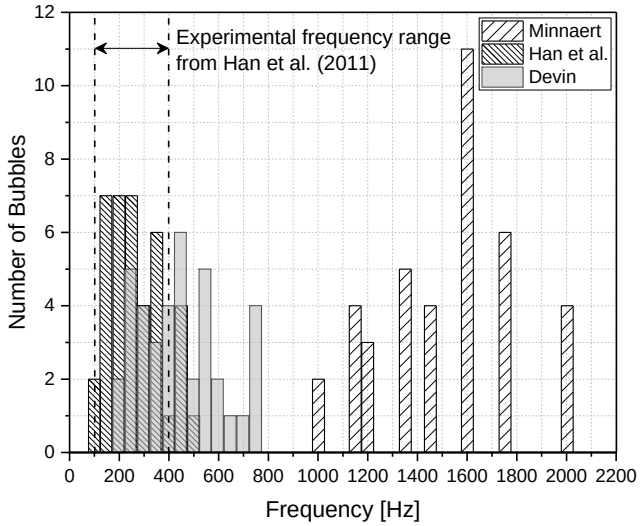

Source: Adapted from Han, Jeong and Kim (2011).

Figure 4 shows the comparison of the natural frequency predicted by methods (MINNAERT, 1933; BLUE, 1967; HAN; JEONG; KIM, 2011) from literature for the refrigerants R134a, R600a, R410a and R22. The capillary tubes are characterized by internal diameters ranging from 0.5 to 3 mm, therefore, according to the models proposed by Minnaert (1933) (Fig. 4a) and Blue (1967) (Fig. 4b) a spherical bubble flowing in a capillary tube presents a minimum natural frequency of 1 kHz for bubble with diameter similar to the internal capillary diameter, increasing as the capillary diameter decreases. Their model, fundamentally, differs from the refrigerant contact angle that is not taken into account by the first. In order to implement the model of Blue (1967) a contact angle of 5^o on a copper surface was considered as suggested by Lu, Liu and Xu (2016). Figure 4(c) illustrates predictions according to the method of Han, Jeong and Kim (2011) comparing the ratio between the bubbles distance and bubble length versus the natural frequency for four distinct tube diameter and three slug lengths based on the pipe diameter. According to Fig. 4(c), as the tube diameter and the bubble length increases the resonance frequency decreases. As show in Fig. 4(d) the natural frequency increases as the

evaporation temperature increases, such result is expected since the saturation pressure increases with temperature, while the liquid density and the polytropic index remains almost constant.

Figure 4 – Natural frequency models proposed by a) Minnaert (1933), b) Blue (1967), c) Han, Jeong and Kim (2011) and d) the frequency prediction models versus evaporation temperature.

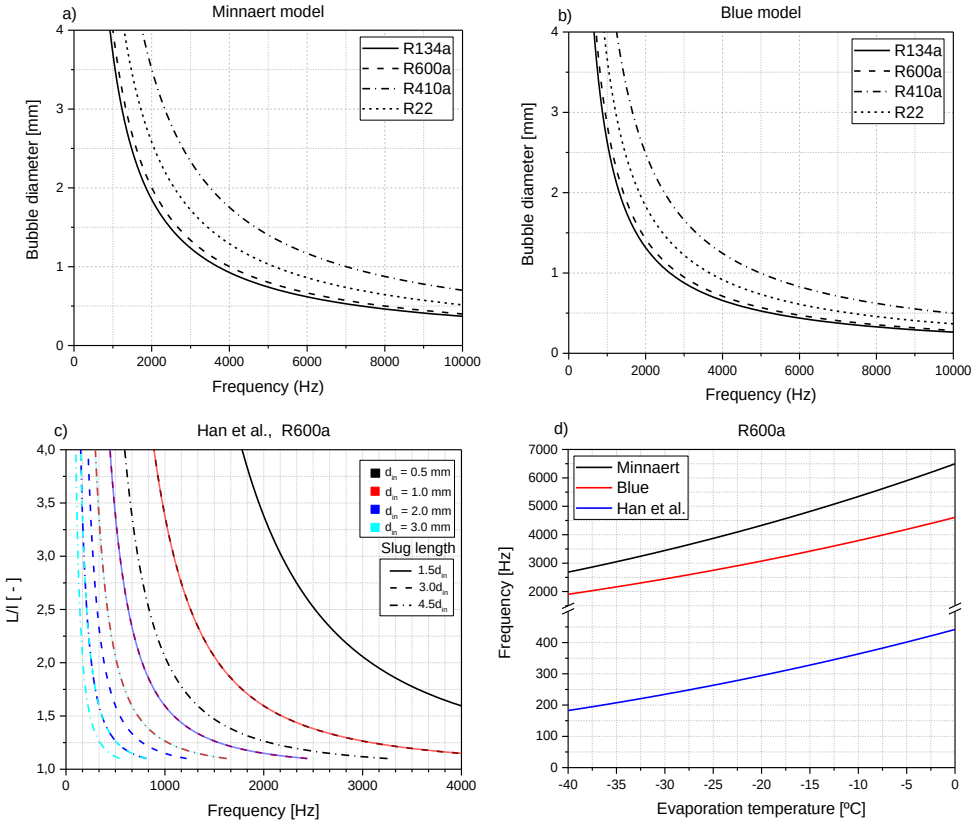

Source: Author

In summary, the available studies concerning natural frequency models for flow-induced noise are based on the derivation of energy equation for spherical and cylindrical bubbles. Therefore, there is a lack in the literature of methods for prediction of the natural frequency for churn, annular and wavy flow patterns, which may be explained by the fact that characterizing geometrically and hydrodynamically such flows is a very difficult task.

2.2 Flow-induced-noise in expansion devices

The investigation of two-phase flow-induced noise of refrigerants in expansion devices is a relatively new topic in literature, with most of the studies being dated from the last two decades. Hence, the investigations on this new topic seems to be at early stages. Tables 2 and 3 present a compilation of the studies in literature concerning flow-induced noise in refrigeration systems by expansion devices. In these tables, the studies are classified according to the expansion device category: capillary tube, short-orifice tube, thermal and electric expansion valves. The majority

of the studies outlined in Tab. 2 and 3 evaluated the SPL for horizontal layout using R600a as test fluid in capillary expansion devices for household refrigerators. Half of these studies evaluated the noise within the flow, while the other half built anechoic chambers to measure de noise from outside. Unfortunately, as an attempt to investigate the cross-correlation between the noise and the flow pattern, only parcel of the authors performed flow visualizations (HAN et al., 2009; HIRAKUNI et al., 2004; HAN; JEONG; KIM, 2011; HAN et al., 2010; TANNERT; HESSE, 2016; CELIK; NSOFOR, 2011; KIM et al., 2019). Researches also evaluated the structural acceleration excitation as an attempt to cross-correlate it to the flow pattern (SINGH et al., 1999; HAN et al., 2009; Boabaid Neto et al., 2014; HAN; JEONG; KIM, 2011; HAN et al., 2009). Flow patterns were characterized based on either visual observations or flow pattern prediction methods from literature.

As one of the pioneer studies, Singh et al. (1999) evaluated the noise within the fluid and the capillary wall acceleration using R134a as test fluid for distinct capillary outlet geometry and length, covering a wide range of experimental conditions, including vapor single-phase at the inlet of the expansion device. Unfortunately, these authors did not perform flow pattern visualizations. Boabaid Neto et al. (2018) performed their experiment employing R600a in a commercial household refrigerator evaluating the SPL within the outlet capillary under distinct refrigerator load and distinct ambient temperature to better understanding the effect of the amount of liquid arriving in the filter-dryer on the SPL. These authors manufactured a transparent filter-dryer in order to visualize the flow pattern at the capillary tube inlet. According to Boabaid Neto et al. (2018), as the liquid interface within the filter-dryer approaches to the capillary inlet, the acceleration of the liquid flow caused by the suction at the capillary tube inlet promotes a vortex formation. The vortex formation depends on the refrigerator load and the inner capillary tube diameter. The vortex was pointed out by the authors as responsible for the entrainment of vapor within the capillary inlet flow, affecting the two-phase flow distribution along the capillary tube and leading to distinct noise behaviour.

Han et al. (2009) also conducted experiments for a household refrigerator. They evaluated the noise from outside the expansion device near the evaporator inlet. The investigation was performed along the operating refrigerator cycle under transient and steady-state conditions evaluating simultaneously the SPL, evaporator temperature, and estimating the vapor quality. According to this study, the intermittent flow should be avoided at the inlet of the evaporator once the vapor quality and void fraction vary irregularly over time as well as the pressure. In a subsequent study, to better capture the SPL and minimize the effect of the noise emitted from other components, Han et al. (2010) positioned the evaporator in an anechoic chamber. Once they concluded that the intermittent flow should be avoided in the previous study, their experiments were performed maintaining the original refrigerator pipe configuration and adjusting the internal diameter at the evaporator inlet to mainly establish annular flow. They have performed experiments for horizontal and vertical pipe configurations at evaporator inlet and concluded that the SPL is reduced under horizontal pipe configuration once annular flow pattern

was observed, rather than intermittent flow pattern for vertical pipe layout. Xia et al. (2014) combined a numerical study of the effect of distinct outlet capillary geometries on the SPL with an experimental investigation in a commercial freezer using R600a as test fluid in order to validate their simulation. In this work, they concluded that by changing the transition pipe geometry from capillary outlet to the evaporator inlet it is possible to reduce the fluid velocity leading to a reduction in the flow-induced noise by the refrigerant. Furthermore, Tannert and Hesse (2016) visually investigated the outlet flow patterns and cross-correlated them to the SPL and the pipe wall acceleration. They were able to distinguish the noise effects under various operating states and correlate the theoretical approach for resonance frequency and experimental results.

As shown in Tab. 3, only three investigations concerning flow-induced noise in orifices were found in literature despite of the comprehensive search performed in this study. Singh et al. (1999) investigated the SPL in orifices for a wide range of experimental conditions. Their study includes an investigation on the effect of screens at the in- and outlet of the orifice on the flow-induced noise. On the other hand, Han, Jeong and Kim (2011) investigated the SPL in an orifice for a narrow range of experimental conditions. Distinctly form the last two researchers, Hirakuni et al. (2004) investigated the effect of a porous metal disc (PMD) disposed on both sides of the orifice. The purpose of the PMD was to break the slug flow into small bubbles, reducing the amplitude of the pressure fluctuations as well as the noise. According to Tab. 3, SPL from expansion valves were studied focusing on air-conditioning applications using as working fluids the refrigerants R134a, R410A, and R22. Some of these studies evaluated the flow-induced noise for cooling and heating cycles with most of them performed for horizontal pipe layout. Almost similar experimental conditions were evaluated for the same refrigerant. The study of Singh et al. (1999) should be highlighted since these authors conducted experiments evaluating the noise within the expansion device for a wide range of vapor quality and distinct valve aperture. Kim et al. (2019), investigated the influence of the cross-correlation between flow pattern at in- and outlet of the EEV on the noise for vertical and horizontal flows. On the other hand, Jeong et al. (2007) investigated the influence of the number of open-steps and the EEV PWM control on the noise. Analogous to Hirakuni et al. (2004), Kim and Song (2020) evaluated the effects of the following flow conditioners at the EEV inlet and outlet: a single and three PMD, and a honeycomb cylinder (HCC) with distinct porous size.

In general, from an analysis of Tab. 2 and 3, it can be concluded that most studies from literature performed a parametric analysis of the effects of the operational conditions such as mass flow rate, in/outlet pressure, subcooling, vapor quality, superheating, and geometric characteristics of the expansion device on the SPL. Based on the fact that is common sense that flow-induced noise is a string function of the two-phase flow topology, the authors have also investigated the relationship between the noise and the flow patterns at the inlet and outlet of the expansion device. In these studies, the flow patterns were characterized based on either visual observations or flow pattern prediction methods from literature.

Table 2 – Summary of the experimental studies concerning refrigerant flow-induced noise in capillary tube.

Authors	Target	Equipment/ system	Fluid/ orientation	Expansion device characteristics	Mass velocity [kg/sm^2]	Flow visualization	Remarks
SPL within capillary tube							
Singh et al. (1999)	Capillary outlet	Refrigerator/ Refrigeration	R134a/ →	1.626 mm I.D.; L=0.8 m Outlet aperture 5º	4553	No	Increasing mass velocity, outlet vapor quality, and pressure difference increases the noise.
				1.626 mm I.D.; L=0.8 m Outlet aperture 10º	4553		
				1.626 mm I.D.; L=0.8 m	4553 6070		
				1.626 mm I.D.; L=1.62 m	3035 4553 6070		
				1.626 mm I.D.; L=322 m	3035		
Boabaid Neto et al. (2014)	Capillary outlet	Refrigerator/ Refrigeration	R600a/-	-	-	No	The oscillatory nature of the refrigerant flowing through the capillary tube inlet leads to high noise oscillation.
Boabaid Neto et al. (2018)	Capillary in/outlet	Refrigerator/ refrigeration	R600a/-	0.643 mm I.D. 0.767 mm I.D.	-	No	Regular and low noise level under continuos vortex formation at the capillary inlet. Noise level increases for intermittent flow pattern at the capillary inlet.
SPL outside capillary tube							
Han et al. (2009)	Evaporator inlet	Refrigerator/ Refrigeration	R600a/ →↑	4.35 mm I.D.	52.3	Yes	The noise level is higher for intermittent flow pattern than for annular, and wavy. For vertical pipe layout the noise level is higher than horizontal, since the intermittent flow is more likely to occurs.
Han et al. (2010)	Evaporator inlet	Refrigerator/ Refrigeration	R600a/ →↑	4.35 mm I.D. () 3.56 mm I.D. ()	51.8 77.3	Yes	Higher noise level manly occurs in vertical line.
Tannert and Hesse (2016)	Capillary outlet	Freezer/ Refrigeration	R600a/ -	-	-	Yes	When single-phase liquid enters in the capillary tube the flow patterns at the inlet and outlet are annular, it leads to a low noise level.
Xia et al. (2014)	Capillary outlet	Freezer/ Refrigeration	R600a/ →	0.7 mm I.D.	-	No	By shifting the outlet geometry of the capillary tube from tapered to straight the SPL was reduced.
Celik and Nsofor (2011)	Evaporator outlet	Refrigerator/ Refrigeration	R600a/ →	6.1 mm I.D.	31.9	Yes	Flow-induced noise under steady-state conditions exhibited inferior SPL than under transient condition.
Ruebeling and Grohmann (2020)	Capillary outlet	Refrigerator/ Refrigeration	R600a/ →	0.6 mm I.D.	421-633	No	The SPL increases as the outlet vapor quality increases, regradless the flow pattern.

Table 3 – Summary of the experimental studies concerning refrigerant flow-induced noise in orifice, TXV, and EEV.

Authors	Target	Equipment/ system	Fluid/ orientation	Expansion device characteristics	Mass velocity [kg/sm^2]	Flow visualization	Remarks
Orifice							
Singh et al. (1999)	Orifice outlet	Refrigerator/ Refrigeration	R134a/ →	1.22 mm I.D.; L=38.1 mm; IS; IOS	8088 and 10784	No	Screen at the orifice downstream reduces significantly the noise.
				1.45 mm I.D.; L=38.1 mm; IS; IOS	2671 - 8397		
				1.7 mm I.D.; L=23.8 mm; NS	2887 - 7997		
				1.7 mm I.D; L=38.1 mm; IS; IOS	3053 - 6547		
Han, Jeong and Kim (2011)	Evaporator inlet	Refrigerator/ Refrigeration	R600a/ ↑	2.0 mm I.D.	238	Yes	Large bubbles passing through the orifice produces noise and vibration at the frequency of the bubble whose radius is the same as the orifice radius.
Hirakuni et al. (2004)	Orifice in/outlet	AC/ Heating	R410a/ →	1.0 mm I.D.	2387 - 4156	Yes	A porous disc of metal positioned at the in and outlet of the orifice was able to reduce the noise by breaking the slug flow pattern into small to bubbles.
Thermostatic and electronic expansion valve*							
Singh et al. (1999)	TXV/EEV outlet	Refrigerator/ Refrigeration	R134a/ -	TXV aperture 100%	45.36	No	The TXV fully open exhibited the higher SPL among the expansion valves.
				EEV aperture 35%	45.36		
				EEV aperture 20%	54.36		
				EEV aperture 20%	33.84		
				EEV aperture 10%	33.84		
Jeong et al. (2007)	Evaporator inlet	Multi-split AC/ Cooling and Heating	R22/ →↑	EEV	60 - 120	No	Flow-induced noise increases as the vapor quality increases.
	EEV inlet						The PWM plays significant role on the noise reduction.
Han et al. (2009)	EEV inlet	Multi-split AC/ Heating	R22/ →	EEV	100 - 120	No	The reduction on the condenter outlet pipe diameter lead to a reduction on the SPL.
Kim et al. (2019)	EEV in/outlet	Multi-split AC/ Refrigeration	R410A/ →↑	EEV	6 - 42	Yes	The flow pattern has a significant influence on the noise level, becoming higher for intermittent flow pattern. Vertical pipe layout is less noisy than horizontal setup.
Hirakuni et al. (2004)	EEV in/outlet	AC/ Heating	R410A/ →	EEV	34 - 55	No	A porous disc of metal at the EEV in and outlet was able to reduced the noise by changing the flow pattern from slug to bubbly flow.
Kim and Song (2020)	EEV in/outlet	Multi-split AC/ Heating	R410A/ →	EEV	15.6 - 61.5	Yes	A honeycomb cylinder at the EEV inlet were able to reduce de SPL by approximately of 10 to 20 dB.

IS = inlet screen IOS = in and outlet screen
NS = no screen

*mass flow rate kg/h

2.2.1 Capillary tube

2.2.1.1 Capillary outlet geometry influence on the SPL

There are few studies in literature concerning the effect of the outlet capillary geometry on the flow-induced noise. Singh et al. (1999) evaluated the TSPL in capillary tubes with flat and conical outlet sections for cone angles of 5° and 10°. The cones were manufactured by stereolithography with dimensional tolerances of 2.54 μm. Figure 5 illustrates the conical and flat geometry evaluated by them and the experimental results obtained in their study.

Figure 5 – Effect of outlet capillary geometry at the sound pressure within the capillary versus a) exit quality, b) pressure drop, c) frequency spectrum under mass velocity of 4553 kg/sm^2 and d) the outlet geometry dimensions in mm.

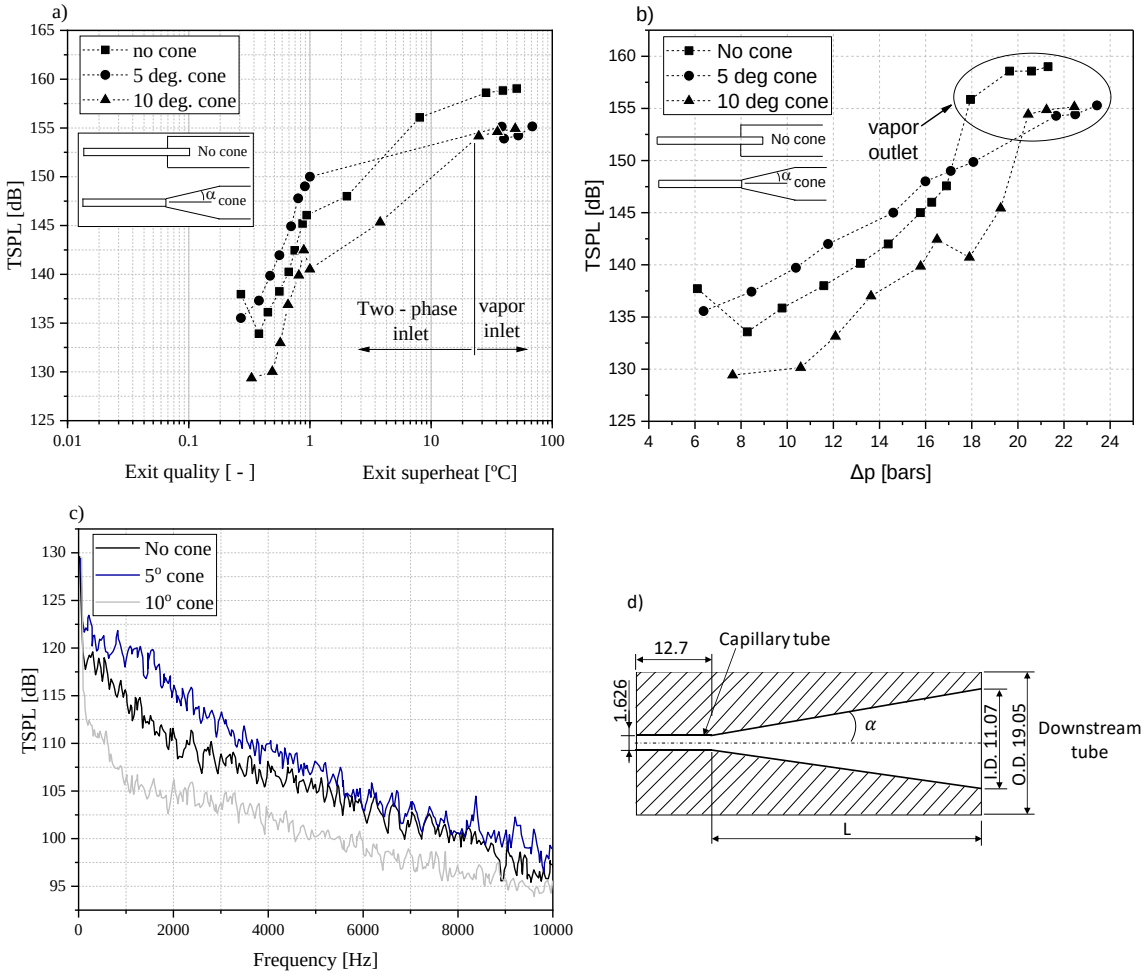

Source: Adapted from Singh et al. (1999)

As shown in Fig. 5, in general, the TSPL increases as the outlet vapor quality and the pressure drop increases, regardless of the geometry of the outlet section. According to Fig. 5a, the cone angle of 5° provides higher TSPL than the cone angle of 10° and the flat geometry for the results obtained under two-phase flow conditions at the capillary inlet. A smoother flow transition

between the capillary and the circuit tubing was pointed out by Singh et al. (1999) as responsible for leading to a lower noise level. However, this explanation is not corroborated by the fact that the flat outlet capillary presents intermediary TSPL values between the two capillaries with conical outlets. On the other hand, under conditions of only vapor flowing along the capillary, the tube with flat outlet section presents higher TSPL than the tubes with conical outlet shape. Moreover, under this condition, the cone angle, as well as the inlet superheat, seems to not affect the level of flow-induced noise. As shown in Fig. 5a and 5b, the TSPL increases abruptly when the outlet fluid shift from two-phase to vapor single-phase, followed by an almost constant TSPL under condition of vapor single-phase at the capillary inlet. Fig. 5c shows the TSPL spectrum over most of the audible frequency range for the distinct outlet capillary geometry. According to Fig. 5c, the 10^{o} cone presents the lower TSPL over the entire frequency range, corresponding to the most of audible frequency range (20 - 20,000 Hz). This result indicates that the geometry of the outlet section may be engineered in order to reduce the flow-induced noise. In addition, Singh et al. (1999) data exhibited relevant structure acceleration at frequency bands around 9 kHz, 15 kHz, and 18 kHz for conical outlet geometries and flat spectrum elsewhere. In general, by increasing the capillary outlet aperture, the acceleration at those frequencies also increases as the outlet vapor quality increases. For superheated outlet vapor, the non-conical geometries provided the highest accelerations of the capillary at similar frequencies.

In order to investigate the noise in a household freezer, Xia et al. (2014) performed a numerical simulation and an experimental investigation of the flow-induced noise for flat and 2^{o} capillary outlet aperture as shown in Fig. 6. Xia et al. (2014) considered R600a as the working fluid, a capillary inlet temperature of 32^{o}C, evaporation temperature of -23^{o}C and a capillary tube with a roughness of $4.6\text{x}10^{-8}$ m. The numerical simulation was performed by dividing the capillary tube into three parts: i) inlet pressure drop due to entrance region from filter-dryer to capillary inlet; ii) sub-cooled liquid flowing through the capillary until saturation pressure; iii) pressure drop along the two-phase flow region estimated from the contribution of frictional and momentum parcels. For single-phase flow, they adopted Churchill (1977) to estimate the pressure drop. Unfortunately, the method employed to evaluate the frictional parcel for two-phase flow was not provided. The capillary outlet results for two-phase flows obtained from the numerical modelling were employed as inlet boundary conditions to the CFD software adopting a two-dimensional axial-symmetric model. However, it is essential to highlight that symmetrical conditions are not suitable for turbulent flow simulations because, as pointed out by Ask and Davidson (2009) and Ask and Davidson (2010), this kind of flow modeling is a three-dimensional problem.

Based on the numerical simulation, Xia et al. (2014) obtained the refrigerant velocity and the turbulent kinetic energy to understand how the capillary outlet transition affects the noise level. They employed standard $k-\varepsilon$ turbulence model, and the Mixture Model for two-phase flow. It is important to highlight that these authors do not specified the mixture model. Eventually, they defined the capillary inlet velocity and the outlet pressure as a constant boundary condition

for both geometries in order to perform the numerical simulations. Their numerical simulation and the capillary outlet structure are illustrated in Fig. 6. According to Fig. 6(b), the capillary outlet tapered transition pipe presents an end velocity of 8.614 m/s, on the other hand, the straight tube presents an end velocity of 6.38 m/s at the outlet tube (Fig. 6a). Xia et al. (2014) suggested that lowering the fluid end velocity leads to a reduction in flow-induced noise by the refrigerant. Both geometries present the maximum turbulent kinetic energy of 90.302 m^2/s^2 for the tapered structure and 102.066 m^2/s^2 for the straight tube at the capillary outlet. Then, the turbulent kinetic energy decreases abruptly, with its value for the tapered structure fluctuating and presenting a less steeper reduction. The average of turbulent kinetic energy for the tapered and straight transition pipe presented values of 19.75 and 9.00 m^2/s^2, respectively. Thus, the straight tube displays a reduction in the kinetic energy of 54.4%. The experimental data obtained by Xia et al. (2014) revealed a reduction of 2 dB for the straight structure leading to smoother noise spectrum in a frequency ranging from 630 to 1600 Hz, despite the fact that the tapered outlet provides a geometrically smoother transition. Moreover, Zhang, Li and Wang (2017) pointed out that the flashing process and turbulence are the main cause of the two-phase flow-induced noise. Corroborating this result, Wei et al. (2015), whose performed their numerical analysis for reducing pressure valve, also found that reducing the outlet valve fluid velocity leads to a reduction in the turbulent intensity, therefore resulting in a lower SPL.

Figure 6 – Numerical simulation of the velocity and turbulent kinetic energy of transition pipe with a) straight and b) tapered structure.

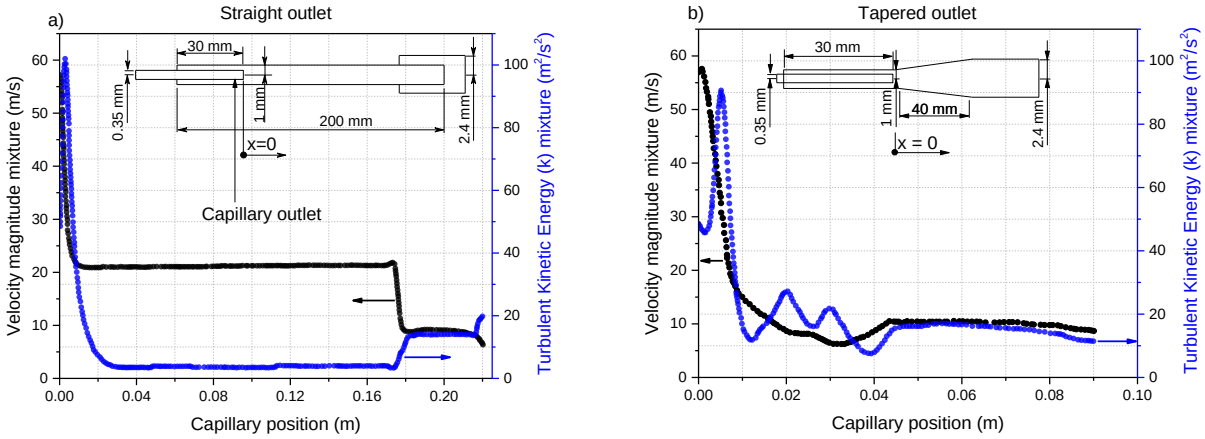

Source: Adapted from Xia et al. (2014)

Xia et al. (2014) also argued that the noise reduction in this frequency band was achieved by adjusting the relative position of the capillary, being able to change the length of the mist flow inhibiting the jet noise spectrum peak at this defined frequency range. However, it is unclear the procedure adopted by these authors to adjust the relative position of the capillary tube once it was not mentioned. Corroborating this result, Singh et al. (1999) also found an increase in the TSPL for tapered structure, however as the aperture angle increases to 10^o the TSPL decreased.

No information about mass velocity and vapor quality at the capillary outlet was provided by Xia et al. (2014).

It can be concluded that the outlet geometry of the capillary tube affects the flow-induced noise, however it is yet not clear how. For capillary outlet transitions of 2^o and 5^o aperture the noise increases, however, for the 10^o Singh et al. (1999) reported a reduction on the TSPL. Therefore, efforts should continue on the investigation of the SPL on the capillary geometry because this is a passive and low-cost alternative to reduce the flow-induced noise.

2.2.1.2 SPL within the capillary

Singh et al. (1999) evaluated the TSPL within the expansion device for distinct capillary lengths and mass velocities as illustrated in Fig. 7. For a capillary length of 0.81 m (Fig. 7a), the TSPL increases as the outlet vapor quality increases, and also increases with increasing mass velocity. Furthermore, according to Fig. 7b, the variation of the TSPL with in- and outlet pressure difference presents an almost constant gradient for both mass velocities until a condition of vapor single-phase reaches the capillary outlet, leading to an abrupt increase in the TSPL, then it is followed by an almost constant value as the inlet fluid becomes vapor single-phase. Such behavior is also observed for the capillary length of 3.22 m (Fig. 7f). From Fig. 7(b), it can be seen that for a given pressure drop the mass velocity of 6070 kg/sm^2 presents higher TSPL, however, for pressure drop superior to 16 bars the TSPL corresponding to the mass velocity of 4553 kg/sm^2 overcome the noise relative to the mass velocity of 6070 kg/sm^2. At this condition, the mass velocity of 4553 kg/sm^2 exhibits single-phase vapor at the outlet, while the mass velocity of 6070 kg/sm^2 presents two-phase flow at the outlet. At the time that the outlet flow shifts from two-phase to only vapor, the mass velocity of 6070 kg/sm^2 exhibits higher noise.

For the 1.62 m capillary length, as shown in Fig. 7(c), the data for the mass velocity of 6070 kg/sm^2 presents an increase on TSPL with an almost constant gradient as the outlet vapor quality increases, exhibiting a higher TSPL among the evaluated mass velocities for outlet vapor qualities superior to 0.4. On the other hand, the data for the mass velocity of 4553 kg/sm^2 shows TSPL fluctuations as the outlet vapor quality increases. In addition, for the mass velocity of 3053 kg/sm^2 (Fig. 7c), the TSPL presents reduced oscillations around 135 dB under two-phase flow conditions at the capillary outlet. For mass velocity of 3053 kg/sm^2 (Fig. 7c and 7d), as the outlet flow shifts from two-phase to only vapor, the TSPL exhibits an abrupt increase of 5 dB. Furthermore, for sub-cooled liquid at the inlet, the mass velocity of 4553 kg/sm^2 presented superior TSPL. According to Fig. 7(d), for the mass velocity of 6071 kg/sm^2 the TSPL increases as the pressure drop increases up to 19 bars. However, for the mass velocities of 3053 and 4553 kg/sm^2 the TSPL exhibits oscillation around 134 and 137 dB, respectively, under condition of two-phase flow at the inlet. For the capillary length of 3.22 m (Fig. 7e and 7f) the experiments were performed only for the mass velocity of 3053 kg/sm^2. According to Fig. 7(e), the TSPL increases up to the condition of saturated liquid at the capillary inlet, then, under two-phase inlet

flow, the TSPL presents an almost constant noise oscillating around 140 dB.

Figure 7 – Effect of outlet quality and pressure drop at the internal sound pressure for three distinct capillary lengths and mass velocity.

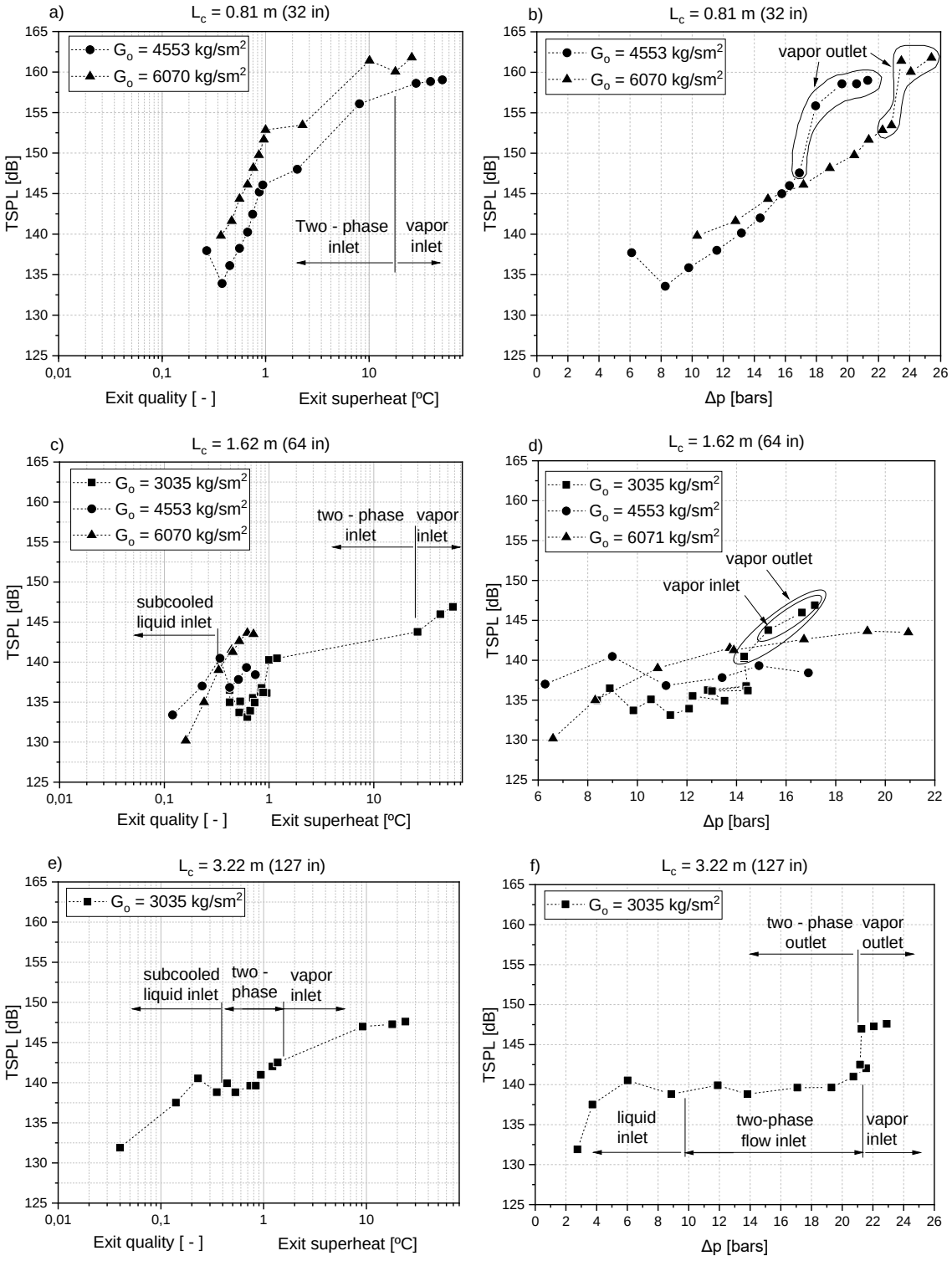

Source: Adapted from Singh et al. (1999).

Overall, the highest TSPL was observed for capillary length of 0.81 m and mass velocity of 6071 kg/sm^2 reaching up to 162 dB. The behavior displayed in these figures indicates, in

general, that the TSPL increases abruptly as the outlet refrigerant becomes superheated vapor. Moreover, only Fig. 7(a) and 7(b) revealed a clear trend of TSPL with varying vapor quality, mass velocity, and pressure drop. Unfortunately, Xia et al. (2014), Singh et al. (1999) did not perform flow pattern visualizations, which would be helpful to understand the flow-induced noise behavior since they performed experiments covering a wide range of experimental conditions. According to the tests performed by Singh et al. (1999) and according to the flow pattern prediction method proposed by Ong and Thome (2011), it can be concluded that Singh et al. (1999) performed all the experiments under conditions of annular flow pattern at the capillary inlet. Therefore, based on this prediction method it is not possible to evaluate the flow pattern influence on the TSPL through the study of Singh et al. (1999).

Figure 8 shows the effect of the frequency ranging from 0 to 20 kHz on the TSPL and on the acceleration of the capillary tube evaluated by Singh et al. (1999) based on a microphone within capillary and on an accelerometer placed on the capillary tube wall, respectively. According to this figure, the TSPL increases for the entire frequency range from 0 to 20 kHz as the outlet vapor quality increases. It is also possible to notice that as the outlet vapor quality increases the overall sound pressure also increases and the frequencies peaks become more pronounced. In addition, under conditions of superheated vapor at the exit the TSPL exhibits white noise signal, presenting a uniform intensity over all the frequency range. As shown in Fig. 8(b), significant peaks in the acceleration spectrum occur around 8 kHz and 14 kHz with a flat spectrum elsewhere and, it diminishes the magnitude of the acceleration as the exit superheat/quality decreases. Comparing both charts in Fig. 8, it is possible to speculate that the capillary structure is acting as a band-pass filter transmitting only determined frequencies, since the mechanism of excitation change from two-phase flow to superheat vapor. Unfortunately, Singh et al. (1999) do not present a discussion about the mechanistic aspects associated with the flow-induced noise phenomenon.

Figure 8 – a) Internal sound pressure level spectrum b) external capillary wall acceleration measurements (1.91 mm I.D., G_o = 4553 kg/sm^2, L = 1.902 m).

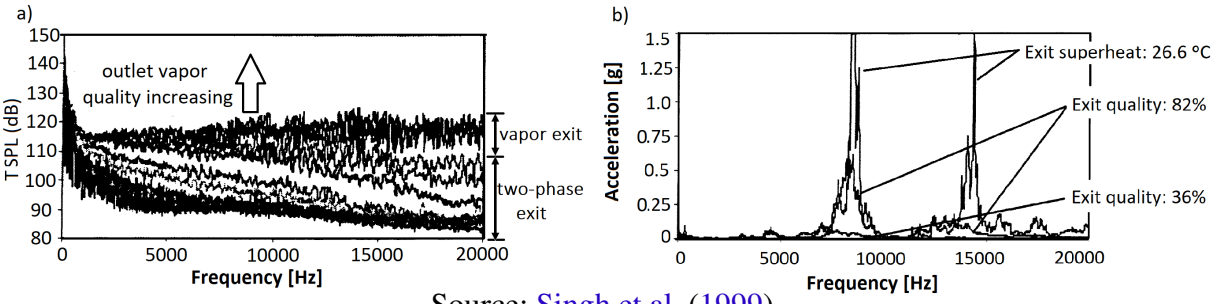

Source: Singh et al. (1999).

Boabaid Neto et al. (2014) evaluated experimentally the SPL and the tube wall acceleration at the capillary exit for a typical household refrigerator. The experiments were performed for R600a and compressor speeds of 2500 and 3500 rpm. Figure 9 shows the acoustic pressure and the tube wall acceleration during the on-cycle of refrigeration and the spectral density recorded at the capillary exit. As shown in Fig. 9(a), acoustic pressure level at the capillary exit ranging from

120 to 145 dB and average noise of 132 dB were observed in their study. According to them, the high amplitude of 25 dB reflects the oscillatory nature of the refrigerant flowing through the pipe and the turbulent jet noise. According to Boabaid Neto et al. (2014), the similarity occurrence between the acoustic pressure (Fig. 9a) and the acceleration level (Fig. 9b) indicates that the acoustic excitation at the exit of the capillary is strong enough to be transmitted to the tube. Moreover, they observed that the acoustic signal presents a strict correlation with the compressor speed revealing its dependence on the mass flow rate at the capillary tube. Their analysis of acoustic pressure (Fig. 9c) and acceleration level (Fig. 9d) on frequency domain indicates that the capillary tube is able to provide significant attenuation on vibration for frequencies inferior to 100 Hz, which is negligible compared to the human frequency hearing (2 Hz to 20 kHz). Although the data shown in Fig. 9(c) is in accordance with the results presented by Singh et al. (1999) (Fig. 8a) under two-phase outlet flow conditions, the behavior of the tube wall acceleration observed by Boabaid Neto et al. (2014) and Singh et al. (1999) are distinct, while the last one (see Fig. 8b) observed acceleration at two determined frequencies, the first one (see Fig. 9d) noted significant acceleration on a wide range of frequencies, which gives a hint that not only the capillary by itself is influencing the transmitted vibrations, but rather the capillary assembly as a whole.

Figure 9 – Acoustic pressure, acceleration, and the spectral density recorded at the capillary outlet during refrigeration cycle.

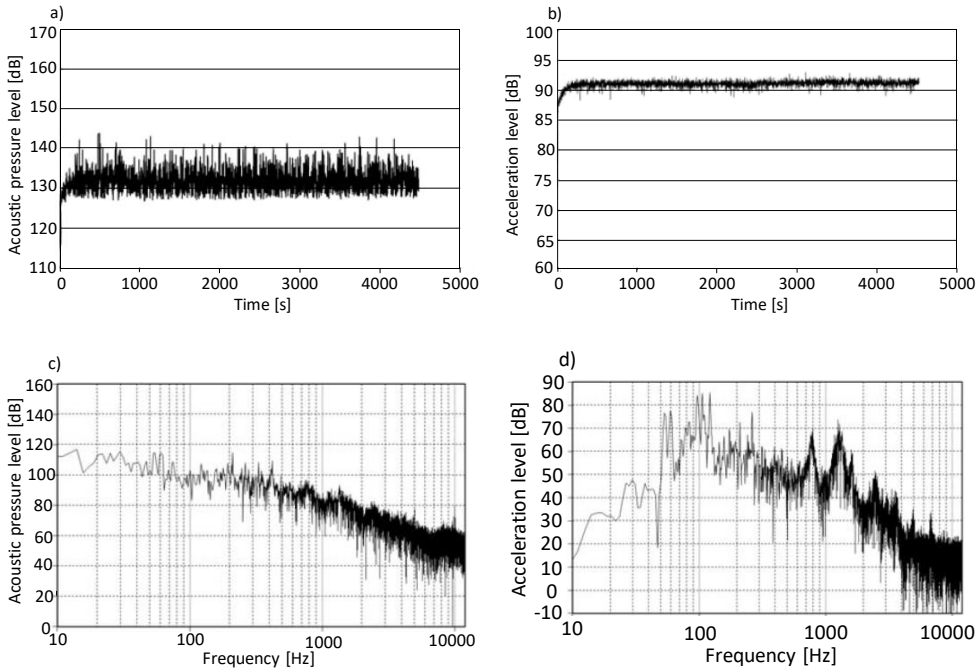

Source: Boabaid Neto et al. (2014).

More recently, Boabaid Neto et al. (2018) conducted an experimental study of SPL in a typical frost-free refrigerator bottom mount compressor with variable speed reciprocating, fin-and-tube evaporator, and a concentric capillary tube-suction line heat exchanger using R600a as working fluid. The acoustic pressure measurements were performed at the capillary outlet for 3.0 m capillary length with internal diameters of 0.520, 0.643, and 0.767 mm. According

to the authors, the inner diameter of the capillary is the main parameter that affects the noise performance of the system. Figure 10 illustrates distinct liquid stratification levels and vortex formation within a transparent filter-dryer developed by Boabaid Neto et al. (2018) in order to visualize the flow condition at the capillary tube inlet. As shown in Fig. 10(a), vortex is not formed for high liquid level. However, as the liquid level decreases the vapor-liquid interface approaches the capillary inlet and the vortex inception occurs, which may assume continuous (Fig. 10b) or intermittent (Fig. 10c) behavior. According to the authors, the balance between the liquid mass flow rate coming from the condenser and the mass flow rate drained by the capillary tube governs the liquid level within the filter-dryer. The rotational speed of the compressor has a substantial effect on the condensing pressure as well on the condenser heat transfer rate, thus reducing the rotational speed leads to a reduction on the condensing pressure and heat transfer rate at the condenser. Therefore, the amount of liquid arriving at the filter-dryer is reduced.

On the other hand, high heat transfer at the condenser enhances the liquid sub-cooling degree, thus more liquid arrives at the filter-dryer allowing a higher mass flow rate through the capillary. However, when the mass flow rate through the capillary overcomes the mass flow rate coming from the condenser, the liquid level at the filter-dryer is reduced approaching the liquid interface to the capillary tip as illustrated in Fig. 10(a). Therefore, the vortex is established due to the liquid acceleration promoted by the capillary suction (Boabaid Neto et al., 2018). The vortex allows vapor to enter in the capillary promoting two-phase flow, which increases the average flow speed as well the pressure drop by viscous dissipation. According to Boabaid Neto et al. (2018), at this point, two arrangement can be observed. First, the flow rate arriving at the filter-dryer is higher than the flow rate leaving through the capillary due to the vapor entrainment, thus the liquid level rises interrupting the vortex formation (Fig. 10c). As result of this, the capillary starts to admit only liquid again increasing the flow rate, and the liquid level reduces, restarting the process. Hence, the vortex is continuously created and interrupted. Secondly, the formation of a continuous vortex indicates that the flow rate through the capillary is equal to the condenser.

Figure 10 – Distinct liquid level at the filter-dryer and vortex formation at the capillary tube inlet.

(a) high liquid level (b) long vortex (c) short vortex

Source: Boabaid Neto et al. (2018).

Boabaid Neto et al. (2018) have found that the smaller capillary diameter (0.520 mm) leads to higher restriction of the flow avoiding the vortex formation, maintaining the filter-dryer full of liquid. For the intermediary diameter (0.643 mm) they observed intermittent vortex regime, while the larger diameter (0.767 mm) provided a reduced restriction resulting in a continuous vortex.

Figure 11 depicts the global level of acoustic pressure for two distinct operational conditions indicating the instant of the vortex formation. The global sound level was evaluated to frequency range from 10 Hz to 10 kHz. According to Fig. 11(a), after 200 seconds of operation, it can be seen an intense fluctuation on the TSPL signal, which is descendent from an intermittent vortex formation at the filter-dryer. According to Boabaid Neto et al. (2018), the fluctuation of TSPL is derived from the oscillation of the strength of the jet flow, which is associated with the discontinuous non-homogeneous two-phase flow pattern at the capillary outlet. In fact, Wang, Cheng and Bergles (2008) mentioned that as the slug flow arrives at the capillary outlet, the jet morphology becomes extremely unstable. On other hand, in Fig. 11(b), the liquid level at the filter-dryer remains stable with a continuous vortex formation, resulting in a reduced pressure level fluctuation as well as lower TSPL. The continuous vortex formation is related to the lower restriction imposed by a higher internal diameter capillary. Besides that, Wei, Lin and Wang (2000) pointed out that for a given helical capillary geometry the mass flow rate decreases as the capillary diameter decreases with this effect becoming more pronounced for reduced capillary coil diameters.

Figure 11 – Global acoustic pressure level a) for intermittent vortex formation and for b) continuous vortex.

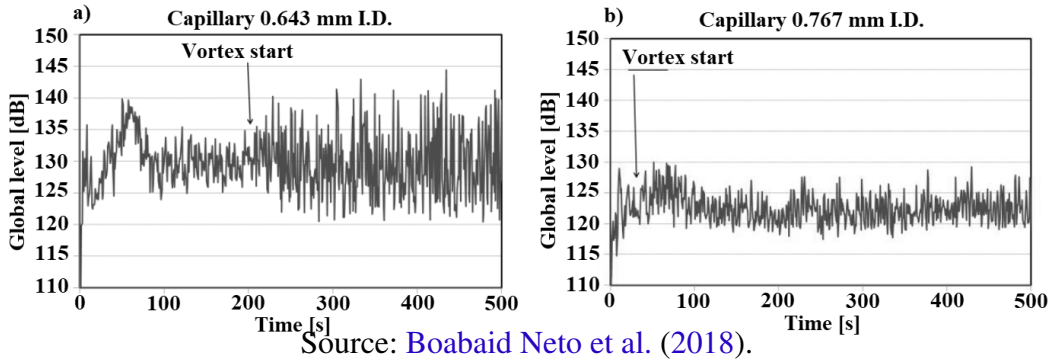

Source: Boabaid Neto et al. (2018).

For the SPL evaluated within the capillary tubes, the noise appears to be primarily function of mass velocity and vapor quality at the exit of the device. Quite different trends of SPL versus pressure drop were observed, thus it is not clear the effect of the pressure drop and mass velocity on the SPL. According to the pipe wall acceleration results obtained by Singh et al. (1999), it also may be speculated that the tube wall acts as a band-pass filter transmitting preferentially certain frequencies, on the other hand Boabaid Neto et al. (2014) diverged from the transmitted frequencies recording a broad frequency band on the acceleration sensor. From the study presented by Boabaid Neto et al. (2018) the intermittent flow at the inlet leads in a

higher SPL than the continuous two-phase flow at the inlet, indicating that the flow pattern may play a significant role on the SPL.

2.2.1.3 SPL outside the capillary

Han et al. (2009) evaluated experimentally the SPL from the region comprising the capillary outlet to the evaporator inlet for a household refrigerator operating with a 4.35 mm inner diameter capillary tube flowing R600a as test fluid at mass velocity of 52.3 kg/sm^2. Figure 12(a) displays the SPL frequency spectrum under steady-state operation, and Fig. 12(b) illustrates the behavior of the SPL with evaporation temperature and vapor quality at the capillary outlet during transient state. The SPL data displayed in Fig 12(a) were obtained under condition of only the evaporator fan turned on and under normal operational condition, that includes the compressor, fan, and fluid flowing through the pipe. Han et al. (2009) assumed that the noise from the compressor is sufficiently low, therefore the superior SPL recorded from 250 to 2000 Hz results from refrigerant flow-induced noise (Fig. 12a). Corroborating these findings, Wang et al. (2021) pointed out that the bubble bursting noise occurs mainly from 300 to 2500 Hz. Ruebeling and Grohmann (2020) were able to identify that the noise generated for bubble flow mainly occurs in a frequency range around 250 Hz. The noise is intensified at frequencies around 850 to 1200 Hz for intermittent flow patterns and reduced at frequencies around 250 Hz. Ruebeling and Grohmann (2020) pointed out that the noise under annular flow conditions mainly occurs around a frequency band of 850 to 1200 Hz, exhibiting components at frequencies around 2.5 kHz and 4.0 kHz. The conversion from frequency spectrum displayed in Fig. 12(a) to sound pressure level reveals that the TSPL of the refrigerator operation is 37.8 dB(A), while only the fan is operating the TSPL is 35.4 dB(A). According to Han et al. (2009), the bubbles developed from the capillary outlet collapse, merge and oscillate promoting noise as they flow to the evaporator inlet.

Figure 12 – a) SPL under normal operational condition and fan only operating condition, and b) overall noise and temperature of the cycle.

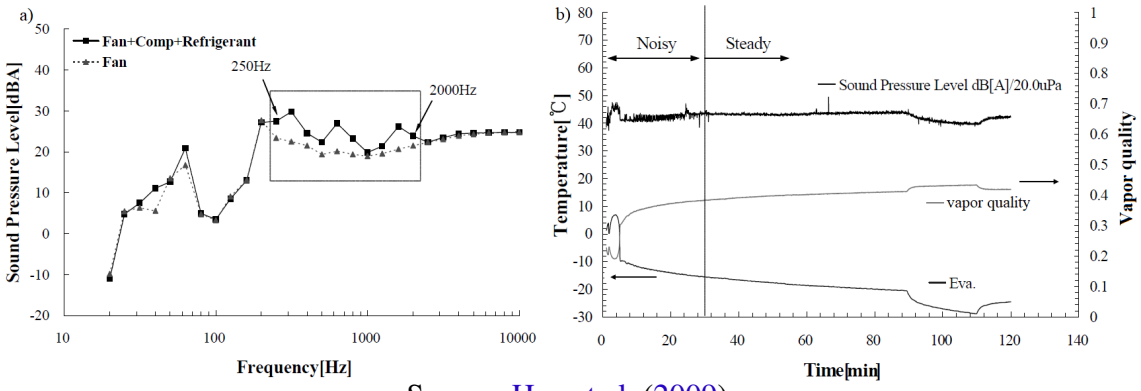

Source: Han et al. (2009).

According to Fig. 12(b), during the first 30 min of refrigerator operation, Han et al.

(2009) observed increment on the vapor quality from 0.2 to 0.38 and a temperature reduction at the evaporator from 8 to –16^{o}C. Simultaneously to this phenomenon, an abrupt increment on the SPL followed by a significant noise fluctuation was noticed, which they described as transient period. The authors visually verified bubbles for the vapor quality of 0.2, while for vapor quality of 0.4 they could not define exactly whether it is annular or churn flow. The annular flow pattern seems to agree with the flow pattern prediction method proposed by Ong and Thome (2011). Slug flow pattern occurs as a transition between bubble and churn/annular pattern, thus a high fluctuation at the SPL may be related to slug flow pattern at the capillary outlet, such behavior was already confirmed by Boabaid Neto et al. (2018), Hirakuni et al. (2004) and Tannert and Hesse (2016). Thereafter, the SPL remained steady until a temperature drop below – 20 °C, followed by a vapor quality increasing from 0.42 to 0.45. At this point, it is possible to notice a reduction on SPL, which may be related to the flow pattern transition to annular, reducing the noise level. On the other hand, Ruebeling and Grohmann (2020) pointed out that bubble and annular flow patterns at capillary outlets result in similar noise, as long as the outlet vapor phase velocities are similar, even under different operational conditions. The characterization of outlet capillary two-phase flow pattern is an important aspect because it seems to be related to the SPL. According to Tibiriçá and Ribatski (2014) the main flow pattern observed in small diameter channels are: isolated bubbles, slug, annular and dryout. Unfortunatelly, the experiments performed for refrigerant R600a (HAN et al., 2010; HAN; JEONG; KIM, 2011; XIA et al., 2014) under conditions of microscale channel (as defined by Ribatski (2013)) did not provided the mass velocity neither the vapor quality, thus it is not possible to estimate the flow patterns occurring in these studies.

According to Singh et al. (1999), the tube wall acts as a band-pass filter, transmitting only certain frequencies, which may explain the peaks in Fig. 12(a) since Han et al. (2009) evaluated the SPL from outside of the capillary. The frequency peaks at 325 and 2000 Hz shown in Fig. 12(a) would be associated to bubble diameters of 10.8 to 12.3 mm and 1.3 to 1.9 mm according to the model proposed by Minnaert (1933) (Eq. 2.1), respectively. However, this model assumes spherical bubble shape, which is not the case because Han et al. (2009) conducted their experiments in a 4.35 mm I.D tube. Therefore, Han et al. (2009) concluded that the large bubbles would assume slug and churn flow patterns, and collapse along the tube in bubbles with diameter inferior to the pipe diameter maintaining spherical shape, whose frequency at range of 2 kHz (1.3 1.9 mm) agrees with Minnaert (1933) model (Eq. 2.1). Han, Jeong and Kim (2011) proposed a model for natural frequency for slug flow (Eq. 2.4), which is in a accordance with the frequency peak of 325 Hz. Ruebeling and Grohmann (2020) pointed out that the noise generated for bubble flow manly occurs in a frequency range around 250 Hz. For intermittent flow pattern, the noise is intensified at frequencies around 850 to 1200 Hz and reduced at frequencies around 250 Hz. Ruebeling and Grohmann (2020) identified that the noise under annular flow conditions manly occurs around a frequency band of 850 to 1200 Hz, also exhibiting components at frequencies around 2.5 kHz and 4.0 kHz.

Figure 13 shows the refrigerant induced noise spectrum for evaporation temperature of -5 and -10ºC under distinct vapor quality conditions at the evaporator inlet. According to the results displayed in this figure, the main frequencies peaks related to the flow-induced noise occurs at 315 and 2000 Hz. For both evaporation temperatures, and frequency ranging from 1 kHz to 3 kHz, the noise decreases as the vapor quality increases. Han et al. (2009) claim that at 315 Hz this behavior is also observed, however, according to Fig. 13, it is not clear since the SPL results for distinct vapor quality are too close from each other. Moreover, the TSPL was estimated by the current author based on the frequency spectrum for each experimental condition given by Han et al. (2009). In general, the TSPL for the evaporation temperature of –5ºC presented higher noise than –10ºC with a maximum difference of 3.9 dB(A). Furthermore, both TSPL decreases as the vapor quality increases. Although the TSPL declined as the vapor quality increased under evaporation temperature of –10ºC, the noise level among the distinct vapor qualities could be barely distinguished by the human ear since it presented similar values and frequency distribution. As expected, based on natural frequency prediction models (see Fig. 2d), a difference of 5ºC on the fluid properties does not play a significant role in the natural frequency value.

Figure 13 – SPL spectrum for evaporation temperature of a) -5 and b) -10ºC for distinct vapor quality and the fan of the evaporator turned on.

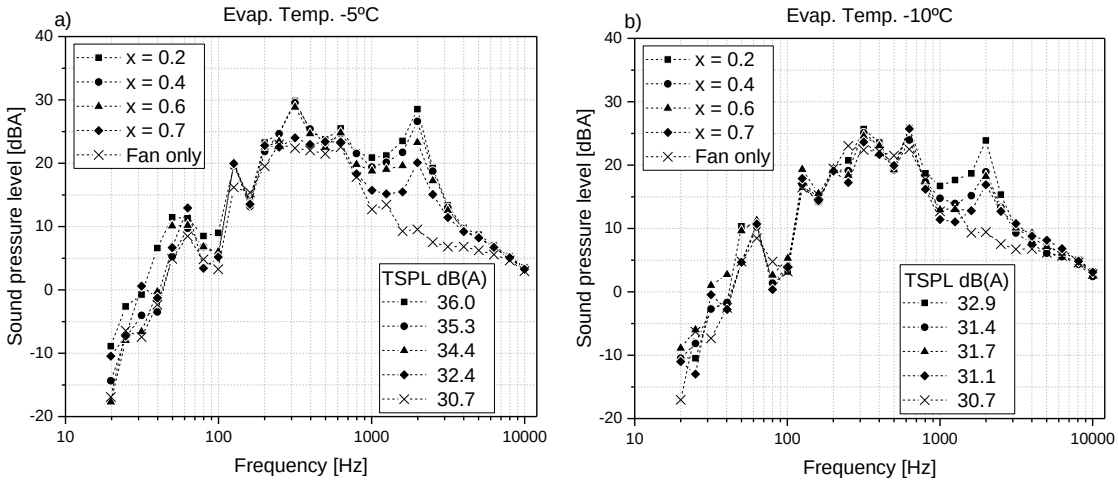

Source: Adapted from Han et al. (2009).

Han et al. (2010) redesigned the evaporator inlet by reducing the I.D. from 4.35 to 3.56 mm and changing the flow orientation from vertical to horizontal, reducing the SPL up to 4 dB(A). The authors claim that by reducing the tube diameter, the mass velocity increases, promoting a transition from intermittent to annular flow at the capillary outlet according to the flow pattern prediction methods of Hewitt and Roberts (1969), Taitel and Dukler (1976) and Oshinowo and Charles (1974). However, such prediction methods do not properly predict the flow patterns once capillary tubes usually present an I.D. ranging from 0.5 to 1.5 mm (BANSAL; RUPASINGHE, 1998), and microscale flow pattern predictions methods should be used under

such circumstances (KANDLIKAR, 2002). Kim et al. (2019) also found churn flow as the source of highest noise among the flow patterns. Opposite to Han et al. (2010) and Kim et al. (2019), Ruebeling and Grohmann (2020) found that the noise increases with increasing vapor quality regardless of the flow pattern, with its effect becoming stepper as the capillary temperature inlet is reduced and, consequently, the vapor specific volume and two-phase flow velocity is increased.

In the study of Han et al. (2010), only the evaporator was placed within the acoustic chamber in order to avoid noise from other components. Figure 14(a) exhibits the comparison between the overall sound pressure level of the evaporator and Fig. 14(b) exhibits the comparison between the SPL spectrum of the conventional and the modified design. According to Han et al. (2010), the SPL were evaluated for the first 20 min of operation (Fig. 14a) because the flow-induced noise at this period is more pronounced. From Fig. 14(a), it is possible to notice that at 2 min the modified evaporator presents SPL higher than the convention one for a short period. Then, the modified evaporator present SPL lower than the conventional, reaching a maximum difference of 4 dB(A). During the operation, the conventional model presented noise ranging from 32 to 38 dB(A) with average value of 35 dB(A), and new design with SPL ranging from 31 to 35 dB(A) with average value of 32 dB(A). From Fig. 14(b), it can be noted a noise reduction from the conventional to the proposed evaporator oscillates that between 2 and 5 dB(A) at the frequency range of 315 to 3150 Hz.

Figure 14 – Comparison between conventional and new evaporator inlet design a) for the first 20 min of operation and b) SPL comparison spectrum.

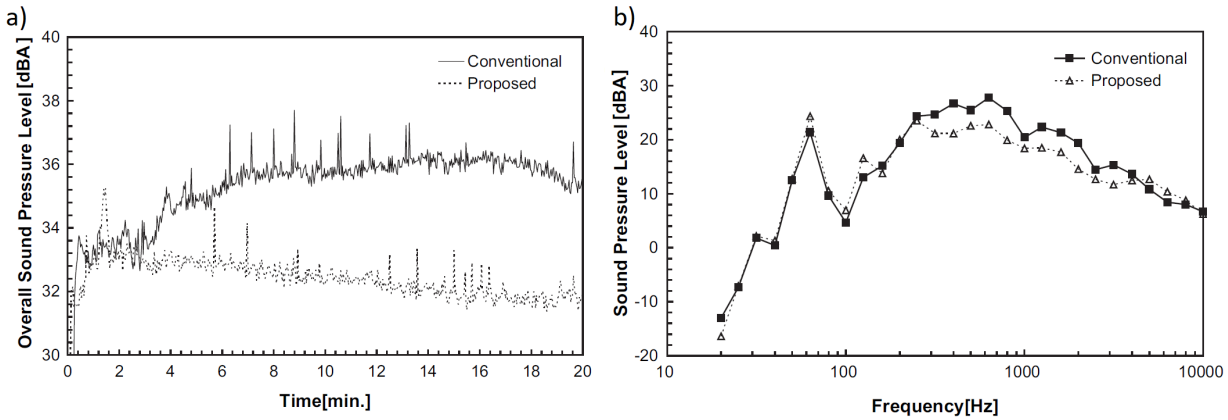

Source: Han et al. (2010).

Celik and Nsofor (2011) investigated the flow-induced noise at the evaporator outlet of a refrigerant system using R600a as working fluid inside an anechoic chamber during transient and steady-state operation. These authors pointed out a dominant band of flow-induced noise frequency from 200 to 500 Hz for annular flow. Based on X-ray images at the last elbow of the evaporator, they were able to observe bubbles with diameter ranging from 2.2 to 5.5 mm, which agrees with the model of Minnaert (1933). In addition, the SPL under transient conditions exhibit higher noise than steady state over the evaluated frequency range.

Xia et al. (2014) evaluated the TSPL during the refrigerator running cycle for tapered capillary outlet and straight geometry. Xia et al. (2014) found an average SPL of 27.9 and 24.7 dB(A) for tapered and straight geometry, respectively. The compressor is situated at the bottom near to right-rear corner. It is interesting to notice that the higher TSPL occurs at the right side of the freezer instead of the rear side, which is not expected since this model of freezer presents aperture at the freezer frame where the compressor is located, allowing the sound propagation free of obstacle. In general, the modification at the capillary reduces the TSPL of 3 dB(A) independent of the positions. Opposite to Xia et al. (2014), Wang et al. (2021) evaluated the noise from outside of a refrigerator founding louder SPL close to the compressor chamber. Wang et al. (2021) were able to reduce the noise from 1.5 dB(A) and the frequency spectrum amplitude by adjusting the vapor admixture at the evaporator entrance inhibiting the bubble burst at the capillary outlet. It is important to highlight that this is a passive and permanent way to reduce the flow-induced noise.

Tannert and Hesse (2016) were able to identify that subcooled liquid, saturated, and two-phase flow at the capillary inlet due to the unsteady refrigerator operation condition promote different flow patterns at the capillary outlet. According to them, the periodicity of inlet flow pattern changes the results in a remarkable variation of SPL at the capillary exit with the same periodicity. Figure 15(a) illustrates the SPL recorded by external microphone, the acceleration level of the capillary structure and the dynamic pressure signal amplitude recorded within the flow just downstream of the capillary outlet presented by Tannert and Hesse (2016). They also registered the flow pattern at the end section of the capillary outlet. From Fig. 15(a), it is possible to notice that the dynamic pressure transducer signal, the TSPL, and the tube acceleration are in phase. Tannert and Hesse (2016) described the low induced noise region, approximately 28 dB, as annular flow leaving the capillary as a continuous jet. On the other hand, the plug flow at the capillary outlet led to an increase in the the SPL, wall acceleration, and pressure signal exhibiting fluctuations with significant peaks, with an unstable free jet at the capillary outlet. However, they could not observe a correlation between the oscillations of fluid vapor mass fraction entering the capillary tube with the alternating SPL. Moreover, Zhang and Liu (2021) pointed out that the time gradient pressure drop is the root cause of the flow induced noise.

During the experiments of Tannert and Hesse (2016), the TSPL oscillates between 27 and 41 dB(A) exhibiting average noise of 32 dB(A). Figure 15(b) illustrates the frequency spectrum during the high noise level for time interval from 1236 to 1237 s. From Fig. 15(b), it can be noticed a peak at certain single frequencies of 280 and 745 Hz as well in a wide band around 2000 Hz. Tannert and Hesse (2016) estimated the resonance frequency of 280 Hz in accordance to such results based on visual observation of a bullet-shape bubble according to the prediction method for natural frequency resonance for slug flow proposed by Han, Jeong and Kim (2011) given by Eq. 2.4. This result is also in agreement with the experimental results of Han, Jeong and Kim (2011) as illustrates in Fig. 3. Although, Tannert and Hesse (2016) could not find another source of excitation responsible for the frequencies peaks, Han et al. (2009) and Han, Jeong and

Kim (2011) also found peaks at frequencies around 700 and 2000 Hz during their experiment, but neither of them were able to explain these frequencies peaks. It can be speculated that the chaotic flashing process at the capillary tube outlet may produce several frequency peaks, however the intrinsic characteristic of the structure only vibrates at certain frequencies and damps the others. Additionally, Espíndola et al. (2020) indicate that is possible to correlate the flow pattern and the expansion noise from an accelerometer at the evaporator inlet. On the other hand, Lorbek et al. (2020) conducted a visual study at the capillary outlet, pointing out that slug flow followed by patches of small bubbles is the dominant flow pattern. The liquid phase is forced against the tube walls from the capillary outlet forward as the vapor core expands, exhibiting a chaotic behavior (ESPÍNDOLA et al., 2020).

Figure 15 – a) Time response of the dynamic pressure signal, sound pressure signal and acceleration and b) frequency response of the noise level.

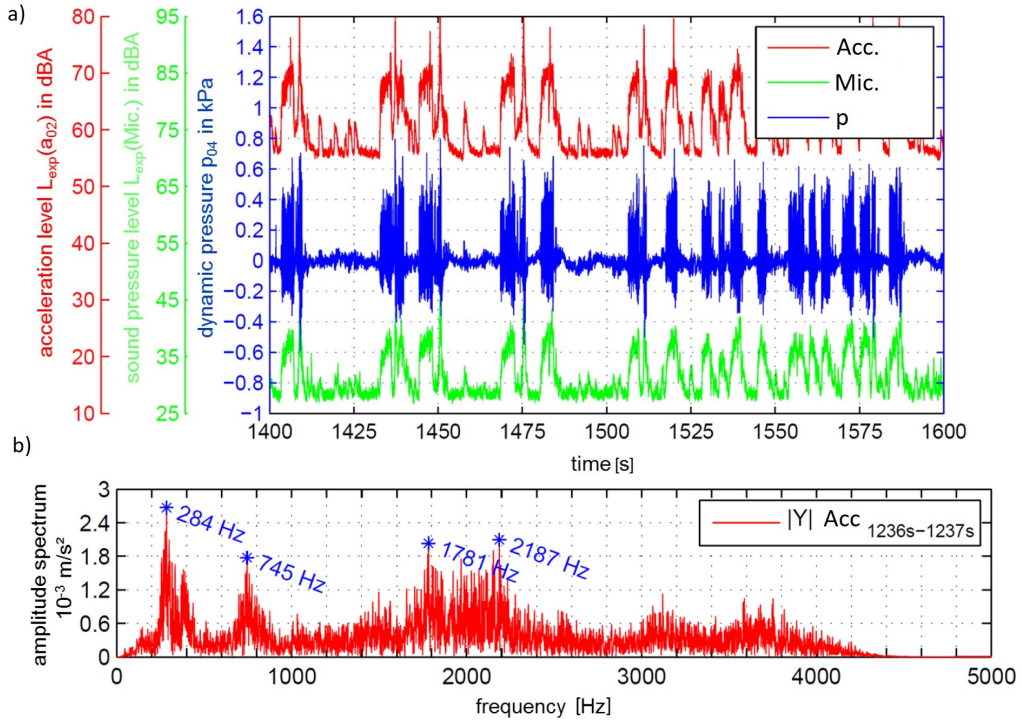

Source: Tannert and Hesse (2016).

Kim, Jeong and Han (2014) experimentally developed a “noise pattern map” based on the Kutateladze and Matinelli parameters that is able to predict the flow-induced noise at the evaporator inlet based on the tube diameter, mass flow rate, fluid pressure, temperature, and vapor quality. These authors developed the “noise pattern map” employing experimental data for tube with inner diameter ranging from 3.56 to 8.0 mm and vapor quality from 0.1 to 0.7. Their noise pattern map takes into account the following flow patterns: (i) liquid single-phase; (ii) slug; (iii) churn; (iv) annular-churn; and (v) annular. Furthermore, Kim et al. [57] were able to reduce the flow-induced noise in a commercial refrigeration unity employing their flow pattern map.

In summary, for the TSPL evaluated outside the capillary, the noise appears to be function of vapor quality at the exit of the device as well as the flow pattern, however only certain frequencies are transmitted through the tube, due to fluid-structure interaction and acoustic insulation/radiation properties of the tubes, which are rather case dependent. Therefore, it is important to highlight that each evaporator design has its intrinsic band-pass characteristic, which to this point, has not been the focus of previous work.

2.2.2 Orifice

Singh et al. (1999) evaluated the TSPL of orifices for refrigerant R134a. According to Fig. 16, the TSPL gradient between in- and outlet of the orifice without screens is higher than for the orifice with screen up to a pressure difference of 9 bar. For the orifices with screen only at their inlet (Fig. 16b), in general, the TSPL increases with increasing the internal diameter of the orifices, however the orifices with inner diameter of 1.45 and 1.70 mm present similar behaviors at pressure differences superior to 8 bars. As shown in Fig. 16(b), the TSPL for the orifices with screens at their inlet and outlet are not affected by the orifice diameters. In general, from Fig. 16, it is possible to notice that the TSPL increases with increasing pressure drop, even though the screens are present or not. In addition, the highest TSPL value for a given pressure drop was observed for the condition without screen, largest orifice diameter and shorter orifice length.

Figure 16 – SPL on orifice versus pressure drop for condition of only vapor at the inlet.

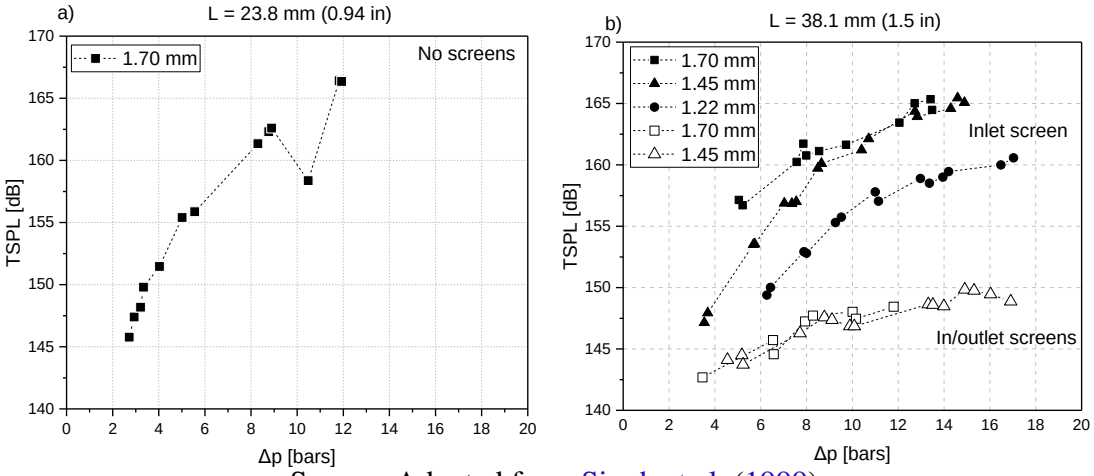

Source: Adapted from Singh et al. (1999).

According to Fig. 17(a) from Singh et al. (1999), for the orifice without screen, the TSPL increases with increasing the mass velocity and outlet pressure, however it is not possible to assert if the data are within the measurements uncertainties band once the sensitivity of their microphone were not provided. Moreover, as shown in this figure, the TSPL increases with increasing the vapor quality and becomes almost constant for vapor superheating higher than 10^{o}C. In addition, as shown in Fig. 17(b), for a given mass velocity, the outlet pressure affects marginally the TSPL and an abrupt increase in the TSPL value is observed when a condition of

superheated vapor at the capillary inlet is established. Further increases in the vapor superheating degree does not affect significantly the TSPL. The behaviors shown in Figs. 17(c) and 17(d) for the orifice with screen at its inlet and outlet are similar to those displayed in Figs. 16(a) and 16(b), respectively, for the orifice with screen only at its inlet. However, by comparing these figures, it can be concluded that an additional screen at the outlet reduces the TSPL significantly independent of the operational condition.

Figure 17 – Effect of outlet quality, pressure drop and downstream screen on the internal sound pressure level for orifice with 1.22 mm I.D. and length of 38.1 mm.

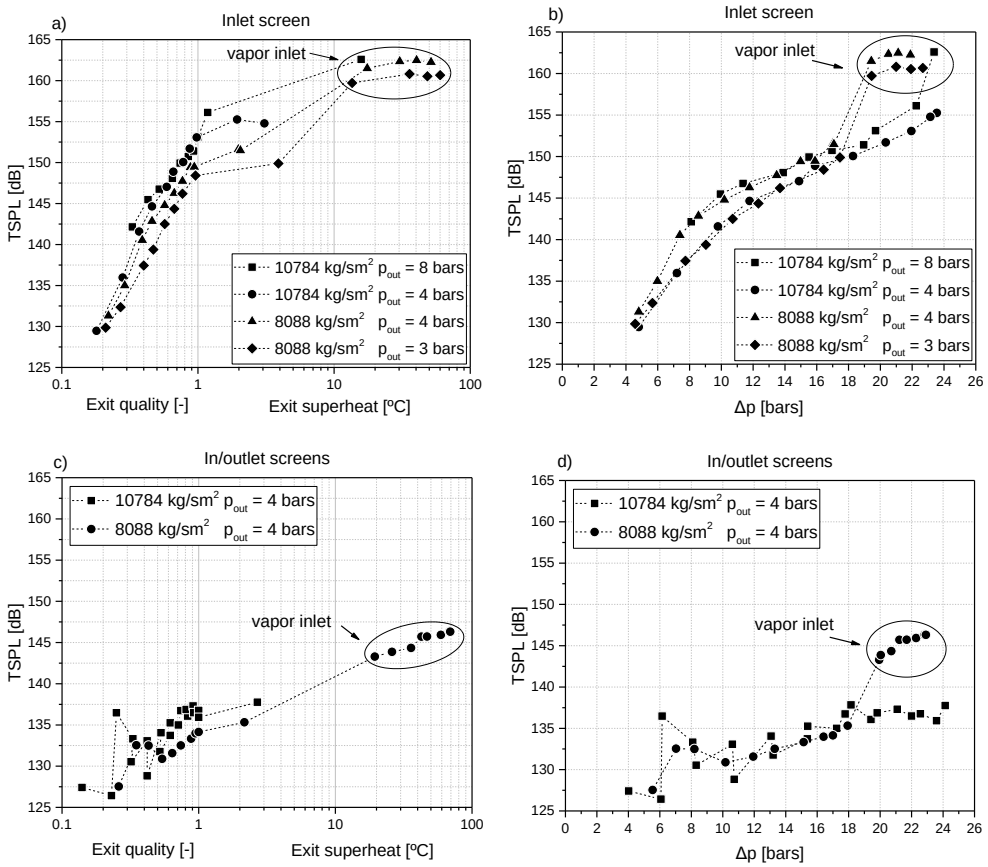

Source: Adapted from Singh et al. (1999).

Singh et al. (1999) also reported that the frequency spectrum for orifice with screens is wavier than for the orifice tubes without screens and a peak around 400 Hz is not present. They speculated that as the pressure difference across the orifice tube increases the acoustic efficiency also may increase, promoting higher TSPL downstream the orifice. They also concluded that the increase on the TSPL as the outlet flow becomes single-phase is due to the increase on the available energy for the sound. According to these authors, increasing the mass flow rate, while all else parameters are held constant, increases the stream power at the orifice exit, hence the available energy for sound increases resulting in a higher TSPL. They also evaluated the TSPL orifice frequency spectrum observing similar behaviors to those of the capillary tube (Fig. 8a). No information about the screen geometry was provided by Singh et al. (1999).

Han, Jeong and Kim (2011) conducted experiments on the evaluation of the noise and acceleration frequency spectrum of Taylor bubbles contracting to pass through a narrow orifice with an inner diameter of 2 mm. In addition, flow visualizations were performed upstream the orifice. Figure 18 illustrates the noise and the orifice acceleration frequency spectrum as the bubble passes through the orifice for vapor qualities of 0.24 and 0.39. According to Fig. 18(a) and 18(c), the SPL of the bubble passing through the orifice is null up to a frequency of 1 kHz. On the other hand, as the slug flow passes through the orifice a noise peak occurs at a frequency ranging from 3 kHz to 4 kHz, with the noise level increasing as the vapor quality increases. According to the model proposed by Minnaert (1933), a bubble passing through an orifice with inner diameter of 2 mm would result in a natural frequency of approximately 3 kHz, which is in agreement with the results found by Han, Jeong and Kim (2011). They were able to record the acceleration of the orifice (Fig. 18b and 18d) indicating that the peaks ranging from 100 to 400 Hz occurs due the Taylor bubble and it increases as the vapor quality increases. In general, the SPL presented by Han, Jeong and Kim (2011) are near to 13 dB, which would produce a noise almost imperceptible to the human hear.

Figure 18 – Sound and acceleration spectrum for a Taylor bubble passing through an orifice.

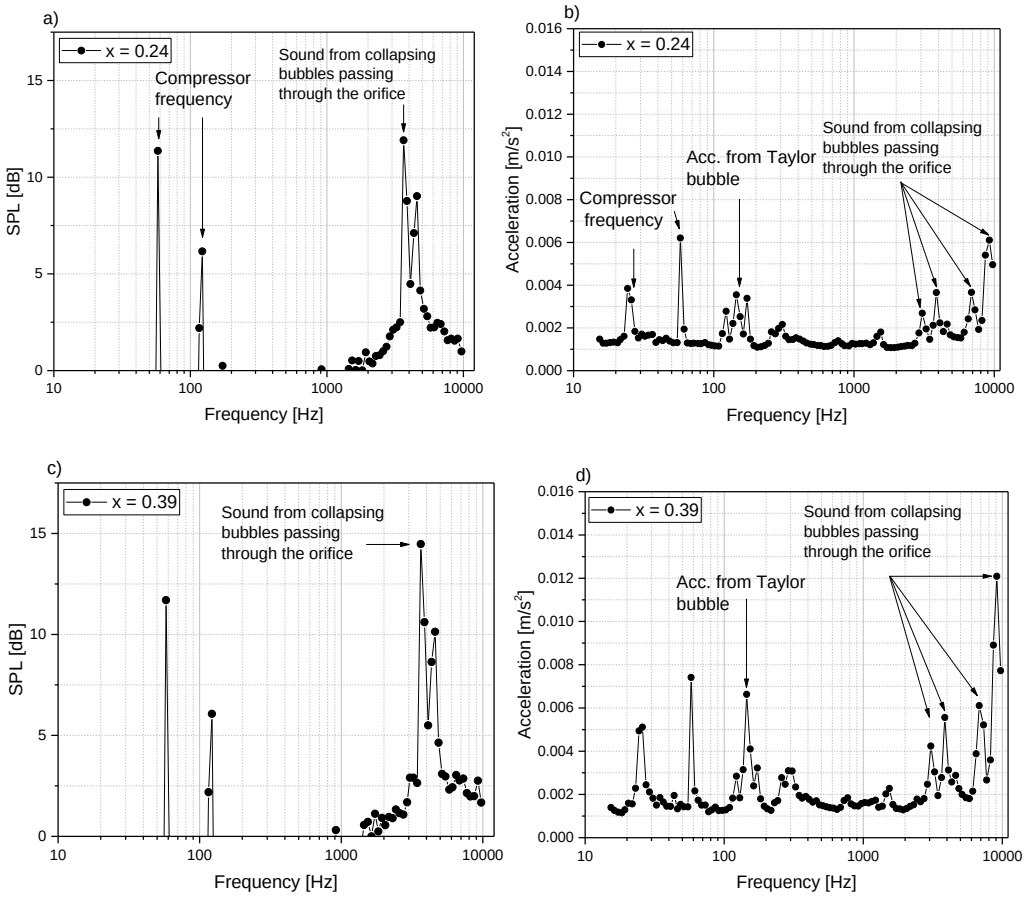

Source: Adapted from Han, Jeong and Kim (2011).

Hirakuni et al. (2004) investigated the effect of a porous metal disposed on both sides of the orifice (Fig. 19). Their porous disc is 3 mm thick and contains holes with diameters of 0.5 mm with a gap ratio of 96%. They related the pressure fluctuation to vapor slugs larger than the orifice, and as they flow through the throttle section the vapor slug upstream the orifice is broken and vibrates. Also, the alternating between liquid and vapor phases passing through the orifice with distinct velocities promotes pressure fluctuations.

Figure 19 – Flow pattern and pressure fluctuation at the inlet and outlet of orifice with and without porous metal.

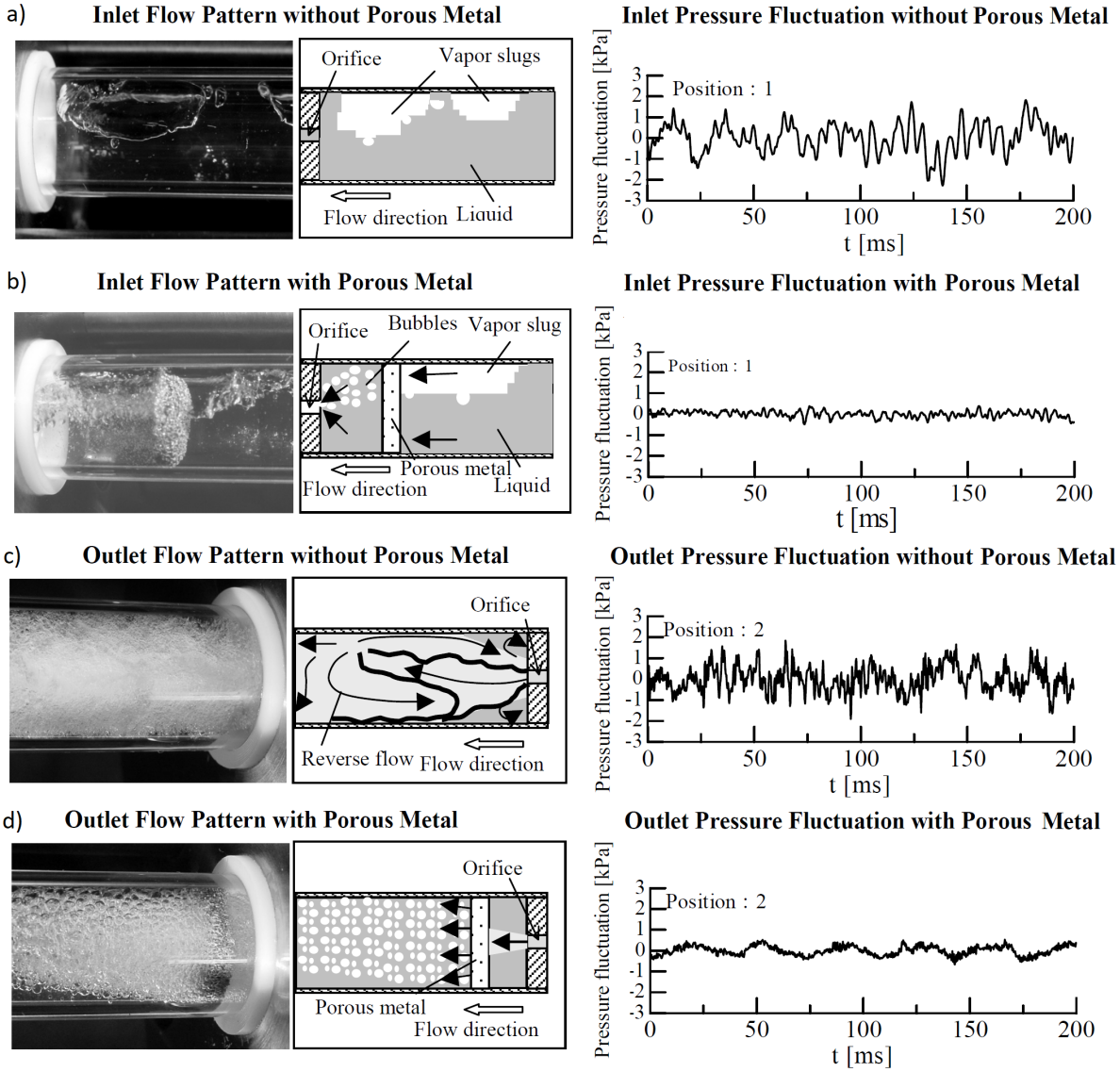

Source: Adapted from Hirakuni et al. (2004).

The porous metal upstream the orifice breaks the slugs into small bubbles homogenizing the flow, allowing the bubble to flow simultaneously with the liquid phase through the orifice, therefore the speed of the refrigerant does not fluctuate, and the pressure fluctuation is reduced as well as the vibration. Downstream the orifice the porous metal also aids to the attenuation of the

noise, shifting the flow pattern from disordered to bubbly flow uniformly distributed implying on a pressure fluctuation around ±0.5 kPa. Hirakuni et al. (2004) pointed out for the orifice without porous metal that the SPL increases as the mass flow rate increases. However, the noise becomes almost independent of the mass velocity with the aid of a porous metal, in general, 5 dB(A) lower than without the porous metal.

Although the studies of Singh et al. (1999) and Han, Jeong and Kim (2011) evaluated the noise in orifices at distinct operational conditions and approaches, both studies found similar trends of the SPL versus vapor quality. Also, the results presented by Singh et al. (1999) in Fig. 16 for only an inlet screen configuration exhibited a clear trend with the SPL increasing as the vapor quality and pressure drop increases. Although Singh et al. (1999) did not provide information about the screen geometry, it may be speculated that the insertion of the outlet screen may change the outlet flow pattern and, at the same time, acts as a restriction reducing the noise as suggested by Hirakuni et al. (2004). According to Nilpueng and Wongwises (2009), which investigated the flow pattern of refrigerant R134a flowing within short-tube orifice under conditions of subcooled liquid inlet, the flow patterns inside short-tube orifices can be divided as follows: metastable liquid flow and two-phase flow. The metastable region is characterized by presenting pressure inferior to the saturation pressure, delaying the vaporization. Increasing the subcooling degree and pressure at the orifice inlet increases the metastable region length ranging from 35 to 67% of the short-tube length (NILPUENG; WONGWISES, 2009). According to Simões-Moreira and Bullard (2003), the flashing point fluctuates periodically, accompanied by fluctuations of mass flow rate, especially for a variable speed compressor. In the two-phase region, it was found by them that the number of bubbles increases gradually downstream the tube length and greatly at the outlet of the short-tube orifice. Therefore, efforts should be put on the evaluation of the two-phase flow topology effect on the flow-induced noise, and simultaneously evaluation of the bubble size and short-tube orifice acceleration frequencies.

2.2.3 Thermal and electric expansion valve

Figure 20 shows the results of Singh et al. (1999) which conducted experiments for thermal expansion valve (TXV) fully open and for electric expansion valve (EEV) with aperture ranging from 10 to 35% using R134a as the test fluid. They investigated the effect of EEV aperture on the noise and on the pipe wall acceleration downstream the EEV under a constant outlet pressure of 4 bars. The TXV has the intake and outtake displaced in horizontal direction while the EEV has vertical intake and horizontal outtake. Singh et al. (1999) employed a tube in the TXV inlet and outlet with outside diameter of 12.7 mm. No information was provided about the inner diameter neither about the intake and outtake diameters employed for the EEV. According to Fig. 20, the fully open TXV presented the highest TSPL among the expansion valves for the entire vapor quality range, even under inferior mass flux of the EEV 20% opening. From Fig. 20(a), it can be noted that the EEV with 35% opening presents a constant TSPL of 133 dB for exit vapor quality inferior to 0.50, however for values superior to this the TSPL increase

until the fluid become single-phase vapor at the valve outlet. Thus, the increase on the saturated vapor temperature leads to increase on the TSPL. For the EEV with 20% aperture, the TSPL increases with increasing mass flow rate for vapor qualities superior to 0.4, while for the mass flow rate of 33.84 kg/h oscillations are observed for the entire vapor quality range. For the EEV with 10% aperture, the TSPL presented a maximum value for a vapor quality of 0.5, followed by a decrease in the TSPL as the vapor quality increases. According to Fig. 20(b), similar behaviors of TSPL were observed as the fluid inlet become single-phase vapor with the TSPL presenting similar noise results near 150 dB. Similar behaviors are displayed in Fig. 20(a) for the TXV and EEV with aperture of 35% under conditions of two-phase outlet flow, characterized by the increase of the TSPL according to a nearly constant gradient as the vapor quality increases for vapor quality superior to 0.4. The results shown in Fig. 20(b) revealed TSPL fluctuations as the pressure drop increases for EEV apertures lower than 35%. Such oscillations could be related to the flow pattern alternance. Unfortunately, Singh et al. (1999) did not provided flow pattern information in their study. It gives a hint that the flow pattern may be affecting the noise level.

Figure 20 – Effect of outlet quality and pressure drop on the internal sound pressure for thermal and electrical expansion valves for distinct openings and mass fluxes.

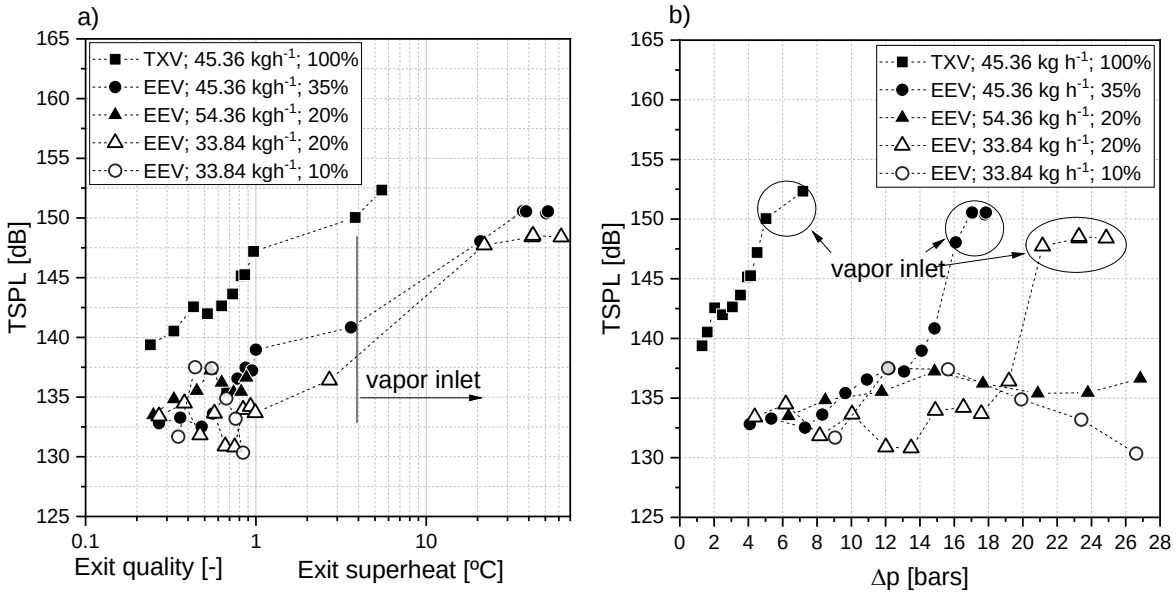

Source: Adapted from Singh et al. (1999).

Singh et al. (1999) observed peaks in the pipe wall acceleration for the EEV for 35% and for 20% (33.84 kg/h) aperture at similar frequencies of 4400, 8700, 9000 and 14900 Hz. They also found peaks in the acceleration for the following conditions: i) EEV 35% at 6 300 Hz and ii) EEV 20% (33.84 kg/h) at 2800 and 18300 Hz, respectively. These frequencies peaks were obtained for vapor flow at the outlet. Unfortunately, these authors do not present a discussion about this phenomenon. For frequency distinct from these, the pipe acceleration magnitude was negligible. Analogous to the capillary tube TSPL frequency (Fig. 8(a)), Singh et al. (1999)

also observed similar behavior for the expansion valves, that the TSPL increases for the entire frequency range from 0 to 20 kHz as the outlet vapor quality increases, while under superheated vapor exit conditions the TSPL exhibits a white noise signal. According to Knabben, Melo and Hermes (2020), the flow in an EEV with hydraulic diameter of 190 μm with aperture ranging from 2 to 95% behave similarly as a 3 m long capillary tube with internal diameter ranging from 0.40 to 0.85 mm. Knabben, Melo and Hermes (2020) performed their experiment for liquid sub-cooling degree at the EEV inlet of 5, 10 and 15^{o}C using R600a and nitrogen as test fluid. Corroborating this result, Singh et al. (1999) also found that the capillary with internal diameter of 1.626 mm and 3.22 m long under sub-cooling of 9^{o}C resulted in TSPL of 133dB, which exhibited similar results to the EEV 20% (54.36 kg/h), EEV 20% (33.84 kg/h) and EEV 10% under nearly saturated liquid inlet conditions.Similar to EEV 20%, the capillary with I.D. of 1.626 mm and 3.22 m long also exhibited high accelerations at frequencies around 9000 and 15000 Hz. Zhang and Elbel (2018) also noticed a similar occurrence of inflow pressure, acceleration, and microphone frequency peak signals distributed around 10 kHz. On the other hand for frequencies under 1 kHz, Zhang and Elbel (2018) found that the sound decay during the flow-induced transmission oscillations trough the TXV wall resulting in imperceptible noise to the human earing.

Jeong et al. (2007) reported noise measurements for R22 under cooling and heating cycles for a small split air-conditioning cassette type IDU and multi-split ASHP for different flow patterns at the EEV inlet. The noise produced by the compressor was neglected because the line connecting the indoor and outdoor unit was sufficiently long to damp down the vibration from the compressor. Under cooling mode, the tests were performed for different refrigeration charges in order to investigate the effect of the vapor quality at EEV inlet on the refrigerant induced noise. Their tests were performed for vapor quality of 0.14, 0.16 and 0.19 at the evaporator inlet leading to SPL of 43.9, 45 and 45.6 dB(A) for frequency ranging from 1 to 5 kHz, respectively. These conditions correspond to annular flow according to the flow pattern maps of Baker et al. (1953) and Hewitt and Roberts (1969), which although considered by the authors, are inappropriate to their study since they were developed for gas-oil and air-water, respectively. It is important to highlight that as the evaporator vapor quality inlet increases, the EEV aperture as well as the mass flow rate also vary, thus the results reported by Jeong et al. (2007) are under effect of more than one parametric variable.

Under heating operation mode, Jeong et al. (2007) investigated the noise effect for distinct EEV open-step and PWM control on the SPL. They found similar values of noise for EEV operating with 200 open steps either if the PWM was turned on or off. On the other hand, for EEV operating with aperture superior to 300 steps the SPL exhibited higher SPL than for 200 steps aperture. Additionally, turning off the PWM control for aperture superior to 300 open steps the SPL near double its value. According to this study, the mass flow rate at the condenser reduces with reducing the EEV aperture. Therefore, these authors were able to verify that for EEV aperture inferior to 200 steps sub-cooled liquid leaves the condenser leading to an inferior

SPL than for 300 steps aperture, when two-phase flow leaving the condenser was observed.

Koberstein et al. (2015) identified an intense whistle noise source at 6.18 kHz in phase with the accelerometer at the suction line of TXV. In order to understand the effect of the inlet TXV geometry on the frequency noise band, Koberstein et al. (2015) varied the TVX pilot suction tube length from 8.0 to 12.0 mm (Fig. 21a), and the connection geometry between pilot tube and suction TXV port (Fig. 21b). According to Koberstein et al. (2015) results, TVX pilot suction tube lengths inferior to 9.0 mm, chamfered pilot tubes, and smoothed TXV suction port edges can suppress the noise at 6.18 kHz while the SPL remained similar at other frequencies. Although Koberstein et al. (2015) identified a clear relation between the flow-induced noise and the shallow cavity between the TXV and the suction pilot tube, a mechanistic explanation about how this relationship is established was not given by them. Zhang and Elbel (2018) found that increasing the TXV wall thickness by 0.2 mm the natural frequency of the structure increases, therefore the hissing noise that was propagated through the TXV wall around 10 kHz could be mitigated. It should be highlighted that the sharpness of the flow-induced noise dominated hissing noise, therefore, decreasing the hissing noise improve the psychoacoustics of human being.

Figure 21 – Effect of the a) length on the suction pilot tube and b) connection geometry between pilot and suction TXV port on the frequency spectrum.

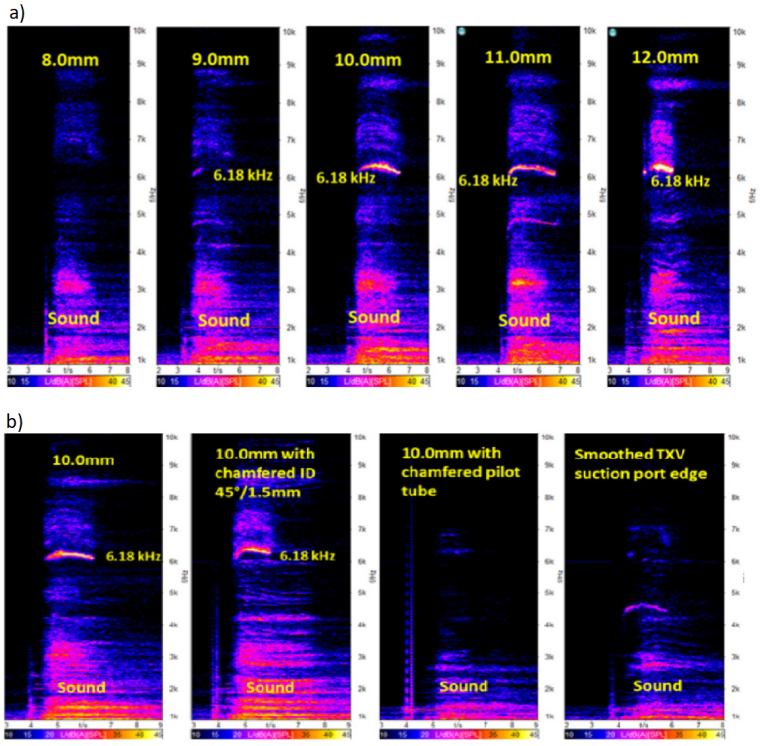

Source: Adapted from Koberstein et al. (2015).

Han et al. (2009) conducted experiments for evaluation of SPL at the evaporator outlet under heating cycle of a small-split air-conditioner with cassette type IDU using R22 as working

fluid. They proposed that reducing condenser outlet diameter from 9.52 to 6.35 mm and with aid of strainer with 60 pore per inch downstream the EEV leads to flow pattern shift from slug to bubbly flow, reducing the flow-induced noise. Unfortunately, these authors did not perform flow pattern visualizations downstream the strainer. According to Han et al. (2009), a considerably reduction on the frequency from 1 kHz to 4 kHz and a increase on the vapor quality at the evaporator outlet from 0 to 0.16 was observed. Analogous to Han et al. (2009), Singh et al. (1999) and Jeong et al. (2007) also observed that as the vapor quality increases the noise also increases until a vapor quality of 0.2. However, Singh et al. (1999) only observed this behavior for EEV with 10 and 20% of aperture. Han et al. (2009) also found that for a given mass flow rate for frequency ranging from 1 KHz to 6 kHz, the noise increases as the vapor quality increases, while at else frequencies the SPL is similar regardless of the vapor quality. In addition, they evaluated the flow pattern, according to the flow pattern map of Baker et al. (1953) suggesting that their experimental conditions corresponds to bubbly flow only. As mentioned above, the flow pattern map developed by Baker et al. (1953) was proposed employing gas-oil flows and tube diameters larger than 101 mm, then it may not properly represent the flow pattern for refrigerants and a tube diameter of 6.35 mm.

Hirakuni et al. (2004) pointed out that the SPL for the orifice without porous metal increases as the mass flow rate increases. However, the aid of a porous metal at the orifice results in almost constant noise as the mass velocity increases, in general, 5 dB(A) lower than without the porous metal. In Fig. 22(a), the EEV with the porous metal was able to produce a SPL 13 dB(A) lower than the original one without the porous metal. Figure 22(b) shows the sound spectrum from 0 to 10 kHz. The expansion valve with porous metal produces a lower noise in the frequency range from 0.5 Hz to 6 kHz, reaching a maximum difference of 25 dB(A).

Figure 22 – Noise level and noise spectrum with and without the porous metal.

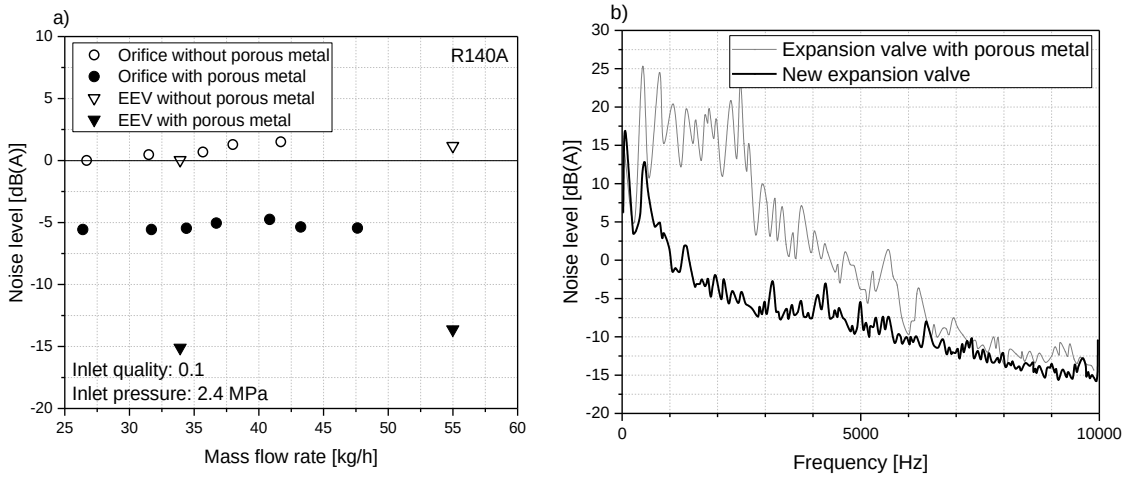

Source: Adapted from Hirakuni et al. (2004).

Kim et al. (2019) carried out an investigation on the sound pressure level during the expansion process in an EEV built inside an anechoic chamber under heating cycle of a commer-

cial mult-split ASHP during transient operational conditions. Kim et al. (2019) simultaneously evaluated the SPL and the flow pattern at the in/outlet of the EEV through quartz tubes of 4.8 mm internal diameter for horizontal and vertical flows and compared it to the flow pattern prediction methods proposed by Hajal, Thome and Cavallini (2003) and Hewitt and Roberts (1969), respectively. Table 4 provides the experimental conditions with respect to the elapsed operating time, beginning with the start of the compressor.

Table 4 – Test conditions at the EEV inlet.

Operating cycle number		1	2	3	4	5	6
Horizontal	Elapsed time [s]	46	71	133	233	289	401
	Temp. Cond. [ºC]	25.7	27.9	26.4	35.3	38.8	38.3
	Pressure [MPa]	1.75	1.73	1.75	2.31	2.48	2.7
	Mass flow rate [kg/h]	6.22	11.5	21.2	43.9	44.5	41.9
Vertical	Elapsed time [s]	48	71	110	218	244	422
	Temp. Cond. [ºC]	24,2	27.5	27.5	34.9	35.7	33.7
	Pressure [MPa]	1.75	1.77	1.76	2.26	2.33	2.71
	Mass flow rate [kg/h]	6.55	15.2	21.7	40.7	40.5	41.8

Source: Kim et al. (2019).

From Fig. 23a, at the beginning of the heating cycle a wavy-annular flow pattern is registered at the EEV inlet while only vapor occurs at the EEV outlet for mass velocity of 95 kg/sm^2. At this condition, the authors recorded the lowest SPL corresponding to 39.4 dB(A). As the operation cycle continues, the mass velocity increases and the quality at the inlet and outlet decreases while the SPL increases. The abrupt increase on the SPL occurs as the inlet flow pattern shifts from annular to intermittent flow (data 3), and when the flow at the outlet of EEV changes to intermittent flow, the SPL increases even more (data 4 and 5). For further cycle operating time, the EEV starts to admit only liquid (data 6) leading to a decrease in the SPL of about 8 dB(A). The higher SPL was observed when the flow patterns at the inlet and outlet were intermittent flow, however under condition of liquid flow at inlet and intermittent flow at the outlet a significant reduction on the noise was observed. Even though the point 3 (327 kg/sm^2) presents half of the mass velocity of point 6 (639 kg/sm^2), the combination of intermittent and annular flow pattern at the inlet and outlet, respectively, resulted in a higher noise.

For vertical flow conditions, the beginning of the heating cycle starts with a small amount of refrigerant flowing with mass velocity of 105 kg/sm^2 and churn flow pattern at the EEV inlet expanding into gas flow, leading to the lowest SPL (data 1). As the heating operation cycle continues, the mass velocity increases leading to a higher SPL (data 2 and 3) in the presence of two-phase flow at both EEV inlet and outlet. At this condition, churn and annular flow pattern occurs at the EEV inlet and outlet, respectively. For further operation time elapsed, the two-phase flow pattern remains annular at the outlet of the EEV, even though the inlet vapor quality decreases and the noise increases (data 4 and 5) as the inlet flow pattern shifts from churn to slug flow pattern. Nevertheless, the fluid state reaches the condition of only liquid at the EEV

inlet while the flow pattern at its outlet is still annular, thus the noise decrease about 7 dB(A). As general conclusion, it is important to highlight that the association of flow pattern at the inlet and outlet play a significant role on the SPL for vertical and horizontal flows. Unfortunately, in their study, the valve aperture was not specified for each operational condition. In general, the two-phase flow pattern considerably influences the noise near the EEV leading to higher SPL for unsteady flow pattern. The horizontal pipe layout (51.4 dBA) promoted a higher SPL than the vertical layout (46.4 dBA). At this condition, for horizontal layout, the outlet two-phase flow assumes intermittent pattern while the outlet for vertical layout is annular. On the other hand, Liu et al. (2015) pointed out the advantageous combination of inclined and horizontal tubes over the vertical layout between the TXV outlet and the evaporator inlet connection, helping to reduce the flow-induced noise, mainly at the frequency range from 1.8 kHz to 6.5 kHz. Analogous to Han et al. (2010) and Han et al. (2009), Liu et al. (2015) claim that such an approach may change the evaporator inlet flow pattern from intermittent to stratified or annular flows, diminishing flow-induced noise.

Figure 23 – Flow pattern and SPL during initial operation of the refrigeration cycle and the flow pattern images near EEV. The flow pattern prediction methods for condensation of R410A, Tsat=40ºC, and diameter of 4.8 mm for: a) horizontal flow pattern map based on Hajal, Thome and Cavallini (2003) map and b) vertical based on Hewitt and Roberts (1969) map.

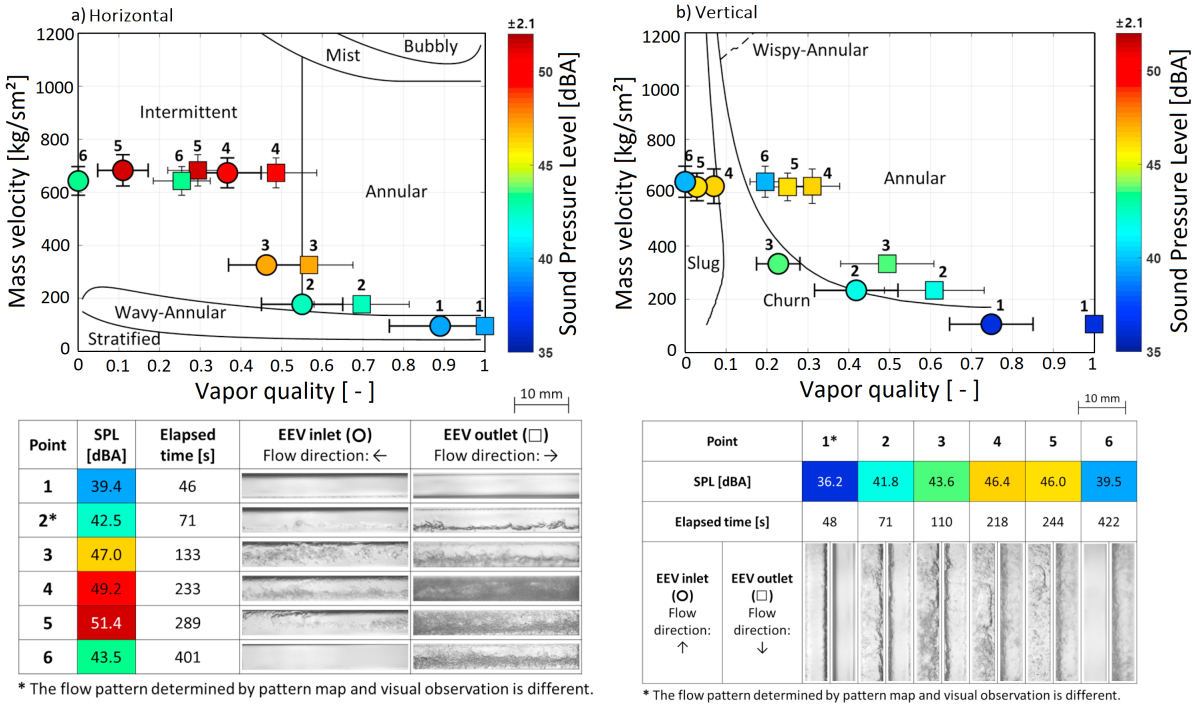

Point	SPL [dBA]	Elapsed time [s]	EEV inlet (O) Flow direction: ←	EEV outlet (□) Flow direction: →
1	39.4	46		
2*	42.5	71		
3	47.0	133		
4	49.2	233		
5	51.4	289		
6	43.5	401		

* The flow pattern determined by pattern map and visual observation is different.

Point	1*	2	3	4	5	6
SPL [dBA]	36.2	41.8	43.6	46.4	46.0	39.5
Elapsed time [s]	48	71	110	218	244	422
EEV inlet (O) Flow direction: ↑ / EEV outlet (□) Flow direction: ↓						

* The flow pattern determined by pattern map and visual observation is different.

Source: Kim et al. (2019).

According to Han, Jeong and Kim (2011), the collapsing bubble flowing through orifice produces noise at natural frequency band near the natural frequency given by the model of Minnaert (1933) with bubbles having the same diameter as the internal diameter of the orifice .

Kim et al. (2019) considered the equivalent radius corresponding to the annular gap between the orifice and the needle of EEV ranging from 300 to 600 μm . It is worth mentioning that such condition would led to a natural frequency ranging from 30 to 60 kHz based on Minnaert (1933) model, overcoming the upper limit of the human audible frequency. Hence, the collapsing bubble may not be the source of the noise. Kim et al. (2019) attributed the higher SPL to the horizontal pipe orientations due to the two-phase flow pattern at the inlet and outlet. On the other hand, opposite behavior to this was observed by Han et al. (2009) and Han et al. (2010), where the horizontal pipe layout was reported as advantageous over the vertical orientation. This discrepancy could be attributed to the difference on the expansion device since Han et al. (2009) and Han et al. (2010) employed capillary tube in their study, refrigerant R600a, and distinct operating conditions while Kim et al. (2019) performed their experiments for R410A. Also, it must be taking into account that the gas density of the R410A used by Kim et al. (2019) is about eight times higher than of R600a employed by Han et al. (2009) and Han et al. (2010), and the liquid density of the R410A is twice the R600a liquid density at evaporation temperature of – 5ºC. As pointed out by Cheng, Ribatski and Thome (2008) and well known in literature, transport properties of the refrigerant significantly affect the flow pattern (HAJAL; THOME; CAVALLINI, 2003) and, consequently, the flow-induced noise.

Analogous to Hirakuni et al. (2004), Kim and Song (2020) evaluated the effects of the following flow conditioners at the EEV inlet and outlet: a single and three porous metal disk (PMD) with porous size of 450 μm; a honeycomb cylinder (HCC) with porous size of 600 and 900 μm. Under normal heating operating mode, the HCC reduced the noise frequency level from 9.0 kHz and 12 kHz to 6000-7000 kHz. On the other hand, the PMD exhibited frequency peaks near 2 kHz. Both behaviors are distinct of the expected one predicted by Minnaert (1933) model, once bubble diameters have been reduced after the flow conditioner (HIRAKUNI et al., 2004), which should have increased the natural frequency. In general, the SPL was reduced by the flow conditioner regardless of their geometry with the HCC 600 μm performing as the best among the evaluated flow conditioners, as illustrated in Fig. 24. Kim and Song (2020) and Jeong et al. (2007) observed similar behaviors as the EEV aperture increases. Under transient operating mode, Kim and Song (2020) concluded that the HCC flow conditioner was able to reduce the SPL by approximately 10 to 20 dB(A), while the PMD achieved a noise reduction of 5 to 15 dB(A). Therefore, the noise reduction seems not to be related to the porous size of the flow conditioner, but to the flow conditioning geometry. Wei et al. (2015) performed a three-dimensional numerical simulation on the evaluation of the SPL in pressure reducing valve with 60% opening with and without a porous media at the valve outlet. These authors found that the porous media was able to effectively reduce the noise. They also pointed out that as higher the inlet pressure, higher is the SPL at high frequencies.

Hirakuni et al. (2004) and Kim and Song (2020) also concluded that the combination of flow patterns at the inlet and outlet plays a significant role on the noise level, with the flow conditioner being an effective way of reducing the SPL (KIM; SONG, 2020). Additionally, Kim

and Sung (2018) carried out numerical simulation for distinct valve plunger designs, concluding that the SPL can be also significantly reduced by changing valve plunger geometry. The flow path geometry between the plunger and the seat comprises the root cause of flow instability (NAKANO; OUTA; TAJIMA, 1988). Kim and Sung (2018) pointed out that a flat plug shape can effectively reduce the flow-induced noise and vibration upstream the valve. On the other hand, Amini and Owen (1995) pointed out that 60º angled conical plug can reduce the valve's noise and vibration downstream the orifice.

Figure 24 – Comparison of SPL affected by distinct flow conditioners for three heating modes: normal heating, excessive EEV opening, and off-operation.

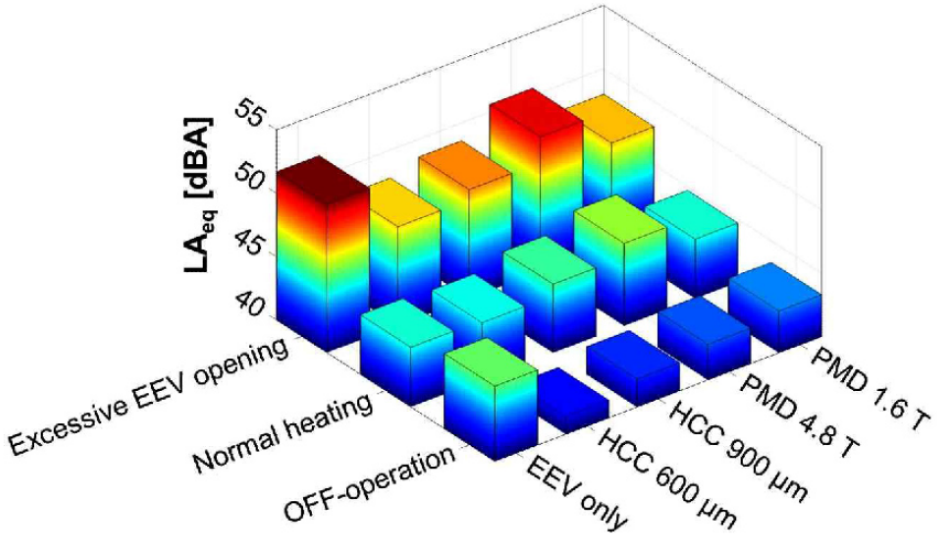

Source: Kim and Song (2020).

According to Huang (2015), the SPL can be reduced by about 3 dB(A) by changing the throttle angle from 35 to 65º. On the other hand, the noise can increase about 6 dB(A) by increasing the length of the opening orifice from 1.88 mm to 2.48 mm (HUANG, 2015). Unfortunately, despite these results, little attention has been paid in the literature to the flow path geometry inside the valve.

At this point, it should be mentioned that independent laboratories adopted distinct approaches for the SPL evaluation in expansion devices. Although Singh et al. (1999) evaluated the SPL within the flow while Jeong et al. (2007) evaluated the noise from outside the tube, both found an increase on the SPL as the mass velocity increases. On other hand Hirakuni et al. (2004) and Kim et al. (2019) concluded that the combination of flow patterns at the inlet and outlet plays a significant role on the noise level.

In summary, from the available studies on flow-induced noise in expansion valves, the following parameter seems to show a significant influence on the SPL: i) inlet and outlet vapor quality; ii) mass flow rate; iii) valve aperture, and iv) the combination of flow patterns at the inlet and outlet. Therefore, for further research it is essential to conduct systematic experiments on expansion valves acquiring simultaneously to the SPL the flow patterns at the in- and outlet,

valve aperture, vapor quality, and PWM control in order to provide a profitable database, capable of providing a parametric analysis of the boundary conditions on the SPL. Furthermore, the acceleration of the device should be evaluated as well as the SPL inside the flow and outside the EEV in order to better understanding how the structure acts as a band-pass filter under distinct vapor qualities. Therefore, the current study aims to fill this literature gap evaluating and cross-correlating the in- and outlet flow pattern, valve orifice aperture, the noise within and outside the expansion device, and its acceleration for distinct operational conditions.

2.3 Comparison of flow-induced noise in expansion devices

Table 5 presents a summary of the literature concerning experimental investigations of the SPL in expansion devices for outlet vapor quality up to 1.0 discussed during this chapter. For the SPL evaluated within the capillary tube, the results from Singh et al. (1999) presents almost the same SPL average value regardless the experimental condition, except for the capillary length of 0.81 m at mass velocity of 6070 kg/sm^2 that exhibited the highest SPL of 153 dB and mean SPL of 147 dB. The lowest SPL value of 117 dB and mean SPL of 122 dB among the expansion devices within the flow were observed by Boabaid Neto et al. (2018) for a capillary of 0.767 mm I.D. with continuous two-phase flow inlet and annular outlet flow. Although Tannert and Hesse (2016) evaluated the noise from outside the capillary, the same trend was found, with the lowest SPL (27 dB) occurring under annular flow conditions at the capillary outlet, while the highest (41 dB) occurs for plug flow pattern at the end section of the capillary leading to a discontinuous outlet jet. On the other hand, Ruebeling and Grohmann (2020) pointed out that the noise increases as the vapor quality increases. Kim et al. (2019) concluded that the SPL can be significantly reduced under condition of liquid single-phase flow at the expansion device inlet even if under condition of intermittent flow pattern at the outlet.

For the noise evaluated outside the capillary tube, independent laboratories presented nearly the same mean SPL under distinct operational conditions (HAN et al., 2009; HAN et al., 2010; TANNERT; HESSE, 2016), except for Ruebeling and Grohmann (2020) that exhibited the lowest mean noise of 17 dB(A). This fact may be related to the specific characteristic of refrigeration device evaluated in their study. Due to the restricted database for orifice and the evaluation of the SPL from different microphone positions the quantitative comparison between the studies (SINGH et al., 1999; HAN; JEONG; KIM, 2011; HIRAKUNI et al., 2004) can be considered as inappropriate.

For the noise evaluated from outside the EEV, Jeong et al. (2007), Han et al. (2009), and Kim et al. (2019) found similar mean SPL, despite Kim et al. (2019), who pointed out the lowest SPL of 36 dB(A) for vertical layout operational condition for annular flow pattern at the inlet and single-phase vapor at the outlet. Furthermore, only Koberstein et al. (2015) mentioned the effect of the connection geometry between the pilot and the TXV suction tube on the flow-induced noise.

Table 5 – Summary of the experimental studies concerning refrigerant flow-induced noise in expansion devices.

Authors	Fluid/ orientation	Expansion device chacateristic	Mass velocity [$kgs^{-1}m^{-2}$]	SPL [dB]	$\overline{SPL}$ [dB]
SPL within capillary tube					
Singh et al. (1999)	R134a/ →	1.626 mm I.D.; L=0.8 m Outlet aperture 5º	4553	135 - 150	143
		1.626 mm I.D.; L=0.8 m Outlet aperture 10º	4553	129 - 140	136
		1.626 mm I.D.; L=0.8 m	4553	138 - 146	140
			6070	140 - 153	147
		1.626 mm I.D.; L=1.62 m	3035	134 - 140	136
			4553	133 - 138	138
			6070	130 - 143	140
		1.626 mm I.D.; L=322 m	3035	132 - 141	139
Boabaid Neto et al. (2014)	R600a/-	-	-	120 - 145	132
Boabaid Neto et al. (2018)	R600a/-	0.643 mm I.D.	-	120 - 142	130
		0.767 mm I.D.		117 - 128	122
SPL outside capillary tube					
Han et al. (2009)	R600a/ →↑	-5ºC; 4.35 mm I.D.	52.3	32 - 36	34
		-10ºC; 4.35 mm I.D.		31 - 33	32
Han et al. (2010)	R600a/ →↑	4.35 mm I.D. (↑)	51.8	32 - 38	35
		3.56mm I.D. (→)	77.3	31 - 35	32
Tannert and Hesse (2016)	R600a/ -	-	-	27 - 41	32
Xia et al. (2014)	R600a/ →	0.7 mm I.D.	-	20 - 38	28
				20 - 30	25
Celik and Nsofor (2011)	R600a/ →	6.0 mm I.D.	31.9	40 - 55	55
Ruebeling and Grohmann (2020)	R600a/ →	0.6 mm I.D.	421 - 633	17 - 27	23
Short-tube orifice					
Singh et al. (1999)	R134a / →	IS; p_{out} = 8bars	10784	142 - 153	148
		IS; p_{out} = 4bars		129 - 153	144
		IS; p_{out} = 4bars	8088	131 - 149	143
		IS; p_{out} = 3bars		130 - 148	140
		IOS; p_{out} = 4bars	10784	127 - 136	133
		IOS; p_{out} = 4bars	8088	127 - 134	132
Han, Jeong and Kim (2011)	R600a/ ↑	2.00 mm I.D.	238	12 - 15	13
Hirakuni et al. (2004)	R600a/ →	1.00 mm I.D.	9549 - 16622	-	-
Thermal and Electrical expansion valve					
Singh et al. (1999)	R134a/ -	TXV aperture 100%	45.36*	139 - 147	143
		EEV aperture 35%	45.36*	133 - 149	135
		EEV aperture 20%	54.36*	133 - 137	136
		EEV aperture 20%	33.84*	131 - 134	133
		EEV aperture 10%	33.84*	130 - 137	134
Jeong et al. (2007)	R22/ →↑	EEV	60 - 120*	44 - 46	44
Han et al. (2009)	R22/ →	EEV	100 - 120*	37 - 40	39
Kim et al. (2019)	R410A →↑	EEV (→)	6-42*	39 - 51	45
		EEV (↑)		36 - 46	42
Hirakuni et al. (2004)	R410A/ →	EEV	34 - 55*	-	-
Kim and Song (2020)	R410A/ →↑	EEV	15.6 - 61.5*	42 - 52	47

IS = inlet screen; IOS = in and outlet screem

NS = no screen * mass flow rate in kgh^{-1}

As a general statement, the SPL evaluated within the expansion devices presented similar values of noise, with mean noise ranging from 132 to 148 dB, regardless the expansion device, fluid and operational condition, except for Boabaid Neto et al. (2018) that found the lowest mean noise of 122 dB. For the noise evaluated outside the expansion device, the expansion valve exhibits higher SPL than the capillary tube even for distinct operational conditions and refrigerant. At this point, it is important to highlight that the simultaneous study of in- and outlet flow pattern and SPL is crucial once most of the studies present in literature concerning flow-induced noise claims that the noise is directly affect by flow pattern.

2.4 Literature conclusion remarks

The behavior and mechanistic aspects of flow-induced noise in expansion devices still needs to be clarified. The evaluated studies from literature rarely provide an in-depth discussion on the flow-induced noise phenomenon in such devices. They involve different analyses, under different conditions, measured either internally or externally to the device, without considering the acoustics of the environment, or even without considering characteristics of fluid-structure interaction (vibro-acoustics), peculiar to each of the used equipment. However, it is still possible to make some comparative and relative analyses for publications reported under similar operational conditions. Another useful approach is given more attention just recently, as flow-induced noise and vibration are being analyzed simultaneously with flow pattern characterization using transparent test sections and high-speed cameras.

Different trends of the SPL have been reported in the literature by independent laboratories with changing vapor quality, mass velocity, pressure drop, flow pattern, use of a screen, and expansion device geometry. Also, as far as the SPL is evaluated outside the expansion devices, some design features will act as a parametric variable influencing the frequency spectrum. In that way, each test section introduces specific characteristics allowing certain frequencies to pass through the environment. Unfortunately, some of these important details are not addressed in these cases, which jeopardizes a thorough metanalysis.

In general, the following main additional issues were extracted from the literature:

- The outlet transition geometry from the capillary tube to the evaporator affects the noise level, however, the associated behavior is not clear since different trends were observed according to the outlet angle aperture.
- The mass velocity and flow pattern have a considerable influence on the noise. Distinct effects of the flow pattern at the capillary outlet on the SPL from independent laboratories were reported in literature. In addition, for a given flow pattern, the SPL increases as the outlet vapor quality increases.
- The outlet orifice screen significantly reduces the noise.

- Different SPL trends were identified in expansion valves according to valve aperture, mass flow rate, and flow pattern. For a given mass velocity, the cross-combination of the inlet and outlet flow pattern seems to play a significant role on the noise level.
- Reducing the pipe diameter or increasing the mass flux shifts the flow pattern from slug to annular, reducing the flow-induced noise.
- Under single-phase vapor conditions at the expansion device inlet, the SPL increases marginally, regardless of the operational condition.
- It may be speculated that, in some cases, the expansion device acts as a band-pass filter, allowing only certain frequencies to be transmitted through the device wall as reported from independent laboratories.
- In general, the expansion valve exhibited higher SPL in dB(A) than the capillary tubes, regardless of the operational conditions.

Most of the present studies concerning flow induced noise in the literature employ hydrocarbons (HCs) refrigerants as R600a, which has a low global warming potential (GWP). However, HCs' applicability in air-conditioning refrigeration systems is questionable due to their high flammability and explosion hazard, impeding its use in large capacity systems (CALM, 2008). Furthermore, as pointed out by Cheng, Ribatski and Thome (2008) and well known in the literature, transport properties (surface tension, phase densities, and viscosity) of the refrigerant significantly affect the flow pattern and, consequently, the flow-induced noise. Considering that new refrigerants are being released, efforts should continue to find a substitute with low flammability and toxicity, low GWP, high coefficient of performance, cost-effectiveness, and compatibility with air-conditioning refrigeration systems.

3 EXPERIMENTAL APPARATUS

This chapter describes the experimental facility adopted in the current study. The chapter also describes the test section characteristics, data acquisition system, the sensors, and the actuators.

3.1 Test bench

The test bench was built at the Heat Transfer Research Group - Engineering School of São Carlos - University of São Paulo. Its previous configuration was built to evaluate flow pattern and pressure drop in tube within twisted tapes (KANIZAWA, 2014; MOGAJI, 2014), and heat transfer coefficient evaluation of hydrocarbons and their mixtures during boiling and condensation (BANDARRA FILHO, 2002; BARBIERI, 2005; OLIVEIRA, 2021; MOREIRA, 2021). In the current work, the test bench was modified to allow the investigation of flow-induced noise during the fluid expansion process along a thermostatic expansion valve with similar capacity of a household air-conditioning. The tube of the test section comprising the thermal expansion valve device was manufactured in glass in order to allow the visualization of the two-phase flow during the expansion process and cross-correlate it to the flow-induced noise. A photograph of the main circuit of the experimental apparatus is depicted in Fig. 25.

Figure 25 – Picture of the experimental apparatus located at the Heat Transfer Research Group EESC/USP.

Source: Author.

3.1.1 Refrigerant loop

Figure 26 illustrates the schematic diagram of the main circuit showing its main components and the locations along the test circuit of temperature, pressure, and mass flow rate measurements. The experimental test bench is basically composed of the main circuit (test fluid) and the auxiliary circuit (ethylene-glycol/water). The auxiliary circuit is responsible to absorbs heat from the main circuit and transfers it to the heat rejection circuit (detailed in the next section), and also to provide heat to the test fluid in the heating section.

Figure 26 – Schematic diagram of the test fluid circuit.

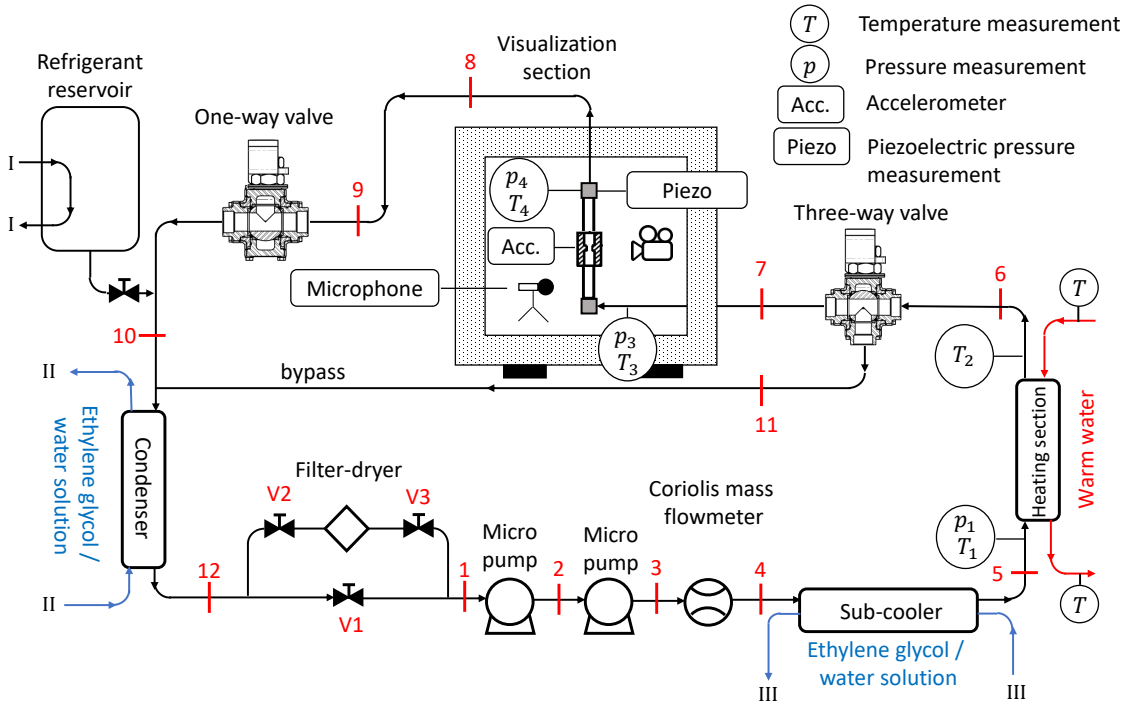

Source: Author.

A refrigerant supply line connects the bottom of the reservoir tank to the closed loop circuit. In the refrigerant loop, subcooled liquid is drained from the condenser by two gear oil-free micropump models GC M23 JKS5 and GD 223/56C operating in a serial arrangement powered by two variable-frequency drives models ABS, ACS355 and Danfoss, FC51, respectively. The mass flow rate is set by a PI control system acting on a frequency inverter drive that powers the pumps. Each pump has its particular operational condition. Based on it, a procedure taking into account the head loss x flow rate curve of each pump was implemented within LabView (2013) code to provide a suitable output signal to each variable frequency drive leading to similar mass flow rates. Downstream the micro pumps is located a mass flow meter operating based on Coriollis principle to evaluate the mass flow rate at the test section. Between the mass flow meter and the heating section, the test fluid flows through a tube-in-tube subcooler to ascertain subcooled state of the refrigerant at the inlet of the heating section. Thereby, at the inlet of the heating section is located an absolute pressure transducer (p_1) and a thermocouple (T_1) immersed within the test fluid to properly evaluate its thermodynamic state. At the heating section, water is

employed as heat source. The heating section consists of a tube-in-tube heat exchanger, with the inner tube made of stainless steel and the outer of chlorinated polyvinyl chloride (CPVC). The internal diameters of the inner and outer tubes are 11.3 and 23.7 mm, respectively, and their total lengths are 8 m. The test fluid flows inside the inner tube and hot water flows counter-currently to the test fluid in the annular region. The water temperature is evaluated at the inlet and outlet of the heating section. Downstream the heating section is located the acoustic chamber, where the test section is situated.

An absolute pressure transducer and a thermocouple immersed within the fluid are located at the inlet and outlet of expansion device to evaluate its thermodynamic state. A piezoelectric pressure sensor (PCB Piezoeletronics 105C03) was also installed at the expansion device outlet to evaluate the pressure fluctuations during the fluid expansion process. A single axis accelerometer (PCB Piezoeletronics 352A24) was positioned at the TXV device to evaluate the acceleration of the test section structure during the fluid expansion process. In order to evaluate the flow-induced noise from outside of the expansion device an acoustic chamber was build to isolate the test section from the laboratory background noise. There is also a thermocouple placed inside the acoustic chamber to monitor the air temperature. The test circuit operates with one- and three-way pneumatic solenoid valves manufactured by Metalúrgica Golden Arts. The valves arrangements are normally open, with the three-way valve allowing the fluid to flow only in the direction of $6 \rightarrow 7$. To minimize heat losses to the environment the fluid line $6 \rightarrow 7$ and bypass line were covered with 3 cm layer of elastomeric foam. A safety system was installed in case of test section glass rupture, automatically closing the one-way valve and opening the three-way valve in direction of $6 \rightarrow 11$ while the line $6 \rightarrow 7$ is closed, allowing the fluid to flow through the bypass line returning directly to the condenser. The safety system is composed of a pressure switch that evaluates the pressure difference between the test section inlet and outlet and triggers the pneumatic solenoid valves in case of a sudden pressure drop as result of glass rupture. Refrigerant is circulated though the filter-dryer (Danfoss®, model ELIMINATOR 1.5) only after charging the test fluid in the apparatus to remove humidity and particles remaining from maintenance, thereby the valves V2 and V3 operates normally closed, and V1 normally opened. Finally, to condense and subcool all the vapor generated during the expansion process a shell-and-tube heat exchanger ($10 \rightarrow 12$) with the refrigerant flowing in the shell and ethylene-glycol/water solution in the tubes is used.

Figure 27 illustrates the thermodynamic states of refrigerant along the main circuit in a pressure vs. enthalpy diagram. According to Fig. 26, from the condenser, the pressure is raised through the first ($1 \rightarrow 2$) and second pump ($2 \rightarrow 3$), and then the refrigerant flows through the Coriolilis mass flow meter ($3 \rightarrow 4$). A heat exchanger, located downstream the Coriollis mass flowmeter is responsible to subcool the fluid ($4 \rightarrow 5$) and ensure a certain thermodynamic subcooled state at the heating section inlet. Downstream the subcooler, the test fluid temperature is raised in heating section ($5 \rightarrow 6$) up to the desired thermodynamic state condition at the expansion device inlet. Once the fluid leaves the heating section, parcel of its heat and pressure

are dissipated up to the test section inlet (6 → 7). Then, the test fluid expands isoenthalpically through the TXV (7 → 8). As the test fluid returns to the condenser (8 → 10), although the tube is insulated with elastomeric foam, the vapor quality increases once its temperature is inferior to the environment and due to the flashing process as pressure decreases along the circuit. Finally, the test fluid is subcooled and condensed in the condenser unity (10 → 12).

Figure 27 – Pressure vs. enthalpy diagram of the refrigerant thermodynamic states along the main circuity.

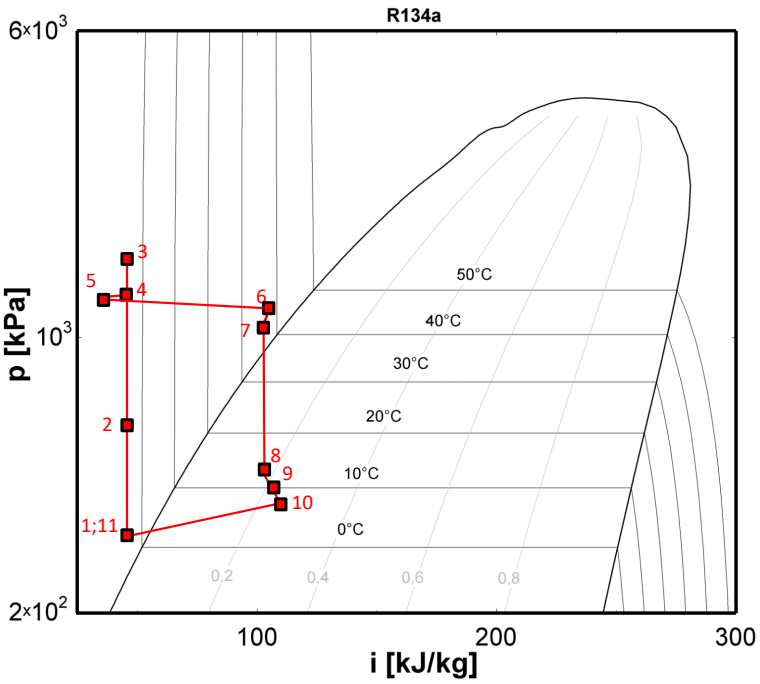

Source: Author.

3.1.2 Auxiliary circuits

This section details the auxiliary circuits employed to control the test fluid thermodynamic conditions along the main circuit.

Vapor compression system

The auxiliary circuit, schematically illustrated in Fig. 28, is composed of a vapor compression system working with R134a, an auxiliary circuit, and a heat rejection circuit. The vapor compression refrigeration system is responsible for cooling a solution of 60% ethylene-glycol/water in the reservoir allowing thermal fluid temperature down to -25 °C, which is accomplished by means of a plate heat exchanger. The compressor, manufactured by Danfoss®, model MT28-3B30, presents a cooling capacity of 1.7 kW at -23 °C. The anti-freezing solution circulates through a closed loop from its reservoir that contains three electrical heater of 6 kW/220V each. The temperature of the anti-freezing solution is set with the help of a proportional–integral–derivative (PID) controller (MARKARE M400) that actuates on a solid-state electrical relay delivering the necessary power to the heaters based on the temperature of the

anti-freezing solution measured by a Pt100 inside the reservoir. During the experimental campaign the temperature of the anti-freezing solution was kept between -14 and -24 ºC. The tubes that connects the auxiliary circuit to the refrigerant circuit are made of PVC and covered with a layer of 3 cm of elastomeric foam for thermal insulation to minimize the heat losses to the environment.

The ethylene-glycol/water solution is employed to subcool the test fluid as it leaves the second pump (III) and to condense/subcool the test fluid as it leaves the test section (II). A centrifugal pump drives the anti-freezing solution from a stainless steel tank, with a capacity of 0.15 m^3, through the circuit. In the compression loop, as the refrigerant R134a leaves the compressor it is condensed in a shell-tube heat exchanger with the cooling effect provided by the water from a cooling tower located outside the laboratory facility.

Figure 28 – Schematic diagram of the auxiliary circuit.

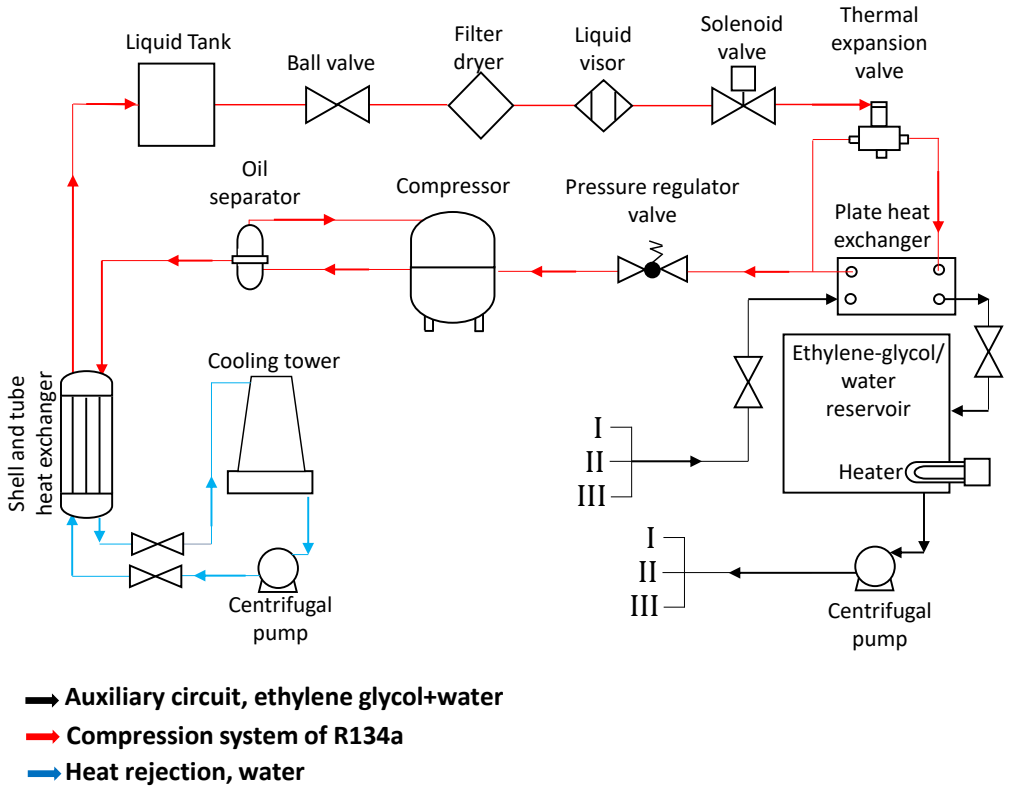

Source: Author.

Heating water circuit (Heater)

The closed heating water circuit, schematically illustrated in Fig. 29, controls the inlet condition of the refrigerant at the test section entry in the refrigerant loop. A supply line connects the water reservoir tank to the stainless-steel centrifugal pump (JACUZI 1JZ1-T, 0.72 kW), which is responsible to drive the warm water through the circuit. It was employed a centrifugal pump manufactured of stainless-steel to avoid oxidation and, consequently, the contamination of the water in the circuit. Also, the centrifugal pump was positioned below the water reservoir

to prevent cavitation. Downstream the centrifugal pump, the water flows through the heating section. Once the water leaves the heating section its mass flow rate is determined by an electromagnetic flow meter (Rosemount, model 8711). The rate of heat exchange between the hot water and the test fluid is regulated by controlling the water mass flow rate through manually manipulating a ball valve opening located in the bypass line. The water temperature within the reservoir is adjusted by a PID controller (Fullgauge, model AutoPID plus), which determines the necessary supply power delivered to the electrical heater to reach the desired condition. During the experimental campaign the water temperature was kept from 25 to 55 ºC. The loop is closed as the water returns to its reservoir.

Figure 29 – Heating water circuit.

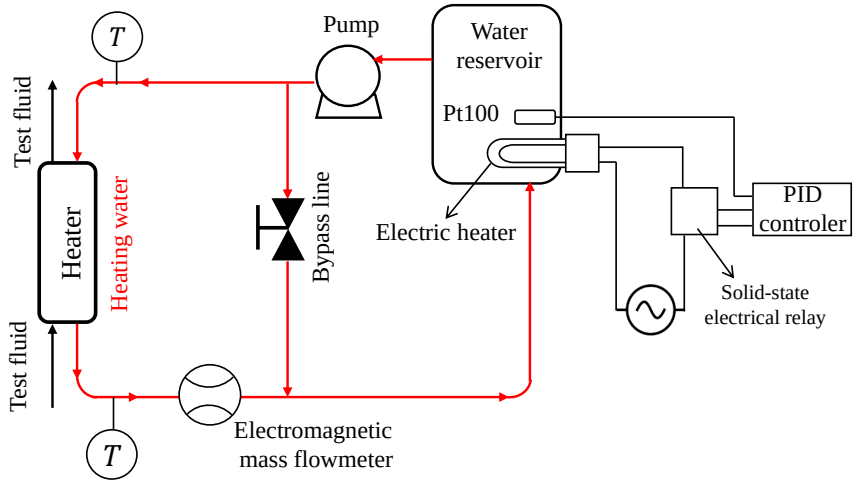

Source: Author.

3.1.3 Acoustic chamber

An acoustic chamber based on multilayer element wall was built in order isolate the flow-induced noise phenomena in the test section from the external environment sound. Also, in order to minimize the propagation of vibrations from the components of the experimental apparatus to the test section, the acoustic chamber was built separated from the main circuit structure. The inlet and outlet of the test section were connected to the test bench employing flexible manifold hosing to aid on damping vibrations. Furthermore, to minimize vibration from the ground the acoustic chamber was installed on the top of anti-vibration dampers feet manufacture by Vibra-stop. The acoustic chamber was built of medium density fiberboard (MDF) with outside dimensions of 1300 x 1000 x 650 mm, and inside dimensions of 900 x 600 x 450 mm.

The acoustic chamber wall is composed of three layers, which consist of a MDF plate 25 mm thick, 150 mm of sand to improve the system impedance as a result of mass increasing and to act like damper since it is not totally rigid, followed by a second MDF plate 25 mm thick. All the MDF plates were joined with screws and the junctions were sealed with instant glue.

The acoustic chamber wall was designed based on the frequency spectrum prediction of the laboratory environment disturbing sound. It was modelled as a single layer element of equivalent mass. Certainly, the coupling elements of the acoustic chamber wall results in a new system which promotes sound isolation different than a system composed by a single layer element. However, in order to keep the simplicity, the sound transmission loss was estimated based on the total wall mass per unit of area. Therefore, it is worth to mention, this is a conservative approach for the design of the acoustic chamber.

The internal surface of the acoustic chamber was covered with acoustic foam panels of 50 mm high to minimize the internal the sound reflection cutoff frequencies superior to 6950 Hz. Figure 30 illustrates the acoustic chamber internal SPL comparison between the working fluid flowing through the bypass line (TSPL = 49 dB) and through the test section with mass flow rate of 0.03 kg/s at nearly saturated condition at temperature of 30ºC (7.7 bar) at the TXV inlet evaporating to 10ºC (4.1 bar) at the TXV outlet (TSPL = 55 dB). Figure 30a comprises the frequency spectrum up to the human audible frequency of 20 kHz and Fig. 30b illustrates the frequency peaks observed on the external noise that may affect the experimental noise. It should be highlighted that the maximum external frequency peak that overcomes the experimental noise is 10 dB.

Figure 30 – Acoustic chamber internal SPL comparison between the working fluid flowing through the bypass line and through the test section with mass flow rate of 0.03 kg/s at saturation condition at the TXV inlet.

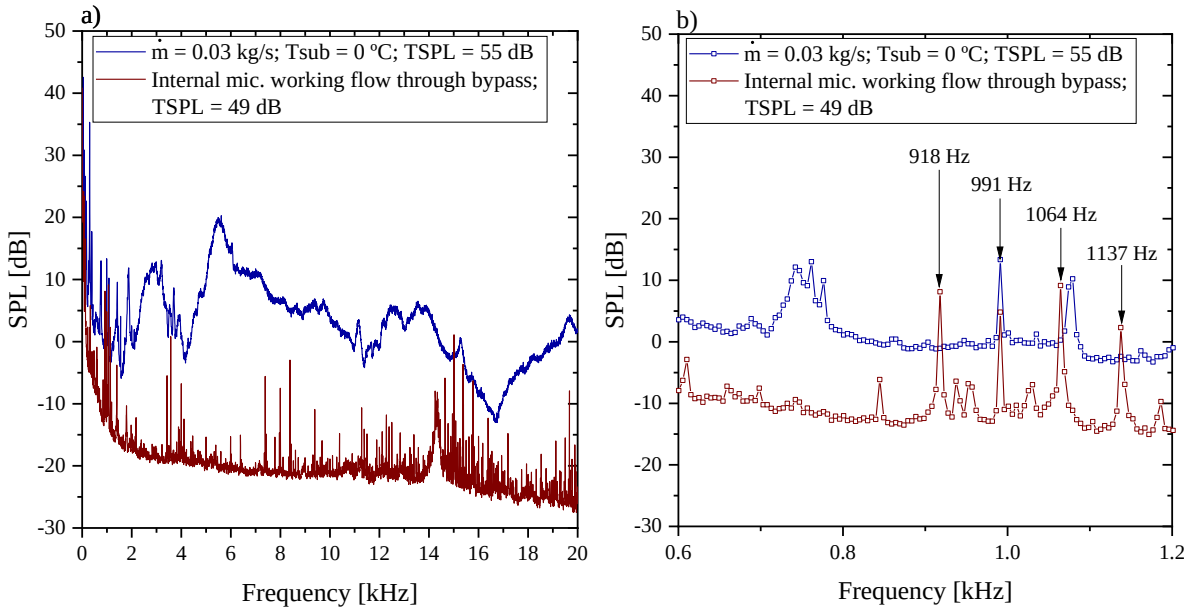

Source: Author.

Its worth mentioning that this is the most critical experimental condition (lowest TSPL among the results), hence it does reveal the external environment frequencies affecting the signal. According to Fig. 30b, frequencies of 918 and 1137 Hz were attenuated, while the frequencies 991 and 1064 Hz are from external environment. As depicted in Fig. 30, the acoustic chamber

was able to satisfactory provide significant attenuation of the laboratory environment disturbing sound. Additionally, the flow-induced noise experiments provided superior frequency spectrum noise than the acoustic chamber background noise. Therefore, it is reasonable to consider that the acoustic chamber provided enough sound transmission loss and its is assumed to be valid.

During the experimental campaign, the internal temperature of the acoustic chamber remained almost constant at 30 $\pm$ 2 ºC, leading to a sound velocity in air of 347 $\pm$ 2 m/s, approximately. Table 6 illustrates the internal acoustic chamber resonance frequency modes estimated as an empty cavity. The flow-induced noise phenomenon in these frequency bands is intensified due to the internal cavity resonance frequency; thus it can be qualitatively evaluated. Certainly, the insertion of the test section apparatus within the acoustic chamber shifts the resonance frequency. Therefore, the resonance frequency peaks illustrated in the discussion section 6.5 may differ from the ones illustrated in Tab. 6.

Table 6 – Acoustic chamber internal resonance frequencies modes.

	Internal dimension		
	0.45 m	0.6 m	0.9 m
Frequency [Hz]	386	289	193
	772	579	386
	1544	1158	772
	3088	2316	1544
	6178	4633	6178

Source: Author.

3.1.4 Test section

Figure 31 shows a picture of the test section inside a glass box containing glycerin (Fig. 31a) and the test section without the glass box (Fig. 31b). The glass box were built and filled with glycerin in order to minimize the effects of light refraction through the test section wall during the acquisition of flow images once the refractive index of the glass and the glycerine are almost similar. This figure also shows the absolute pressure transducers, thermocouples, piezoelectric pressure transducer, stepper motor, accelerometer, and microphone. The pressure drop along the test section is measured from the difference between the absolute pressure transducers. The inlet and outlet temperature are measured from thermocouples immersed within the test fluid. The fluid expansion process was performed by assembling the thermal expansion valve manufactured by commercial valve with evaporator capacity of 12000 Btu (3.5 kW) between two borosilicate glass tubes vertically displayed. Considering that, under such configuration the experimental apparatus was able to produce a maximum pressure drop of 800 kPa.

One of the main goals of the current study is to observe the two-phase flow morphology just before and after the expansion device, therefore the glass tubes were not insulated. The

inner and outer diameters of the tubes are 10.12 and 17.02 mm, with lengths of 90 and 260 mm upstream and downstream of the expansion orifice, respectively. The microphone was positioned 10 mm apart from the TXV outlet with its tip pointing to the test section. The accelerometer was fixed onto the external tube wall close to the TXV outlet. An adhesive Petro Wax model 080A109 was employed between the sensor and the tested object to ensure the frequency response from the accelerometer. To ensure that the accelerometer would remain fixed onto the test section during the experimental campaign, two plastic clamps were employed to hold together the sensor to the test section.

Figure 31 – a) Photograph illustrating the test section inside the glass box and b) solely the test section.

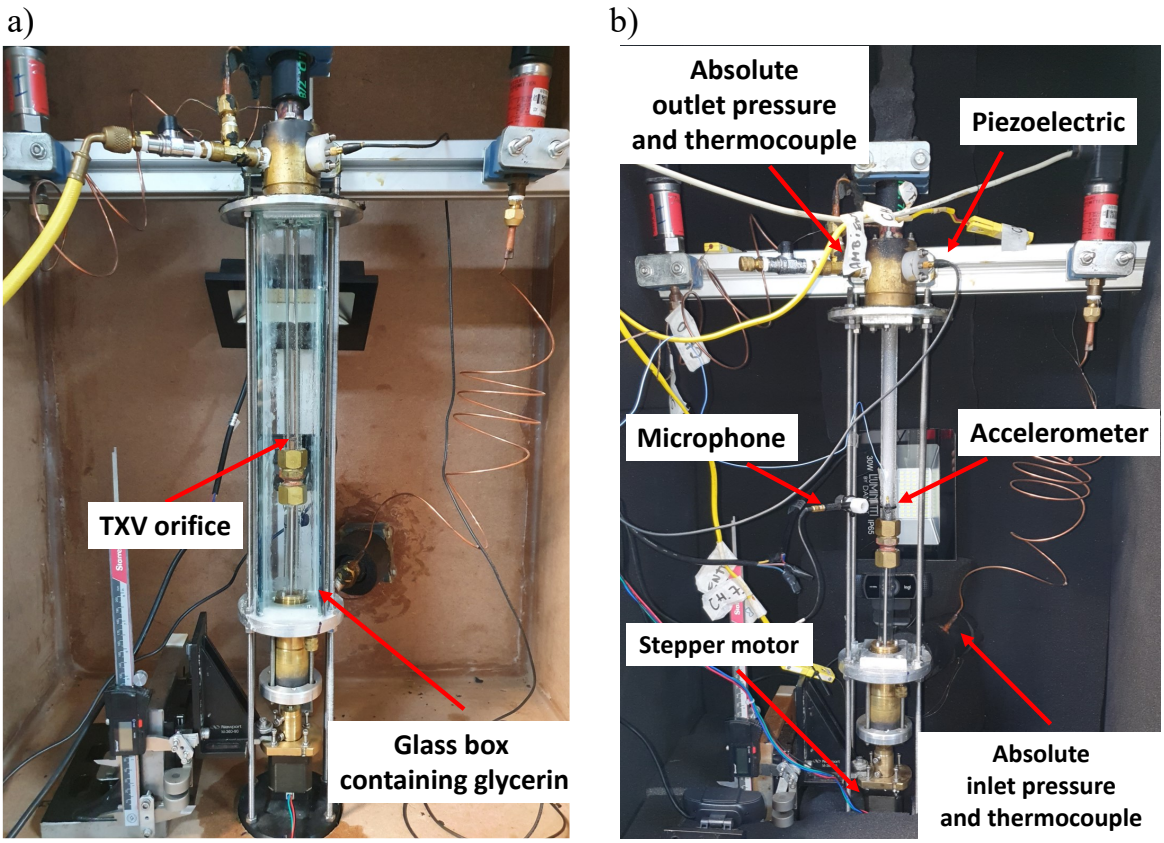

Source: Author.

The thermocouples employed to measure the local temperatures of the refrigerant at the inlet and outlet of the section were positioned inside a capillary tube (tip welded) made of copper with an outer diameter of 1.3 mm, as illustrated in Fig. 32. The end of the capillary bulbs were positioned within the refrigerant and oriented in the same direction of the flow to avoid stagnation effects on the temperature measurement. The body of the capillary tube was fixed by welding its surface to the external wall of the inlet and outlet test section tube. The leaving thermocouples wires from the capillary tube were fixed by employing glue to guarantee that the thermocouples did not move during the tests.

Figure 32 – Schematics of the thermocouple used to measure the refrigerant temperature.

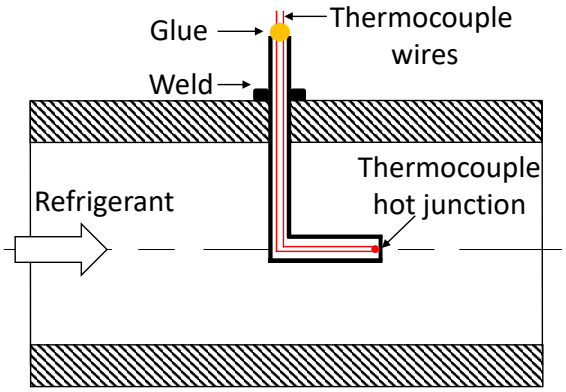

Source: Author.

A stepper motor was connected to the valve plunger controlling the valve opening. Figure 33 illustrates a schematic drawing of the expansion device containing the main elements and dimensions in millimeter. Before assembling the TXV valve, a plunger vertical displacement to number of steps (performed by the stepper motor) conversion factor was estimated. A digital calliper was employed to evaluated the vertical plunger displacement, resulting in a conversion factor of 0.00012 mm/step.

Figure 33 – Schematic drawn of the valve with its main dimensions (dimensions in millimeters).

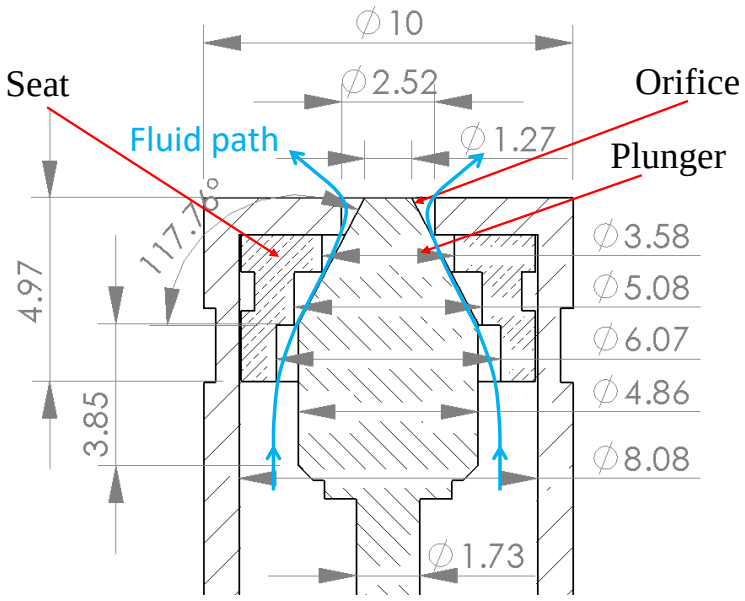

Source: Author.

Figure 34 illustrates the fully closed and opened TXV set ups. The TXV is assumed to be fully closed when the upper plunger face is immediately close to upper orifice face (Fig. 34a), remaining a initial gap for the fluid to path. The total diaphragm displacement was evaluated by cutting the TXV in half and measuring its displacement from initial position to total distended with a digital calliper. Finally, the fully opened TXV was estimated as the maximum diaphragm vertical displacement, as a result of plunger displacement of 0.87 mm (Fig. 34b).

Figure 34 – Schematic draw of the thermostatic expansion valve a) fully closed and b) fully opened (dimensions in millimeters).

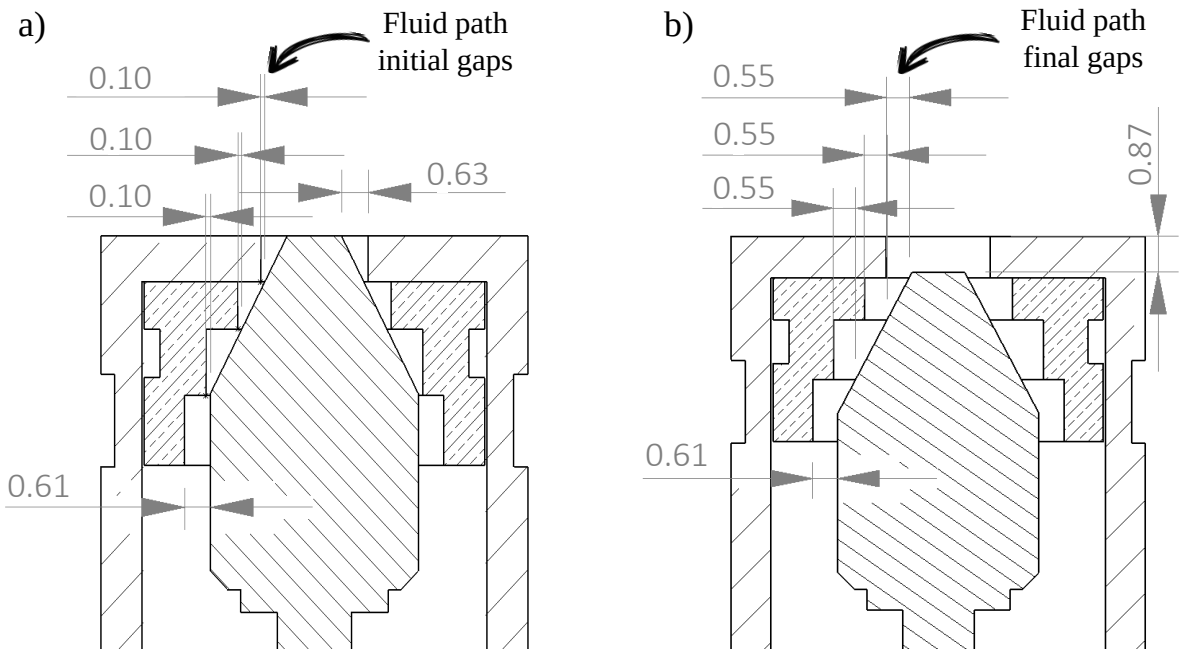

Source: Author.

3.1.5 Opening valve control

The opening valve control system was performed employing the Arduino® programming platform. Arduino is an open-source electronics platform based on a microcontroller with flexible hardware assembling capable of controlling a stepper motor. Figure 35 shows a picture of the Arduino assembly employed to control the TXV aperture.

Figure 35 – Schematic diagram of opening valve control based on Arduino interface.

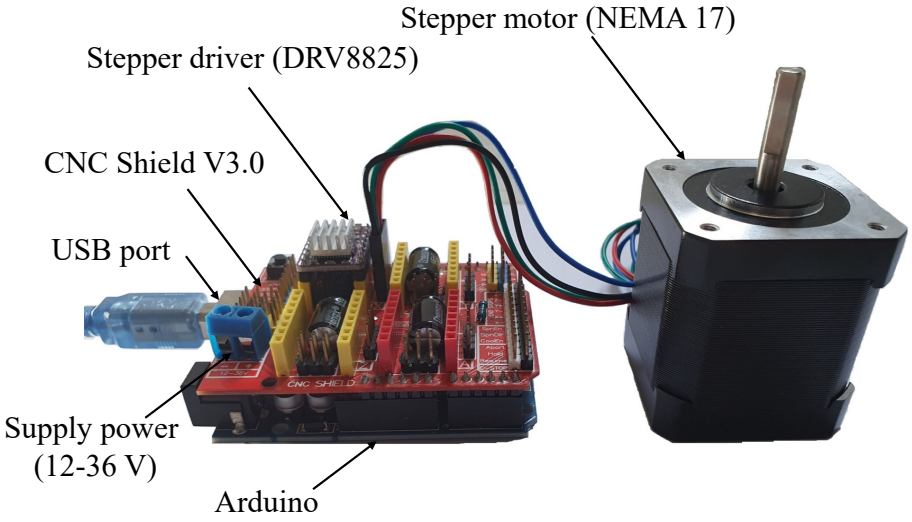

Source: Author.

An Arduino UNO microcontroller (ATMEGA328p) was assembled to a Computer Numerical Control (CNC) driver expansion board model CNC Shield V3.0 that is able to provide necessary power to drive the stepper motor and to control its movements via stepping driver model DRV8825. This stepper drive is able to provide a precision of 6400 steps per revolution (0.05625º/step). A Stepper motor model NEMA 17 with torque of 0.4 Nm was employed to open/close the TXV valve. One output pin of the Arduino imposes the rotation direction (clockwise and counter clockwise) and the other controls the number of steps. A power supply of 8-35 V and 1-5 A was employed to drive the stepper motor.

3.1.6 Flow pattern visualization

The transparent test section for flow visualizations is composed of two borosilicate glass tube with inner and outer diameters of 10.12 and 17.02 mm, with lengths of 90 and 260 mm upstream and downstream the TXV orifice, respectively. A high speed camera manufactured by Vision Research®, model Phantom v2012, with recording rate up to 1,000,000 frames per second with objective lens of 60 mm MICRO NIKKOR AF f/2.8D was employed to record the fluid dynamic upstream and downstream the TXV orifice. The images were acquired with resolution of 208 x 1280 at 70,000 frames per second at three different positions as illustrated in Fig 36.

Figure 36 – Schematic diagram of the test section illustrating the region for which flow images were recorded.

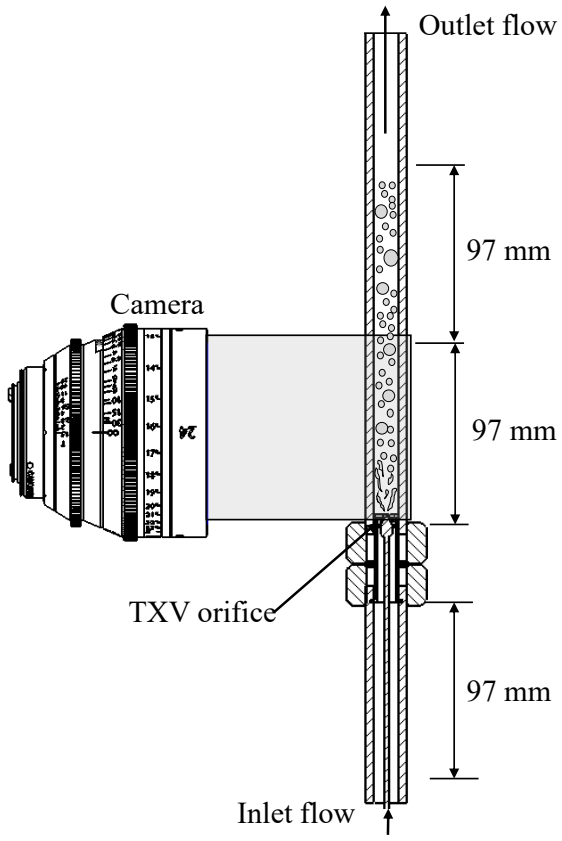

Source: Author.

The resolution of the recorded image decreases with the increasing of the acquisition rate. By increasing the image acquisition rate the exposure time is also reduced, thus a high light intensity source is necessary in order to obtain satisfactory images. Therefore, a softbox containing a white LED (6 W) was installed behind the test section to provide a homogeneous and diffuse lighting. In this figure, it is also noticed that each region of interest correspond to a length of 97 mm (the camera was fixed as close as possible from the test section). One region is located just upstream the TXV while the other two are downstream the TXV orifice.

3.1.7 Instrumentation and apparatus

Test fluid mass flow meter

A mass flow meter operating based on the Coriolis principle manufactured by TRICOR®, model TCM-5500, was employed to evaluate the refrigerant flow rate. This device provides an output electrical current ranging from 4 to 20 mA linearly proportional to the current mass flow rate. The mass flow meter also reports the volumetric flow rate, density, and temperature. The mass flow meter cover a range from 0 to 5500 kg/h with an associated absolute error of 0.3% of full scale. This device is located downstream of the second pump.

Water volumetric flow meter

A mass flow meter operating based on the electromagnetic principle manufactured by Rosemount®, model 8711, was employed to evaluate the water volumetric flow rate. This device provides an output electrical current ranging from 4 to 20 mA linearly proportional to the current volumetric flow rate. The accuracy of the volumetric flow rate measurements was obtained from the manufacturer as 0.25% of the measured value. The relative uncertainty of the test section inlet vapor quality is function of the water mass flow rate and its temperature difference between the heating section inlet and outlet. Once the relative error of the measured volumetric flow rate increases with increasing the flow rate, it was adopted the minimum warm water mass flow rate of 0.078 kg/s that is capable of simultaneously attending the experimental test matrix conditions and provide a reduced error propagation. A reduced water mass flow rate results in a higher water temperature difference between the heating section inlet and outlet, which also reduces the relative temperature error propagation. The density of the water was evaluated based on the thermocouple measurement at the heating section inlet, which presented an uncertainty of 0.1°C (see Fig. 26).

Micropumps and variable frequency drives

Two magnetic drive gear pumps manufactured by Micropump®, models GC M23 JKS5 and GD 223/56C were employed to drive the refrigerant through the main circuit. The pump GC M23 JKS5 and GD 223/56C mass flow rates were controlled by variable-frequency-drives from ABB®, model ACS355-03E-09A8-2 of 3.0HP/ 220V and Danfoss®, model VLT Micro Drive FC 51 of 1.0HP/ 220V, which act on the pump rotation through a signal of 0 to 10 V provided by

the acquisition system.

Table 7 – Pump characteristics.

Parameter	Pump model	
	GC M23	GD 223
Max. Δp	8.6 bar	6.9 bar
Max. system pressure	103 bar	103 bar
Min. flow rate	405 ml/min	1.7 L/min
Max. flow rate	13.9 L/min	13.9 L/min
Temperature range	-46 to 177ºC	-46 to 204ºC

Source: Author.

Absolute pressure transducer

Three piezoresistive absolute pressure transducers were placed along the test circuit. The pressure transducer at the refrigerant tank was manufactured by Endress Hauser® with full scale of 1 MPa with an associate absolute error of 0.5% of full scale (5 kPa), the second and third one, manufactured by Danfoss®, were installed at the test section inlet and outlet with full scale of 2400 kPa and 1600 kPa with associate absolute errors of 0.8% of the full scale. At the test section, the absolute pressure transducers were positioned 185 and 310 mm upstream and downstream of the TXV orifice, respectively. The absolute pressure transducers have output electrical signals ranging from 4 to 20 mA.

Piezoelectric transducer

A piezoelectric micro sensor manufactured by PCB Piezoeletronics® model 105C03 with full scale of 690 kPa with associate absolute error of 0.01% of the full scale was placed 310 mm downstream the TXV orifice. The piezoelectric transducer is feed with a supply voltage of 24-30 V provided by the National Instruments SCXI-1530 acquisition board and return, as output signal, an electrical voltage equivalent to 1.45 mV/kPa.

Thermocouples

The National Instruments acquisition board channels containing the thermocouples type K (chromel/alumel) manufactured by Omega® with 76 μm wire diameter were calibrated using a thermal bath (Haake AC200-A40) associated with a precision thermometer as reference (FLUKE-1523-P1 reference thermometer, probe 5616 PRT, uncertainty of 0.011°C). A LabView (2013) program was developed to automatically change the thermal bath temperature and record the calibration data once the stability criteria of reference temperature oscillations inferior to 0.04°C for a period of 2 minutes was achieved. If such criterion was satisfied, the data were acquired for a period of 60 seconds and a new temperature was set at the thermal bath.

The errors associated with the temperature readings by the type K thermocouples were

determined by a curve calibration procedure for temperatures ranging from 25 to 55°C for the thermocouple at the test section inlet and from -14 to 20°C for the thermocouple employed in the test section outlet, and from 5 to 55°C for the thermocouples positioned along the test circuit and within the acoustic chamber. The uncertainty related to each of the thermocouples was estimated similarly to the procedure suggested by Abernethy and Thompson Jr. (1973) using a total of 20 calibration runs, half of them increasing thermostatic bath temperature, and the other half reducing the temperature of the thermostatic bath. Then, calibration curves were adjusted for each thermocouple-extension-channel set.

The maximum average uncertainty of the thermocouples achieved was 0.08°C. Thus, an absolute uncertainty of 0.1°C was assumed for all temperature measurements. The uncertainties associated with estimated parameters were calculated using the method proposed by Moffat (1988) and their estimatives are detailed in Appendix B.1.

Microphone

The mult-filed microphone type 4961 manufactured by Brüel Kjaer was employed to sound measurements with measurement frequency range from 5 to 20,000 Hz, dynamic range 20 - 130 dB with uncertainty of $\pm$0.3dB. The microphone is feed with a supply voltage of 22-28 V from the National Instruments SCXI-1530 acquisition board and return, as output signal, an electrical voltage equivalent to 54.2 mV/Pa. The microphone was calibrated using a sound calibrator model NC-74-002 manufactured by RION with uncertainty of $\pm$0.3dB.

3.1.8 Data Acquisition System and Test Bench Control

A National Instruments data acquisition and control system programmed via LabView interface was employed to acquire and register the transducers and temperature signals, as well as to control the micro pumps. The National Instruments data acquisition system was installed in a computer DELL Inspiron 530 (Pentium dual-core) through two multifunctional PCI-6021 acquisition boards connected to the computer motherboard through a 32-bit PCI slot. The data acquisition system is comprised of two multiplexed Chassis SCXI-1000. Each PCI slot received one multiplexed Chassis. One of the multiplexed Chassis is associated with a module SCXI-1112 that is composed of 8 channels for voltage reading developed exclusively for temperature measurements using thermocouples, presenting one individual cold junction for each channel, one module SCXI-1303, composed of 32 channels for voltage readings generally used for thermocouples and pressure transducers, and one module SCXI-1302, composed of 2 channels for voltage output used for communication and control of the variable-frequency drives. The second Chassis SCXI-1000 host a module SCXI-1530 (4-channel microphone/accelerometer) responsible for conditioning the microphone, piezoelectric, and accelerometer signals. An Arduino microcontroller was connected to the computer through a USB port. The Arduino is responsible for controlling the valve opening by acting on the stepper motor. An schematic diagram of the data acquisition system is illustrated in Fig. 37.

Shunt resistors with thermal precision of 250Ω ± 0.1%°C were used to convert electrical current (4-20 mA) from the absolute pressure transducers and mass flow rate meters into voltage (1-5 V) for the readings by the module SCXI-1302. In addition to the National Instruments devices, a 12 V DC power supply was employed as a power source for the absolute pressure transducers and the mass flow rate meters.

Figure 37 – Schematic diagram of data acquisition system.

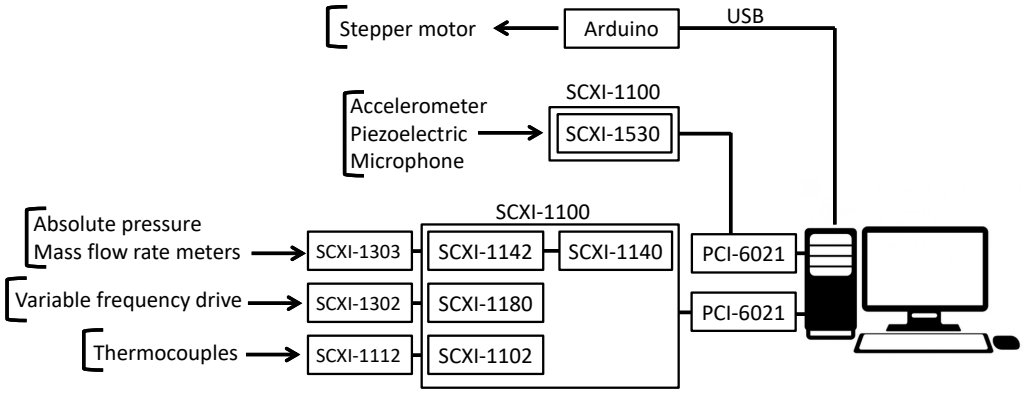

Source: Author.

A LabVIEW routine was developed to record the data, control the experimental test bench, and monitor the experimental conditions. In this program, it was included the calibration and conversion equations for the temperature readings and pressure transducers. Two controls of the gear pumps rotation through the actuation of the SCXI-1302 module on the variable-frequency drive was also included. A rough estimative of the TSPL and pressure x enthalpy diagram were also included to monitor and help the operation of the test bench. The data were recorded during 30 seconds using an acquisition rate of 80 kHz in the format ".TDMS". Figure 38 shows the front panel of LabVIEW interface to control and monitor test bench.

Figure 38 – Front panel of LabVIEW interface.

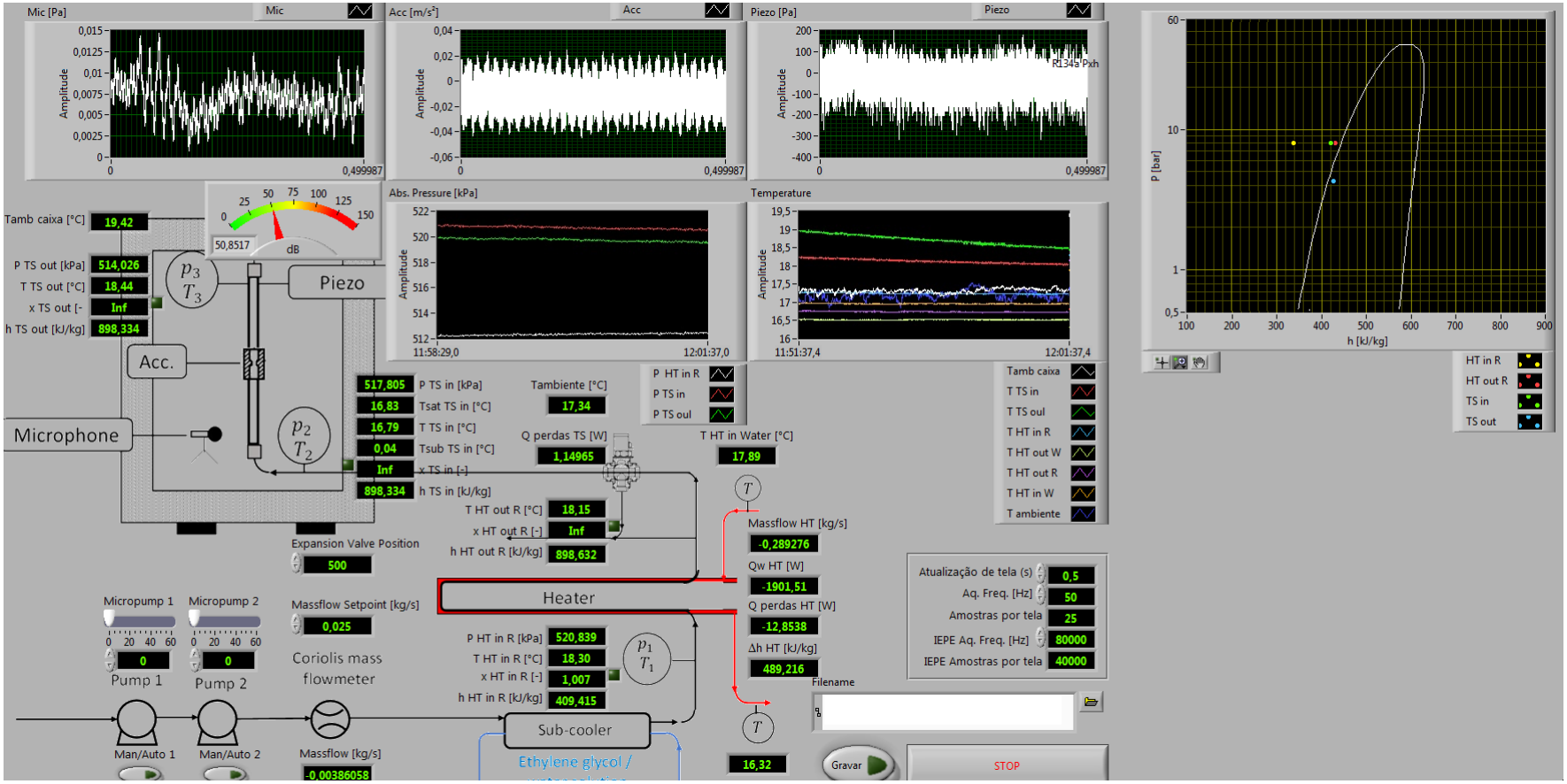

Source: Author.

4 DATA REGRESSION AND EXPERIMENTAL PROCEDURE

This chapter describes the data regression methodology employed to estimate the main experimental parameters from the measured signals, such as thermodynamic states of the fluid at the TXV inlet and outlet, sound pressure level, and test section wall acceleration. The chapter also details the data regression procedure adopted to determine the liquid-vapour wave jet velocity downstream the TXV outlet. Then, at the end of this chapter, it is presented the experimental uncertainties, the experimental procedure adopted during the experimental campaign, and the experimental test matrix.

4.1 Heat losses estimation

In this section, the experimental procedure based on energy balance adopted to determine the heat losses at the heating section and from the heated section outlet to the test section inlet are detailed. Then, the analytical expression to determine the heat losses derived from energy balances based on experimental data is presented. The range of experimental conditions and main results of the diabatic single-phase tests for estimating the relative heat losses to the environment in the heating section and from the heating section outlet to inlet test section inlet are summarized in Tab. 8.

Table 8 – Experimental conditions and main results of the diabatic single-phase tests for estimating the relative heat losses to the environment in the heating section and from the outlet heating section to inlet test section.

	Heating section	Heating section outlet to test section inlet
Re_{R134a}	11572 to 17962	11572 to 27962
Re_{water}	13894 to 23459	-
Working fluid mass flow rate	0.02 to 0.04 [kg/s]	0.02 to 0.04 [kg/s]
Working fluid temperature	20 to 40 ºC	20 to 40 ºC
Water temperature	28 to 55 ºC	-
Relative heat losses	20 to 82 %	22 to 67 %
Absolute heat losses	5.9 to 8.8 W	5.9 to 8.8 W
Number of data points	106	93

Heat losses at the heating section

The heat losses to the environment along the heating section were estimated based on tests performed by flowing water in the annular region and working fluid under single-phase counter-currently to the water. The range of the experimental working fluid conditions were defined for mass flow rates ranging from 0.02 to 0.04 kg/s (Reynolds from 11572 to 27962),

saturation temperature of 30, 35, and 40ºC, and subcooling degree from 20 to 0ºC. The tests were performed keeping the room temperature between 17 and 19ºC. The range of the tested experimental conditions were carefully set to provide values similar to the ones employed during the experimental campaign. The heat losses to the environment (Q_{loss}) for each test were estimated as the product of the water mass flow rate by the difference between the water outlet and inlet enthalpy less the product of the working fluid mass flow rate by the difference between its outlet and inlet enthalpy, defined as follows:

$$Q_{loss} = \dot{m}_{water}(i_{hs_{out,water}} - i_{hs_{in,water}}) - \dot{m}_{R134a}(i_{hs_{out,R134a}} - i_{hs_{in,R134a}}) \quad (4.1)$$

where $\dot{m}_{water}$ is the water mass flow rate given by the electromagnetic mass flow meter, and $i_{hs_{in,water}}$ and $i_{hs_{out,water}}$ are the water enthalpy estimated at heating section inlet and outlet, respectively, $\dot{m}_{R134a}$ is the mass flow rate of the working fluid given by the Coriollis mass flow meter, and $i_{hs_{in,R134a}}$ and $i_{hs_{out,R134a}}$ are the working fluid enthalpies estimated at the heating section inlet and outlet, respectively, based on the corresponding local temperature and pressure measurements. The water mean pressure was estimated as 200 kPa. Once there were no pressure taps at the heating section outlet, the working fluid outlet pressure was estimated as the average pressure between the heating section inlet and the test section inlet. Figure 39 shows the heat losses at the heating section.

Figure 39 – Heat losses to the environment at the heating section vs. the difference between the average working fluid temperature and the room temperature.

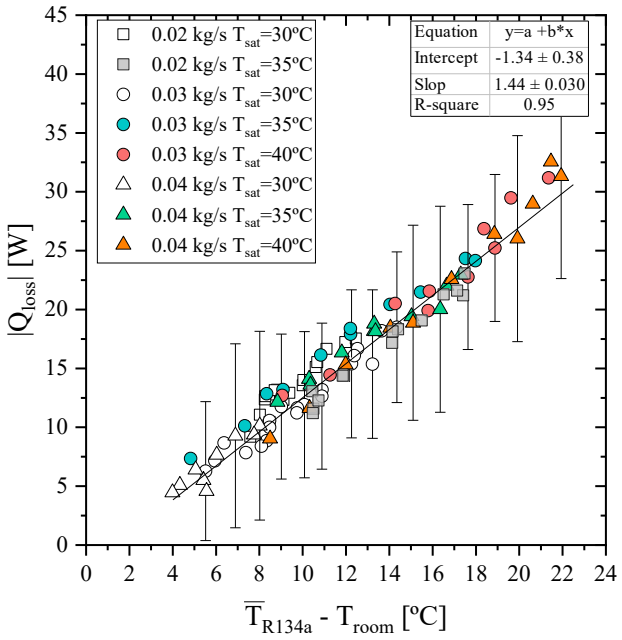

Source: Autor

According to this figure, a linear expression was derived to estimated the heat losses with R-square of 0.95. The analytical expression indicates that the heat losses are directly proportional

to the difference between the average working fluid temperature and the room temperature. This result was expected once the total thermal resistance is almost constant between the water internal flow and the room natural convection. The uncertainty associated to the absolute pressure transducer, mass flow meter, and thermocouples resulted in a heat loss uncertainty from 5.9 to 8.8 W. The heat losses uncertainty increases as the working fluid mass flow rate increases.

Heat losses from the heating section outlet to the test section inlet

The heat losses to the environment were also evaluated for the region from the heating section outlet to the test section inlet (See Fig. 26, 6 → 7) and were determined as follows:

$$Q_{loss} = \dot{m}_{R134a}(i_{ts_{in,R134a}} - i_{hs_{out,R134a}}) \tag{4.2}$$

where $i_{ts_{in,R134a}}$ is the working fluid enthalpy estimated at the test section inlet based on the corresponding local temperature and pressure measurements. Figure 40 shows the heat losses from the heating section outlet until the test section inlet.

Figure 40 – Heat losses to the environment from the heating section until the test section inlet vs. the difference between the average working fluid temperature and the room temperature.

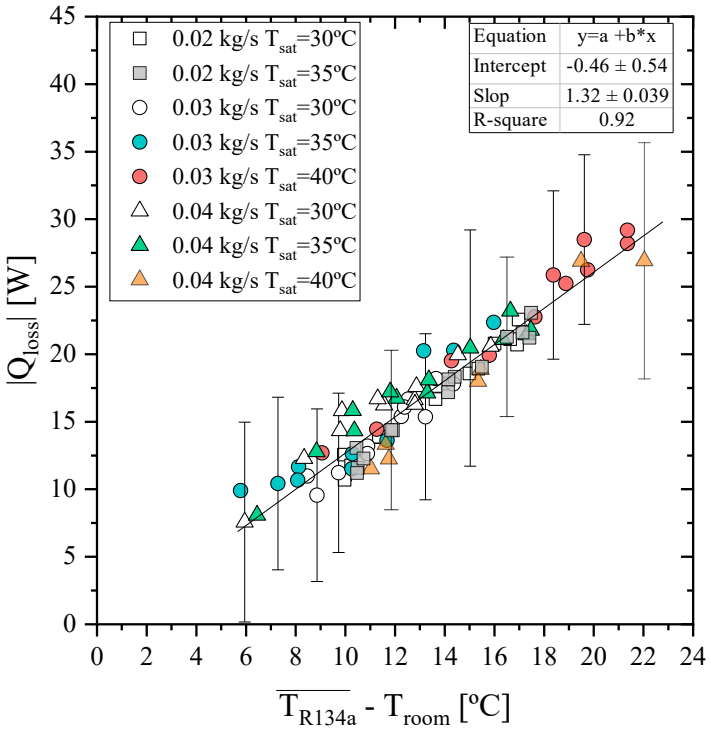

Source: Autor

Similar to the heating section, the heat losses were correlated based on the difference between the average working fluid temperature and the room temperature. According to this

figure, it can be noted a reasonable agreement between the linear expression derived to estimated the heat losses and the database with R-square of 0.92.

The validation of the heating section is illustrated in Fig. 41. To evaluated the accuracy of the heat losses estimated above, single-phase heat transfer experiments were performed. In order to estimate the refrigerant heat transfer coefficient (h_{R134a}), first an energy balance was applied in a counter flow heat exchanger arrangement as follows:

$$h_{R134a} = \left[\left(\frac{\triangle T_{lm}}{\dot{m}_{R134a}(i_{ts_{out,R134a}} - i_{hs_{it,R134a}})} - \frac{\ln(D_{ext}/D_{int})}{2\pi L K_{ss}} - \frac{1}{h_{water} A_{ext}} \right) A_{int} \right]^{-1} \quad (4.3)$$

where $\triangle T_{lm}$ is the mean logarithm temperature difference, D is the external and internal diameter, L is the heat exchanger length, k_{ss} is the conductivity of the stainless steel, h_{water} is the water heat transfer coefficient, and A is the internal and external area. In order to apply this equation, the water heat transfer coefficient was estimated based on the Gnielinski (1976) prediction method.

The experimental Nusselt number at the heating section were compared against methods from the literature for mass flow rate varying from 0.02 to 0.04 kg/s at saturation temperature of 35 ºC (p_{sat} = 8.9 bar). From Fig. 41, it is seen that the experimental results agrees reasonable well with the prediction methods from the literature. The data for single-phase heat transfer coefficient provided accurate results; therefore, the heat losses estimation procedure is assumed to be valid.

Figure 41 – Comparison between predictions methods for the single-phase Nusselt and the corresponding experimental results on heating section.

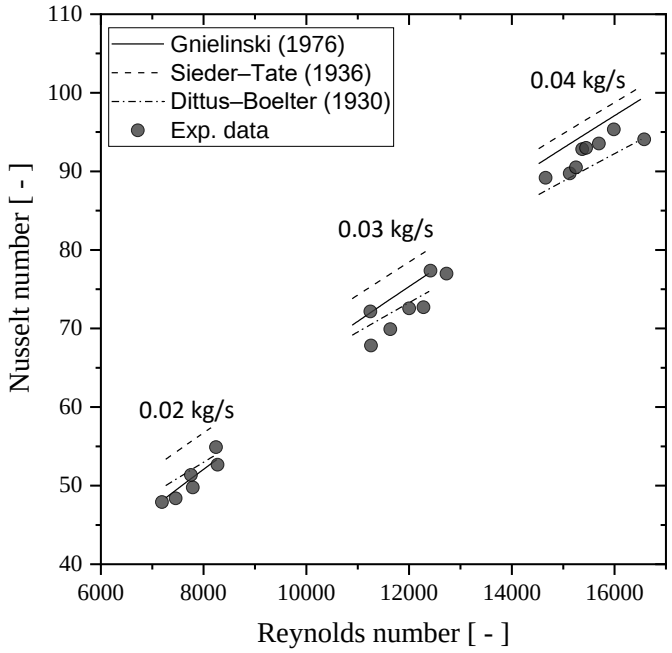

Source: Autor

4.2 Thermodynamic data regression procedure

Test section inlet vapor quality estimation

In this section, the data reduction procedure developed for estimating the vapor quality at the test section inlet is detailed. The first step consisted of importing the data gathered during the experimental campaign from a .TDMS file using MATLAB. Each .TDMS imported file contains a series vector with the following parameters: temperatures, pressures, and TXV opening. The model was implemented in a MATLAB (2020a) code with the thermodynamic and transport properties of the fluid evaluated according to CoolProp (V6.3).

The data regression procedure described in this section assumes two possibilities to determine the working fluid condition at the test section inlet. In the first condition, the fluid is subcooled at the test section entry, therefore the local enthalpy was estimated from the fluid inlet pressure p_3 and temperature T_3 (see Fig. 26). In the second condition, the fluid is saturated at the test section entry and the vapor quality was estimated based on an energy balance from the heating section inlet until the test section entry, as follows:

$$i_{ts_{in,R134a}} = \frac{\dot{m}_{water}(i_{hs_{in,water}} - i_{hs_{out,water}}) - Q_{loss,1} - Q_{loss,2}}{\dot{m}_{R134a}} + i_{hs_{in,R134a}} \tag{4.4}$$

The $Q_{loss,1}$ and $Q_{loss,2}$ are the heat losses to the environment in the heating section and between the heating section and the test section entry obtained from the linear equations illustrated in Figs. 39 and 40, respectively given as follows:

$$Q_{loss,1} = -1.34 + 1.44(\overline{T}_{R134a} - T_{room}) \tag{4.5}$$

$$Q_{loss,2} = -0.46 + 1.32(\overline{T}_{R134a} - T_{room}) \tag{4.6}$$

The fluid local thermodynamic vapour quality $x_{ts_{in,R134a}}$ was determined based on the local enthalpy $i_{ts_{in,R134a}}$ and the local pressure p_3 or local temperature T_3, as follows:

$$x_{ts_{in,R134a}} = \text{Vaporquality}(p = p_3; i = i_{ts_{in,R134a}}; \text{R134a}) \tag{4.7}$$

Finally, the thermodynamic vapor quality at the TXV outlet $x_{ts_{out,R134a}}$ was determined assuming a isoenthalpic expansion $i_{ts_{out,R134a}} = i_{ts_{in,R134a}}$ and from the test section outlet local pressure p_4, defined as follows:

$$x_{ts_{out,R134a}} = \text{Vaporquality}(p = p_4; i_{ts_{out,R134a}} = i_{ts_{in,R134a}}; \text{R134a}) \tag{4.8}$$

Pressure drop along the visualization section

This section presents an estimative of the pressure drop solely along the glass tube. The pressure drop is composed of frictional, accelerational, and gravitational parcels. For single-phase flow conditions upstream the TXV the pressure drop along the visualization section inlet was estimated as the sum of the contributions of the frictional and the gravitational pressure drop. The frictional pressure drop was estimated as follows:

$$\Delta p = \frac{2fG^2}{D_{int}\rho_l}\Delta L \tag{4.9}$$

where ρ_l is the liquid density estimated based on the test section inlet. The fanning friction factor f was evaluated according to the correlation proposed by Churchill (1977), given as follows:

$$f = \left[\left(\frac{8}{Re}\right)^{12} + \frac{1}{(A_1 + B_1)^{1.5}}\right]^{\frac{1}{12}} \tag{4.10a}$$

$$A_1 = \left[-2.457\ln\left(\left(\frac{7}{Re}\right)^{0.9} + 0.27\frac{\varepsilon}{D}\right)\right]^{16} \tag{4.10b}$$

$$B_1 = \left(\frac{37530}{Re}\right)^{16} \tag{4.10c}$$

where ε/D represents the relative roughness.

The gravitational parcel of the gas-liquid flow pressure drop is given as follows:

$$\triangle p_{grav} = [\rho_l(1-\alpha) + \rho_v\alpha]gLsin\Theta \tag{4.11}$$

where Θ is the angle between the channel orientation and the horizontal plane. For two-phase flow conditions, the pressure drop along along the test section is estimated by the sum of the gravitational ($\triangle p_{grav}$), accelerational ($\triangle p_{accel}$), and frictional ($\triangle p_{fric}$) pressure drop components, as follows:

$$\triangle p_{Total} = \triangle p_{grav} + \triangle p_{accel} + \triangle p_{fric} \tag{4.12}$$

In an adiabatic two-phase flow, the vapor quality is generally constant and consequently the kinetic energy variation is negligible. Therefore, assuming the test section as adiabatic, the accelerational pressure drop was considered null. The methods of Friedel (1979), Grönnerud (1972), and Müller-Steinhagen and Heck (1986) were employed to predict the frictional pressure drop along the test section. Among the experimental conditions it was evaluated the highest total pressure drop taking into account the contribution of the gravitational and frictional forces upstream and downstream the TXV orifice, which resulted in a total pressure drop of 1.10, 1.06, and 0.94 kPa according to the method mentioned above, respectively. The pressure drop (frictional and gravitational) along the glass section represents a maximum of 0.3% of the pressure drop through the TXV orifice, therefore it was neglected in the data reduction procedure.

4.3 Acoustic data regression procedure

In this section, the data reduction procedures developed for estimating the frequency domain signal and the SPL at the test section were detailed. The first step consisted of importing the data gathered during the experimental campaign from a .TDMS file using MATLAB. Each .TDMS imported file contains a series vector with the following parameters: microphone sound pressure, piezoelectric pressure fluctuation, and acceleration. The model was implemented in a MATLAB (2020a).

The data from the sensors were recorded for 30 seconds using an acquisition rate of 80 kHz. According to the Nyquist theorem the largest bandwidth that can be sampled without aliasing is one-half the sample-rate, which is 40 kHz. The humans can detect sound frequency range from 20 Hz up to 20 kHz, one-half of the maximum bandwidth determined according to the Nyquist theorem based on the current acquisition sample rate.

The calculations proceeds transforming the data into frequency domain by employing the Fourier transformation of the input signal in MATLAB using the function *spectogram* as follows:

$$\text{Signal} = \text{spectogram(sample)} \tag{4.13}$$

For the microphone and the piezoelectric sensors, the output signal return as Pascal, therefore the SPL in dB can be determined as follows:

$$\text{SPL} = 20\log\left(\frac{p}{p_{ref}}\right) \tag{4.14}$$

where p_{ref} is 20μPa, defined as the minimum threshold of human ear audibility at 1000 Hz. The Total Sound Pressure Level TSPL in dB was determined as the logarithmic measure of the root-mean-square of the signal relative to a reference pressure, as follows:

$$\text{TSPL} = 20\log\left(\frac{p_{rms}}{p_{ref}}\right) \tag{4.15}$$

The root-mean-square (rms) of the pressure signal was calculated as the root of the ratio between the sum of the squared pressures by the number of sample.

4.4 Two-phase flow velocity image characterization

In this section, a description of the data regression procedure to estimate the two-phase flow jet velocity at the TXV outlet through image processing is presented. The two-phase flow images were obtained employing a high-speed video camera with a resolution of 208 x 1280 px at 70,000 fps. The images were acquired at greyscale level with the intensities of the pixels scored between 0 and 255, where 0 indicates totally black and 255 completely white.

The two-phase flow jet velocity at the TXV outlet was analyzed at six equally spaced positions of 31.05 mm, initiating from position 12.4 and finishing at 167.65 mm. The position

zero was defined as the TXV orifice outlet. Initially, at each position defined above, three distinct sizes of region of interest (ROI) were analyzed in order to identify the average pixel color signal fluctuation. Figure 42 illustrates the ROI dimensions of 10 X 110, 30 X 110, and 50 X 110 px at each position of interest.

Figure 42 – Distinct ROI dimensions at different positions.

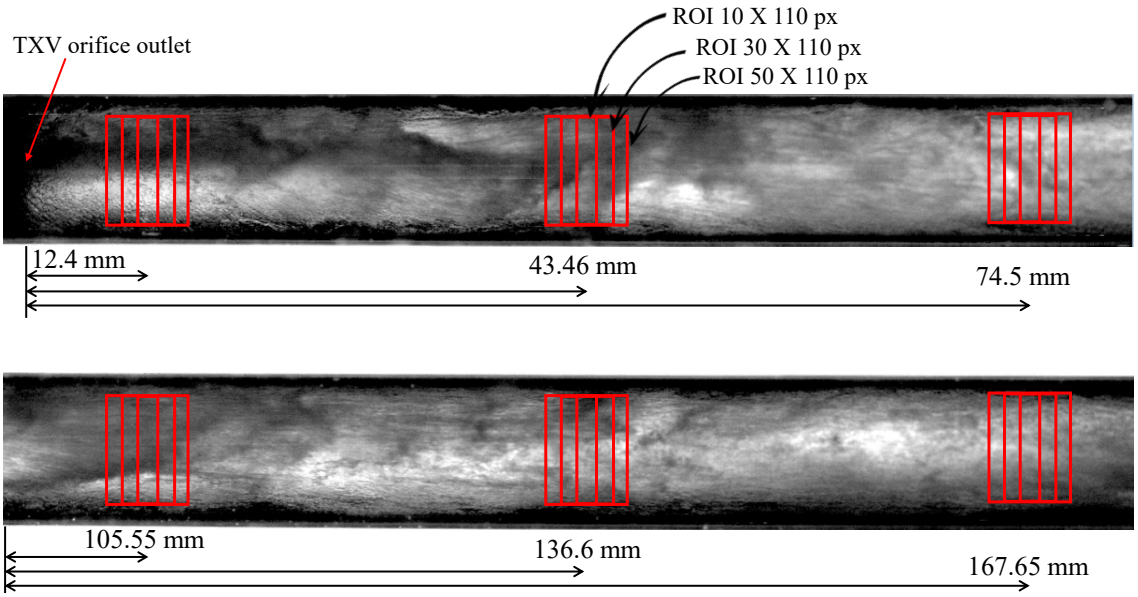

Source: Author.

After defining the distinct sizes of ROI at each position, the average pixel color intensity were estimated for each ROI dimension and position through each frame, as illustrated in Fig. 43. According to Fig. 43, the amplitude of the average pixel intensity increases as the ROI size diminishes. Therefore, it was adopted the ROI with dimension of 10 X 110 px to apply the cross-correlation to determine the two-phase flow jet velocity at the TXV outlet. Cross-correlation is a measure of similarity of two series as a function of the displacement of one relative to the other, which allows the estimation of the time interval necessary to the signal to present similar characteristics. In order to apply the cross-correlation function two ROI were created, where each ROI was shifted backward and forward by 1.24 mm from each position previously defined above. In this way, it was possible to determine the period necessary for the signal characteristics recorded in the first ROI to be indicated in the second ROI. This lag between the ROIs can be converted in time by dividing the number of frames that the signal took to travel from the first position to the second one by the camera acquisition frame rate (70,000 fps). Therefore, knowing the distance between the two ROIs (2.48 ± 0.07 mm) and the period that the signal took to travel it was possible to define the jet velocity.

Figure 43 – Average pixel intensity at different positions and with distinct ROI dimensions.

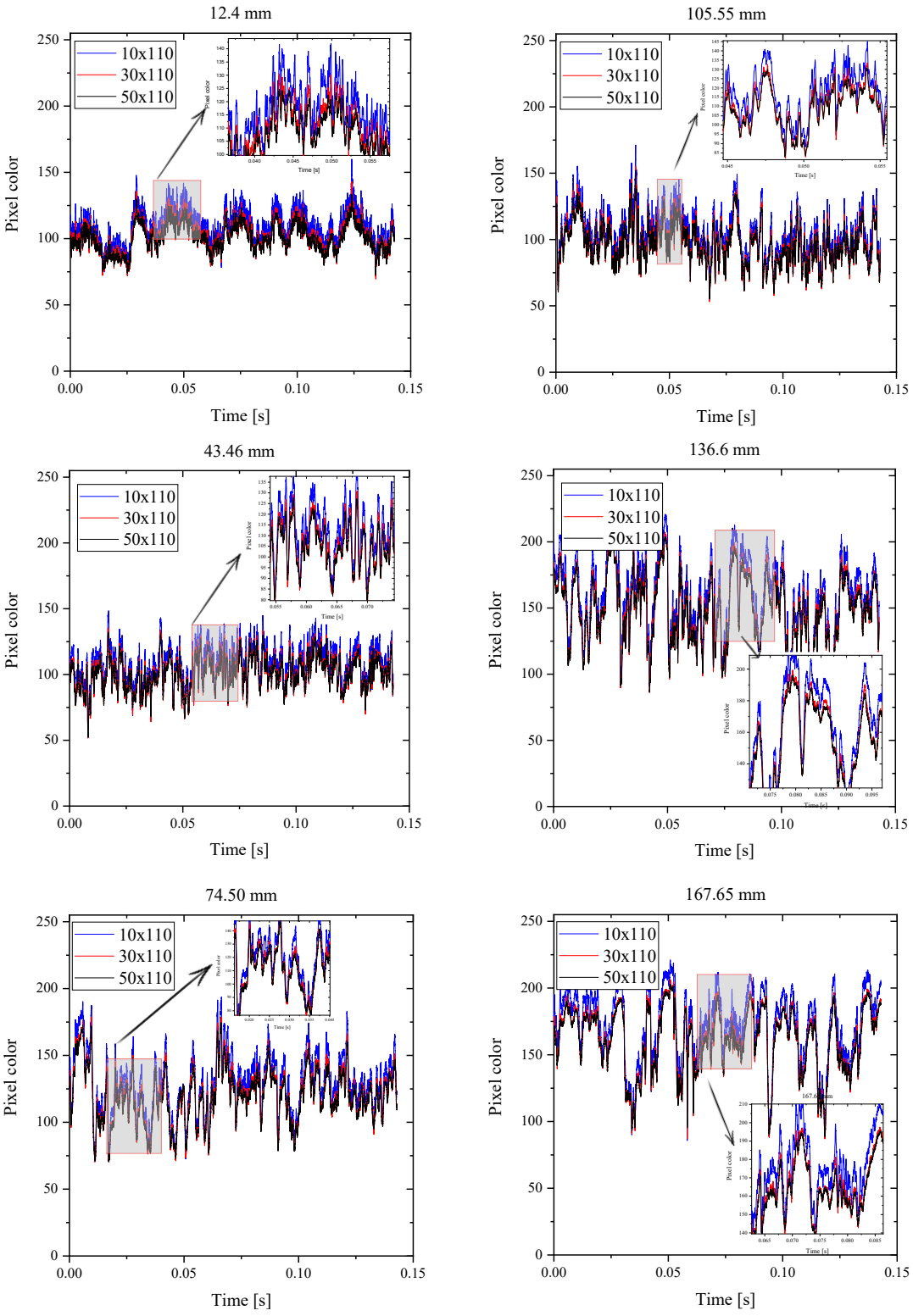

Source: Author.

4.5 Experimental uncertainties

Table 9 summarizes the experimental uncertainties related to the measured and the estimated parameters. The measurement uncertainties associated with the absolute pressure transducers, water and working fluid mass flow meters, accelerometer, microphone, and piezoelectric transducer were obtained from the datasheet provided by the manufacturers. A digital caliper of 150 mm total length and 10 μm resolution was used for measuring the test section internal diameter and its measurement error was assumed as equal to its resolution. Despite not being shown in Tab. 9, under subcooled liquid state at the test section inlet, the outlet vapor quality uncertainty varies from 0.5 to 1.4 %. This reduced uncertainty is because the outlet vapor quality was directly estimated from the inlet enthalpy and the outlet local saturation temperature or pressure. On the other hand, the high uncertainty associated with the inlet vapor quality is related to vapor qualities inferior to 4.0 %. As expected, as the vapor quality increases the relative uncertainty of this parameter reduces. Therefore, for inlet vapor qualities superior to 6.0% the relative uncertainty is inferior to 15.0%.

Table 9 – Experimental uncertainties associated with measured (left) and estimated (right) parameters.

Measured paramter	Uncertainty
D	0.01 mm
Microphone	0.3 dB
Piezoelectric	0.069 kPa
Accelerometer	5%
$p_{ts_{in}}$	19.2 kPa
$p_{ts_{out}}$	12.8 kPa
T	0.1 ºC
$\dot{m}_{R134a}$	0.3%
$\dot{m}_{water}$	0.25%

Extimated parameter	Uncertainty
xts_{in}	5.3 to 25.0%
$x_{ts_{out}}$	2.4 to 6.8%
Jet velocity	0.46 to 1.22 m/s

Source: Author.

The uncertainties associated with estimated parameters were calculated using the method proposed by Moffat (1988) and their estimative are detailed in Appendix A.2.

4.6 Experimental procedure

The following steps were performed for each series of experiments to ensure repeatability and accuracy of the experimental results during the experimental campaign. First, the air-conditioning system of the room contained the experimental apparatus was turned on and set

to 17 °C to keep almost the same environment temperature during the tests. The acquisition systems, the sensors, and the test bench computer were turned on. Then, the cooling tower was powered on and the valves in the main circuit were opened. In the test section, the TXV was totally opened to avoid peaks of pressure during the test bench start. Thereafter, the micropumps were turned on by the variable-frequency drives through the LabView interface and the mass flow rate was gradually increased until the working fluid started to circulate through the main circuit. Once the working fluid was flowing in the main circuit, the condenser unity, the centrifugal pump of ethylene-glycol/water reservoir, and the heating water centrifugal pump were turned on. Next, the temperature of the anti-freezing solution was controlled by setting the temperature at the PID module, which controls electrical heaters within the ethylene-glycol/water reservoir. Once the working fluid mass flow rate reached steady-state, the TXV was gradually closed until the desired test condition was reached. After this, the electrical heater within the reservoir in the water circuit heater loop was turned on and the water temperature was gradually adjusted until achieving the desired subcooling temperature of the working fluid for the first experimental condition at the test section inlet. Then, the working fluid mass flow rate was kept constant while the heating water temperature was increased from its lowest up to its highest value to match the working fluid experimental conditions of the test matrix. The steady-state condition was identified in each experimental condition through stable signals of the temperature and absolute pressure transducers at the test section inlet and outlet, and mass flow rate close to their uncertainty.

The data acquisition was initiated five minutes after the test bench reached stable condition. The data from the sensors were recorded for 30 seconds using an acquisition rate of 80 kHz. Then, after finishing the recording data of a experimental condition, a new experimental condition was set and the data acquired. If there were no new experiments to conduct, the experiments were ended and the protocol to turn off the test bench was initiated. First, the electrical heater and the PID control system of the water heating loop were turned off, and then the centrifugal pump was also powered off. Next, the TXV was fully opened and the two micropumps were turned off. The test fluid was recovered and stored within the condenser unity as the auxiliary circuit circulated cold ethylene-glycol/water (II). After that, the test bench valves were closed, and the auxiliary circuit and the cooling tower were turned off. Then, the TXV aperture was fully closed to ensure the same starting opening point in the next experiments section.

4.7 Experimental investigation

Based on the characteristics of the experimental apparatus capabilities and the TXV model, a test matrix was elaborated to investigate the effects of the two-phase flow morphology on the flow-induced noise in a TXV. Figure 44 illustrates the test matrix conditions in a pressure x enthalpy diagram. As can be seen from Fig. 44, the experimental tests were performed for inlet subcooling degree ranging from 15ºC to inlet vapor quality of 15% for three distinct saturation

temperatures ranging from 30 (7.7 bar) to 40ºC (10.2 bar), and mass flow rate ranging from 0.02 to 0.04 kg/s for each saturation temperature, resulting in a total of 80 experimental conditions. Figure 44 also illustrates the outlet experimental conditions as a result of the fluid expansion process through the TXV for a given outlet temperature of 10ºC (4.1 bar) with outlet vapor quality ranging from 8 to 34%. Additionally, the two-phase flow images were recorded for each experimental condition mentioned above at three distinct positions, resulting in a total of 214 data movies of 0.14 seconds corresponding to 10000 frames each one.

The experimental tests were not performed for mass flow rate of 0.02 kg/s under inlet saturation temperature of 40ºC because the TXV fully closed couldn't provide enough pressure drop; therefore, it resulted in a evaporation temperature superior to 10ºC (p_{sat} =4.1 bar). The maximum inlet vapor quality was limited based on the maximum capability of the auxiliary circuit to provide enough cooling in the condenser unity (See Fig. 26, 10 $\rightarrow$ 12) to cool and condense the test fluid downstream the expansion process.

Figure 44 – Test matrix.

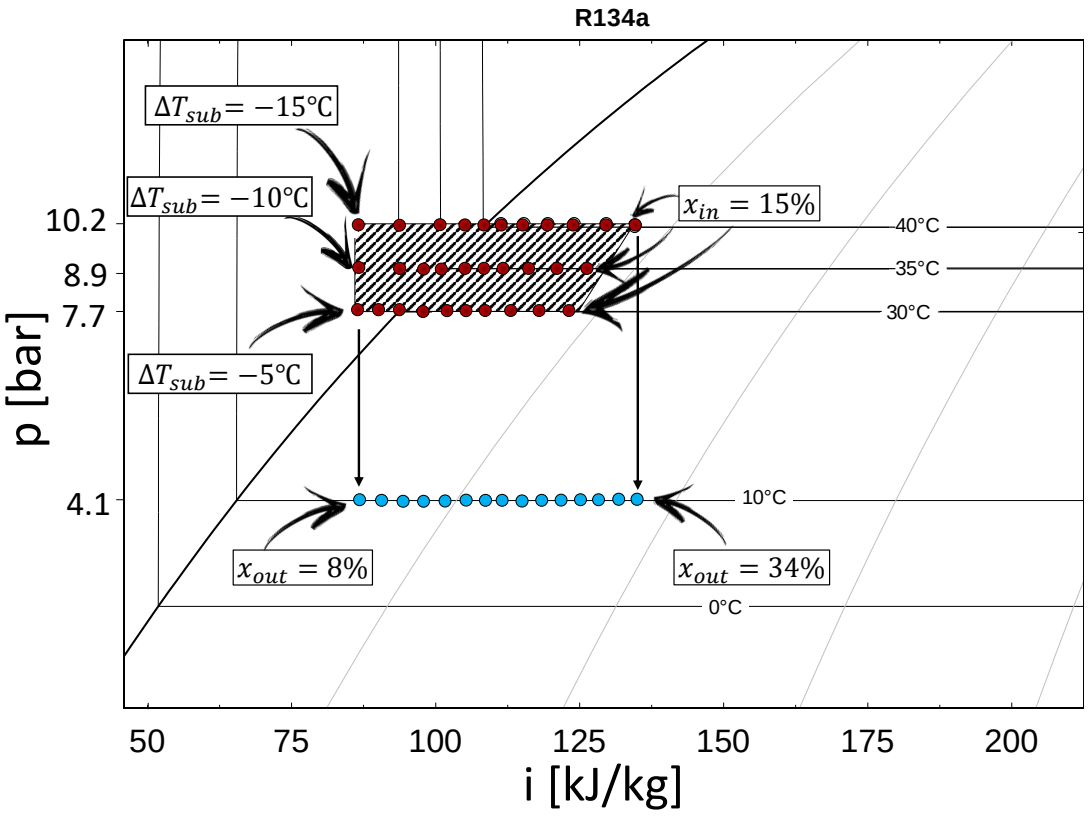

Source: Author.

5 EXPERIMENTAL RESULTS AND DISCUSSION

This chapter describes and analyses the experimental results of the outlet jet velocity, structure acceleration, and external and internal noise obtained in this study for single and two-phase flows at the TXV inlet. In Section 5.1, a parametric analysis of the effects of mass flow rate, pressure drop, inlet vapor quality, flow pattern, and flow development length on the outlet jet velocity is addressed. Sections 5.2 to 5.4, the discussions proceed to a parametric analysis of the pressure drop, mass flow rate, inlet vapor quality, and inlet flow pattern on the external noise, fluid structure acceleration, and internal noise intensities. In Section 5.5, the analysis of the structure acceleration, external and internal noise frequency spectrum, and coherence signal are performed. Then, in Section 5.6 a global parametric analysis was carried out cross-correlating the main variables. During the experiments, as the fluid inlet condition shifted from only liquid to two-phase flow the TXV had to be partially opened in order to keep the same pressure drop across the TXV orifice, regardless of the experimental condition. In this chapter, the noise results are referenced to the standard value of $2(10)^{-5}$Pa.

5.1 Analysis of two-phase flow jet velocity at the TXV outlet

TXV inlet flow pattern

Figure 45 shows a comparison between the flow pattern prediction method proposed by Hewitt and Roberts (1969) and the corresponding results performed in the current work. The well-known empirical flow pattern map proposed by Hewitt and Roberts (1969) was developed for vertical air-water and steam-water flow. The flow pattern transitions are dependent on the phase momentum fluxes.

Current visual observations of isolated bubble and annular flow are classified as slug and churn according to their proposed method, respectively. Based on it, their flow pattern map does not adequately predict the flow pattern of the current study. Therefore, the flow pattern map proposed by Hewitt and Roberts (1969) is inappropriately to predicted the flow pattern as employed by Jeong et al. (2007). According to this, the TXV inlet flow pattern was characterized through visual observations named as: isolated bubble (I.B.), coalescence bubble (C.B.) , churn, and annular flow (Annular). For simplicity, the churn and annular flow patterns were classified as one flow regime, named annular flow.

Figure 45 – Comparison between the experimental results and the flow pattern prediction method proposed by Hewitt and Roberts (1969).

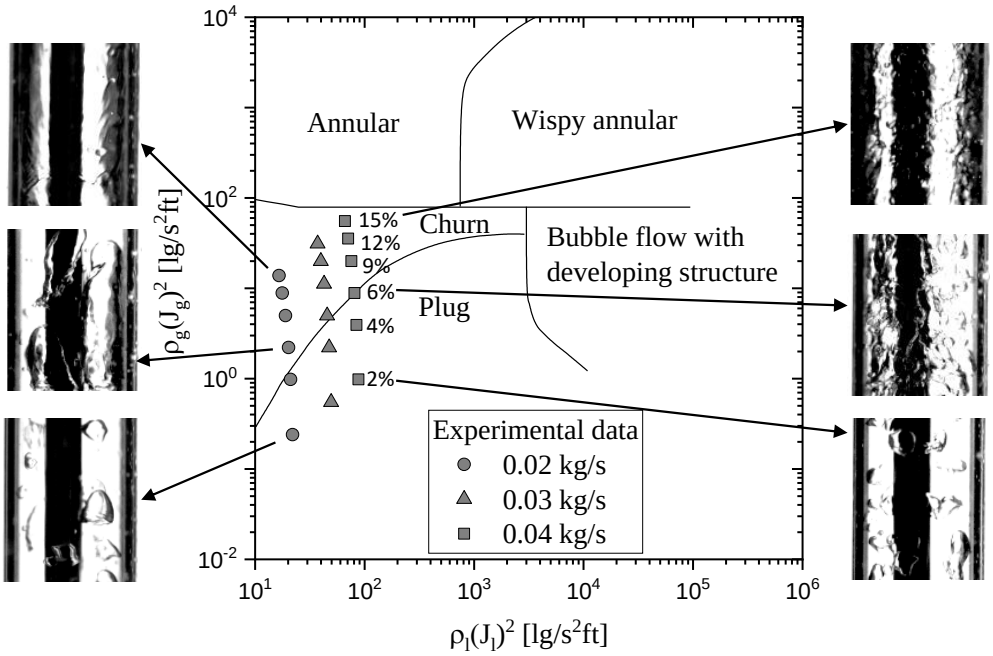

Source: Author

TXV outlet flow pattern

Figure 46 shows the jet evolution along the flow path and with time of the two-phase flow downstream of the TXV orifice. The flashing jet was characterized as the passage of a liquid front followed by dispersed bubbles within the liquid. It is worth to highlighted that, as far as the authors known, the studies involving the flashing spray characteristics of R134a (ZHIFU et al., 2012; WANG et al., 2017; LI et al., 2019) expanding into a low pressure reservoir (ambient) exhibited an well-defined spray morphology; therefore, such experimental condition is distinct from the ones performed in the study. From the first segment of the visualization section, it is possible to observe the jet leaving the TXV orifice according a parabolic shape from 0 to 97 mm (dark grey). It is also noted that as the jet wave moves along the flow path its shape changes progressively to a flat pattern. The images in the first and second visualization sections were not acquired simultaneously.

It was possible to identify a swirling zone close to the TXV outlet characterized by backflow in the zone comprised by the two-phase flow jet at the core and the test section wall. Furthermore, backflow patches close to the tube wall along the test section are intermittently observed. Although Hirakuni et al. (2004) performed their experiments for short-tube orifice, these authors also found a swirling zone close to the TXV outlet and backflows downstream the expansion device as shown in Fig. 19. In addition, it can be observed fractions of fluid from the swirling joining within the jet as it leaves the TXV. Such phenomena were observed regardless of the experimental conditions.

Figure 46 – Two-phase flow images downstream the TXV for mass flow rate of 0.03 kg/s for a pressure drop of 4.8 bar and inlet and outlet vapor qualities of 4% and 16%.

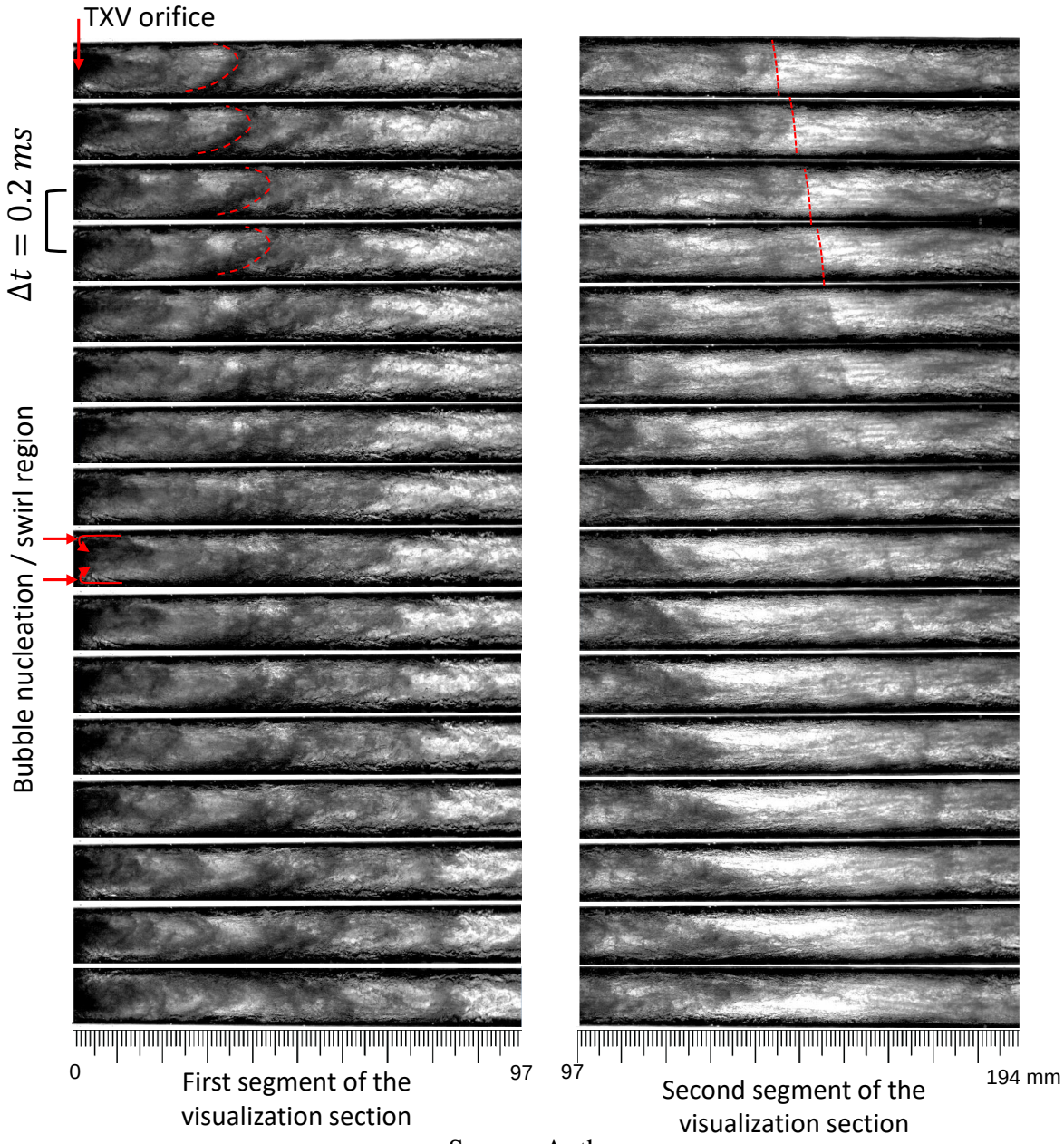

Source: Author

Figure 47 shows images of the two-phase flow morphology along the test section for a fixed pressure drop at the expansion device and different fluid enthalpy at the TXV inlet. From the analysis of these images, it can be seen an intense bubble nucleation region close to the TXV orifice, which may be related to a reduced pressure region. Such a phenomenon could be observed regardless of the experimental conditions. As depicted in Fig. 47, the images downstream the TXV up to inlet vapor quality of 6% are sharp, however, for inlet vapor quality superior to this, the image recorded starts to blur pointing out an increase on the jet velocity. Such a phenomenon is more pronounced in the second fraction of the outlet visualization section.

Figure 47 – Flow images upstream and downstream the TXV valve for mass flow rate of 0.02 kg/s and a pressure drop of 3.6 bar.

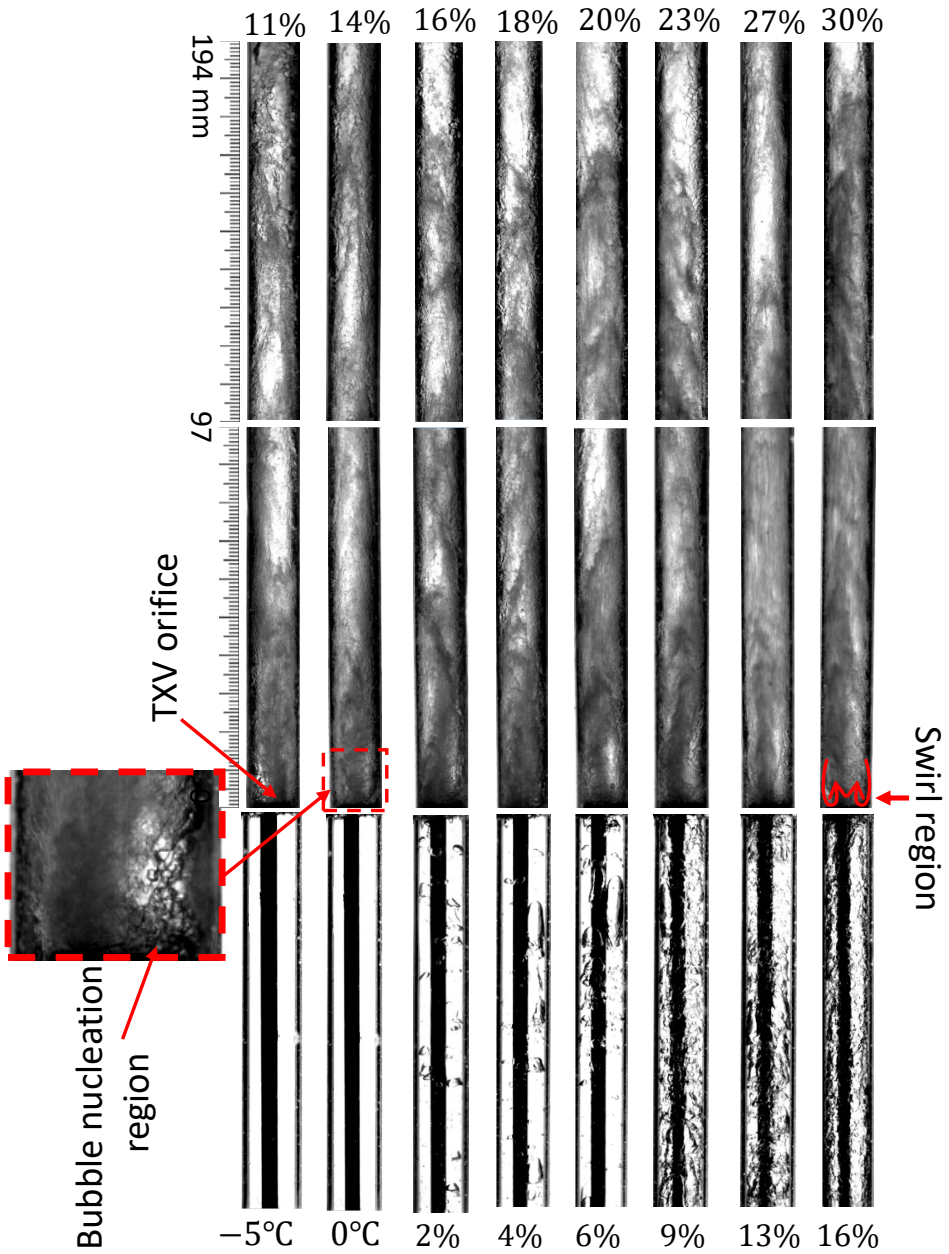

Source: Author

Despite being qualitatively evaluated, it could not be identified an increase in the bubble nucleation intensity region close to the TXV orifice; however, from the images recorded, it was observed an increase in the recirculation intensity region close to the orifice as the mass flow rate and the inlet vapor quality increases, which may be explained to the reduction of the local pressure.

At this point, it should be mentioned that at the end of the visualization section the flow morphology is still developing, therefore it could not be characterized according to the well-known flow pattern maps proposed in the literature.

Two-phase flow jet velocity

Figure 48 depicts the jet velocity at the first ROI (12.4 mm) clustered employing the k-means algorithm according to the inlet flow pattern containing 81 data. The dimensions are the two main components based on the Principle Component Analysis. The axis x and y illustrate that the first and second component accounts for 85% and 12.6% of the total variation. Then, together they account for 97.6 % of the variation.

Figure 48 – Jet velocity k-means clustering.

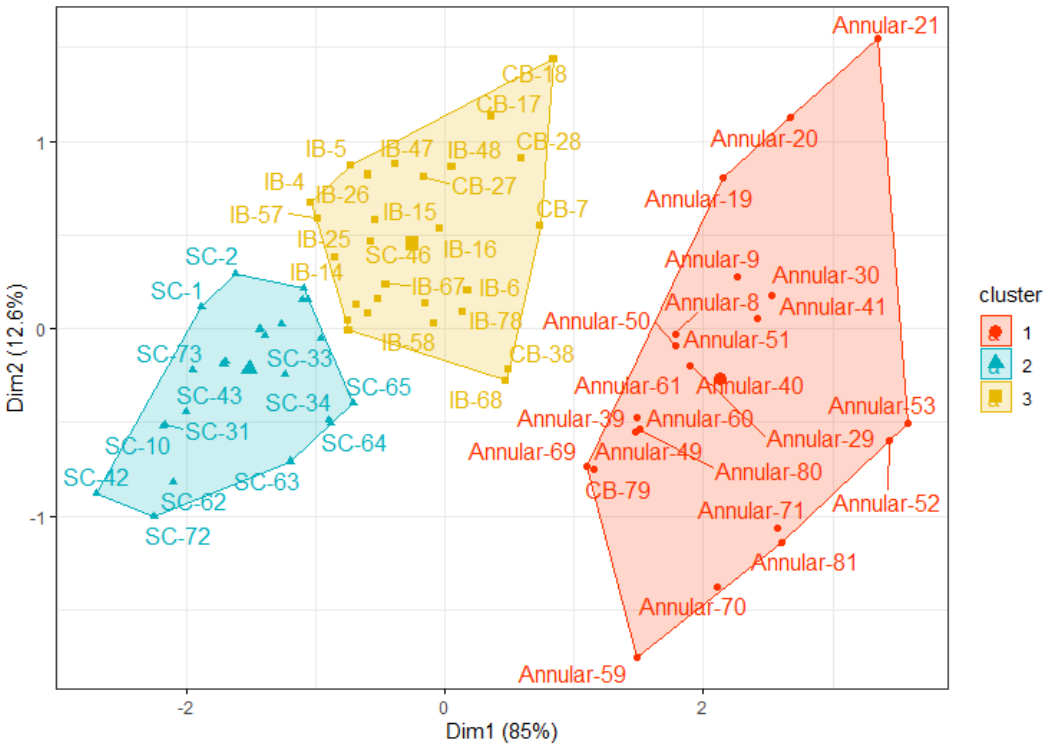

Source: Author

The k-means clustering algorithm is an unsupervised machine learning technique. The main concept of clustering is to divide the data into k groups, maximize the similarity of objects within the group, and minimize the similarity between groups. In the clustering procedure, it was adopted the following variables as input parameter: inlet vapor quality, outlet vapor quality, jet velocity, and flow pattern at the TXV inlet. To detect the optimum number of clusters the within-cluster sum of squares method was adopted (WSS), which is defined as the sum of distance functions of each point in the cluster to the k centers. Then, based on the WSS method, it was adopted the number of clusters as three. The inspection of Fig. 48, allows identifying that the jet velocities were clustered mainly in SC, IB-CB, and annular groups suggesting that the jet velocity are function of the inlet flow pattern. The p-value statistical test was performed to determine the significance of the variables on the creation of the k-means clusters. P-values inferior to 0.05 points out the hypothesis that the variables are statistically significant in the creation of the groups. Such analysis leaded to a significance value of $1.11(10^{-16})$ taking into account inlet and outlet vapor quality, and the jet velocity variables.

Figure 49 illustrates the effect of the pressure drop, inlet and outlet vapor quality on the evolution of jet velocity for distinct mass flow rates. The symbols were colored based on the k-means clustering procedure described above. According to Fig. 49, in general, for a given mass flow rate similar jet velocities are found regardless of the pressure drop. As depicted in this figure, the jet velocity is almost constant under inlet subcooled state; however, as the inlet thermodynamic state shifts from only liquid to IB-CB pattern, the jet velocity increases up to annular flow pattern. As the inlet flow pattern evolves into annular flow the jet velocity assumes a constant value in most of the experimental conditions and superior to the previous flow patterns. The observed trend is corroborated by the sharpness of the pictures illustrated in Fig. 47 described in the previous section.

Figure 49 – Two-phase flow jet velocity at the first ROI (12.4 mm) for mass flow rate of a) 0.02. b) 0.03. and c) 0.04 kg/s coloured based on k-means cluster algorithm (cyan - S.C.; yellow - I.B-C.B.; red - Annular).

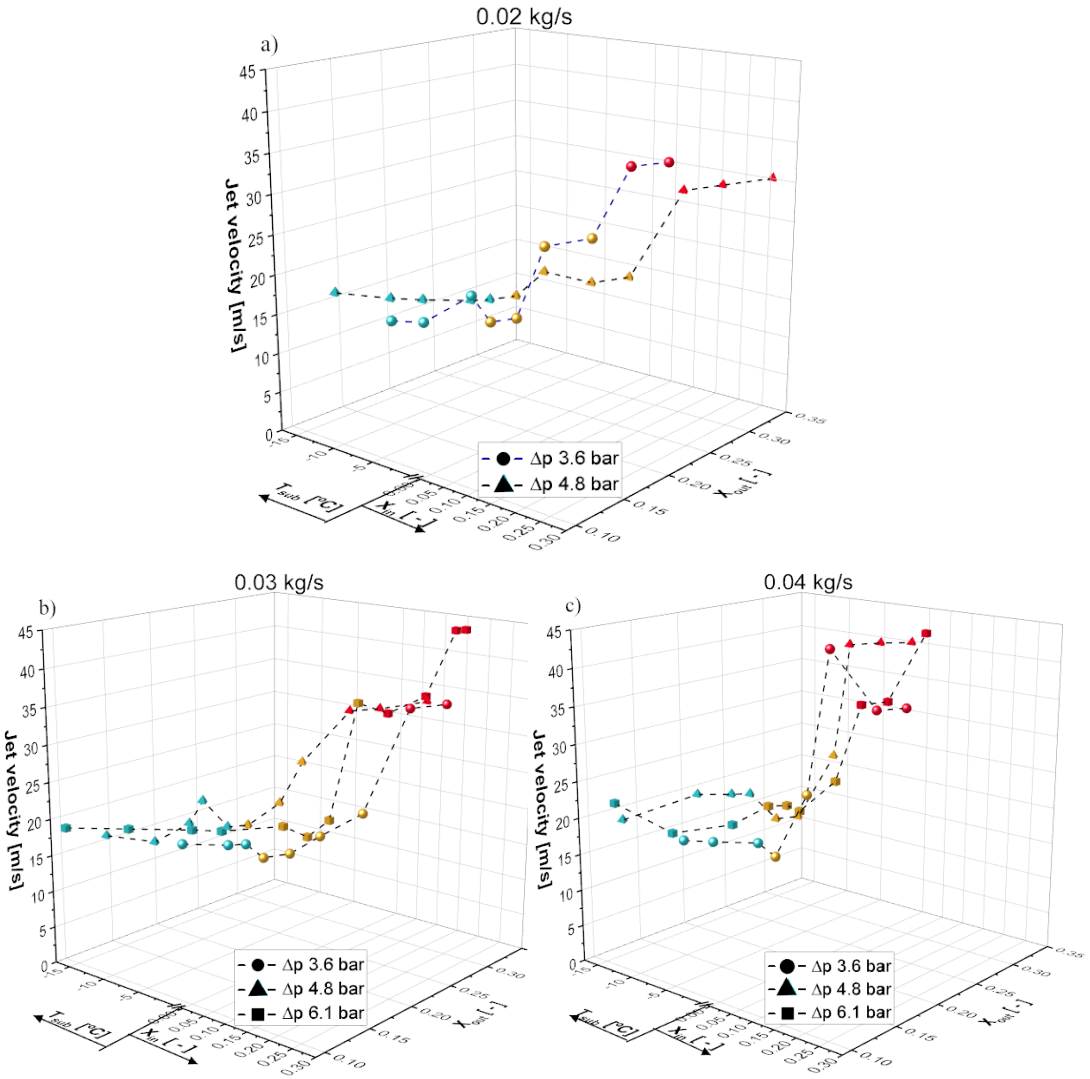

Source: Author

According to Fig. 49a, for inlet vapor qualities superior to 13% the two-phase flow jet velocity exhibited slightly superior velocity for a pressure drop of 3.6 compared to 4.8 bar. On the other hand, for mass flow rate of 0.03 kg/s (Fig. 49b), the jet velocity exhibited superior velocity under pressure drop of 4.8 bar for I.B. and C.B. flow patterns. As the flow pattern evolves into annular pattern it can be found superior jet velocity for the pressure drop of 6.1 bar. Overall, under subcooled state at the TXV inlet, the jet exhibits a constant velocity of 20 m/s, approximately, increasing sharply for inlet vapor qualities superior to 4%, regardless of the mass flow rate and pressure drop. Thereafter, it was found a constant jet velocity under annular flow pattern. One should be noticed that under inlet annular flow pattern the jet velocity increases as the mass flow rate increases. As the mass velocity increases, the shear effects are enhanced dragging the jet waves faster. Such behavior is associated to higher slips ratio due to higher vapor quality, overlaying the gravitational effects. It is worth to mention that the k-means clustering procedure classified a reduced parcel of data for I.B. (2-4%) and S.C. into distinct clusters although the jet exhibited similar velocities. In general, the k-means clustering procedure were able to satisfactory capture the jet velocity trend according to inlet flow pattern and vapor quality.

Table 10 summarizes the mains finds of the jet velocities at the visualization section positions of 12.4, 74.5, and 167.6 mm downstream the orifice for inlet subcooling degrees from -15ºC up to vapor quality of 18%. The first row at position 12.4 mm for each experimental condition displays the jet velocity in m/s, while the rows corresponding the positions of 74.5 and 167.6 mm show the ratio between the local velocity and the velocity at a position of 12.4 mm for a given experimental condition. The black cells are associated to conditions for which the cross-correlation employed in the data reduction procedure was not able to capture the signal similarity in the image processing, suggesting that the jet wave was dissipated and does not achieve at that position.

From Tab. 10, is reasonable to say that a clear dependence on the jet velocity can be noticed for changes in the mass velocity, test section axial position, and inlet thermodynamic state. It should be highlighted that as the mass flow rate increases the jets were able to travel further along the visualization section reaching the last ROI more frequently. In addition, under subcooled state at the TXV inlet, most of the jets were not able to reach the last fraction of the test section for mass flow rates of 0.02 and 0.03 kg/s. According to the data presented in Tab. 10, for inlet vapor qualities superior to 9%, as the jet travels along the visualization section its velocity reduces. It can be speculated that the nucleation starts within the TXV valve and it proceeds as the jet expands; then, the small vapor bubbles dispersed within the jet waves grow continually into the low-pressure reservoir until the bubbles mature and, finally, burst as illustrated in Fig. 50.

Table 10 – Summary of the two-phase flow jet velocity at visualization section positions of 12.4, 74.5, and 167.6 mm downstream the flow restriction.

$\dot{m}$ / Δp	T_{sub} / x_{in}	-15 ºC	-10 ºC	-5 ºC	-2.5 ºC	0	2 %	4%	6%	9%	13%	16%	18%
0.02 kg/s 3.6 bar	12.4 mm			16.53	16.53	19.84	16.53	16.53	24.80	24.80	33.06	33.06	
	74.5 mm			0.47	0.47	0.83	1.00	1.00	0.67	0.67	1.00	0.75	
	167.6 mm			-	-	-	-	-	-	0.33	0.33	-	
0.02 kg/s 4.8 bar	12.4 mm		19.29	19.29	19.29	19.29	19.29	19.29	21.70	19.29	28.93	28.93	
	74.5 mm		0.59	0.50	0.41	0.50	1.00	1.00	0,67	1.00	0.75	0.75	
	167.6 mm		-	-	-	-	-	-	-	1.00	0,75	0.75	
0.03 kg/s 3.6 bar	12.4 mm			19.29	19.29	19.29	19.29	17.36	17.36	19.29	21.70	34.72	34.72
	74.5 mm			0.50	0.69	0.63	0.63	0.77	0.77	0.77	0.80	0.56	0.55
	167.6 mm			-	-	-	0.71	0.71	0.69	0.62	-	-	0.36
0.03 kg/s 4.8 bar	12.4 mm		19.29	19.29	21.70	24.80	21.70	34.72	28.93	34.72	34.72	34.72	
	74.5 mm		0.50	0.62	0.62	0.50	0,57	1.00	0.75	0.71	0.56	0.62	
	167.6 mm		-	-	-	-	-	0.56	0.67	0.56	0.42	0.42	
0.03 kg/s 6.1 bar	12.4 mm	19.29	19.29	19.29	19.29	19.29	17.36	19.29	34.72	28.93	34.72	43.40	43.40
	74.5 mm	-	1.00	1.00	1.00	1.00	1.11	0.75	1.00	0.75	0.71	0.31	0.36
	167.6 mm	-	-	-	-	1.00	0.71	0.9	0.63	0.60	0.42	0.29	0.31
0.04 kg/s 3.6 bar	12.4 mm			19.29	19.29	19.29	17.36	24.80	43.40	34.72	34.72		
	74.5 mm			1.00	1.00	1.00	0.90	1.00	0.57	0.38	0.50		
	167.6 mm			1.00	0.90	0.90	0.77	0.54	0.50	0.63	0.56		
0.04 kg/s 4.8 bar	12.4 mm		21.70	24.80	24.80	24.80	21.70	21.70	28.93	43.40	43.40	43.40	
	74.5 mm		0.57	0.54	0.54	0.54	0.62	0.62	0.60	0.44	0.44	0.31	
	167.6 mm		0.62	0.54	0.54	0.54	0.89	0.89	0.67	0.31	0.24	0.22	
0.04 kg/s 6.1 bar	12.4 mm	21.70	19.29	19.29	21,70	21.70	21.70	24.80	34.72	34.72	43.40		
	74.5 mm	0.77	0.62	0.62	0.62	0.62	0.56	0.62	0.56	0.56	0.29		
	167.6 mm	-	0.62	0.62	0.62	0.53	0.53	0.62	0.56	0.40	0.29		

Figure 50 – Schematic diagram of jet waves illustrating the bubble lifetime along the outlet visualization section.

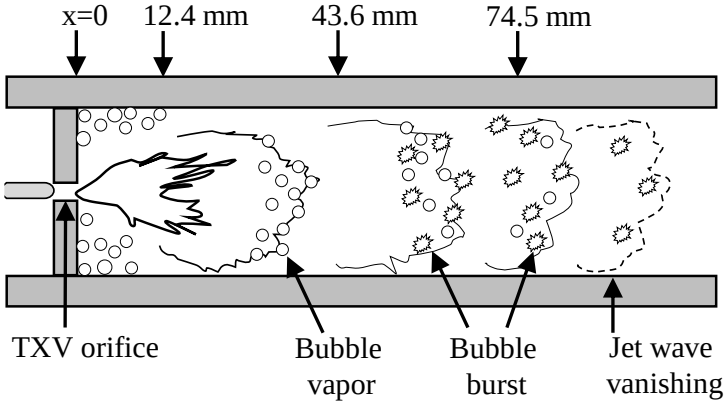

Source: Author

It could be noticed that the vapor bubbles dispersed within the jet waves were less frequently observed on the visualization section downstream the TXV orifice from 97 to 194 mm than from 0 to 97 mm. Such behavior is intensified as the mass flow rate and the inlet vapor quality decreases. According to Pan et al. (2012), the bubble life time is almost proportional to the bubble initial size. Therefore, the increase in the mass flow rate and inlet vapor quality may lead to higher steam jet energy, traveling the vapor bubble further before its lifetime overs. For the experimental conditions of the present study, the mean cross-sectional velocity estimated based on the homogeneous model varies from 1.22 up to 5.95 m/s. Therefore, the homogeneous model is not suitable to the evaluation of flow velocity near a TXV orifice. This result is related to the fact of the homogeneous consider non-drift between the phases and uniform velocity along

the channel cross-section. In addition to this, based on the mass conservation law the velocity of the flow within the tube core is increased due to the backward liquid on the tube wall coming from the upper part of the test section.

Figure 51 illustrates the frequency spectrum of the images recorded for ROIs at positions of 12.4, 74.5, and 167.6 mm for inlet vapor quality of 9%. The images displayed in Fig. 51 corroborate the main findings of Tab. 10 described above, pointing out that the frequency and the intensity of jets flowing through ROIs decrease as the distance from the TXV outlet increases, regardless of the experimental condition. The data for ROI at positions of 12.4 mm under mass flow rate of 0.02 kg/s are not shown in Fig. 51 due to their reduced variation of the pixel intensity.

Figure 51 – Two-phase flow jet frequency at visualization section positions of 12.4, 74.5, and 167.6 mm for mass flow rates of a) 0.02. b) 0.03, and c) 0.04 kg/s under pressure drop of 3.6 bar and inlet vapor quality of 9%.

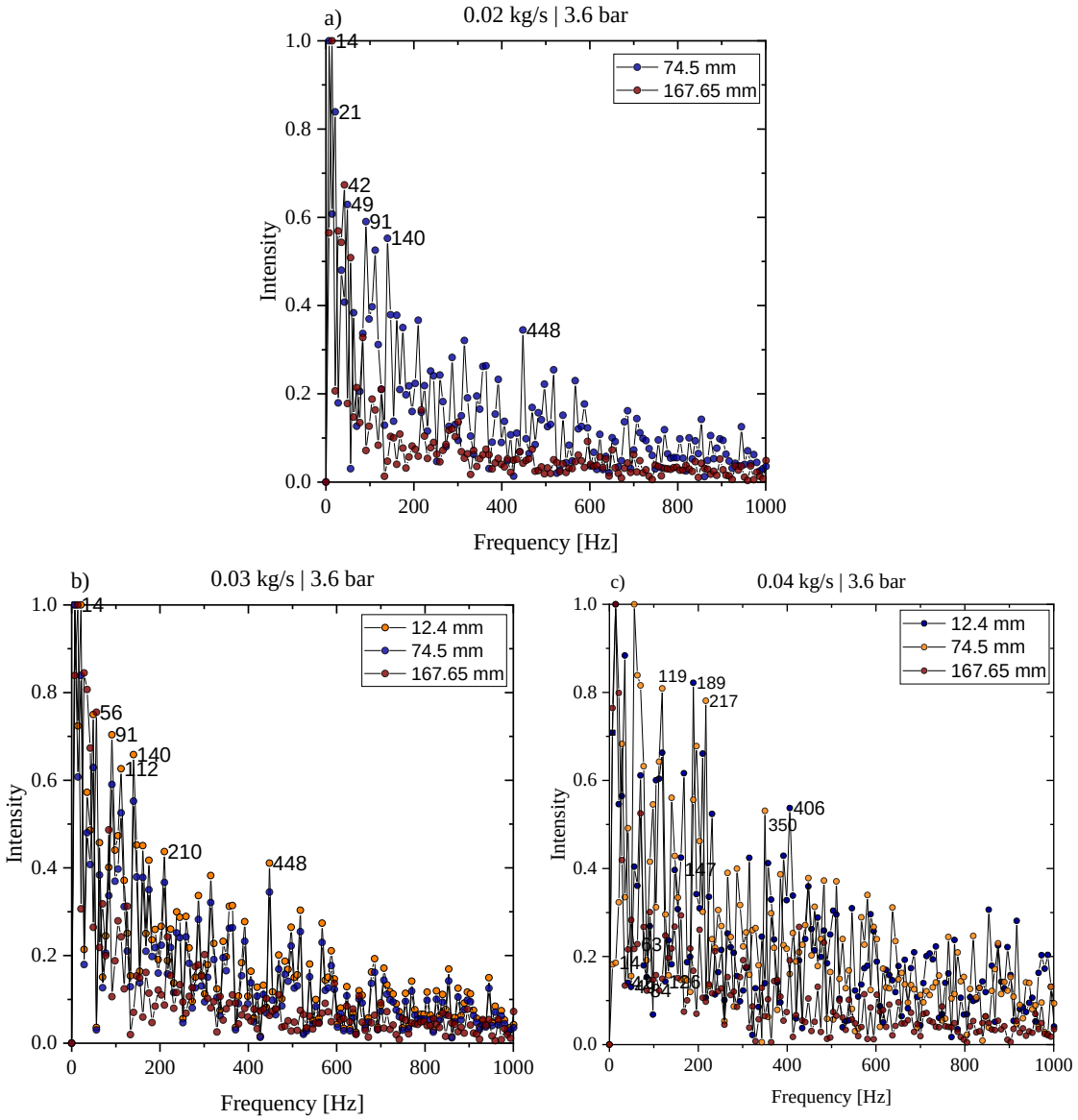

Source: Author

As general behavior displayed in Fig. 51, the grey scale level within the ROI at 167.6 mm exhibits reduced intensity, pointing out that the jet waves reaches this region less often. On the other hand, it could be found frequency components from 350 to 448 Hz at positions of 12.4 and 74.5 mm, regardless of the mass flow rate. In addition, as the frequency decreases the intensity of the frequency components increases, regardless of the mass flow rate and visualization section position. At the last ROI, it can be found a frequency peak at 14 Hz, regardless of the experimental condition; pointing out that jet waves seldom reaches this region. Therefore, these results corroborates the hypothesis that the bubble lifetime within the jet wave overs before it reaches the last ROI dissipating the jet. At this point, it should be highlighted that for a given visualization section position similar frequency components are found, indicating that the mass flow rate has no effect on the jet frequency. Analogously to what was presented in Fig. 51, such behaviors can be extended for the remaining experimental conditions not illustrated in this figure.

Two-phase flow jet velocity parametric study

A parametric analysis of the effects of the inlet and outlet thermodynamic vapor quality, mass flow rate, pressure drop, axial position, and inlet flow pattern effects on the jet velocity was performed employing Pearson's Correlation Coefficient (PCC), determined as follows:

$$\Gamma_{xy} = \frac{\sum_{i=1}^{n}(X_i - \overline{X})(Y_i - \overline{Y})}{\sqrt{\sum_{i=1}^{n}(X_i - \overline{X})^2}\sqrt{\sum_{i=1}^{n}(Y_i - \overline{Y})^2}} \tag{5.1}$$

where the variables X and Y are the sample points indexed with i. The PCC is a statistical measure of how closely two variables are related through a linear association. The Pearson coefficient may assume values ranging from -1 to 1, where -1 is the condition when the variables are perfectly in sync, however in opposite directions (as one variable increases, the other decreases), and when PCC assumes values equal to unity the variables as are also perfectly in sync, but in the same direction (both variable increases simultaneously). Therefore, PCC indicates how closed two measures are related.

Figure 52 illustrates the parametric correlation among the experimental and estimated parameters contemplating 415 data points. In this figure, the main diagonal illustrates the data histograms, the lower element diagonal illustrates the cross-correlation experimental conditions between the respective variables, and the upper diagonal elements illustrates the PCC. With the aim of employing Pearson's correlation, the flow pattern was transformed into numeric values defined as follows: (0) only liquid; (1) isolated bubbles; (2) coalescence bubbles; and (3) annular. The flow patterns were characterized based on visual observations. P-value indicates the lowest significance level observed that would lead to the rejection of the null hypothesis. The null hypothesis in this case is the statement that the two variable are unrelated. It is common to define a threshold of statistically significant for p-values inferior to 0.05. In Fig. 52 the asterisk illustrates: (i) * p-value=0.1, (ii) ** p-value=0.05, and (iii) *** p-value=0.01.

From Fig. 52, it is possible to observe an average correlation between the inlet and outlet

thermodynamic vapor qualities and the jet velocity of 0.4 and 0.45, respectively. Despite not shown in this figure, taking into account only the jet velocity data at the first ROI (12.4 mm), the PCC correlation is increased to 0.60 and 0.64 for inlet and outlet vapor qualities, respectively, suggesting a strong association between the inlet and outlet vapor qualities with the jet velocity. Once the TXV downstream experimental conditions were held approximately constant during the experimental campaign, such results suggest that the increase in the mixture specific volume (increase of vapor quality) downstream the TXV orifice increases the jet velocity. Corroborating these findings, Simões-Moreira and Bullard (2003) performed a numerical study of flashing mechanism in refrigerant expansion devices, founding an increase in the two-phase flow velocity emerging from the evaporation wave front as the outlet vapor quality increases.

Figure 52 – Parametric analysis of the influence of the experimental parameters on the jet velocity.

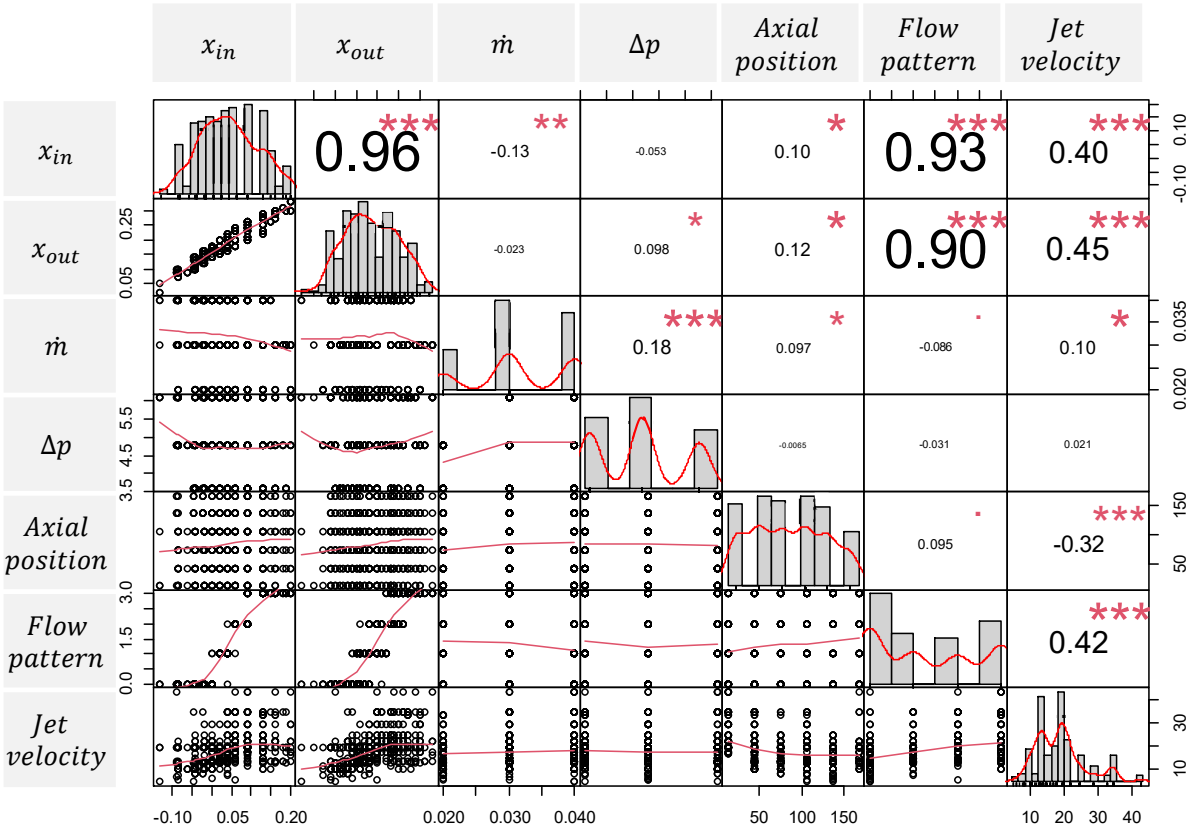

Source: Author

According to this figure, the jet velocity is also correlated to the test section axial position by a PCC of -0.32, decreasing its velocity along the test section. Taking into account only the database for the first (12.4 mm) and the last (167.55 mm) ROIs, the PCC correlation is decreased to -0.45, strengthening the hypothesis that the jet velocity decreases along the visualization section. This observation may be related to the decrease in the jet kinetic energy due to the interfacial friction between the jet interface and the liquid core as it flows along the visualization section. In addition to this, as discussed earlier, there are a swirling region (backflow) close to

the TXV outlet orifice. Then, applying the mass conservation law in this region the backward liquid in the axial direction contributes to an increase in the jet velocity. The inspection of Fig. 52 suggests that the jet velocity also has a strong correlation with the flow pattern of 0.42. On the other hand, the jet velocity does not have a clear correlation with the mass flow rate and the pressure drop across the TXV.

5.2 External flow-induced noise

Pressure drop effect on the flow-induced noise

Figure 53 depicts the effect of the pressure drop on the external TSPL noise for distinct mass flow rates.

Figure 53 – Illustration of the effect of the pressure drop on the external TSPL for mass flow rates of a) 0.02 b) 0.03. and c) 0.04 kg/s.

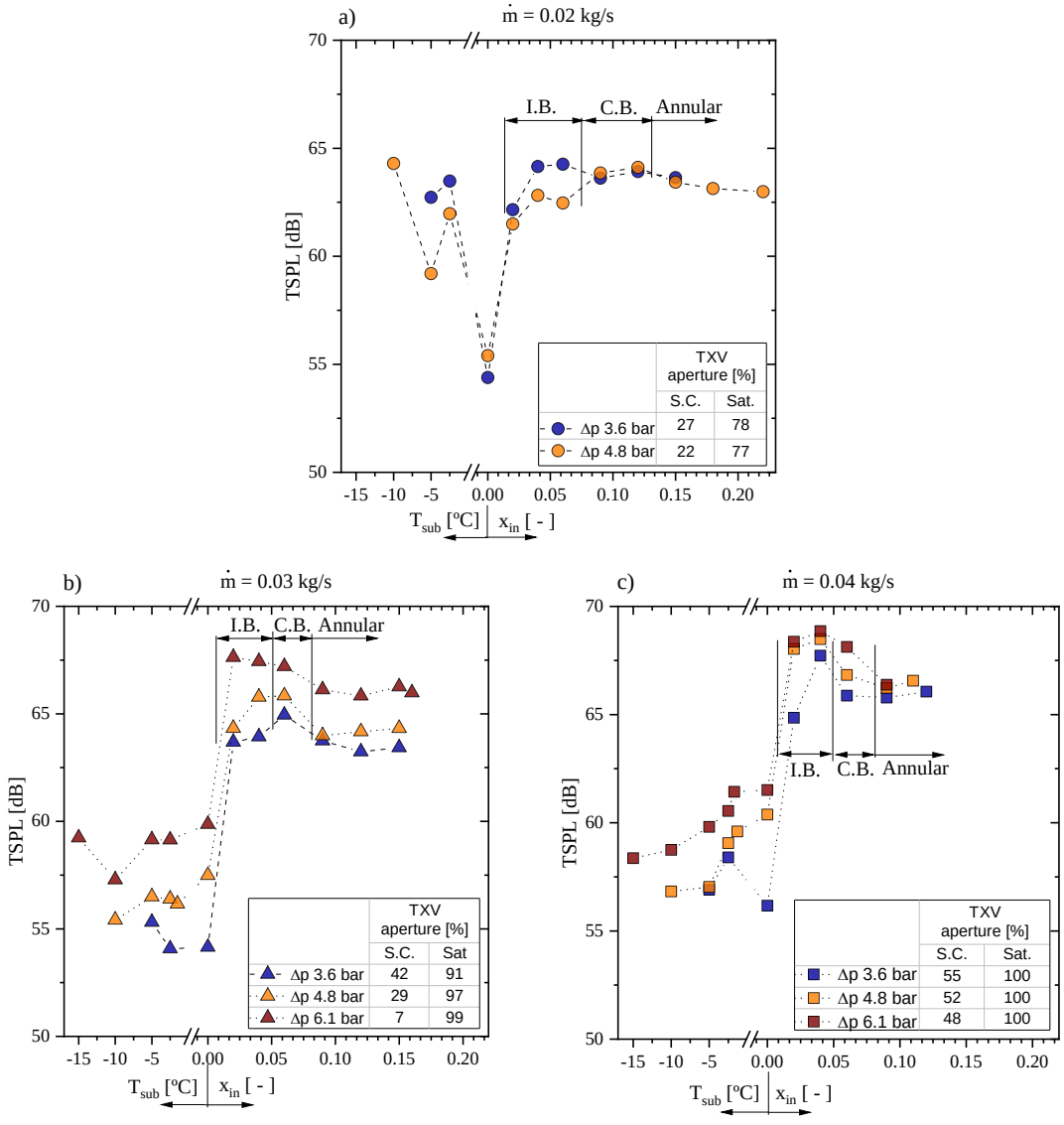

Source: Author

As general behavior displayed in Fig. 53, the TSPL increases as the pressure drop across the TXV increases. Such effect is more pronounced for mass flow rate of 0.03 kg/s, regardless of inlet vapor quality. In addition to this, in general, under I.B. flow pattern as the vapor quality rises from 2% to 4% the TSPL increases, such effect may be related to the increase in the number and volume of the bubbles, leading to a superior amount of energy converted into a shock wave as the bubbles contract and expand through the TXV orifice. Corroborating these results, Ishii and Watanabe (2018) found that the energy of a spherical bubble shock wave increases as its pressure and volume increase. The opposite behavior is observed for the mass flow rate of 0.02 kg/s under I.B. flow pattern, which exhibits a slightly superior noise for the pressure drop of 3.6 bar and similar TSPL for C.B. and annular flow pattern for pressure drops of 3.6 and 4.8 bar.

The tests were double checked for subcooled liquid under mass flow rate of 0.02 kg/s once such experimental condition exhibited distinct behavior from the 0.03 and 0.04 kg/s. No reasonable explanation could be found for superior TSPL under subcooled liquid for 0.02 kg/s over 0.03 and 0.04 kg/s. Furthermore, as depicted in Fig. 53, in general, the I.B. exhibits superior noise among the inlet flow patterns, decreasing as the inlet flow pattern shifts to C.B., and subsequently from C.B. to annular. Based on visual observations of the images recorded for vapor quality of 6% (C.B.) (Fig. 54), as the vapor bubbles start to coalesce their shape becomes non-spherical.

Figure 54 – Coalescence bubble effect near the TXV inlet for vapor quality of 6% and mass flow rate of 0.02 kg/s.

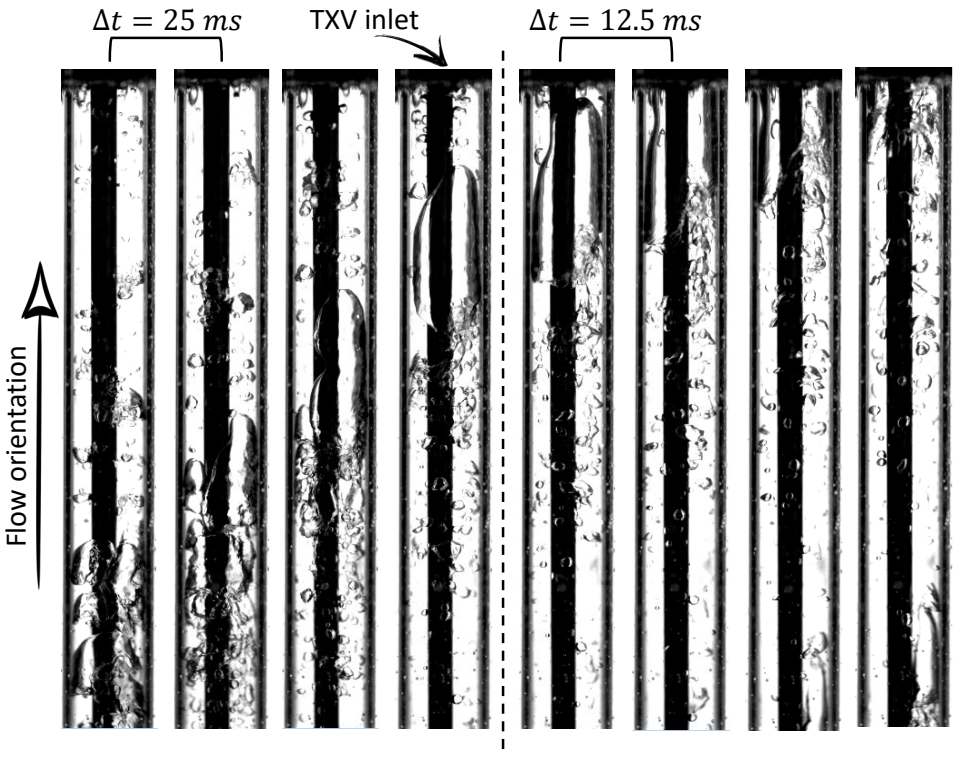

Source: Author

As mentioned by Supponen et al. (2017), the collapsing of a non-spherical bubble leads to a lower energy conversion rate than a spherical bubble. Therefore, as depicted in 53b and 53c, it can be speculated that the reduction in TSPL as the flow pattern shifts from I.B. to C.B. may be related to the bubble's non-spherical shape collapsing as it flows through the TXV orifice. In addition to this, as the bubbles approach the TXV inlet the coalescence effect becomes more pronounced due to the restricted flow path between the plunger and the valve seat; then, larger patches of vapor are found in this region for longer periods, as illustrated in Fig. 54. Based on it, it can be speculated that under such circumstances the intermittent frequency between the liquid and gas-phase is reduced, leading to inferior noise.

In general, by comparing the results for annular flow pattern, the TSPL remains almost at constant levels with increasing vapor quality. It is worthwhile to highlight that under such conditions marginal effect of the pressure drop on the noise can be observed for mass flow rates of 0.02 and 0.04 kg/s; on the other hand, for mass flow rate of 0.03 kg/s the TSPL increases as the pressure drop increases. Although Boabaid Neto et al. (2018) and Tannert and Hesse (2016) performed their experiments for capillary tube flowing R600a, and Kim et al. (2019) employed an EEV flowing R410A as test fluid, these authors also found superior noise under inlet intermittent flow pattern ($x_{in} < 8\%$), reducing as it shifts to only liquid or annular flow.

For mass flow rates of 0.03 and 0.04 kg/s as the TXV inlet flow shifts to two-phase, the TSPL sharply increases, regardless of the pressure drop. In contrast to this, a different trend is noted for mass flow rate of 0.02 kg/s, which exhibits an almost constant TSPL of 64 dB regardless of the thermodynamic state at the TXV inlet for both pressures drop; except for saturated liquid that presented inferior noise of 55 dB. The lowest TSPL of 55 dB was found for pressure drop across the TXV of 3.6 bar under saturated liquid at the TXV inlet for mass flow rates of 0.02 and 0.03 kg/s. At this point, it is important to highlight that during the experimental campaign, although qualitatively, it was possible to distinguish the I.B. from the other flow patterns by hearing the flow through the TXV. As each bubble flows through the TXV orifice a characteristic popping noise was heard. The popping noise is very similar to that which occurs when the popcorn pops in a metal pan. As mentioned by Hartmann and Melo (2013), the popping noise occurs when vapor bubbles collapses inside the capillary tube leading to a worse noise.

Kim et al. (2019), Kim and Song (2020), Han et al. (2009), and Jeong et al. (2007) performed their experiments for EEV and mass flow rates varying from 0.012 to 0.033 kg/s, founding a maximum TSPL of 52 dB(A), which is inferior to the minimum TSPL found in the current study. This may be related to the geometry of the original expansion valve employed in their study, which possesses bends close to the in/outlet valve device; therefore, it could significantly attenuate the noise by damping the two-phase flow vibrations and avoiding it to be transmitted to the surround environment.

Mass flow rate effect on the flow-induced noise

Figure 55 displays the effect of the mass flow rate on the external TSPL noise for distinct

pressure drops. As general behavior displayed in this figure, under two-phase flow at the TXV inlet the TSPL increases as the mass flow rate increases. It can be speculated that the increase in the mass flow rate, while all else parameter are held constant, increases the stream energy at the TXV exit; hence the fluid-structure intensity interaction (vibro-acoustics) increases leading to a superior noise. On the other hand, opposite behavior is observed for subcooled liquid at the TXV inlet, once the mass flow rate of 0.02 kg/s exhibited superior noise over the mass flow rates of 0.03 and 0.04 kg/s.

Figure 55 – Illustration of the effect of the mass flow rate on the external TSPL flow-induced noise for pressure drops of a) 3.6, b) 4.8, and c) 6.1 bar.

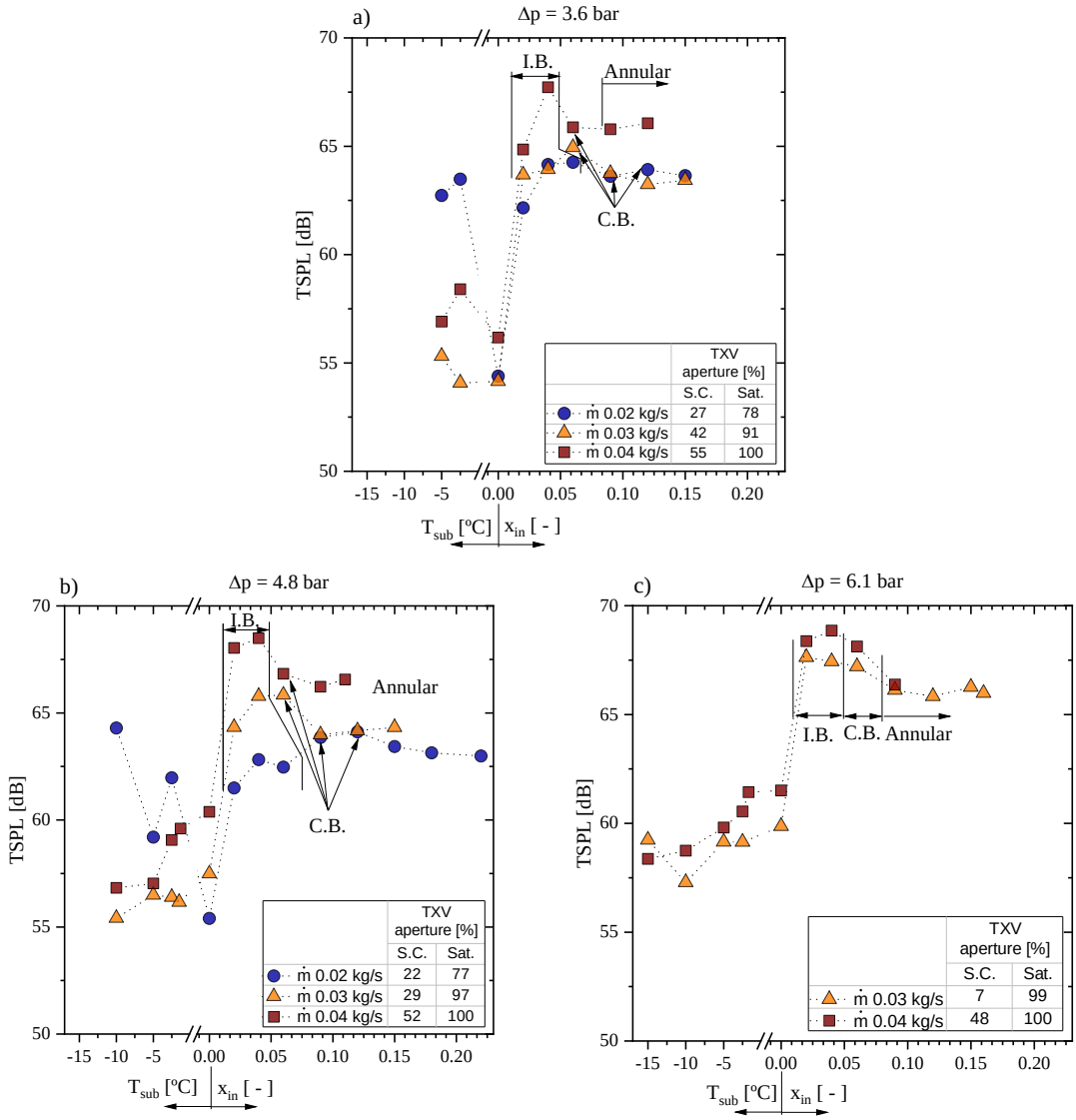

Source: Author

The increase in mass flow rate shifts the flow pattern transition from C.B. to annular at earlier vapor qualities. Based on it, as illustrated in Fig. 55a and 55b, despite the lower mass flow rate of 0.02 kg/s the C.B. flow pattern exhibited similar noise than annular flow at 0.03 kg/s

for inlet vapor quality of 9%. This indicates that the bubble releasing energy as it contract and expand through the TXV orifice under 0.02 kg/s are more relevant than the stream energy of 0.03 kg/s for for inlet vapor quality of 9%. On the other hand, despite being under annular flow, the mass flow rate of 0.04 kg/s exhibited superior noise than C.B. flow pattern flowing at 0.02 kg/s for inlet vapor quality of 9%. In this case, the experimental results indicate that the stream energy is more relevant than the bubbles releasing energy as it contract and expands through the TXV orifice.

According to Fig. 55a, it is possible to notice that the TSPL reduces as the inlet subcooling degree reduces up to saturated liquid, regardless of mass flow rate. Such behavior can be also found for pressure drop of 4.8 bar (Fig. 55b), however only for mass flow rate of 0.02 kg/s. On the other hand, opposite trend can be noticed for mass velocities of 0.03 and 0.04 kg/s under pressure drops of 4.8 and 6.1 bar, increasing the TSPL as the subcooling degree reduces. Although Ruebeling and Grohmann (2020) have performed experiments for capillary tube flowing R600a, these authors found that the noise generation and the mass flow rate are not directly related.

Xia et al. (2014) found a maximum noise of 35.6 dB(A), which is inferior to the minimum noise exhibited in the current study. This may be related to the small fridge with a capillary tube as an expansion device employed in their study. In addition, although not specified in their study, it may be speculated low mass flow rate through the capillary tube due to the reduced fridge cooling capacity, leading to an inferior flow-induced noise. Besides that, the fridge structure may attenuate the noise; therefore, fridge structure affected the evaluation of the flow-induced noise.

5.3 Fluid-structure acceleration

Pressure drop effects on the fluid-structure acceleration

Figure 56 depicts the acceleration trends with varying inlet vapor quality under distinct pressure drops for mass flow rates of 0.02, 0.03, and 0.04 kg/s. In general, the structure acceleration increases as the pressure drop across the TXV increases. Such effect is more pronounced for mass flow rates of 0.03 and 0.04 kg/s, regardless of inlet vapor quality. This behavior may be related to the increase in the released energy of a bubble shock wave as its pressure drop increases during the fluid flashing process trhough the TXV orifice (ISHII; WATANABE, 2018). Opposite behavior to these can be noticed for mass flow rate of 0.02 kg/s, which exhibits similar structure acceleration oscillating around 0.81 m/s^2 and 0.89 m/s^2 for only liquid and two-phase flow at the TXV inlet, respectively, regardless of the pressure drop.

According to Fig. 56b and 56c, as the I.B./C.B. evolves into annular flow pattern at the valve inlet the fluid-structure excitation decreases. The above-mentioned behavior could be explained by fluid-structure interaction of the bubble releasing energy as shock waves as it crosses the TXV orifice. The marginal effect of pressure drop on the structure acceleration under mass flow rate of 0.02 kg/s for I.B. and C.B. flow pattern at the TXV inlet may be related

to the reduced bubble frequency crossing the TXV orifice, which is not enough to excite the test section structure and being distinguishable. Although Tannert and Hesse (2016) performed experiments employing a capillary tube, these authors also verified a reduction in the structure acceleration as the flow pattern at the end section of the capillary shifted from intermittent to annular. Moreover, these authors also found that the external microphone and the accelerometer were in phase. Finally, the structure acceleration trends displayed in Fig. 56 are similar to ones recorded by the external microphone (Fig. 53), regardless of mass flow rate and pressure drop, as illustrated in Fig. 57. The only exception is the structure acceleration behavior of mass flow rate of 0.02 kg/s under condition of subcooled state, which exhibited a distinct trend from the ones recorded by the external microphone.

Figure 56 – Illustration of the effect of the pressure drop on the structure acceleration for mass flow rates of a) 0.02, b) 0.03, and c) 0.04 kg/s.

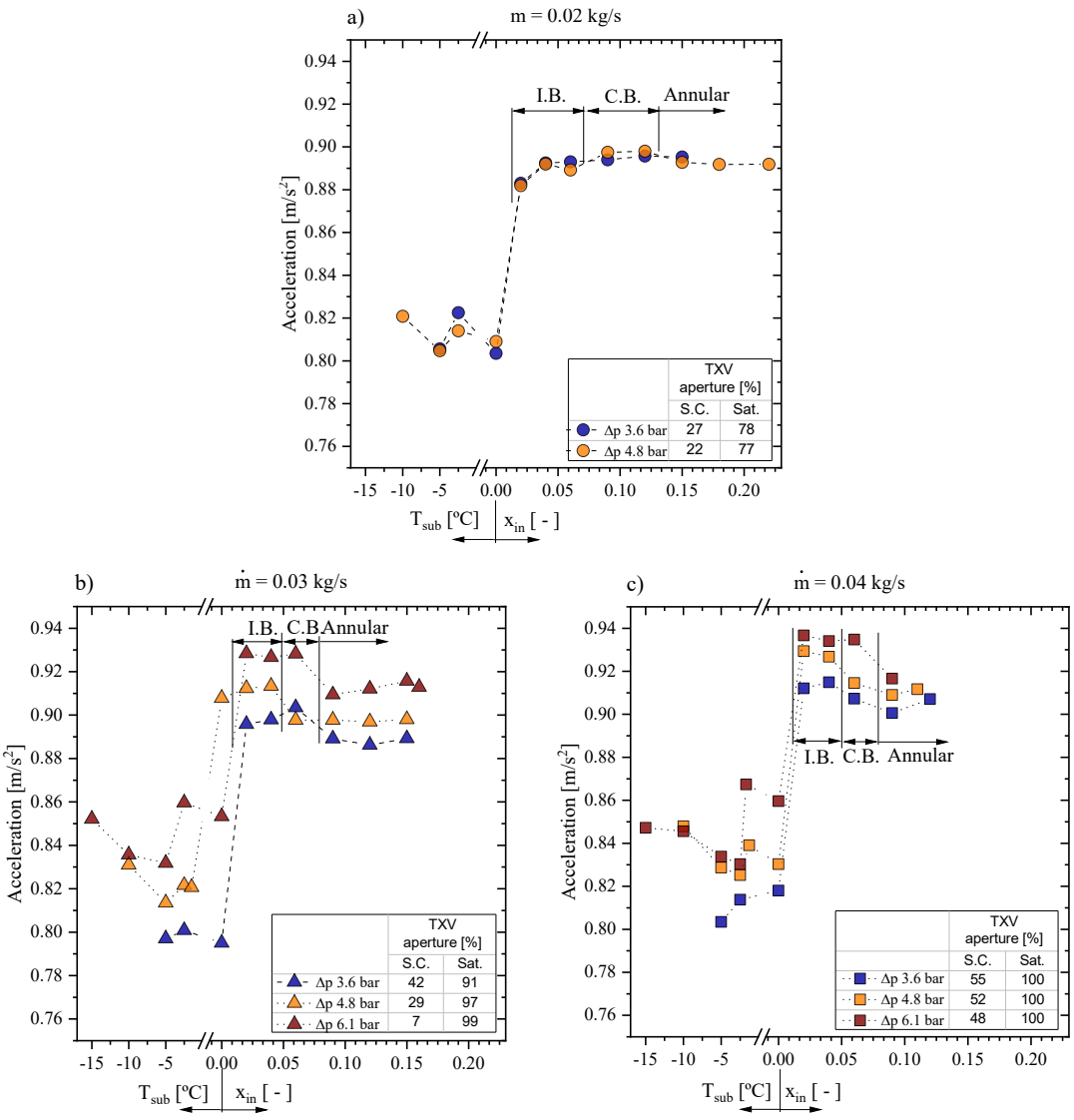

Source: Author

Figure 57 – Comparison between the external noise and the structure acceleration for mass flow rates of a) 0.02, b) 0.03, and c) 0.04 kg/s.

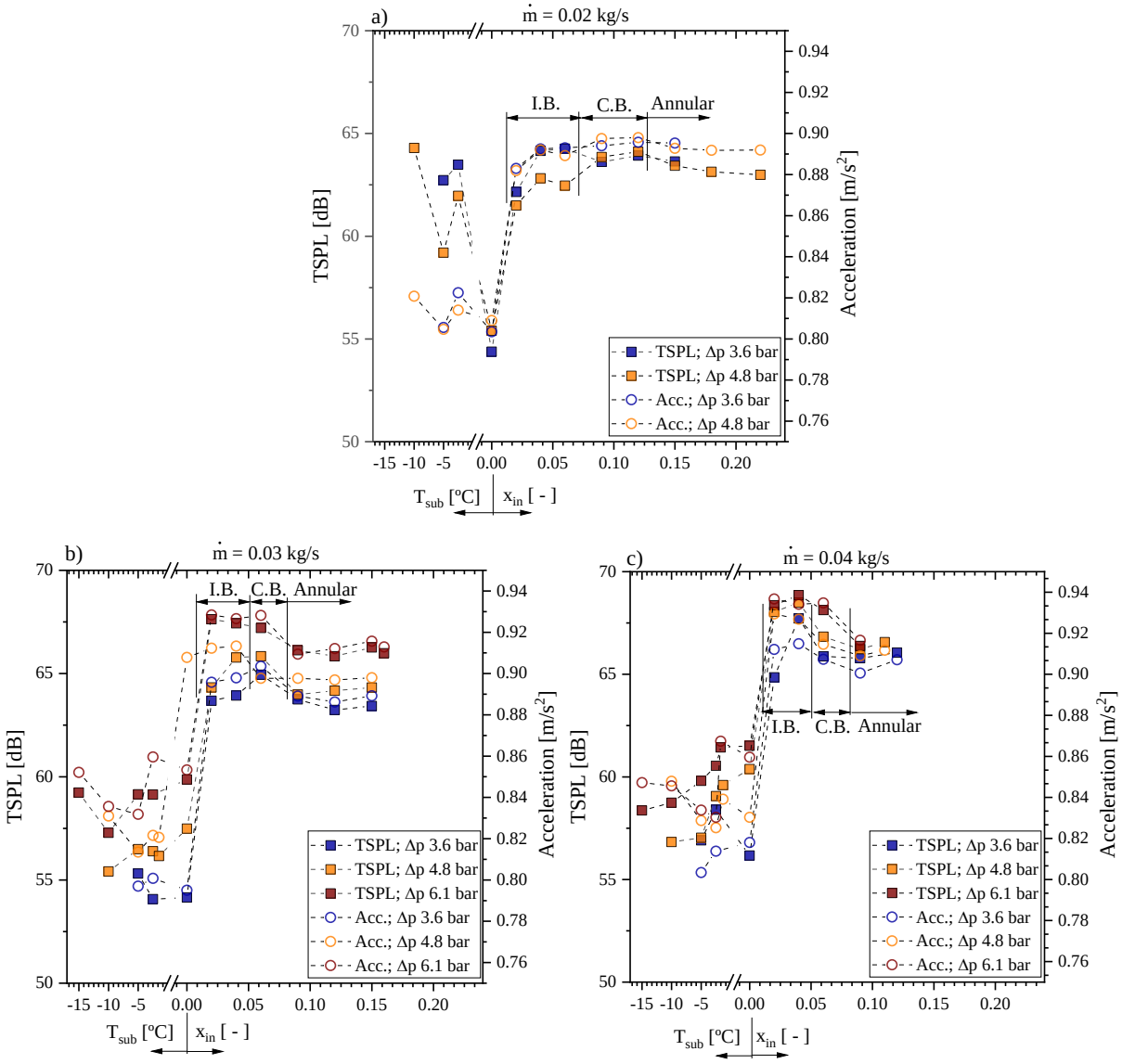

Source: Author

Mass flow rate effect on the fluid-structure acceleration

The plots displayed in Fig. 58 illustrate the effect of the mass flow rate on the structure acceleration for distinct pressure drops. In general, according to this figure, the structure acceleration increases as the mass flow rate increases, mainly under I.B. and C.B. flow patterns. It suggests that the frequency of bubbles crossing the TXV orifice also increases with the mass flow rate, resulting in more often and more intense fluid-structure interactions. In addition, the structure acceleration increases abruptly as the inlet thermodynamic state of the fluid changes from subcooled liquid into two-phase flow.

As depicted in Fig. 58b, the structure acceleration increases as the mass flow rate increases

under subcooled liquid at the TXV. On the other hand, the mass flow rate has a marginal effect on the structure acceleration for subcooled liquid under pressure drop of 6.1 bar. In addition, similar trends were observed by comparing the external noise and the structure acceleration under a pressure drop of 6.1 bar. Espíndola et al. (2020) in their experiments for capillary tube found that the capillary acceleration is directly dependent on the mass flow rate.

Figure 58 – Illustration of the effect of the mass flow rate on the structure acceleration for pressure drops of a) 3.6 b) 4.8. and c) 6.1 bar.

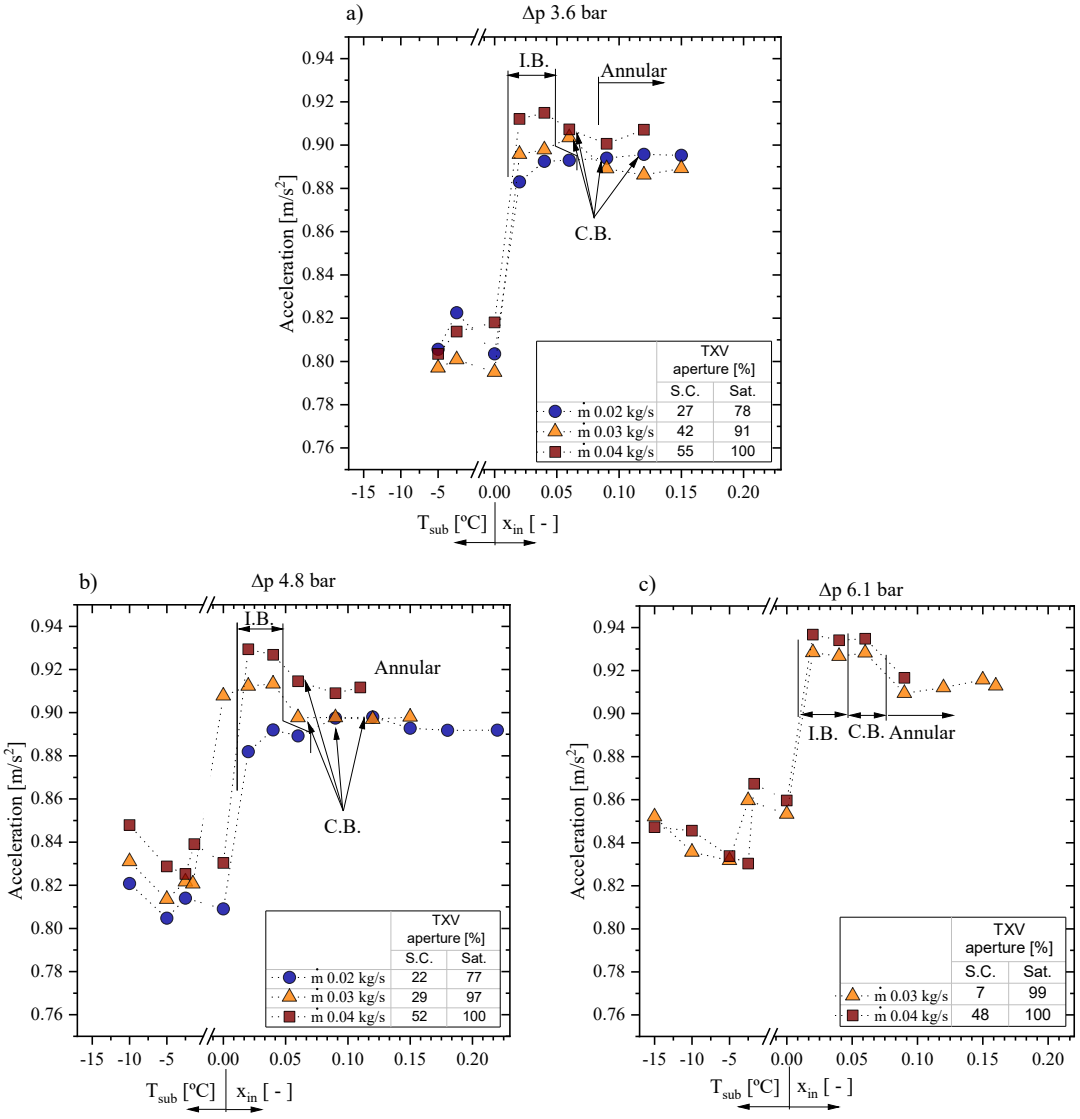

Source: Author

As already mentioned, the increase in mass flow rate shifts the flow pattern transition from C.B. to annular to lower vapor qualities. Based on it, as illustrated in Fig. 58a, despite the lower mass flow rate of 0.02 kg/s, the C.B. flow pattern (6% and 9%) exhibited structure acceleration almost similar to annular flow at 0.03 and 0.04 kg/s for inlet vapor quality of 9%. This may suggest that the bubble releasing energy as it contracts and expands through the TXV

orifice is more relevant than the stream energy of annular flow to the couple fluid-structure interaction under such experimental conditions. Similar behavior to this can be also notice in Fig. 58b, that exhibited similar structure accelerations of 0.90 m/s^2 for mass flow rates of 0.02 and 0.03 kg/s under C.B. and annular flow pattern, respectively. On the other hand, at inlet vapor quality of 9% the test section structure exhibited superior acceleration under mass flow rate of 0.04 kg/s (annular flow pattern) over 0.02 kg/s (C.B.). Under such experimental condition, this result indicates that the stream energy is more relevant than the bubbles releasing energy as it contract and expand through the TXV orifice. Finally, it should be mentioned that the effect of the mass flow rate on the external noise (Fig. 55) and on the structure acceleration exhibited similar behaviors mainly under two-phase flow at the TXV inlet as illustrated in Fig. 59.

Figure 59 – Comparison between the external noise and the structure acceleration for pressure drops of a) 3.6, b) 4.8, and c) 6.1 bar.

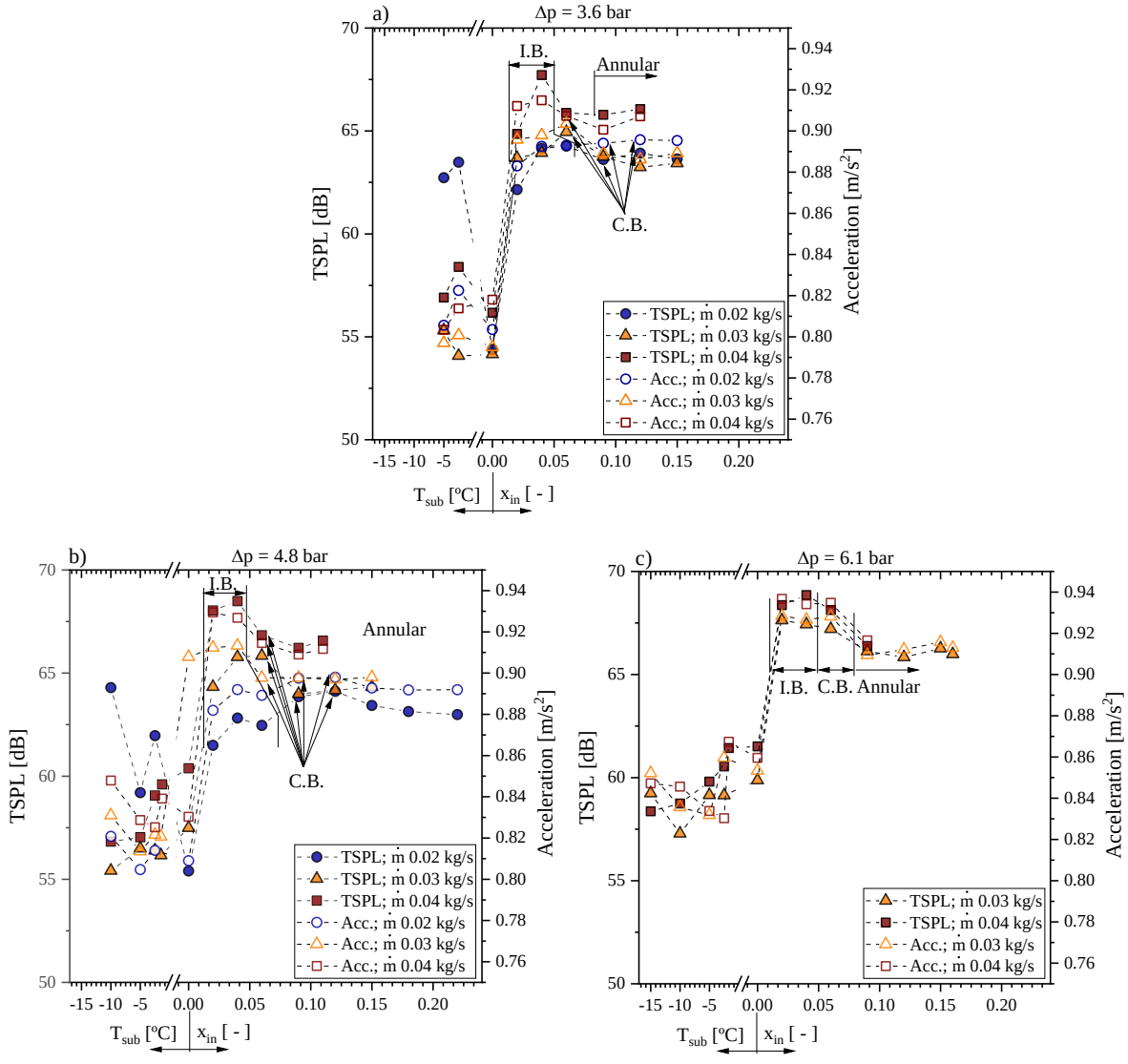

Source: Author

Although Boabaid Neto et al. (2014) performed their experiments for capillary tube and R600a as working fluid, these authors found a structure acceleration at the outlet of the capillary of approximately 0.77 m/s^2, which is similar to the current study acceleration. Unfortunately, Boabaid Neto et al. (2014) do not present the mass flow rate and the vapor quality at the capillary outlet. More recently, Espíndola et al. (2020) found capillary structure acceleration varying from 0.3 to 1.0 m/s^2 for mass flow rate from 0.0002 to 0.0005 kg/s. Despite Singh et al. (1999) performed extensive experiments evaluating the acceleration frequency spectrum of the capillary, short-orifice tube, TXV, and EEV devices, these authors did not provide the total acceleration. Unfortunately, despite the broad literature search performed in the present study, there are a reduced number of studies dealing with the evaluation of the flow-induced vibration in expansion devices.

5.4 Internal flow-induced noise

Pressure drop effect on the flow-induced noise

Figure 60 depicts the effect of the pressure drop on the internal TSPL noise for distinct mass flow rates. As general behavior according to this figure, the TSPL increases as the inlet vapor quality increases up to 6-9%, then the TSPL decreases, except for the pressure drop of 3.6 bar and mass flow rate of 0.02 kg/s that the TSPL still increases (Fig. 60a). Such behavior may suggest a change in the governing mechanism of the pressure oscillation for mass flow rate of 0.02 kg/s under pressure drop of 3.6 bar. According to Tab. 10, the jet velocity could not be detected at the last ROI (167.55 mm) for vapor qualities inferior to 6% under mass flow rate of 0.02 kg/s and pressure drops of 3.6. Therefore, the marginal oscillation on the TSPL for vapor quality inferior to 6-9% under such operational conditions can be related to the dissipation of the jet waves before the region at which the piezoelectric sensor is installed at the end of the test section. On the other hand, the sharp increase in the TSPL for vapor qualities superior to 6-9% could be related to the more intense jet waves achieving the sensor as illustrated in Tab. 10. Furthermore, the results shown in Fig. 60a revealed that the TSPL increases as the pressure drop increases. On the other hand, a distinct trend was noticed for the external TSPL evaluation (Fig. 53a), which may indicate that the structure is acting as a band-pass filter.

Under two-phase flow conditions at the TXV inlet, Singh et al. (1999) found an almost constant increase in the TSPL as the vapor quality increases for mass flow rate of 0.0126 kg/s for a given pressure drop. These authors also found an increase in the TSPL as the pressure drop increases for a given vapor quality. It should be stressed here that the maximum TSPL found by these authors was 153 dB (superheated vapor at the TXV inlet), which is inferior to the minimum TSPL found in the current work. This fact may be explained by the geometry of the original expansion valve employed in their study, which possesses bends close to the in/outlet valve device and is horizontally displayed; therefore, the bends could significantly dampen the flow leading to an attenuated noise. Although Boabaid Neto et al. (2014) and Boabaid Neto et al.

(2018) evaluated the noise at capillary tube outlet for R600a, these authors found a mean TSPL of 135 and 130 dB at the capillary outlet, respectively. Unfortunately, no information about the mass flow rate was provided by them. Besides, these authors do not provided the distance from the capillary outlet to the piezoelectric sensor position.

Figure 60 – Illustration of the effect of the pressure drop on the internal TSPL flow-induced noise for mass flow rates of a) 0.02 b) 0.03. and c) 0.04 kg/s.

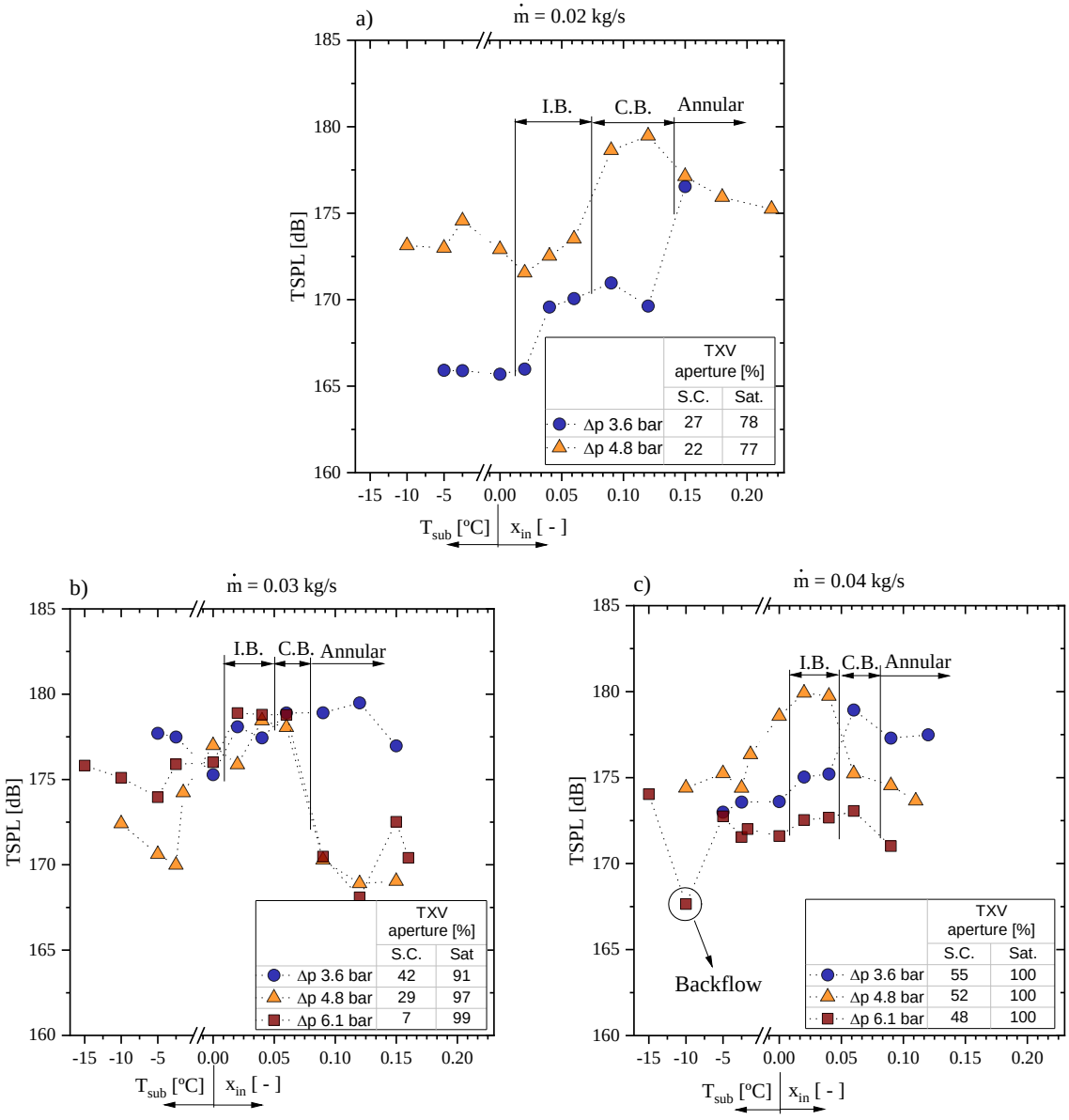

Source: Author

One may observe from Fig. 60b marginal oscillations on the TSPL for pressure drops of 3.6 bar, regardless of the inlet vapor quality. On the other hand, under pressure drops of 4.8 and 6.1 bar the TSPL increases from the inlet subcooling degree of -15ºC up to C.B. (6%) flow pattern; then, the TSPL abruptly decreases as the flow pattern evolves into annular. According to Fig. 60c, marginal oscillations around 171 dB are noticed under pressure drop of 6.1 bar, regardless of the

inlet vapor quality. Yet, under such operational conditions, it should be highlighted that at inlet subcooling degree of -10ºC the minimum TSPL of 167 dB could be attributed to backflow effects visually observed at the last fraction of the visualization section through the images recorded during the experimental campaign, whereas the TSPL increases with increasing vapor quality up to C.B. and I.B. for pressure drops of 3.6 and 4.8 bar, respectively. The backflow, mainly near the tube wall could mitigate the waves of pressure that reaches the piezoelectric sensor.

As general comment, through the comparison of Figs. 53 and 60, it can be observed distinct behaviors for the internal and external TSPL regardless of mass flow rate and pressure drop. Therefore, it can be concluded that the intrinsic characteristic of the structure is acting as a band-pass filter transmitting only determined frequencies according to the operational condition. Besides that, such distinct behavior can be related to a damping effect on the flow as it travels towards the sensor housing, which is corroborated through the PPC of -0.45 between the jet velocity and the visualization section position.

Mass flow rate effect on the flow-induced noise

The plots displayed in Fig. 61 illustrate the effect of the mass flow rate on the internal TSPL for distinct pressure drops. According to Fig. 61a, the TSPL increases as the vapor quality increases for mass flow rates of 0.02 and 0.04 kg/s; however, for mass flow rate of 0.03 kg/s the TSPL remains almost constant, oscillating around 177 dB, regardless of the inlet vapor quality. One should be noticed that the mass flow rates of 0.03 and 0.04 kg/s under C.B. exhibited similar TSPL, whereas under annular flow similar TSPL could be noticed regardless of the mass flow rate. At this point, it should be highlighted that under subcooled liquid conditions the mass flow rates of 0.02 and 0.03 kg/s exhibited opposite trends to the ones observed during the evaluation of the external noise (Fig. 55a).

As can be seen from Fig. 61b, in general, the TSPL increases up inlet vapor quality of approximately 6%, for mass flow rates of 0.03 and 0.04 kg/s, then the TSPL decreases as the inlet flow pattern evolves into annular. The TSPL increases as the mass flow rate increases under I.B. flow pattern, such behavior is similar to the one observed for the external noise evaluation (Fig. 55b). Contrary to what was expected, the mass flow rate of 0.02 kg/s exhibited superior TSPL for vapor qualities superior to 9% under such experimental conditions once the mass flow rate of 0.03 and 0.04 kg/s has superior kinetic energy. As far as the author knows, the effect of the mass flow rate and inlet subcooling degree/vapor quality on the internal TSPL has not been elucidated in literature. Therefore, it may be speculated that under mass flow rate of 0.03 kg/s (Fig. 55b and c) the inherent flow-induced noise vibration mechanism may intensify the excitation at the piezoelectric sensor.

According to Fig. 61c, the internal TSPL increases with reducing the mass flow rate for inlet subcooling degree ranging from -5ºC up to vapor quality of 6%. For inlet subcooling degree inferior to -5ºC, even under distinct TXV aperture, both mass flow rates exhibited almost similar TSPL. Furthermore, under annular flow similar TSPL could be observed regardless of

the mass flow rate. For the pressure drop of 6.1 bar the mass flow rate of 0.04 kg/s exhibited an almost constant TSPL oscillating around 171 dB as the inlet vapor quality increases. As a general comment, it should be remarked that it is noticed a distinct trend from the internal e external TSPL, regardless of the operational condition. Such behavior is related to the intrinsic structure characteristic acting as a band-pass filter allowing only determined frequencies to be transmitted through the device wall. In addition, superior TSPL was found for inlet vapor qualities of 4% (I.B.) and 6% (C.B.).

Figure 61 – Illustration of the effect of the mass flow rate on the internal TSPL flow-induced noise for pressure drops of a) 3.6 b) 4.8. and c) 6.1 bar.

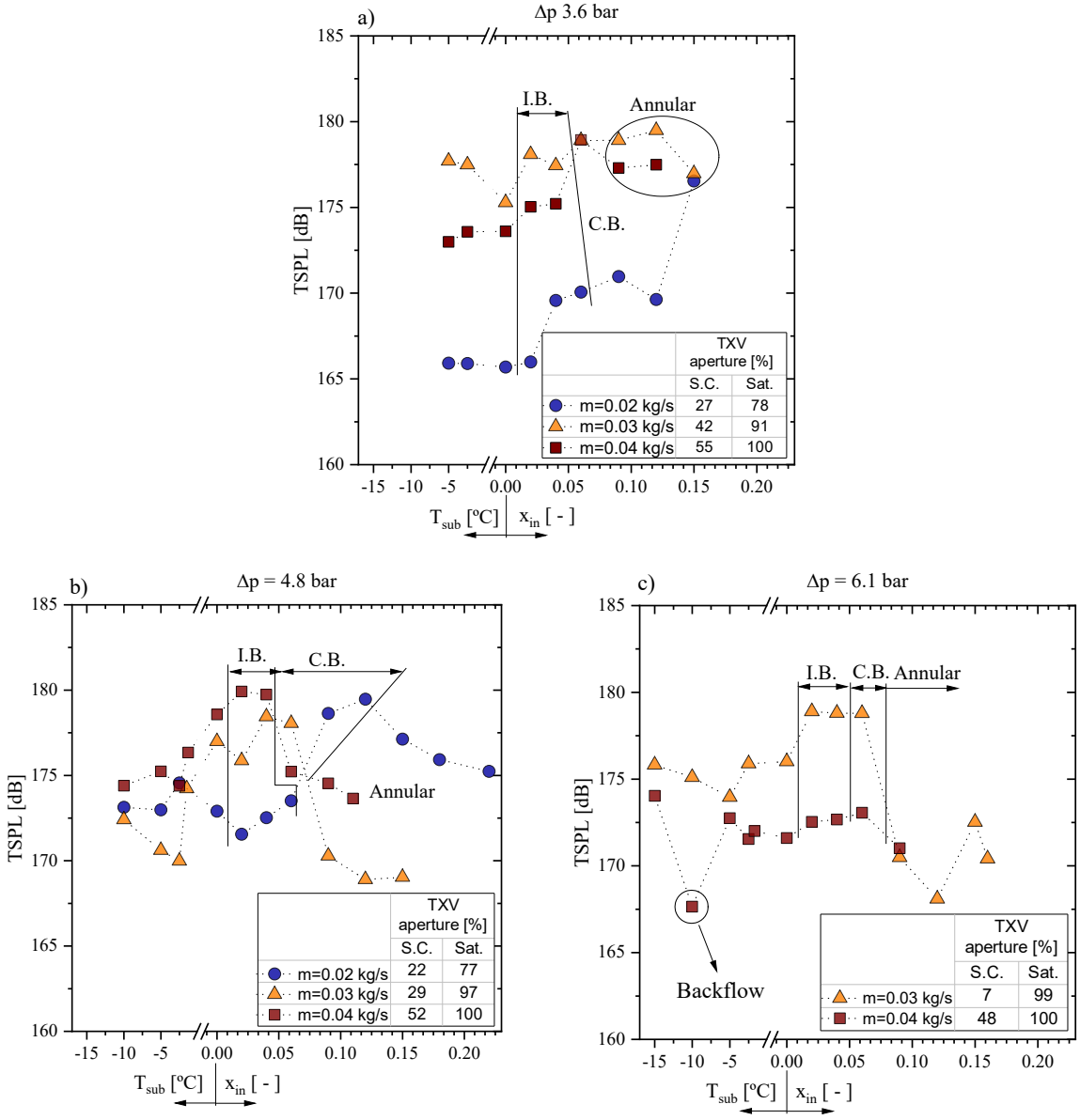

Source: Author

5.5 Frequency spectrum and signal coherence

An important step to understanding the transmission of the flow-induced noise to the environment is investigating the frequency spectrum of the structure acceleration through which the sound is travelling and the microphone noise spectrum. In order to elucidate the agreement between the structure acceleration and the external noise behaviors, an ordinary coherence (γ_{xy}) spectral analysis was also conducted. The ordinary coherence signal function may assume values ranging from zero to unity, where: i) for $\gamma_{xy} < 0.5$ low confidence degree; ii) $0.5 < \gamma_{xy} < 0.7$ medium confidence degree; and iii) $\gamma_{xy} > 0.7$ high confidence degree that the peak is a resonant frequency. The ordinary coherence signal function is defined as follows:

$$\gamma_{xy} = \frac{|G_{xy}|^2}{G_{xx}G_{yy}} \tag{5.2}$$

where G_{xy} is the cross-spectral density between x and y, and G_{xx} and G_{yy} are the power spectral density of the signals x and y, respectively.

Figures 62, 64, and 65 depict the effect of the inlet vapor quality on the external noise, structure acceleration, and coherence signal frequency spectrum for mass flow rates varying from 0.02 to 0.04 kg/s under pressure drop of 4.8 bar. As an attempt to cross-correlate the noise and the structure acceleration the coherence signal was clustered as only liquid and two-phase flow at the TXV inlet once it showed similar behaviors. The noise and structure acceleration signals presented frequency peaks at 48 and 96 Hz, and at 64 and 128 Hz, respectively, which can be cross-correlated to similar jet frequency peaks leaving the TXV orifice at the visualization section positions of 12.4 and 74.5 mm as shown in Fig. 51. In fact, such ROIs are close to the acceleration and microphone sensors. The coherence signal up to 200 Hz illustrates a low confidence level due to the distinct frequency peaks between the microphone (48 and 96 Hz) and the accelerometer (64 and 128 Hz). It should be emphasized that frequencies inferior to 100 Hz are negligible compared to the human hearing frequency. Besides that, it should be remarked that the coherence signals exhibited similar confidence levels regardless of the inlet thermodynamic state of the fluid, mass flow rate, and pressure drop for the entire frequency range, except for the frequency peaks at 304, 912, and 1536 Hz under subcooled liquid conditions (10ºC and 5ºC). A confidence high coherence signal degree peak at 912 and 1500 Hz can be observed for mass flow rates of 0.02 and 0.04 kg/s, only for subcooled liquid; therefore, it was not possible to correlate these results with the bubble resonance frequency theory.

Frequency peaks around 2.7, 5.5, 8.5, and 13.5 kHz would be associated with bubble diameters of 6.4, 3.4, 2.1, and 1.3 mm, respectively, according to the model proposed by Minnaert (1933). In fact, the images recorded upstream the TXV revealed bubbles with dimensions ranging from 1.0 to 7.0 mm as illustrated in Fig. 63. However, it is essential to highlight that these frequency peaks mentioned above also occurs under subcooled liquid and annular flow, which makes the bubble resonance frequency theory not suitable for such justification. Therefore, it

may be speculated that the reduced flow path between the plunger and the seat of the TXV is normalizing the flow morphology during the flashing process once its path is inferior to most of the bubbles diameter; thus, resulting in a similar frequency spectrum regardless of the inlet subcooling degree/ vapor quality condition.

Figure 62 – Microphone, accelerometer, and coherence frequency spectrum for mass flow rate of 0.02 kg/s under pressure drop of 4.8 bar.

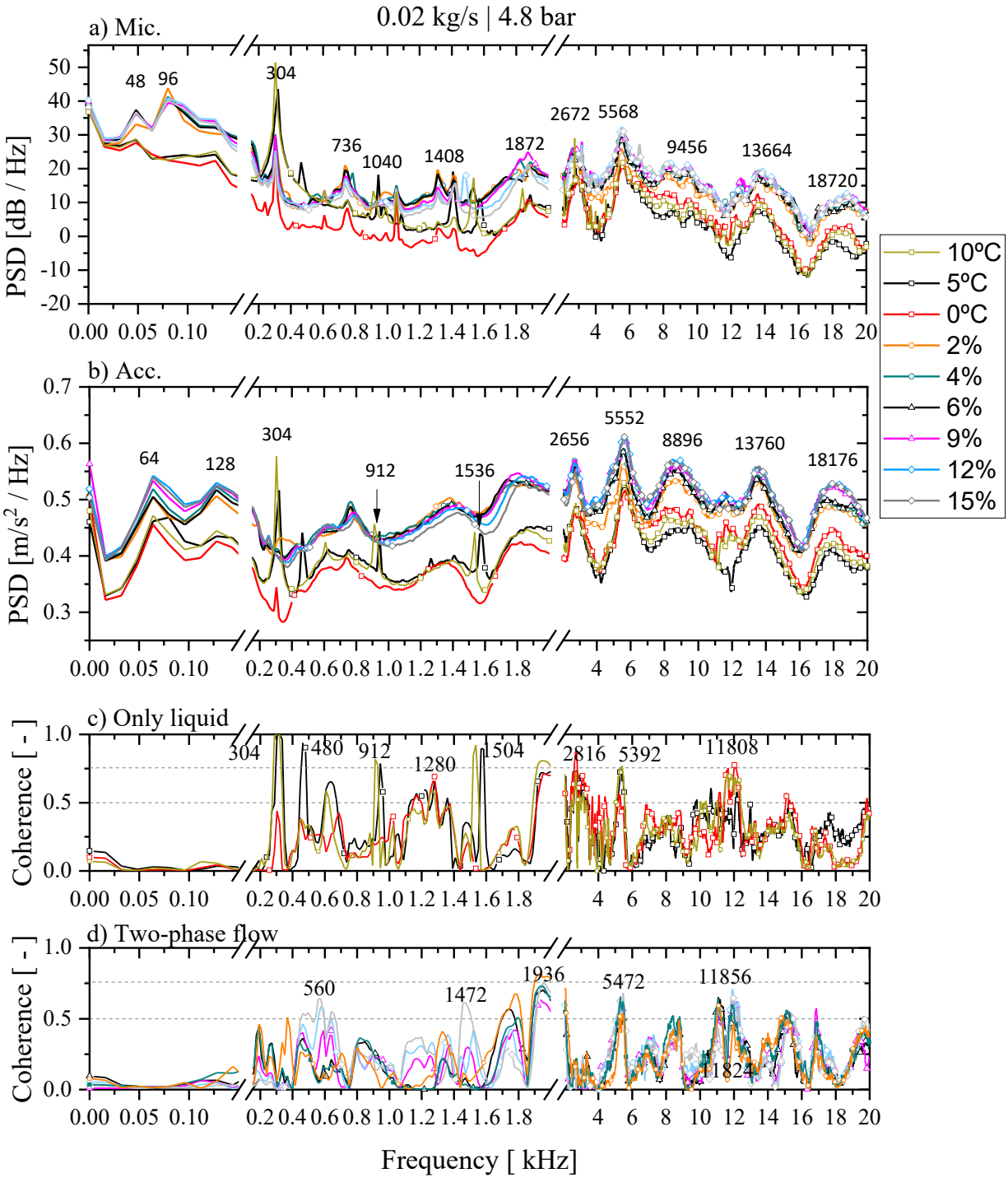

Source: Author

Figure 63 – Image of the bubbles diameter upstream the TXV inlet at mass flow rate of 0.03 kg/s, vapor quality of 4%, and saturation pressure of 7.7 bar (30ºC) (dimensions in millimeters).

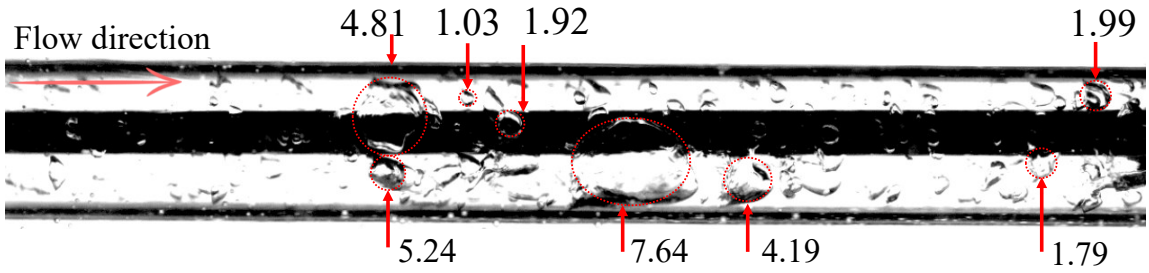

Source: Author

As mentioned by Simões-Moreira and Bullard (2003), the liquid reaches metastable state within the expansion valve turning into high-speed two-phase flow. Based on it, the fluid-structure excitation mechanism can be related to the chaotic flashing process at the TXV outlet once similar behaviors can be identified regardless of the inlet vapor quality.

One may observe from these figures that the noise and structure acceleration frequency peak intensity at 304 Hz decreases as the mass flow rate increases. In addition to this, the structure acceleration intensity increases as the subcooling degree increases, and as the pressure drop decreases for a given mass flow rate. It should be mentioned that this frequency could not be correlated to the bubble resonance frequency theory once such a peak occurs only for subcooled liquid and it would result in a bubble with diameter of 55 mm according to Minnaert (1933) model, which is superior to the visualization section internal diameter (10.12 mm). On the other hand, the frequency peak around 1 kHz intensifies as the mass flow rate increases. Distinctly from the remaining frequency band, it occurs only for subcooled liquid at the TXV inlet; therefore, it may be speculated that the flow-induced noise mechanism aspects of only flashing liquid may differ from the two-phase flow at the TXV inlet.

Koberstein et al. (2015) identified an intense whistle noise source at 6.18 kHz in phase with the accelerometer at the TXV suction line. These authors also found a frequency peak band around 2.5 kHz, which is similar to the ones found in the current study. Although Singh et al. (1999) performed their experiments for horizontal inlet and outlet flow, these authors found relevant acceleration at frequency bands around 5, 9, 14, and 18 kHz for TXV, which is in agreement with the current data.

It is worth mentioning that, a bubble with equivalent radius of the annular gap between the valve seat and the plunger of the TXV(ranging from 0.1 to 0.55 mm) would lead to a natural frequency superior to 42 kHz based on Minnaert (1933) model, overcoming the upper limit of the human audible frequency. Hence, the collapsing bubble may not be the source of the noise. In addition, it can be speculated that the bubble resonance frequency upstream of the TXV may result in an inferior noise than the fluid flashing process.

Figure 64 – Microphone, accelerometer, and coherence frequency spectrum for mass flow rate of 0.03 kg/s under pressure drop of 4.8 bar.

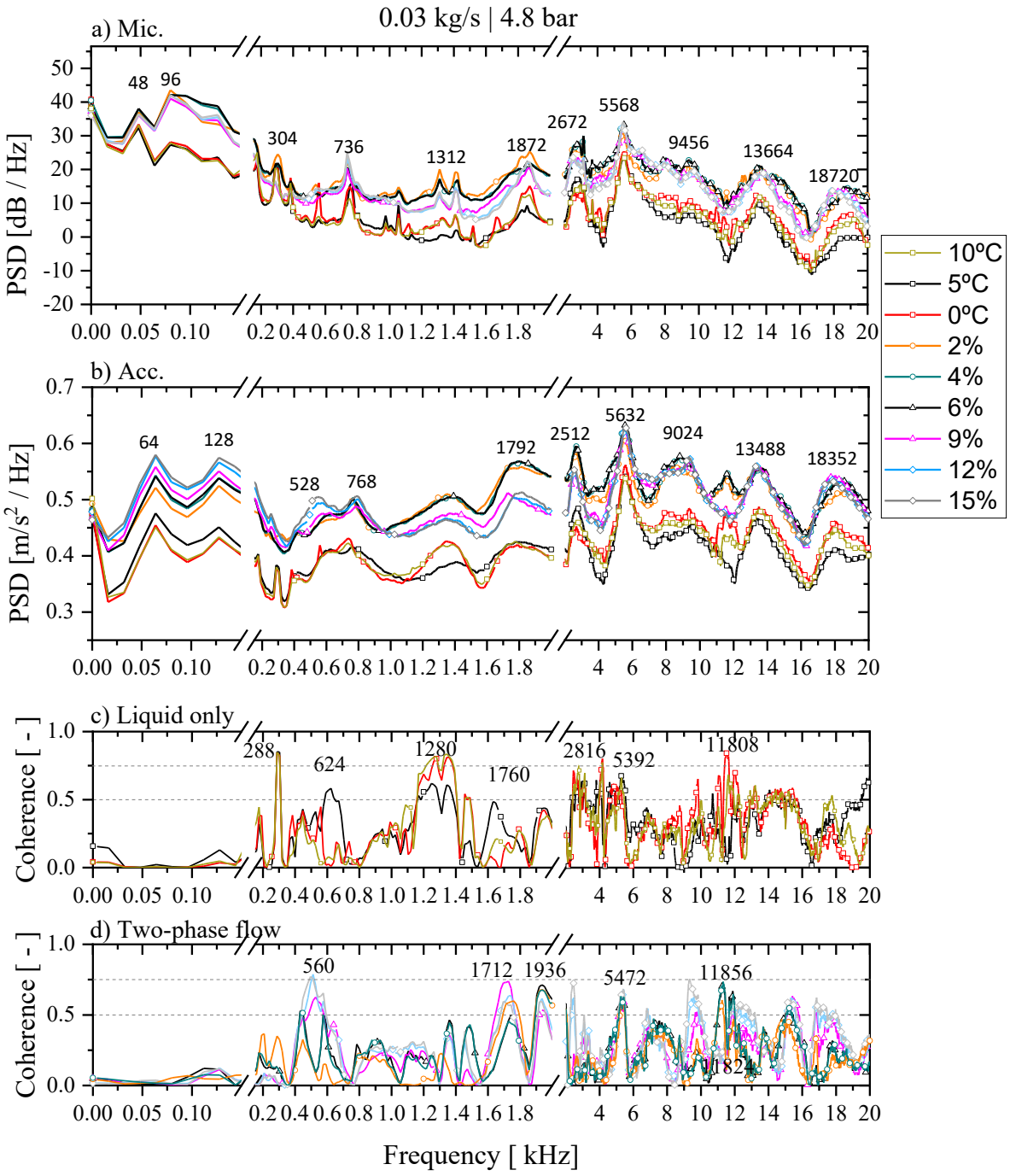

Source: Author

The plots displayed in Fig. 66 depict the effect of the inlet vapor quality on the microphone, accelerometer, piezoelectric frequency spectrum, and the coherence signal between these sensors for mass flow rate of 0.04 under pressure drop of 6.1 bar. As already described above, the microphone and the accelerometer exhibited similar trends to the previous samples. On the other hand, a different trend is noted for the piezoelectric signal decreasing asymptotically with no

apparent frequency peaks, except for 8000 and 15168 Hz, regardless of the vapor quality. These frequency bands may be intensified due to the housing piezoelectric sensor geometry resonance frequency modes. According to the Minnaert (1933) model, the frequencies of 8000 and 15168 Hz would lead to a bubble diameter of 0.67 and 0.35 mm, respectively, which is likely to occur.

Figure 65 – Microphone, accelerometer, and coherence frequency spectrum for mass flow rate of 0.04 kg/s under pressure drop of 4.8 bar.

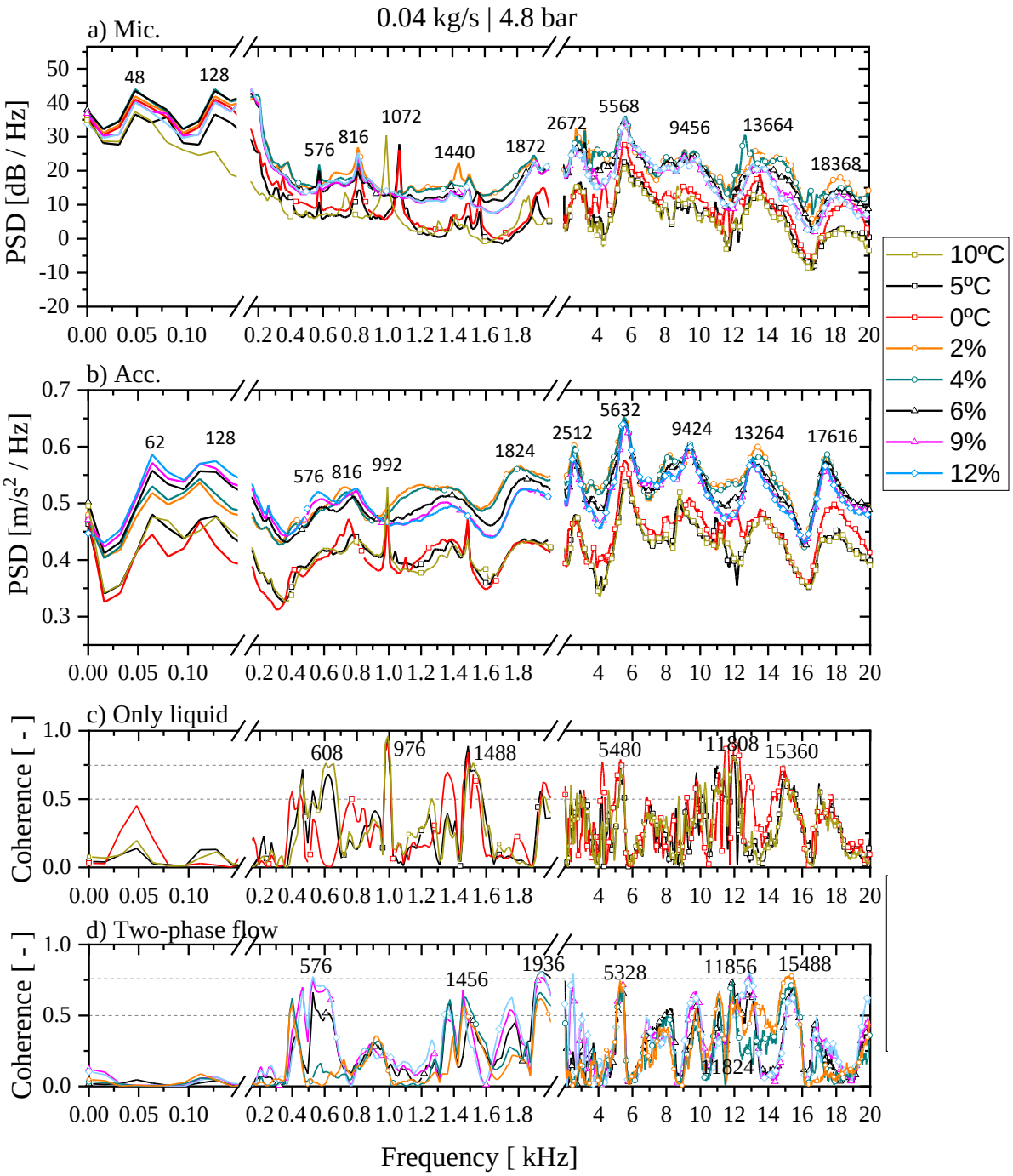

Source: Author

Figure 66 – Microphone, accelerometer, piezoelectric, and coherence frequency spectrum for mass flow rate of 0.04 kg/s under pressure drop of 3.6 bar.

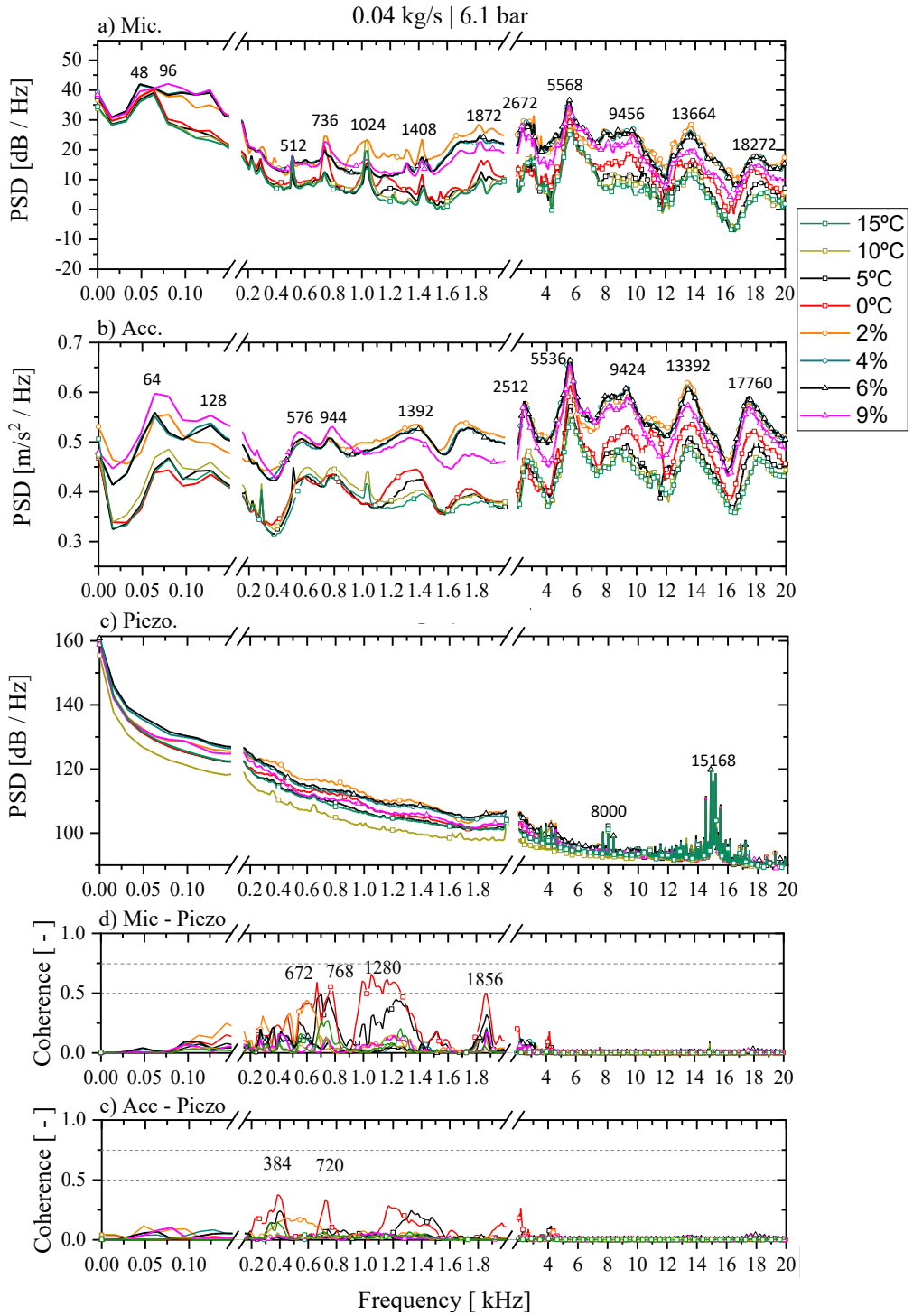

Source: Author

The reduced fluctuation on the piezoelectric signals with no significant frequency peaks can be related to the jet dissipation effect as it travels toward the piezoelectric housing sensor. Hence, the lack of independence between the Mic-Piezo and Acc-Piezo signals is illustrated by the low confidence levels of the coherence signals (Fig. 66d and 66e). In general, Singh et al.

(1999) could not find frequency peaks during the evaluation of the internal noise for capillary, orifice tube, EEV, and TXV. These authors also found an asymptotic decrease on the internal noise signal as the frequency increases, however, with superior amplitude. The remaining data for the internal noise exhibited similar trend to the ones in Fig. 66c, regardless of the experimental condition. From this analysis, it can be concluded that the intrinsic characteristic of the fluid-structure interaction (vibro-acoustics) is mitigating the SPL and acting as a band-pass filter, allowing only certain frequencies to be transmitted through the device wall, which is peculiar to each of the used equipment.

As a general statement, the SPL evaluated within the expansion devices presented similar trends regardless mass flow rate and pressure drop. As a final comment, the external noise and structure acceleration spectrum distributions exhibit similar trends and frequency peaks for the entire frequency range, regardless of the inlet vapor quality and mass flow rate. Corroborating these findings, Han et al. (2009) found similar trends for the external noise frequency spectrum regardless of the vapor quality and the evaporation temperature.

5.6 Flow-induced noise parametric study

In this section, a parametric analysis of the experimental data employing Pearson's Correlation Coefficient is performed to determine the influence of the inlet and outlet thermodynamic vapor quality, mass flow rate, pressure drop, flow pattern, and jet velocity on the internal and external noise, and structure acceleration, as illustrated in Fig. 67. The database is composed of 81 data points of each variable. The jet velocity dataset employed contemplates only the visualization section at the ROI of 12.4 mm, which is closer to the position of the microphone and the accelerometer. From Fig. 67, the main diagonal illustrates the data histograms, the bottom panel allows the evaluation of the main trend of the results according to each variable cross-correlation, and the upper panel illustrates if the correlation between the variables is statically significant.

In general, the results displayed in Fig. 67 show a strong PCC correlation between the inlet/outlet vapor quality, flow pattern, microphone, accelerometer, and jet velocity. Besides that, those variables are statistically significant cross-correlated for p-values inferior to 0.01. The cross-correlation between piezoelectric sensor and inlet/outlet vapor, mass flow rate, microphone, pressure drop, and jet velocity exhibits low values of PCC and p-values superior to 0.05, pointing out that those variable are statistically unrelated with the internal noise as already expected and speculated in the previous section. Moreover, the test section acceleration and the microphone are statistically unrelated with the mass flow rate and pressure drop exhibiting p-values superior to 0.1. On the other hand, the test section acceleration and the microphone are statistically related with the in/outlet vapor quality, jet velocity, and flow pattern. As expected, the microphone and the accelerometer are strong cross-correlated with each other exhibiting a PCC of 0.84, as already mentioned in the previous section, once these sensors showed similar trends.

Figure 67 – Parametric analysis study of the influence of several parameters on the flow induced noise and structure acceleration.

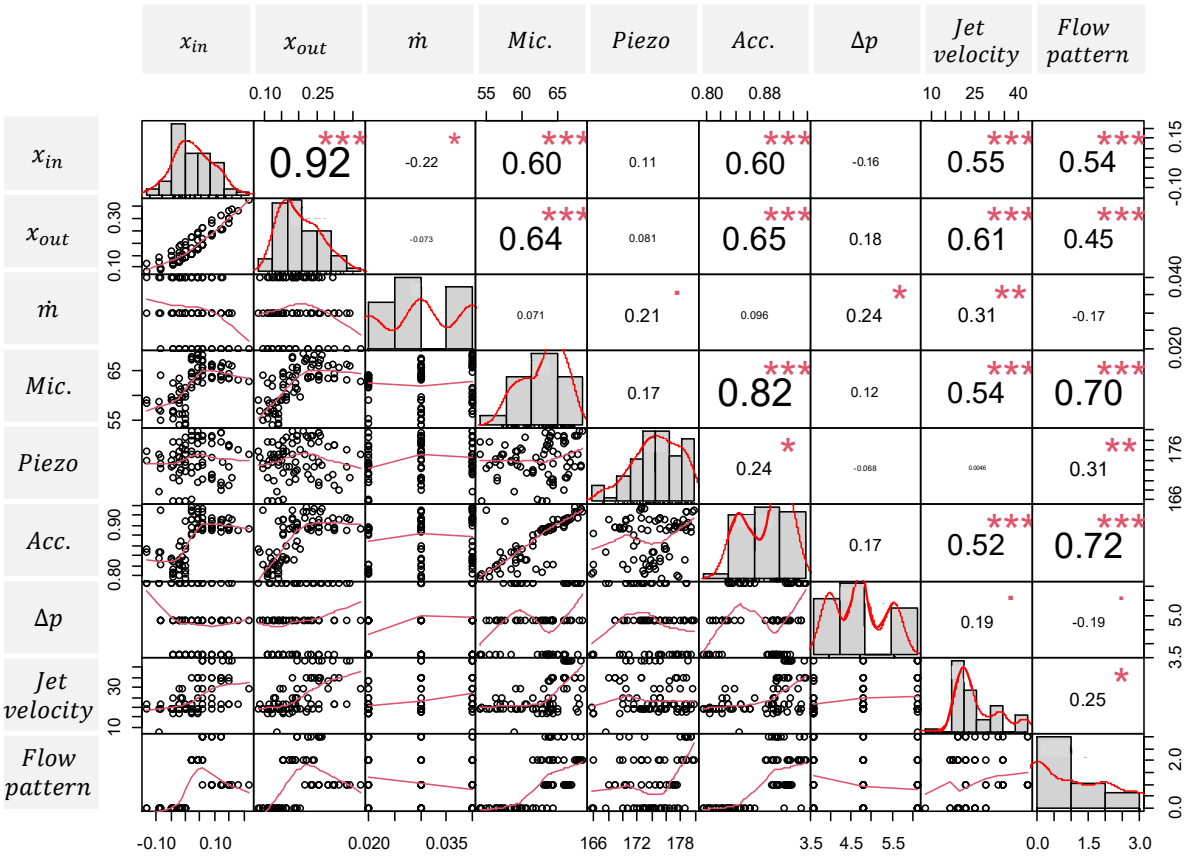

Source: Author

6 CONCLUDING REMARKS AND FUTURE RESEARCH RECOMMENDATIONS

In this chapter, initially, the main findings concerning the investigation of jet velocity, external and internal flow-induced noise, and structure acceleration are presented and summarized. Then a parametric analysis of several parameters is presented. At the end, a list of suggestions and recommendations for future studies is presented

6.1 Conclusions

The investigation of the effect of flow morphology just upstream and along the outlet section of a TXV has been unprecedented in the literature. The images recorded by a high-speed video camera upstream and downstream of the TXV outlet allowed the investigation of the jet frequency and velocity along the outlet visualization section. Moreover, the study presented an evaluation of the effect of the flow morphology upstream and downstream of TXV, mass flow rate, pressure drop, and vapor quality effect on the internal and external noise and structure acceleration by performing a cross-correlation between these variables to clarify the fluid-structure interaction (vibro-acoustics) of R134a under conditions similar to residential and commercial air-conditioning and refrigeration applications, which as far as the author knows has unparalleled in the literature.

Two-phase flow images and jet velocity

- Based on the images recorded downstream of the TXV, no visual distinction could be made among the tested experimental condition concerning flow pattern characterization, revealing a chaotic flashing process. In addition, in the last fraction of the visualization section, the flow does not exhibit a well-defined morphology according to the well-known flow patterns proposed in the literature.

- It was possible to identify a region characterized by swirling flow and bubble nucleation between the TXV leaving jet and the tube walls close to the TXV orifice. This region is characterized by a low local pressure, which draws flow from upward and onset the bubble nucleation. Besides that, parcels of the nucleated bubbles and the backflow join within the main steam periodically. Such phenomenon was observed regardless of the operational condition.

- At first instances, flow visualization analysis of the recorded images downstream of the TXV indicated that, although qualitatively, the inlet vapor quality affects the velocity of the jet waves exiting the TXV. This behavior is corroborated by the measurements of the jet velocities based on the cross-correlation function. Under subcooled liquid conditions, the jet velocity remains almost constant and has similar values regardless of the experimental

condition. As the subcooled liquid shifts to two-phase flow, the jet velocity increases sharply as the vapor quality increases, up to annular flow at the TXV inlet; then, it remains almost at a constant level with further increase in the vapor quality for annular flow. Under annular flow conditions at the TXV inlet, the jet velocity increases as the mass flow rates increases. These jet velocity trends could be well-clustered in flow pattern groups of SC, IB-CB, and annular by employing the k-means unsupervised machined learning algorithm.

- The jet velocity could be well-captured at the first ROI (12.4 mm) regardless of the mass flow rate. On the other hand, the jet velocities could be barely tracked at the last fraction of the visualization section (167.65 mm) under mass flow rates of 0.02 and 0.03 kg/s for vapor qualities inferior to 9%. Through such an evaluation, it is speculated that the small vapor bubbles dispersed in a liquid phase (within the jet waves) grow continually into the low-pressure reservoir until the bubbles mature and, finally, burst in the early portions of the visualization section. The increase in the mass flow rate and the vapor quality allowed the vapor bubbles to travel further before their lifetime overs, being traceable by the cross-correlation function at the last fraction of the test section.

- The two-phase flow jet frequency spectrum analysis indicated that the intensity of the frequency spectrum peaks decreases as the distance from the TXV outlet orifice increases. These results agree with the jet dissipation effects through bubbles bursting at early portions of the visualization section. In addition, jet frequency peaks could be found from 14 to 140 Hz at a visualization axial position of 12.4 mm, regardless of the mass flow rate and pressure drop. These frequency peaks are in accordance with the frequency peaks found by the external noise at 28 and 96 Hz and by the structure acceleration of 64 and 128 Hz.

- A parametric analysis of the effects of inlet and outlet vapor quality, mass flow rate, pressure drop, visualization section axial position, and flow pattern on the jet velocity was performed based on a database with 2905 data points employing PCC, and the main conclusions are drawn: i) the inlet and outlet vapor quality, and inlet flow pattern exhibit a strong correlation with the outlet jet velocity, ii) no clear trend could be found between the mass flow rate and the jet velocity, however under annular inlet flow pattern the jet velocity increases as the mass flow rate increases, iii) there is no evidence of significant effects of the pressure drop on the jet velocities, and iv) a negative PCC was found between visualization axial position and the jet velocity indicating opposite behavior of these variables.

External flow-induced noise

- The analysis of the external noise indicates that the TSPL increases as the pressure drop across the TXV orifice increases for mass flow rates of 0.03 and 0.04 kg/s. In addition, under such experimental conditions, the noise increases sharply as the subcooled liquid at

the TXV inlet shifts into two-phase flow. On the other hand, a distinct trend was observed for mass flow rate of 0.02 kg/s, exhibiting an external noise almost constant of 64 dB regardless of the pressure drop, inlet subcooling degree, and vapor quality.

- Regarding the inlet flow pattern, superior external noise is found for I.B. increasing as the pressure drop increases. Such phenomenon is assigned to the bubble energy increase as its pressure increases, leading to superior energy released as shock waves as the bubbles burst. As the inlet vapor quality increases the flow pattern shifts into annular; then, the noise displays almost a constant TSPL and inferior to the C.B. flow pattern. In a particular experimental condition of inlet vapor quality of 6% (C.B.), visual observations of the recorded images revealed that as the vapor bubbles approach the TXV inlet the coalescence effect becomes more pronounced due to the restricted flow path between the plunger and the valve seat. Then, even for a short period, the intermittent frequency between the liquid and gas phase is reduced leading to an inferior noise.

- The minimum TSPL of 54 dB found in the current study is superior to the maximum SPL of 52 dB(A) found by Kim et al. (2019), Kim and Song (2020), Han et al. (2009), and Jeong et al. (2007) for EEV and mass flow rates varying from 0.012 to 0.033 kg/s. These results may suggest that the geometry of the original expansion valve employed in their study, which possesses bends close to the in/outlet valve device could significantly attenuate the noise; Therefore, the intrinsic characteristic of the structure is damping the noise.

- Although qualitatively, it was possible to distinguish the I.B. from the other flow patterns by hearing it; as each bubble passed through the TXV orifice, it resulted in a characteristic popping noise. Despite Hartmann and Melo (2013) having performed their experiments for capillary tube, they also found a popping noise.

- For a given pressure drop, in general, the TSPL increases as the mass flow rate increases under two-phase flow at the TXV inlet; for subcooled liquid, at the TXV inlet, no clear trend could be identified. Under pressure drop of 6.1 bar, the mass flow rates of 0.03 and 0.04 kg/s exhibited similar noise regardless of the thermodynamic state of the fluid.

Structure acceleration

- The analysis of the structure acceleration revealed that its acceleration appears to be primarily function of pressure drop through the expansion device, increasing as the pressure drop increases under mass flow rates of 0.03 and 0.04 kg/s. On the other hand, no clear effect of the pressure drop on the structure acceleration could be identified for the mass flow rate of 0.02 kg/s. Superior structure oscillation was found for I.B. and C.B. flow patterns at the TXV inlet for mass flow rates of 0.03 and 0.04 kg/s, decreasing as the flow pattern evolves into annular flow. This behavior can be attributed to the superior energy

released by the bubbles as it flows through the TXV orifice, enhancing for higher pressure drop. Moreover, for a given mass flow rate, the external noise and the structure acceleration exhibited similar trends.

- The structure acceleration is found to increase as the mass flow rate increases for pressure drop of 4.8 bar; however, for a given pressure drop of 3.6 and 6.1 bar, the structure exhibited similar values regardless of the mass flow rate. Under subcooled liquid at the TXV, distinct trends were observed for the external noise and the structure acceleration for a given pressure drop.

- A restricted number of experimental studies evaluating the structure acceleration are available in the literature. Although Boabaid Neto et al. (2014) performed their study for capillary expansion device, these authors found a structure acceleration of 0.77 m/s^2, similar to the minimum acceleration found in the current study. These results may suggest that the intrinsic characteristic geometry/type and how the expansion device is coupled may affect its acceleration intensity.

Internal flow-induced noise

- In general, there is no clear parametric effect of the measured and estimated variables on the internal flow-induced noise.

- A restricted database for evaluation of the internal noise of a TXV is available in the open literature; therefore, a quantitative comparison between the studies can be considered inappropriate. Superior TSPL of 180 dB was found for I.B. and C.B. flow patterns. On the other hand, Singh et al. (1999) found a maximum TSPL of 153 dB (superheated vapor TXV inlet, 0.0126 kg/s), which is inferior to the minimum TSPL found in the current work. This fact can be attributed to the original expansion valve employed in their study, with its inlet and outlet displayed in a horizontal direction holding bend close to the TXV orifice; which could significantly dampen the flow leading to an attenuated noise. Furthermore, these authors did not provide information about the existence of a strainer at the TXV inlet, which could attenuate the noise by changing the flow pattern. Therefore, it suggests that the intrinsic characteristics of the device design may result in a distinct fluid-structure interaction, which may not be suitable as a direct comparison.

Frequency spectrum and signal coherence

- Frequency peaks were found at 48 and 96 Hz, and 64 and 128 Hz for the external noise and structure acceleration, respectively, regardless of the experimental conditions. These results are in agreement with the frequency peaks found for jets leaving the TXV.

- Frequency peaks were found around 2.7, 5.5, 8.5, 13.5, and 18.7 kHz regardless of the thermodynamic state of the fluid (only liquid and two-phase flow) at the TXV inlet; therefore, the bubble resonance frequency theory is not suitable for such a justification. These results suggest that the TXV orifice is normalizing the flow morphology during the flashing process once the fluid path within the valve device is inferior to the diameters of the bubbles. In addition, the coherence signal between the external noise and the fluid-structure acceleration exhibited values superior to 0.5 in these frequency bands, indicating medium or high confidence degree that such frequency is resonant.

- In general, a similar frequency spectrum behavior is found for the external noise and the structure acceleration regardless of the experimental condition. On the other hand, the internal noise exhibited a completely distinct trend. Such behavior is corroborated by the reduced coherence degree between the microphone/accelerometer and the piezoelectric sensor for the entire frequency range, regardless of the operational condition. Moreover, Singh et al. (1999) also found an asymptotic decrease in the SPL for capillary, orifice tube, EEV, and TXV. In addition, Han et al. (2009) found similar trends for the external noise frequency spectrum regardless of the vapor quality and the evaporation temperature.

Parametric effect of several variable

- The parametric analysis indicated that the far-field expansion noise and the structure acceleration are primary functions of the inlet flow pattern illustrated by a PCC of 0.7. Besides that, the jet velocity can be correlated with these sensors with a PCC of 0.50. Besides that, the similar trends found by the external noise and the structure acceleration led to a PPC of 0.82. The mass flow rate and the pressure drop could not be well straight correlated to the external noise and structure acceleration. On the other hand, the internal flow-induced noise could not be correlated to any of the measured and estimated parameters.

As a final comment, the evaluation of the flow-induced noise and structure acceleration of a TXV seems to be in the early stage, given that the pioneering studies in this area are still recent and in small numbers up to the present date. Furthermore, the available studies in the literature introduce the intrinsic characteristics of the device design (vibro-acoustic) and, sometimes, the entire refrigeration system (variable speed compressor and evaporator) making a quantitative comparison between the studies inappropriate. On the other hand, a qualitative comparison was performed founding similar behavior, even between different expansion devices.

6.2 Recommendations for future studies

The following recommendations are made to future studies pertinent to flow-induced noise in a TXV:

- Perform experiments for hydrocarbon refrigerants, null ODP, and low GWP, focusing on generating a wide database once such fluid are suitable to domestic refrigeration and air-conditioning.

- In the present study, performing experiments for high vapor qualities were not possible due to the restricted cooling capacity of the test bench. The increase in the cooling capacity of the test bench would allow increase the inlet vapor quality at the TXV. Therefore, the effects of the annular flow pattern for superior vapor qualities and superheated vapor could be studied.

- Hirakuni et al. (2004) indicated that a porous media at the expansion device inlet and outlet reduces the flow-induced noise by changing the flow pattern. Therefore, the analysis of distinct porous media geometry would allow simulating the effect of the strainer found at the commercial TXV inlet on the flow-induced noise and structure acceleration. A strainer/porous media is a passive and permanent way to reduce the flow-induced noise at a low cost.

- Performing a simultaneous analysis of the intermittent flow pattern flowing through the TXV orifice and the recorded images would allow studying the transient behavior of the flow pattern on the flow-induced noise and structure acceleration. Quantify the effect of the bubble diameter and circularity for low vapor qualities (up to 9%) on the flow-induced noise and structure acceleration by developing an image analysis routine. However, it would be necessary the development of a larger acoustic chamber to host a high-speed camera with the expansion device.

- Performed experiments for distinct plunger and orifice geometry. Additionally, it would be also interesting to introduce a smooth transition at the TXV outlet guiding the outlet jet to evaluate its effect on the external noise and structure acceleration. Moreover, it could be manufactured inlet and outlet bend close to the TXV inlet/outlet in glass to study its effect on the flow pattern, jet velocity and morphology, flow-induced noise, and structure acceleration.

BIBLIOGRAPHY

AARON, D.; DOMANSKI, P. Experimentation, analysis, and correlation of refrigerant-22 flow through short tube restrictors. **Ashrae Transactions**, v. 96, n. 1, p. 729–742, 1990.

ABERNETHY, R.; THOMPSON JR., J. **Handbook of uncertainty in gas turbine measurements**. : National Technical Information Service, 1973.

AMINI, A.; OWEN, I. A practical solution to the problem of noise and vibration in a pressure-reducing valve. **Experimental Thermal and Fluid Science**, v. 10, n. 1, p. 136–141, 1995.

AOYAMA, S. et al. Analyzing for refrigerant induced noise for split type air conditioner indoor unit. **Transactions of the Korean Society for Noise and Vibration Engineering**, v. 16, n. 3, p. 240–246, 2006.

APAYDIN, T.; HEPERKAN, H. Experimental investigation of r600a refrigerant flow inside adiabatic capillary tube. **Sigma Journal Engineering and Natural Sciences**, v. 34, n. 2, p. 241–252, 2016.

ASHRAE, F. Fundamentals handbook. **IP Edition**, v. 21, 2013.

ASK, J.; DAVIDSON, L. A numerical investigation of the flow past a generic side mirror and its impact on sound generation. **Journal of Fluids Engineering**, v. 131, n. 6, 2009.

____. Flow and dipole source evaluation of a generic suv. **Journal of Fluids Engineering**, v. 132, n. 5, 2010.

BAARS, E.; LENZI, A.; NUNES, R. Sound quality of hermetic compressors and refrigerators. In: **International Refrigeration and Air Conditioning Conference, Indiana at Purdue. Indiana, USA**. 2002.

BAKER, O. et al. Design of pipelines for the simultaneous flow of oil and gas. In: . : Fall Meeting of the Petroleum Branch of AIME, Dallas, Texas, October, 1953.

BANDARRA FILHO, E. P. **Um estudo experimental da ebulição convectiva de refrigerantes no interior de tubos lisos e internamente ranhurados**. 2002. Tese (Doutorado) — Universidade de São Paulo, 2002.

BANSAL, P.; RUPASINGHE, A. An homogeneous model for adiabatic capillary tubes. **Applied Thermal Engineering**, v. 18, n. 3-4, p. 207–219, 1998.

BARBIERI, P. E. L. **Estudo teórico-experimental da ebulição convectiva do refrigerante R-134a em tubos lisos**. 2005. Tese (Doutorado) — Universidade de São Paulo, 2005.

BENNETT, B. et al. Flow visualization studies of boiling at high pressure. In: . : Institution of Mechanical Engineers, London, 1965. v. 180, n. 3, p. 260–283.

BLEVINS, R. D.; PLUNKETT, R. Formulas for natural frequency and mode shape. **Journal of Applied Mechanics**, v. 47, p. 461, 1980.

BLUE, J. Resonance of a bubble on an infinite rigid boundary. **The Journal of the Acoustical Society of America**, v. 41, n. 2, p. 369–372, 1967.

Boabaid Neto, C. et al. Noise generation in household refrigerators: an experimental study on fluid borne noise. In: **International Refrigeration and Air Conditioning Conference, Indiana at Purdue. Indiana, USA**. 2014.

____. Noise generation in household refrigerators: an experimental study on fluid borne noise. In: **17th Brazilian Congress of Thermal Sciences and Engineering**. 2018.

CALM, J. M. The next generation of refrigerants–historical review, considerations, and outlook. **international Journal of Refrigeration**, v. 31, n. 7, p. 1123–1133, 2008.

CARDOSO, L. C. d. S. M. et al. Interacçao vibroacústica do sistema placa-cavidade fechada: Modelaçao, experimentaçao e análise. 2010.

CELIK, S.; NSOFOR, E. C. Studies on the flow-induced noise at the evaporator of a refrigerating system. **Applied Thermal Engineering**, v. 31, n. 14-15, p. 2485–2493, 2011.

CHEN, D.-K. **Flashing flow of refrigerant HFC-134a through a diabatic capillary tube**. 1997. Tese (Doutorado) — Concordia University, 1997.

CHENG, L.; RIBATSKI, G.; THOME, J. R. Two-phase flow patterns and flow-pattern maps: fundamentals and applications. **Applied Mechanics Reviews**, v. 61, n. 5, p. 050802, 2008.

CHURCHILL, S. W. Friction-factor equation spans all fluid-flow regimes. **Chemical Engineering**, v. 84, n. 24, p. 91–92, 1977.

COLLIER, J. G.; THOME, J. R. **Convective Boiling and Condensation**. : Clarendon Press, 1996.

CREMER, L. Theorie der schalldämmung dünner wände bei schrägem einfall. **Akust Zeitschrift**, v. 7, n. 3, p. 81, 1942.

CREMER, L.; HECKL, M. **Structure-borne sound: structural vibrations and sound radiation at audio frequencies**. : Springer Science & Business Media, 2013.

DEVIN, C. Resonance frequencies of pulsating air bubbles generated in short, open-ended pipes. **Hydromechanics Laboratory**, 1961.

ESPÍNDOLA, R. S. et al. Performance evaluation of household refrigerators running with r600a contaminated with non-condensable gases. **International Journal of Refrigeration**, Elsevier, v. 111, p. 86–93, 2020.

FAHY, F. J.; GARDONIO, P. **Sound and structural vibration: radiation, transmission and response**. : Elsevier, 2007.

FANG, X. Flow calculations for fixed-area expansion devices. **ASHRAE Transactions**, American Society of Heating, Refrigeration and Air Conditioning Engineers, Inc., v. 107, p. 130, 2001.

FRIEDEL, L. Improved friction pressure drop correlation for horizontal and vertical two-phase pipe flow. In: . 1979.

GAO, Z.-K.; JIN, N.-D.; WANG, W.-X. **Nonlinear analysis of gas-water/oil-water two-phase flow in complex networks**. : Springer Science & Business Media, 2013.

GERGES, S. N. Ruído: fundamentos e controle. In: **Ruído: fundamentos e controle**. 1992.

GNIELINSKI, V. New equations for heat and mass transfer in turbulent pipe and channel flow. **Int. Chem. Eng.**, v. 16, n. 2, p. 359–368, 1976.

GRÖNNERUD, R. Investigation of liquid hold-up, flow-resistance and heat transfer in circulation type evaporators, part iv: two-phase flow resistance in boiling refrigerants. **Bull. De l'Inst. Du Froid, Annexe**, v. 1, 1972.

HAJAL, J. E.; THOME, J. R.; CAVALLINI, A. Condensation in horizontal tubes, part 1: two-phase flow pattern map. **International Journal of Heat and Mass Transfer**, v. 46, n. 18, p. 3349–3363, 2003.

HAN, H. S. et al. Experimental analysis for reducing refrigerant-induced noise of 4-way cassette type air conditioner. **Journal of Mechanical Science and Technology**, v. 23, n. 5, p. 1456–1467, 2009.

HAN, H. S.; JEONG, W. B.; KIM, M. S. Frequency characteristics of the noise of r600a refrigerant flowing in a pipe with intermittent flow pattern. **International journal of refrigeration**, v. 34, n. 6, p. 1497–1506, 2011.

HAN, H. S. et al. Analysis of the root causes of refrigerant-induced noise in refrigerators. **Journal of Mechanical Science and Technology**, v. 23, n. 12, p. 3245–3256, 2009.

____. Reduction of the refrigerant-induced noise from the evaporator-inlet pipe in a refrigerator. **International Journal of Refrigeration**, Elsevier, v. 33, n. 7, p. 1478–1488, 2010.

HANSEN, C. H. Fundamentals of acoustics. **Occupational Exposure to Noise: Evaluation, Prevention and Control. World Health Organization**, p. 38–39, 2001.

HARRISON, M. **Vehicle refinement: controlling noise and vibration in road vehicles**. : Elsevier, 2004.

HARTMANN, D.; MELO, C. Popping noise in household refrigerators: Fundamentals and practical solutions. **Applied Thermal Engineering**, v. 51, n. 1-2, p. 40–47, 2013.

HEWITT, G. F.; ROBERTS, D. **Studies of two-phase flow patterns by simultaneous x-ray and flast photography**. 1969.

HIRAKUNI, S. et al. Noise reduction technology with porous metal for refrigerant two-phase flow through the expansion valve. In: **International Refrigeration and Air Conditioning Conference, Indiana at Purdue. West Lafayette, USA**. 2004.

HUANG, H. Numerical simulation of throttling noise of electronic expansion valve. **Hangzhou: Zhejiang Sci-Tech University**, 2015.

ISHII, K.; WATANABE, N. Shock wave generation by collapse of an explosive bubble in water. **Proceedings of the Combustion Institute**, 2018.

ISO:12001. **Acoustics - Noise emitted by machinery and equipment - Rules for the drafting and presentation of a noise test code**. 1996.

ISO12354-1. **Building acoustics – Estimation of acoustic performance of buildings from the performance of elements – Part 1: Airborne sound insulation between rooms**. 2000.

JEON, J. Y.; YOU, J.; CHANG, H. Y. Sound radiation and sound quality characteristics of refrigerator noise in real living environments. **Applied Acoustics**, Elsevier, v. 68, n. 10, p. 1118–1134, 2007.

JEONG, W. B. et al. Experimental study of the effects of the cycle characteristics on the refrigerant-induced noise in system air-conditioner. **Journal of Mechanical Science and Technology**, v. 21, n. 7, p. 1112–1119, 2007.

KANDLIKAR, S. G. Fundamental issues related to flow boiling in minichannels and microchannels. **Experimental Thermal and Fluid Science**, v. 26, n. 2-4, p. 389–407, 2002.

KANIZAWA, F. T. **Estudo teórico e experimental sobre padrões de escoamento, fração de vazio e perda de pressão durante escoamento bifásico água-ar cruzado ascendente externo a banco de tubos**. 2014. Tese (Doutorado) — Universidade de São Paulo, 2014.

KIM, G. et al. Flow visualization and noise measurement of r410a two-phase flow near electric expansion valve for heating cycle of multi-split air-source heat pump. **Applied Thermal Engineering**, v. 33, n. 7, p. 1478–1488, 2019.

KIM, G.; SONG, S. Noise reduction of refrigerant two-phase flow using flow conditioners near the electric expansion valve. **Journal of Mechanical Science and Technology**, Springer, v. 34, n. 2, p. 719–725, 2020.

KIM, M. S.; JEONG, W. B.; HAN, H. S. Development of noise pattern map for predicting refrigerant-induced noise in refrigerators. **Journal of Mechanical Science and Technology**, Springer, v. 28, n. 9, p. 3499–3510, 2014.

KIM, S. J.; SUNG, H. J. Design of the solenoid valve of an antilock braking system with reduced flow noise. **Journal of Fluids Engineering**, American Society of Mechanical Engineers Digital Collection, v. 140, n. 3, 2018.

KIM, Y.; O'NEAL, D. A comparison of critical flow models for estimating two-phase flow of hcfc22 and hfc134a through short tube orifices. **International Journal of Refrigeration**, v. 18, n. 7, p. 447–455, 1995.

KNABBEN, F. T.; MELO, C.; HERMES, C. J. A study of flow characteristics of electronic expansion valves for household refrigeration applications. **International Journal of Refrigeration**, v. 113, p. 1–9, 2020.

KOBERSTEIN, M. et al. Flow-induced whistle in the joint of thermal expansion valve and suction tube in automotive refrigerant system. **SAE International Journal of Passenger Cars-Mechanical Systems**, v. 8, n. 2015-01-2275, p. 973–976, 2015.

LEISSA, A. W. **Vibration of plates**. 1969.

____. The free vibration of rectangular plates. **Journal of sound and vibration**, Elsevier, v. 31, n. 3, p. 257–293, 1973.

LEPPINGTON, F. G.; BROADBENT, E. G.; HERON, K. The acoustic radiation efficiency of rectangular panels. **Proceedings of the Royal Society of London A**, v. 382, n. 1783, p. 245–271, 1982.

LEVINE, H. On the short wave acoustic radiation from planar panels or beams of rectangular shape. **The Journal of the Acoustical Society of America**, ASA, v. 76, n. 2, p. 608–615, 1984.

LI, W.; GIBELING, H. Determination of the mutual radiation resistances of a rectangular plate and their impact on the radiated sound power. **Journal of Sound and Vibration**, v. 229, n. 5, p. 1213–1233, 2000.

LI, Y. et al. Spray morphology transformation of propane, n-hexane and iso-octane under flash-boiling conditions. **Fuel**, v. 236, p. 677–685, 2019.

LIGHTHILL, M. J. Jet noise. **AIAA Journal**, v. 1, n. 7, p. 1507–1517, 1963.

LIU, J. et al. Experimentation and correlation of r744 two-phase flow through short tubes. **Experimental thermal and fluid science**, v. 28, n. 6, p. 565–573, 2004.

LIU, Y.; DONG, Y.; ZHAO, L. Comparison of noise calculation methods of air conditioning duct system used in china and usa. **Procedia Engineering**, v. 205, p. 1592–1599, 2017.

LIU, Z. et al. Flow-induced gurgling noise in automotive refrigerant systems. **SAE International Journal of Passenger Cars-Mechanical Systems**, v. 8, n. 2015-01-2276, p. 977–981, 2015.

LORBEK, L. et al. Two-phase flow patterns in adiabatic refrigerant flow through capillary tubes. **International Journal of Refrigeration**, v. 115, p. 107–116, 2020.

LU, X.; LIU, J.; XU, X. Contact angle measurements of pure refrigerants. **International Journal of Heat and Mass Transfer**, Elsevier, v. 102, p. 877–883, 2016.

MCLEVIGE, S. M.; MILLER, N. **Experimental investigation of the source of acoustic bursts produced by household refrigerators**. 2001.

MINNAERT, M. Xvi. on musical air-bubbles and the sounds of running water. **The London, Edinburgh, and Dublin Philosophical Magazine and Journal of Science**, Taylor & Francis, v. 16, n. 104, p. 235–248, 1933.

MOFFAT, R. J. Describing the uncertainties in experimental results. **Experimental Thermal and Fluid Science**, Elsevier, v. 1, n. 1, p. 3–17, 1988.

MOGAJI, T. S. **Theoretical and experimental study on convective boiling inside tubes containing twisted-tape inserts**. 2014. Tese (Doutorado) — Universidade de São Paulo, 2014.

MOREIRA, T. A. **Two-phase flow constructive parameters characterization, and heat transfer performance of hydrocarbons and their mixtures during condensation**. 2021. Tese (Doutorado) — Universidade de São Paulo, 2021.

MÜLLER-STEINHAGEN, H.; HECK, K. A simple friction pressure drop correlation for two-phase flow in pipes. **Chemical Engineering and Processing: Process Intensification**, v. 20, n. 6, p. 297–308, 1986.

NAKANO, M.; OUTA, E.; TAJIMA, K. Noise and vibration related to the patterns of supersonic annular flow in a pressure reducing gas valve. **Journal of Fluids Engineering**, 1988.

NILPUENG, K.; WONGWISES, S. Experimental investigation of two-phase flow characteristics of hfc-134a through short-tube orifices. **International Journal of Refrigeration**, Elsevier, v. 32, n. 5, p. 854–864, 2009.

____. A review of numerical modelling studies on short-tube orifice performance with applications to air-conditioning systems. **International Journal of Refrigeration**, v. 35, n. 4, p. 740–749, 2012.

NOVAK, A. **Studies of Sound Insulation in Buildings**. 1995.

OGUZ, H.; PROSPERETTI, A. The natural frequency of oscillation of gas bubbles in tubes. **The Journal of the Acoustical Society of America**, ASA, v. 103, n. 6, p. 3301–3308, 1998.

OLIVEIRA, G. H. d. S. **Análise experimental da ebulição convectiva de hidrocarbonetos e suas misturas zeotrópicas no interior de tubos horizontais**. 2021. Tese (Doutorado) — Universidade de São Paulo, 2021.

ONG, C. L.; THOME, J. Macro-to-microchannel transition in two-phase flow: Part 1–two-phase flow patterns and film thickness measurements. **Experimental Thermal and Fluid Science**, v. 35, n. 1, p. 37–47, 2011.

OSHINOWO, T.; CHARLES, M. Vertical two-phase flow part i. flow pattern correlations. **the Canadian Journal of Chemical Engineering**, v. 52, n. 1, p. 25–35, 1974.

PAN, L.-m. et al. Numerical investigation of vapor bubble condensation characteristics of subcooled flow boiling in vertical rectangular channel. **Nuclear Engineering and Design**, v. 248, p. 126–136, 2012.

REETHOF, G. Control valve and regulator noise generation, propagation, and reduction. **Noise Control Engineering**, v. 9, n. 2, p. 74–85, 1977.

____. Turbulence-generated noise in pipe flow. **Annual Review of Fluid Mechanics**, v. 10, n. 1, p. 333–367, 1978.

REVELLIN, R. et al. Characterization of diabatic two-phase flows in microchannels: Flow parameter results for r-134a in a 0.5 mm channel. **International Journal of Multiphase Flow**, v. 32, n. 7, p. 755–774, 2006.

REVELLIN, R.; THOME, J. A new type of diabatic flow pattern map for boiling heat transfer in microchannels. **Journal of Micromechanics and Microengineering**, v. 17, n. 4, p. 788, 2007.

RIBATSKI, G. A critical overview on the recent literature concerning flow boiling and two-phase flows inside micro-scale channels. **Experimental Heat Transfer**, v. 26, n. 2-3, p. 198–246, 2013.

RUEBELING, J.; GROHMANN, S. Flow-induced noise generation at the outlet of a capillary tube. **International Journal of Refrigeration**, v. 111, p. 188–196, 2020.

SARAVANAN, A. L.; LAL, D. M.; SELVAM, C. Experimental investigation on the performance of condenser for charge reduction of hc-290 in a split air-conditioning system. **Heat Transfer Engineering**, v. 41, n. 17, p. 1499–1511, 2020.

SEWELL, E. Transmission of reverberant sound through a single-leaf partition surrounded by an infinite rigid baffle. **Journal of Sound and Vibration**, v. 12, n. 1, p. 21–32, 1970.

SHAH, R. K. Automotive air-conditioning systems—historical developments, the state of technology, and future trends. **Heat Transfer Engineering**, v. 30, n. 9, p. 720–735, 2009.

Simões-Moreira and Bullard. Pressure drop and flashing mechanisms in refrigerant expansion devices. **International Journal of Refrigeration**, v. 26, n. 7, p. 840–848, 2003.

SINGH, G. M. et al. **Noise generation from expansion devices in refrigerant**. 1999.

SNYDER, S. D.; TANAKA, N. Calculating total acoustic power output using modal radiation efficiencies. **The Journal of the Acoustical Society of America**, ASA, v. 97, n. 3, p. 1702–1709, 1995.

SOETA, Y.; SHIMOKURA, R. Sound quality evaluation of air-conditioner noise based on factors of the autocorrelation function. **Applied Acoustics**, v. 124, p. 11–19, 2017.

SUN, P. et al. Auditory fatigue model applications to predict noise induced hearing loss in human and chinchilla. **Applied Acoustics**, v. 119, p. 57–65, 2017.

SUPPONEN, O. et al. Shock waves from nonspherical cavitation bubbles. **Physical Review Fluids**, APS, v. 2, n. 9, p. 093601, 2017.

TAITEL, Y.; BARNEA, D.; DUKLER, A. Modelling flow pattern transitions for steady upward gas-liquid flow in vertical tubes. **AIChE Journal**, v. 26, n. 3, p. 345–354, 1980.

TAITEL, Y.; DUKLER, A. A model for predicting flow regime transitions in horizontal and near horizontal gas-liquid flow. **AIChE Journal**, v. 22, n. 1, p. 47–55, 1976.

TANNERT, T.; HESSE, U. Noise effects in capillary tubes caused by refrigerant flow. In: **16th International Refrigeration and Air Conditioning Conference at Purdue. West Lafayette, USA**. 2016.

THOME, J. R. **Engineering Data Book III**. : Wolverine Tube, 2004.

TIBIRIÇÁ, C. B.; CZELUSNIAK, L. E.; RIBATSKI, G. Critical heat flux in a 0.38 mm microchannel and actions for suppression of flow boiling instabilities. **Experimental Thermal and Fluid Science**, v. 67, p. 48–56, 2015.

TIBIRIÇÁ, C. B.; RIBATSKI, G. Flow patterns and bubble departure fundamental characteristics during flow boiling in microscale channels. **Experimental Thermal and Fluid Science**, v. 59, p. 152–165, 2014.

TREVOR, J.; D'ANTONIO, P. **Acoustic absorbers and diffusers**. : Taylor & Francis, 2009.

TUZE, E.; K, E.; M, C. Sound quality characteristics of refrigerators. In: **International NTER-NOISE and NOISE-CON Congress and Conference. Seoul, South Korea**. 2020.

UMEDA, T. Noise caused by gas-liquid two-phase flow with single large gas bubble through an orifice (1st report, experimental study using air-water two phase flow). **Japanese Society Mechanical Engineering**, v. 60, p. 56–63, 1994.

VALES, L. F. **Análise numérica da influência de parâmetros estruturais no desempenho vibroacústico de placas flexíveis**. 2017. Dissertação (Mestrado) — Universidade de São Paulo, 2017.

VER, I.; ENCLOSURES, C.; WRAPPINGS, N. **Vibration Control Engineering, Principles and Applications, Ver, IL and Beranek, LL**. : Wiley, Hoboken, New Jersey, 2006.

VIGRAN, T. E. **Building acoustics**. : CRC Press, 2008.

WALLACE, C. Radiation resistance of a rectangular panel. **The Journal of the Acoustical Society of America**, ASA, v. 51, n. 3B, p. 946–952, 1972.

WANG, G.; CHENG, P.; BERGLES, A. Effects of inlet/outlet configurations on flow boiling instability in parallel microchannels. **International Journal of Heat and Mass Transfer**, Elsevier, v. 51, n. 9-10, p. 2267–2281, 2008.

WANG, Q. et al. Experimental study of vapor supercavitation suppression of capillary outlet jet noise. **Journal of Mathematics**, 2021.

WANG, X.-S. et al. Experimental study on the relation between internal flow and flashing spray characteristics of r134a using straight tube nozzles. **International Journal of Heat and Mass Transfer**, v. 115, p. 524–536, 2017.

WEI, C.-S.; LIN, Y.-T.; WANG, C.-C. A performance comparison between coiled and straight capillary tubes. **Heat Transfer Engineering**, v. 21, n. 2, p. 62–66, 2000.

WEI, L. et al. Numerical simulation of flow-induced noise in high pressure reducing valve. **PloS one**, v. 10, n. 6, 2015.

XIA, Y. et al. Experimental study on reducing the noise of horizontal household freezers. **Applied Thermal Engineering**, v. 68, n. 1-2, p. 107–114, 2014.

ZHANG, C.; LI, K.; WANG, J. Numerical simulation of gas-liquid two-phase flow noise. **Mineral Engineering Research**, School of Civil Engineering, Hunan University of Science and Technology, v. 31, n. 1, 2017.

ZHANG, Y.; ELBEL, S. Experimental analysis to mitigate flow induced noise in expansion devices. In: . : International Refrigeration and Air Conditioning Conference, Indiana at Purdue. Indiana, USA, 2018.

ZHANG, Y.; LIU, Y.-c. Progress in two-phase flow-induced noise of small scale refrigeration system. **Journal of ZheJiang University**, v. 55, n. 4, p. 775–792, 2021.

ZHAO, B.; WU, C. J. Sound quality evaluation of electronic expansion valve using gaussian restricted boltzmann machines based dbn. **Applied Acoustics**, v. 170, p. 107493, 2020.

ZHIFU, Z. et al. An experimental study on the spray and thermal characteristics of r134a two-phase flashing spray. **International Journal of Heat and Mass Transfer**, v. 55, n. 15-16, p. 4460–4468, 2012.

ZWICKER, E.; FASTL, H. **Psychoacoustics: Facts and models**. 2013. v. 22.

Appendix

APPENDIX A – FUNDAMENTALS

A.1 Fundamentals of two-phase flow

In this chapter, the definitions and the terminology usually employed to describe the gas-liquid flow are presented. Also, the flow pattern occurring in macro and microscale channels are described.

A.1.1 Definitions and terminology of two-phase flow

This section introduces the primary variables employed to describe gas-liquid flow. Figure 68 illustrates a schematic of a gas-liquid flow inside an inclined channel. The subscripts 'g' and 'l' denote the gas and the liquid phases, respectively. The infinitesimal channel length is denoted by dz.

Figure 68 – Two-phase flow.

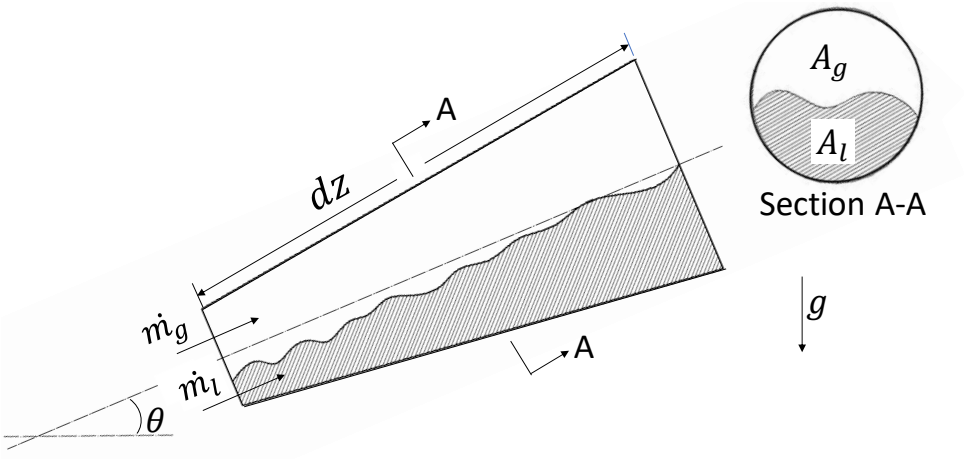

Source: Author

Mass flow rate

The total mass flow rate ($\dot{m}$) is given as the sum of the mass flow rate of the liquid ($\dot{m}_l$) and gas phase ($\dot{m}_g$) as follows:

$$\dot{m} = \dot{m}_l + \dot{m}_g \tag{A.1}$$

The mass flow rates of each phase are determined as a function of vapor quality x assuming thermodynamic equilibrium, as follows:

$$\dot{m}_l = (1 - x)\dot{m} \tag{A.2}$$

$$\dot{m}_g = x\dot{m} \tag{A.3}$$

Vapor quality

The vapor quality associated to the parcel of the mixture flowing as vapor, $x_{\dot{m}}$, is defined as the ratio between the gas mass flow rate and the total mass flow rate, as follows:

$$x_{\dot{m}} = \frac{\dot{m}_g}{\dot{m}} \tag{A.4}$$

The vapor quality is also defined based on the local enthalpy, and it is named as the equilibrium thermodynamic vapour quality x_i. This definition is useful for non-equilibrium thermodynamic state such as observed in boiling and condensation process under subcooled and superheated conditions. The equilibrium thermodynamic vapor quality is defined as follows:

$$x_i = \frac{i_{2\varphi} - i_{l_{sat}}}{i_{lg_{sat}}} \tag{A.5}$$

where $i_{2\varphi}$ is the local enthalpy of two-phase mixture, $i_{l_{sat}}$ is the local enthalpy of the saturated liquid, and $i_{lg_{sat}}$ is the local vaporization enthalpy. The equilibrium thermodynamic vapor quality assumes negative values under subcooled conditions and values greater than one for superheated conditions. Under thermodynamic equilibrium conditions the vapour quality related to the mass flow is equal to thermodynamic vapor quality.

Mass velocity

The mass velocity $\dot{G}$ of each phase is calculated as the the ratio between the mass flow rate of each phase and the channel cross-sectional area A:

$$G_l = \frac{\dot{m}_l}{A} \tag{A.6}$$

$$G_g = \frac{\dot{m}_g}{A} \tag{A.7}$$

The total mass velocity is given as the sum of the mass velocity of each component:

$$G = G_l + G_g \tag{A.8}$$

Superficial void fraction

The superficial void fraction α is a necessary parameter to characterize the two-phase flow. Its value allows to evaluate the mixture density and viscosity, two-phase velocity, flow pattern transitions coefficient, heat transfer and pressure drop (THOME, 2004). The void fraction is defined as the ratio between the temporal average channel cross-sectional area occupied by the gas phase and the channel cross-sectional area, as follows:

$$\alpha = \frac{A_g}{A} = \frac{A_g}{A_l + A_g} \tag{A.9}$$

The void fraction assumes values between zero and one, corresponding to only liquid and vapor flows, respectively.

A.1.2 Two-phase flow patterns

Gas-liquid flowing in a pipe may assume different distribution along the channel. Flow patterns are commonly determined visually based on flow images captured by a photo camera or a high speed video camera. Both may result in a high degree of subjectivity depending on the observer judgement. Some objectives methods based on signal analyses (X-ray, γ-ray, optical, wire-mesh, acoustic) are also employed to characterize the flow pattern. As indicated by Cheng, Ribatski and Thome (2008), the two-phase flow patterns are dependent on conditions such as channel geometry and size (macro and microscale), flow orientation, and two-phase flow parameters such as mass velocity, fluid physical properties and heat flux. A great number of studies concerning two-phase flow pattern transitions led to the development of different flow pattern prediction methods for diabatic and adiabatic flow conditions. The characterization of two-phase flow patterns is an important aspect because they are intrinsically related to the heat transfer and pressure drop behavior under flow boiling conditions. The flow patterns are also employed to cross-correlate it to the flow-induced noise and acceleration of the expansion device. The most common two-phase flow patterns occurring in macro and microscale channels are described in the following sub-sections.

Flow pattern in macrochannel

Figure 69 illustrates the flow patterns commonly observed for adiabatic vertical upwards flow according to Collier and Thome (1996).

Figure 69 – Flow patterns in a vertical co-current flow.

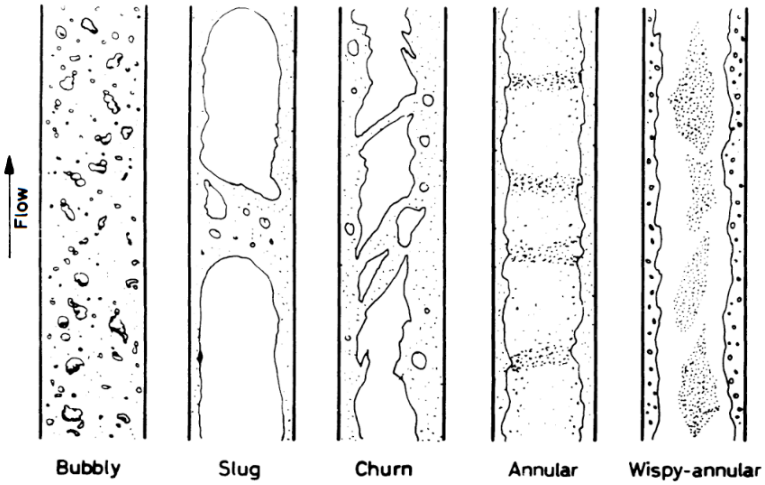

Source: Collier and Thome (1996).

- **Bubbly flow**: The bubbly flow is characterized by discrete small bubbles of gas (vapor) with characteristic dimension inferior to the pipe diameter distributed within a continuous liquid phase. This flow-pattern is verified for low vapor qualities. According to Taitel, Barnea and Dukler (1980), bubbles with diameter inferior to 15 mm behave as rigid sphere rising in a linear motion. However, for diameter greater than this, the bubbles become deformed rising in a randomness motion colliding and coalescing, forming larger bubbles similar to Taylor bubbles.

- **Slug flow**: The upper end of the bubble is similar to a spherical cap, while the lower part approach to a flat surface. The bubbles are separated by liquid slugs, which may contain small gas bubbles. The length of the main gas bubble may considerably vary.

- **Churn flow**: As the velocity of the two-phase flow mixture increases, the slug structure becomes unstable leading to the larger bubbles breakdown. This instability results in a complete destruction of the slug flow deriving in a irregular and chaotic flow named churned flow. The churn flow is also oscillatory, associated with the moving of liquid phase alternately upward and downward in the channel (GAO; JIN; WANG, 2013). This flow pattern is also referenced as semi-annular flow or slug-annular flow (COLLIER; THOME, 1996).

- **Annular flow**: The annular flow pattern is characterized by a continuous gas flow along the pipe core and a liquid film flowing on the channel wall. This flow pattern is verified for high gas velocities. Large amplitudes of liquid waves are usually present on the liquid film interface and the continuous break up of these waves lead to a liquid phase entrained as droplets within the gas core.

- **Wispy-annular flow**: Wispy-annular flow was first identified by Bennett et al. (1965). These authors noted that if the mass velocity is further increased under annular flow condition a considerably amount of liquid within the gas core may be observed.

The flow patterns in a adiabatic horizontal pipes present asymmetric distributions of the phases due to the gravitational effect. Figure 70 illustrates the flow patterns generally observed for horizontal flows.

- **Bubbly flow**: This flow flow pattern is similar to the vertical flow except for the tendency of the bubbles to flow in the upper part of the channel.

- **Plug flow**: Plug flow is somewhat similar to slug flow in vertical channels. Under horizontal flow, the bubbles tend to travel in the upper part of the channel leading to a thicker liquid film at the bottom of the channel. In addition, the nose of the bubble is asymmetric.

- **Stratified flow**: This flow pattern occurs under conditions of low liquid and vapour velocities. Stratified flows are dominated by the gravitational effects with the liquid phase flowing at the bottom part of the pipe. A smooth interface separates the phases.
- **Wavy flow**: As the gas flow velocity increases, waves are formed on the gas-liquid interface.
- **Slug flow**: As the gas velocity further increases from wavy flow, the waves become high enough to reach the top of the channel propagating at high velocity. These waves leave a liquid film wetting the superior part of the channel, which is dragged by gas phase.
- **Annular flow**: Under horizontal flow the liquid film is thicker on the bottom part of the channel due to the gravitational force.

Figure 70 – Flow patterns in horizontal tubes.

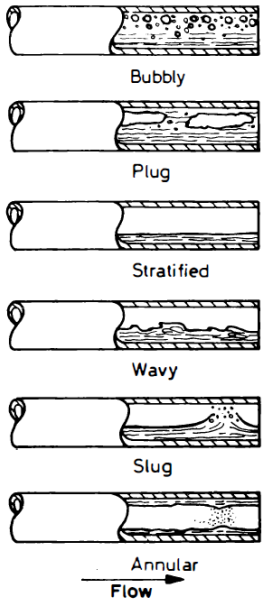

Source: Collier and Thome (1996).

A.2 Fundamentals of acoustics

In this item, the definitions and terminologies used to the main acoustic parameters are presented. It is also discussed the sound transmission loss for a single layer element by excitation of airborne sound.

A.2.1 Sound field definition (ISO:12001, 1996)

- **Free field**: is a region in space where sound propagates free of obstructions and reflections.

- **Near field**: is defined as a region close to the source where the sound pressure and the acoustic particle are not in phase. In this region, the sound does not decrease by 6 dB as the distance from the source is increased, as it does in the far field. The near field is restricted to a distance from the source equal to about a wavelength of the sound, or equal to three times the largest dimension of the sound source.

- **Far field**: the far field begins where the near field ends, and extend to the infinity. In the far field region, the sound field radiated by the most machines decreases 6 dB as the distance from the source is doubled.

- **Direct field**: is the region where the sound field has not suffered any reflection, that is, the sound measured in this region is attributed to the sound source itself.

- **Reverberant field**: is defined as a sound wave that suffered at least one reflection from a boundary of the room.

A.2.2 Sound transmission

Sound is a vibration that propagates as a wave of pressure through a transmission medium such as gas, liquid, or solid. Individual particles are not transmitted with the wave, but the propagation of the wave causes particles to oscillate around an equilibrium position. During the propagation, a wave that strikes a surface can be transmitted, absorbed, or reflected; the amount of energy that is divided into transmission, absorption, and reflection depends on the surface acoustics properties. Figure 71 illustrates temporal and spatial characteristics of absorption, reflection and diffusion.

The reflection of sound waves can be either reflected by a flat surface (specular reflection) or scattered by a diffusing surface. For flat surfaces, the incidence angle of the sound wave is equal to the reflected angle. According to Hansen (2001), the amount of energy absorbed depends on the characteristics of the obstacle. A hard, compact, and smooth surface will reflect more, and absorb less acoustic energy than a porous and soft surface. For a room built with material that reflects the incident sound, the wave produced by the source will bounce from one to another boundary giving origin to the reflected sound, this phenomenon is called reverberation. A receiver in this room will receive sound not only from the direct source but also from the boundary reflections, resulting in a sound level higher than the sound produced by the source. As the surface becomes less reflective and absorb more sound wave, the room tends to a situation of "free field" where only the significant noise is from the sound source, such place is named as anechoic chamber.

Figure 72 illustrates different forms of sound transmission from one room to another based on airborne sound. The sound transmission varies depending on the wall composition. The complexity of the prediction methods increases as the number of the wall layers is increased, and also when these layers are mechanically coupled.

Figure 71 – Temporal and spatial characteristics of absorption, reflection and diffusion.

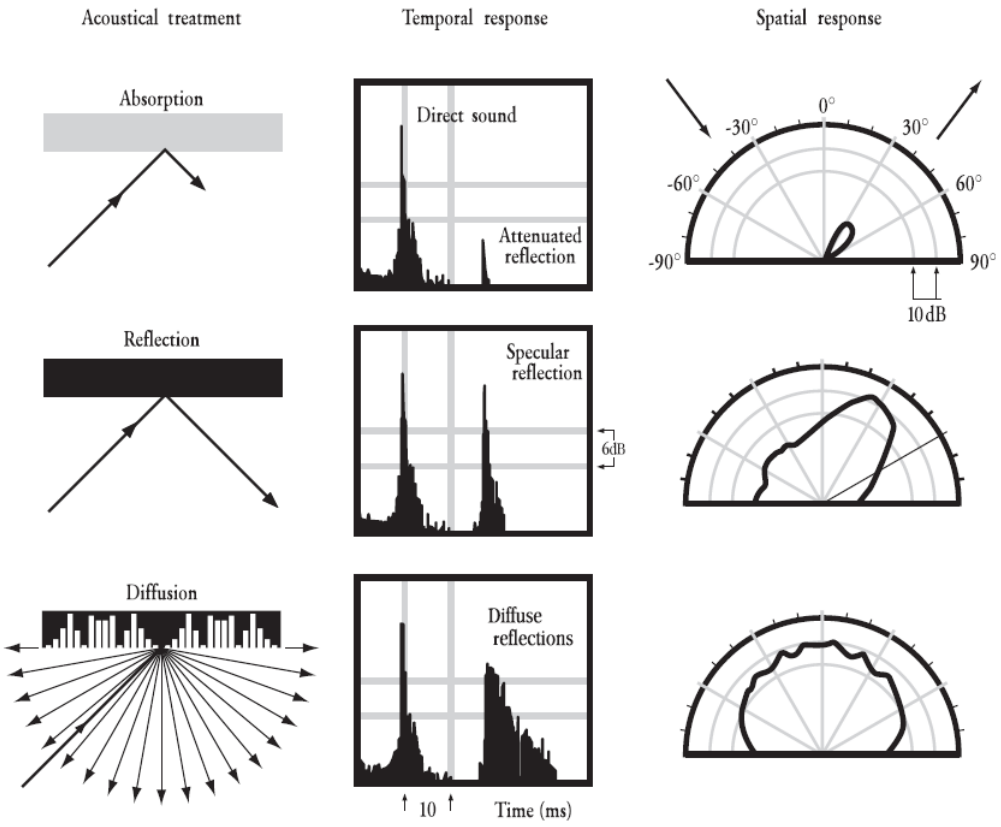

Source: Trevor and D'Antonio (2009)

Figure 72 – Sound transmission paths between rooms.

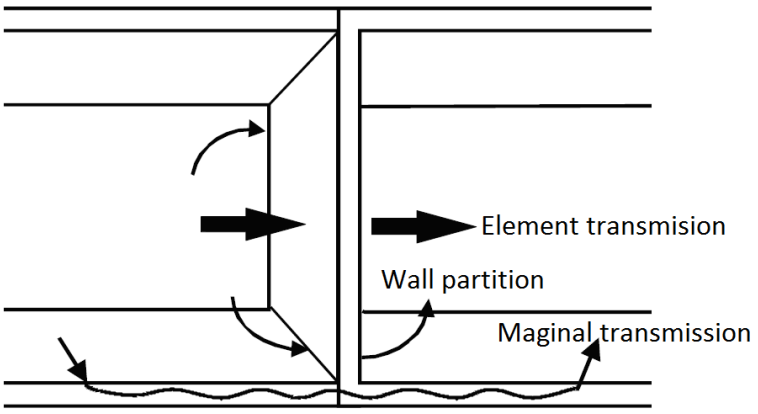

Source: Adapted from Vigran (2008)

A.2.3 Definitions and terminology of acoustics

This section introduces the acoustics fundamentals, and relate them to noise evaluation and its prevention. Figure 73 illustrates a sound propagation as a longitudinal wave, involving a succession of compression and rarefaction in a elastic medium.

Figure 73 – Longitudinal sound wave propagation.

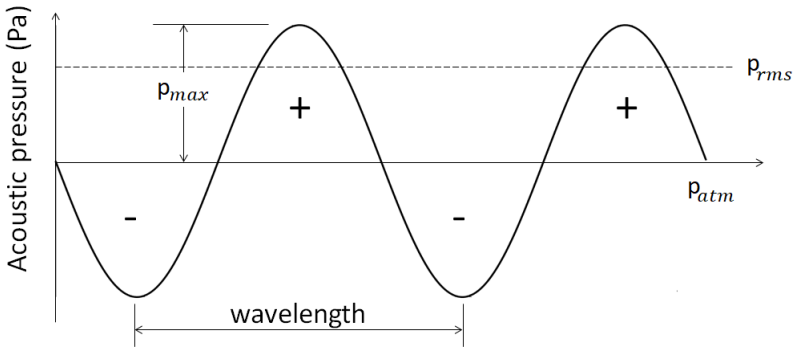

Source: Adapted from Hansen (2001)

Amplitude

Amplitude is defined as the maximum pressure (p_{max}) disturbance of the medium from its equilibrium, therefore , its value corresponds to the half of the pressure difference between maximum compression and maximum rarefaction.

Acoustic pressure

The acoustic pressure can be characterized as the root-mean-square pressure p_{rms}, that is defined as the square root of the average of the square of the pressure of the sound signal over a cycle.

Frequency

Frequency $\dot{f}$ is the number of pressure variation cycles per unit of time, or simply, the number of cycles per seconds, and is expressed in Hertz (Hz).

Wavelength

Wavelength λ is defined as the distance between two successive crests or valleys of a wave.

Period

Period is defined as the time taken for one cycle of oscillation at a fixed position.

Speed of sound

The speed of sound (c) for fluids in general, is given by the Newton-Laplace equation, as follows:

$$c = \sqrt{\frac{K}{\rho}} \tag{A.10}$$

where K is the bulk modulus. The speed propagation of sound in air is 342 m/s at 20°C and 1 atmosphere pressure. Alternatively, the speed of sound may be written using the equation of state of gases, as follows:

$$c = \sqrt{kRTM} \tag{A.11}$$

where k is the polytropic index (c_p/c_v), R is the universal gas constant (approximately 8314.5 J/molK), T is the absolute temperature, and M is the molar mass of the gas (g/mol).

Wave number

The wave number $\varkappa$ in the medium (air) around a plate is defined as follows:

$$\varkappa_{air} = \frac{\omega}{c} \tag{A.12}$$

where ω is the angular frequency (rad/s). According to Fahy and Gardonio (2007), the wave number of a plate $\varkappa_p$ is defined as follows:

$$\varkappa_p = \left(\frac{\omega^2 \rho h}{B}\right)^{1/4} \tag{A.13}$$

where B is the bending stiffness (Nm) and h is the wall thickness (m). The bending stiffness is defined as follows:

$$B = \frac{Eh^3}{12(1-\nu^2)} \tag{A.14}$$

where E is the Young Module (Pa), and ν is de Possion' ratio (-).

Critical frequency (coincidence frequency)

The critical frequency $\dot{f}_c$ occurs when the acoustic wavelength incident on the structure is equal to the length of the free bending wave of that structure $\varkappa_{air} = \varkappa_p$. In other words, the phase speed in the solid medium is equal to the phase speed in the surrounding medium (air). At critical frequency the acoustic energy will be transmitted through the material almost without attenuation. The critical frequency for a homogeneous plate is defined as follows:

$$\dot{f}_c = \frac{c^2}{2\pi}\sqrt{\frac{m}{B}} \tag{A.15}$$

where m (kg/m^2) is the mass per unit of area and c is the sound speed (m/s) in the medium surrounding the plate. For homogeneous plate, the critical frequency can be also defined as follows:

$$\dot{f}_c = \frac{c^2}{1.8hc_l} \tag{A.16}$$

where c_l is the longitudinal wave speed in the medium, which is defined as follows:

$$c_l = \sqrt{\frac{E}{\rho(1-\nu^2)}} \tag{A.17}$$

Figure 74 illustrates frequency bands in which bending waves propagate at speeds lower than the speed of sound in a medium, equal to critical frequency, and speeds higher than the speed of sound in a medium.

Figure 74 – Bending wave velocity with frequency.

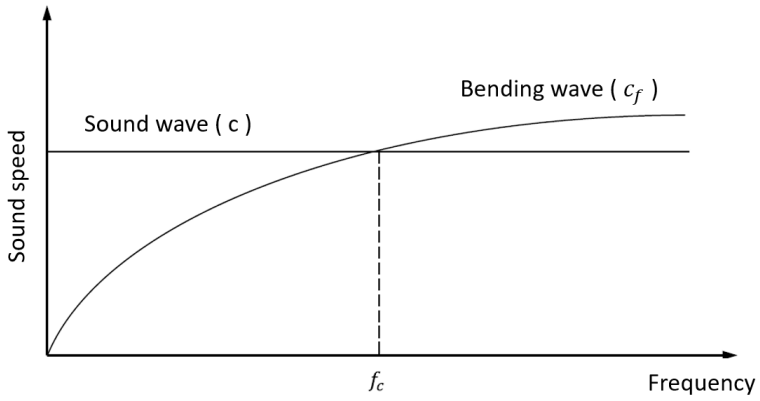

Source: Adapted from Fahy and Gardonio (2007)

- Sub critical frequency: In this case, $\dot{f} < \dot{f}_c$ and $\lambda_{\dot{f}} < \lambda_{air}$. The speed of the mechanical wave is slower than the speed of the acoustic wave, thus cancellation process occurs, and there is no sound radiation for the free field.

- Critical frequency: In this case, $\dot{f} = \dot{f}_c$ and $\lambda_{\dot{f}} = \lambda_{air}$. The velocity of the mechanical wave is equal to the velocity of the acoustic wave, resulting in a acoustic wave parallel to the surface of the plate, thus the maximum sound radiation is transmitted.

- Supercritical frequency: In this case, $\dot{f} > \dot{f}_c$ and $\lambda_{\dot{f}} > \lambda_{air}$. The propagation of the mechanical wave occurs at a speed much greater than the velocity of the acoustic wave, and there is no cancellation resulting in a intense sound radiation.

Sound pressure level

The sound pressure level SPL (dB) is defined as a logarithmic measure of the root-mean-square (rms) pressure of a sound relative to a reference value, as follows:

$$SPL = 20\log\left(\frac{p_{rms}}{p_{ref}}\right) \tag{A.18}$$

where $p_{ref} = 20\mu Pa$ is defined as the minimum threshold of human ear audibility at 1000 Hz.

Sound intensity level and sound power level

The sound intensity I (W/m^2) is defined as the sound power transmitted through a surface area of 1 m^2 perpendicular to the direction of propagation, as illustrated in Fig. 75a.

The sound intensity level I_L (dB) is given by the following equation:

$$I_L = 10\log\left(\frac{I}{I_{ref}}\right) \tag{A.19}$$

where I is the absolute value of the normal sound intensity and I_{ref} is the reference value for the intensity ($10^{-12} W/m^2$), which corresponds to the inferior threshold of human ear audibility for a pure tone of 1000 Hz. The total sound power Π (W) emitted from a given source is calculated by integrating the sound intensity over a surface enclosing the source (Fig. 75b), as follows:

$$\Pi = \oint I(s)\mathbf{n}dA \tag{A.20}$$

Figure 75 – a) power through a surface of area 1 m^2 normal to the direction of wave propagation. b) The sound intensity integrated over a closed surface enclosing the sound source gives the total emitted power of a source.

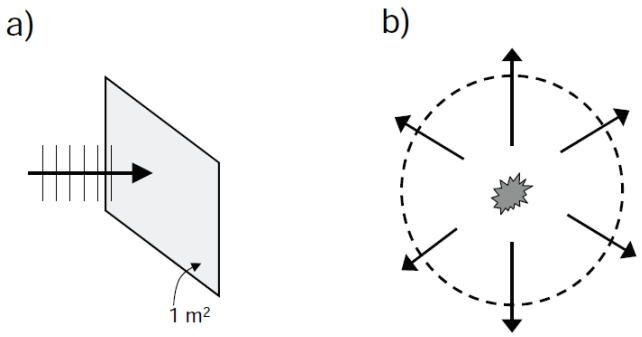

Source: Vigran (2008)

The sound power level L_W (dB) is defined similarly to sound intensity level, as follows:

$$L_W = 10\log\left(\frac{\Pi}{\Pi_{ref}}\right) \tag{A.21}$$

where Π_{ref} is the reference value for the sound power ($10^{-12} W$). Contrary to intensity and sound pressure, power does not depend on the environment or the distance from the source, since it is related to the total energy emitted by the source. For instance, the sound pressure level may change significantly from one to another ambient, since it is closed related to the characteristics of the environment, such as absorption and reflections. The sound power, however, will remain unchanged and, therefore, constitutes an important parameter for the characterization of the noise level generated by a machine or a vibrating structure.

A.2.4 Sound radiation efficiency

The study of the natural vibration modes of a plate is helpful in order to understand the phenomenon of acoustic radiation. Different modes of vibration may result in distinct radiation modes, and the contribution of certain modes may be insignificant for the noise level generated by the structure.This characteristic is associated to the cancellation of the radiation sound power, which occurs when regions of the structure vibrate in opposition phase, resulting in annulment of the sonorous field near the plate. Figure 76 illustrates the flux of radiation energy of a plate in a resonance frequency, for which cancellation phenomenon occurs. In this case, the intensity vector near to the plate may be negative, while the intensity vector is always positive in the open field. In this particular case, the radiated sound power is mainly due to the plate corners.

Figure 76 – Characteristic flow of energy radiated by a rectangular plate in resonance.

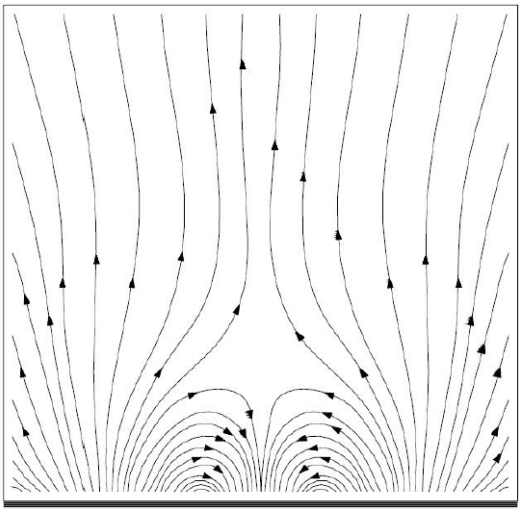

Source: Adapted from Cardoso et al. (2010)

According to Gerges (1992), finite plates radiate sound even in frequencies lower than the critical frequency, such phenomenon is illustrated in Fig. 77. The fluid adjacent to the plate is displaced from a positive (high pressure) to a negative (low pressure) region, as shown by the arrows, while the only significant compression occurs at the ends of the plate. Thus, the acoustic radiation response of a structure depends on the radiation resistance of the structure itself. Therefore, depending on the mode of vibration (either symmetric or antisymmetric), either destructive or constructive, cancellation mechanism of the sound field may occurs, as shown in Fig. 78.

Figure 77 – Sound radiation in a finite plate.

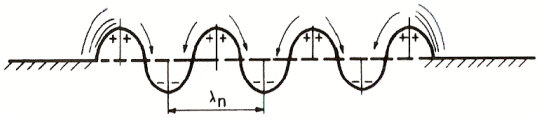

Source: Gerges (1992)

Figure 78 – Mechanism of cancellation of the sound field in vibrating plates.

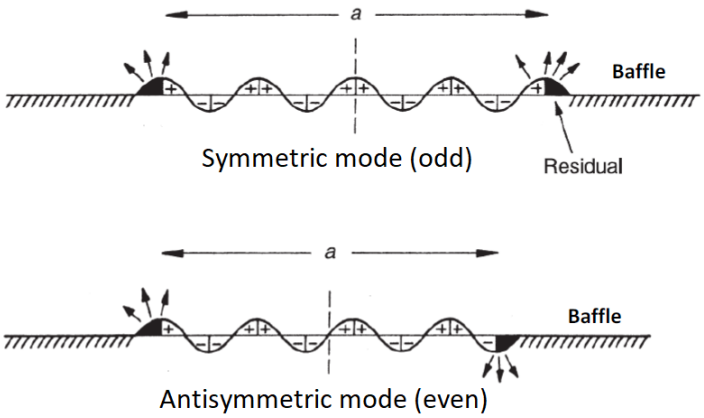

Source: Gerges (1992)

Wallace (1972) developed analytic expressions to estimate the radiation efficiency of rectangular plates valid for acoustic wavelength much larger than the structural wavelengths. Since then, authors have focused on complementing his formulation expanding the frequency limit application (LEPPINGTON; BROADBENT; HERON, 1982; LEVINE, 1984; LI; GIBELING, 2000). Table 11 presents the expressions obtained by Wallace (1972) for each type of vibration mode, where a and b are the dimensions of the plate according to the directions x and y, respectively, m and n are the modal index according to the directions x and y, and ξ is defined as the wavenumber ratio, as follows:

$$\xi = \frac{\varkappa_{air}}{\varkappa_p} \tag{A.22}$$

where $\varkappa_p$ is defined as the wavenumber plate, as follows:

$$\varkappa_p = \left(\frac{m\pi}{a}\right)^2 + \left(\frac{n\pi}{b}\right)^2 \tag{A.23}$$

For a rectangular, homogeneous and free plate on all sides, the natural frequencies can be determined as follows (BLEVINS; PLUNKETT, 1980) :

$$f_{mn} = \frac{1}{2\pi}\left[\frac{Eh^2}{12\rho(1-\nu^2)}\right]^{1/2}\left[\left(\frac{m\pi}{a}\right)^2 + \left(\frac{n\pi}{b}\right)^2\right] \tag{A.24}$$

Figure 79 shows graphically the differences between the modal radiation efficiency values presented in Tab. 12. It is possible to notice that, in general, odd-odd modes present much higher radiation efficiencies than the others. This behaviour is associated to the fact that the destructive cancellation mechanism of the sound field in asymmetric (even) modes occurs more intensely than in symmetric modes (odd). Besides that, the radiation efficiency is reduced for modes superior to 7. Therefore, in the development of acoustic noise control systems, not all

the vibration modes should receive the same importance, since the sound radiates according to distinct magnitude for distinct modes.

Table 11 – Analytic expressions proposed by Wallace (1972) to calculate the modal radiation efficiency of rectangular plates.

Vibration mode	**Radiation efficiency**
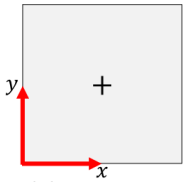 (a) odd- odd	$$\sigma_{mn} \approx \frac{32}{mn\pi^3}\left(\frac{an}{mb}+\frac{mb}{an}\right)\xi^2\left\{1-\left[\left(1-\frac{8}{(m\pi)^2}\right)\frac{a}{b}+\left(1-\frac{8}{(n\pi)^2}\right)\frac{b}{a}\right]\left(\frac{an}{mb}+\frac{mb}{an}\right)\frac{mn\pi}{12}\xi^2\right\} \quad \xi^2 \ll 1 \quad \text{(A.25)}$$
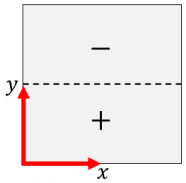 (b) odd - even	$$\sigma_{mn} \approx \frac{8}{3\pi}\left(\frac{an}{mb}+\frac{mb}{an}\right)^2\xi^4\frac{b}{a}\left\{1-\left[\left(1-\frac{8}{(m\pi)^2}\right)\frac{a}{b}+\left(1-\frac{24}{(n\pi)^2}\right)\frac{b}{a}\right]\left(\frac{an}{mb}+\frac{mb}{an}\right)\frac{mn\pi}{20}\xi^2\right\} \quad \xi^2 \ll 1 \quad \text{(A.26)}$$
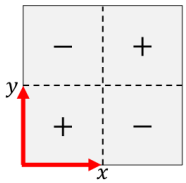 (c) even - even	$$\sigma_{mn} \approx \frac{2mn\pi}{15}\left(\frac{an}{mb}+\frac{mb}{an}\right)^3\xi^6\left\{1-\left[\left(1-\frac{24}{(m\pi)^2}\right)\frac{a}{b}+\left(1-\frac{24}{(n\pi)^2}\right)\frac{b}{a}\right]\left(\frac{an}{mb}+\frac{mb}{an}\right)\frac{5mn\pi}{64}\xi^2\right\} \quad \xi^2 \ll 1 \quad \text{(A.27)}$$
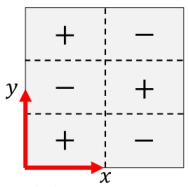 (d) even - odd	$$\sigma_{mn} \approx \frac{8}{3\pi}\left(\frac{mb}{an}+\frac{an}{mb}\right)^2\xi^4\frac{a}{b}\left\{1-\left[\left(1-\frac{8}{(n\pi)^2}\right)\frac{b}{a}+\left(1-\frac{24}{(m\pi)^2}\right)\frac{a}{b}\right]\left(\frac{mb}{an}+\frac{an}{mb}\right)\frac{mn\pi}{20}\xi^2\right\} \quad \xi^2 \ll 1 \quad \text{(A.28)}$$

Source: Author.

Table 12 – Vibration modes, frequencies and radiation efficiencies of a rectangular plate simply supported.

Mode	**(m,n)**	**Freq. [Hz]**	$\sigma_{mn}10^3$
1	(1,1)	77.04	3.86
2	(2,1)	130.04	0.02
3	(3,1)	218.37	1.21
4	(1,2)	255.17	0.02
5	(2,2)	308.17	0.0
6	(4,1)	342.03	0.03
7	(3,2)	396.50	0.01
8	(4,2)	520.16	0.0
9	(1,3)	552.06	3.06
10	(2,3)	605.06	0.04
11	(3,3)	693.39	0.42
12	(4,3)	817.05	0.02

Source: Author.

Figure 79 – Radiation efficiency of rectangular plate.

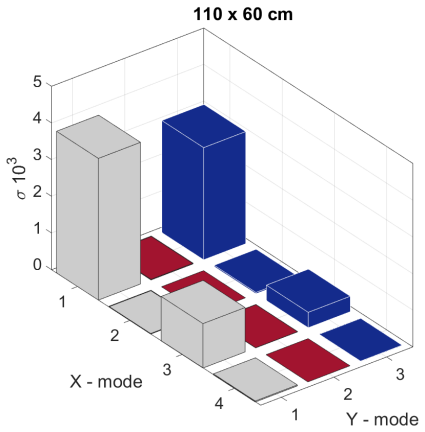

Source: Author.

According to Blevins and Plunkett (1980) , the exact natural frequencies of the first 6 vibrating modes of a rectangular, homogeneous and clamped plate on all sides can be determined by the following expression:

$$f_{mn} = \frac{\lambda_{mn}^2}{2\pi a^2}\left[\frac{Eh^2}{12\rho(1-\nu^2)}\right]^{1/2} \tag{A.29}$$

where λ^2_{mn} is a modal parameter based on the ratio a/b according to (LEISSA, 1973), as shown in Table 13.

Table 13 – Dimensionless frequency coefficient (λ^2_{mn}).

Mode	a/b = 1.0		a/b = 1.5		a/b = 2.5	
	(m,n)	λ^2_{mn}	(m,n)	λ^2_{mn}	(m,n)	λ^2_{mn}
1	(1, 1)	35.992	(1, 1)	60.772	(1, 1)	147.80
2	(2, 1)	73.413	(2, 1)	93.860	(2, 1)	173.85
3	(1, 2)	73.413	(1, 2)	148.82	(3, 1)	221.54
4	(2, 2)	108.27	(3, 1)	149.74	(4, 1)	291.89
5	(3, 1)	131.64	(2, 2)	179.66	(5, 1)	384.71
6	(1, 3)	132.24	(4, 1)	226.92	(1, 2)	394.37

Source: Leissa (1973).

For plates that do not follow the a/b ratios given in Tab. 13, the natural frequency can be obtained based on Rayleigh method (LEISSA, 1969) given as the following expression:

$$f_{mn} = \frac{\pi}{2}\sqrt{\frac{B}{\rho h}}\left\{\frac{\dot{G}_x^4}{a^4} + \frac{\dot{G}_y^4}{b^4} + \frac{2}{a^2b^2}\left[\nu H_x H_y + (1-\nu)J_x J_y\right]\right\} \tag{A.30}$$

where $\dot{G}_x, H_x$ and J_x are functions determined from Tab. 14. The values of $\dot{G}_y, H_y$ and J_y are obtained by replacing x by y and m by n in Eq. A.30.

Table 14 – Dimensionless frequency coefficient.

Mode (m,n)	$\dot{G}_x$	H_x	J_x
1	1.506	1.248	1.248
2,3,4,...	$m+\frac{1}{2}$	$\left(m+\frac{1}{2}\right)\left[1-\frac{2}{\left(m+\frac{1}{2}\right)\pi}\right]$	$\left(m+\frac{1}{2}\right)\left[1-\frac{2}{\left(m+\frac{1}{2}\right)\pi}\right]$

Source: Leissa (1969).

As indicated by Vales (2017), it is also important to know the frequency behaviour of a vibrating structure between modes where there is a significant contribution of two or more vibration modes. In this context, Snyder and Tanaka (1995) developed a set of equations that allows to determine the radiated sound even in frequencies between modes. Later, Li and Gibeling (2000) extended this equation for the whole frequency domain.

A.2.5 Indoor acoustics

In acoustical problems, it is common to verify an acoustic source confined within small cavities to reduce sound irradiation to the external environment. For low frequencies, the length of the acoustic wave is large compared to the dimensions of the cavity and therefore the sound pressure is uniform throughout de cavity. On the other hand, large cavities (or for high frequencies in small cavities), the sound pressure field is no longer uniform and is described deterministically through the modal characteristics of the acoustic cavity. Therefore, the knowledge of the natural modes and frequencies of a cavity is essential to understanding acoustic properties, since it strongly responds to composed sounds of frequencies equal to or close to the natural frequencies.

Characteristic frequencies

In this section, an analytical solution for free oscillations of an rectangular acoustic cavity with rigid walls is developed. According to Fahy and Gardonio (2007), the following hypotheses are assumed: negligible gravitational forces, isotropic, compressive and inviscid fluid. The instantaneous pressure field of the rigid-walled rectangular acoustic cavity with dimensions L_x, L_y and L_z is given as follows:

$$\nabla^2 p(x, y, z, t) - \frac{1}{c^2}\frac{\partial}{\partial t^2} p(x, y, z, t) = 0 \tag{A.31}$$

where $p(x, y, z, t)$ is the instantaneous and local sound pressure at the point (x, y, z), c is the velocity of sound in the fluid, t represents time. In order to solve Eq. A.31, there are several boundary conditions for distinct interactions between fluid-structure described by the acoustic impedance and vibration of the cavity walls (VER; ENCLOSURES; WRAPPINGS, 2006). In the present study, the acoustic cavity owns perfectly rigid walls (zero absorption) thus as a boundary condition the particles velocities are considered null at the walls. Therefore, the acoustic wave equation can be written as follows:

$$\nabla^2 p(x, y, z) - \frac{\omega^2}{c} p(x, y, z) = 0 \tag{A.32}$$

Solving Eq. A.32, the natural frequency for acoustic cavity is defined as follows:

$$f_{ijk} = \frac{c}{2}\sqrt{\left(\frac{i}{L_x}\right)^2 + \left(\frac{j}{L_y}\right)^2 + \left(\frac{k}{L_z}\right)^2} \tag{A.33}$$

where i, j and k are defined as natural numbers related to each frequency mode. According to Gerges (1992), stationary waves in a rectangular acoustic cavity are defined as follows:

- Axial wave : Two indices are zeros, situation in which the wave moves parallel to one of the axes (x, y or z);
- Tangential waves: One of the indices is zero and therefore the waves move parallel to a plane (xy, yz or zx);

- Oblique waves: None of the indices is null and the wave moves in the three directions (x, y, and z).

The knowledge of the natural modes and frequencies of a cavity is essential for understanding it's acoustic properties. For instance, for natural frequency there are higher pressure levels in certain regions of the cavity.

A.2.6 Airborne sound reduction

The sound transmission is exclusively related to the properties of the object under investigation (VALES, 2017). As result, the dependence of sound transmission on a single panel with frequency can be segregated according to five regions (Fig. 80), where each region is defined as a function of the material and of the topology of the studied structure.

Figure 80 – Characteristic curve of sound transmission loss through a homogeneous plate.

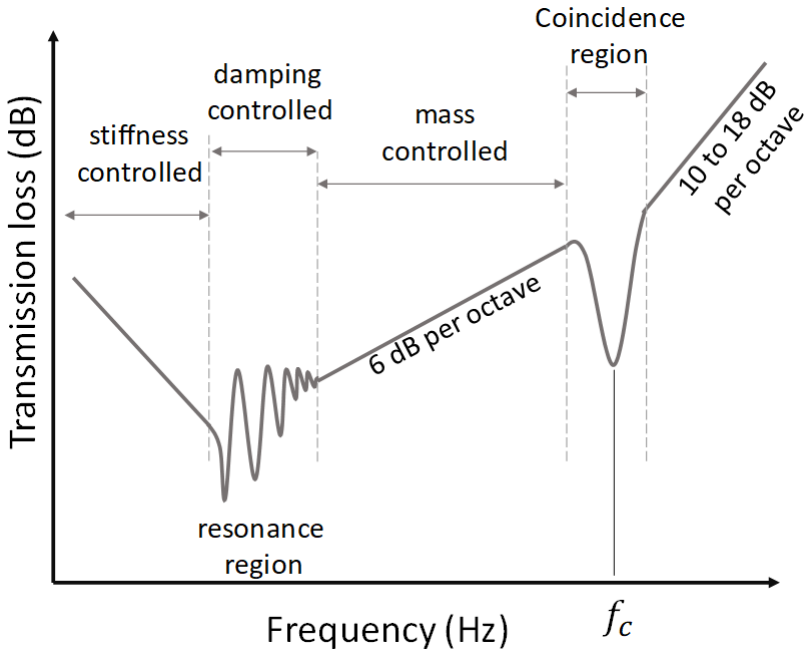

Source: Adapted from Gerges (1992)

- **Stiffness controlled region**: This region occurs bellow the first panel resonance, where the sound transmission loss is controlled by the bending stiffness of the panel. The increasing on bending stiffness leads to increasing sound transmission loss, thus more energy is required to vibrate the panel.

- **Resonance region**: This region is characterised by oscillations of the sound transmission loss, which coincide with the first natural frequency of the panel. At these frequencies, the incident acoustic waves excite structural modes leading to a significant vibration, therefore to an increase of the transmitted sound . In this region, the sound transmission phenomenon

is mainly controlled by damping effect, then higher the damping effect lower the dips on the resonance region (VIGRAN, 2008).

- **Mass law**: As the modal density increases, the resonant frequency become closer to each other and the resonant modes vibrate with similar amount of energy. Therefore, the sound transmission loss curve associated to the resonance is no longer distinguishable. In this region, the phenomenon of sound transmission is governed by the mass per unit of area. The sound reduction index increases by 6 dB by each doubling of frequency and/or mass per unit area.

- **Coincidence region**: As discussed in section 3.4, the coincidence condition occurs when the projected acoustic wave length in the structure is equal to the panel free bending wavelength. According to Vigran (2008), critical frequency phenomenon is governed by complex transmission mechanisms and its prediction does not present a reasonable accuracy. As suggest by Harrison (2004), orthotropic materials presents more than one critical frequency.

- **Region above coincidence frequency**: In this region, the excitation frequencies assume values higher than the critical frequency and the transmission loss is controlled by the stiffness, presenting a sound reduction of 10 to 18 dB per octave.

Therefore, the knowledge of the noise spectrum and the physical phenomena that govern sound transmission in each region of spectrum is of fundamental importance for the definition of the most adequate design to control the sound transmission through a flexible structure.

A.2.6.1 Sound reduction index of a plate characterized by its mass impedance

The acoustic impedance is characterized as the resistance offered by a medium to the propagation of acoustic wave. The surface impedance (Z_g) can be defined as follows:

$$Z_g = \rho_{air} c_{air} + j\omega m = Z_0 + j\omega m \tag{A.34}$$

where Z_0 is the air impedance. The transmission factor (τ) of the plate is defined as follows:

$$\tau = \frac{1}{1 + \left(\frac{\omega m}{2Z_0}\right)^2} \tag{A.35}$$

By assuming a normal sound incidence on the plate, the sound reduction index (R_0) is given as follows:

$$R_0 = 10\log\frac{1}{\tau} = 10\log\left\{1 + \left(\frac{\omega m}{2Z_0}\right)^2\right\} \tag{A.36}$$

Equation A.36 is named as *mass law* in its simplest form. Considering that the mass impedance of a plate is much larger than the characteristic impedance of the air (20°C), the sound reduction index can be represented as follows:

$$R_0 = 20\log\left(\frac{\pi \dot{f} m}{Z_0}\right) \approx 20\log(\dot{f} m) - 42\text{dB} \tag{A.37}$$

The mass-law gives an increase in the reduction index of +6 dB/octave.

A.2.6.2 Sound reduction index of a plate by diffuse sound incidence

In real buildings, the sound incidence angle is considered as diffuse since its distribution is unknown (TREVOR; D'ANTONIO, 2009). Then, the only viable solution is to assume sound incidence evenly distributed over all angles. Limiting the solution to frequency lower than the critical frequency, the sound diffuse index for a diffuse sound incidence (R_d) is given as follows:

$$R_d = R_0 - 10\log(0.23R_0) \tag{A.38}$$

Equation A.38 is commonly referred in literature as the *diffuse mass law*. Cremer (1942) defined the sound reduction index for frequencies above the critical frequency as follows:

$$R_d = 10\log\left(\frac{\pi \dot{f} m}{Z_0}\right) + 10\log\left(\frac{2\eta \dot{f}}{f_c}\right) - 5 \quad \text{for} \quad \dot{f} \gg \dot{f}_c \tag{A.39}$$

where η is the loss factor, which is a function of the internal energy losses in the material.

A.2.6.3 Sound transmission through a homogeneous single wall

In practical applications, a model for sound reduction is given as the following equation:

$$R_d = R_0 - 5 \approx 20\log(\dot{f} m) - 47\text{dB} \tag{A.40}$$

Equation A.40 is more accurate to predict the sound transmission loss because its take into account sound wave angle incidence with upper limit of 78°, which explain the fact that sound wave for high incidence angles has less importance for finite size partitions (TREVOR; D'ANTONIO, 2009). According to ISO12354-1 (2000), the sound reduction can be calculated based on transmission factor, as follows:

$$\tau = \left(\frac{Z_0}{\pi \dot{f} m}\right)^2 \left(2\sigma_{\dot{f}} + \frac{(a_w + b_w)^2}{a_w{}^2 + b_w{}^2}\sqrt{\frac{\dot{f}_c}{\dot{f}}}\frac{\sigma^2}{\eta}\right) \qquad \dot{f} < \dot{f}_c \tag{A.41a}$$

$$\tau = \left(\frac{Z_0}{\pi \dot{f} m}\right)^2 \left(\frac{\pi\sigma^2}{2\eta}\right) \qquad \dot{f} = \dot{f}_c \tag{A.41b}$$

$$\tau = \left(\frac{Z_0}{\pi \dot{f} m}\right)^2 \left(\frac{\pi \dot{f}_c \sigma^2}{2\dot{f}\eta}\right) \qquad \dot{f} > \dot{f}_c \tag{A.41c}$$

where a and b represents the wall dimension, σ and $\sigma_{\dot{f}}$ are the radiation factor for resonant and non-resonant transmission, respectively. Fahy and Gardonio (2007) suggested that the sound reduction can be estimated as follows:

$$R_d = R_0 - 10\log\left[\ln\left(\frac{2\pi\dot{f}}{c_0}\sqrt{ab}\right)\right] + 20\log\left[1 - \left(\frac{\dot{f}}{\dot{f}_c}\right)^2\right] \qquad \dot{f} < \dot{f}_c \qquad \text{(A.42a)}$$

$$R_d = R_0 + 10\log\left(\frac{2\eta\dot{f}}{\dot{f}_c}\right) - 5\text{dB} \qquad \dot{f} > \dot{f}_c \qquad \text{(A.42b)}$$

A accepted approximation of the sound reduction index of a wall (VIGRAN, 2008) is given by the following equation:

$$R_d = R_0 - 10\log\left[\ln\left(\frac{2\pi\dot{f}}{c_0}\sqrt{ab}\right)\right] + 20\log\left[1 - \left(\frac{\dot{f}}{\dot{f}_c}\right)^2\right] + 5\text{dB} \qquad \dot{f} < \dot{f}_c \qquad \text{(A.43a)}$$

$$R_d = R_0 + 10\log\left(\frac{2\eta\dot{f}}{\dot{f}_c}\right) \qquad \dot{f} > \dot{f}_c \qquad \text{(A.43b)}$$

According to the above equations, the term containing the ratio between the frequency and the critical frequency, are neglected at low frequencies. However, as the frequency approaches to the critical frequency, this term approaches to $-\infty$, leading to low reduction index at the critical frequency. For frequencies higher than the critical, the damping (η) of the plate may play a significant hole on the sound reduction. Additional expressions to predict sound radiation in plates are given by the following authors: Sewell (1970), Novak (1995), Cremer and Heckl (2013), suggested here as additional references.

In summary, the models presented above are suitable to predict the sound transmission loss for isotropic materials based on single layer element. In practical applications, a major problem to predict the sound transmission loss is the availability of a complete set of specifications of the measured object. Without these informations, the sound reduction index in frequency range around the critical frequency is quite uncertain.

APPENDIX B – CALIBRATION OF TEMPERATURE MEASUREMENTS

The thermocouples channels of the National Instruments data acquisition board were calibrated employing a thermostatic bath manufactured by LAUDA E 200, a precision thermometer manufactured by FLUKE®, model 1523 connected to a probe model 5616-6 made of inconel with an error of 0.021 °C in the temperature measurements. The measurement of the immersed thermocouples in the bath were to the reference thermometer FLUKE®.

Figure 81 – Thermostatic bath, precision thermometer, and probe employed on the thermocouple calibration.

Source: Author

The calibration were divided into the following temperature ranges in order to decrease the uncertainty of the temperature measurement: (i) from -14°C to 20°C and (ii) from 5°C to 55°C. The data was acquired in temperature increments of 2°C. A thermocouple support, as shown in Fig. 82, was developed to keep them fixed inside the thermostatic bath and to obtain a symmetrical distribution of them around the thermometer probe.

Figure 82 – Support developed to calibrate the thermocouples .

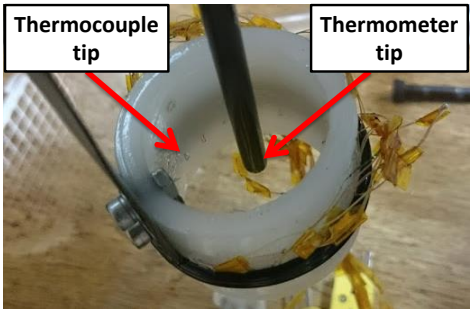

Source: Author

The calibration and uncertainties evaluation are based on the procedure proposed by Abernethy and Thompson Jr. (1973), which consists of the following steps:

- 1: Measurement of *N* upward (increasing bath temperature) and downward curves (decreasing bath temperature). After each step the temperatures of thermometer and thermocouples were recorded;
- 2: curve adjustment based on each calibrated thermocouple channel considering the data for increasing/decreasing the temperature;
- 3: uncertainty evaluation;

B.1 Curve lifting

A LabVIEW routine was designed to control and record the temperatures calibration data. Ten calibration curves were performed to reduce the measurement uncertainty for each acquisition channel. Between each increment or decrement the data points were logged when stable conditions were verified, characterized for temperature oscillations inferior to 0.01ºC by the FLUKE thermometer tip reading. During the calibration procedure, the room temperature was kept at an almost constant temperature (16-19ºC) through an air-conditioning system designed for this purpose.

B.2 Curve lifting and adjustment based on calibration data

After acquiring the calibration data, linear functions were adjusted through the least square method for each thermocouple channel. The linear function is given as follows:

$$T_m = T_{real} m + b \tag{B.1}$$

where T_{real}, is the value provided by the precision thermometer, *m* is the angular coefficient from the curve adjustment, *b* is the linear coefficient, and T_m is the measured temperature by the thermocouple channel.

B.3 Uncertainty of calibration process

The calibration uncertainty (U) was estimated based on the most widely employed standard method adopted and recommended by National Institute of Standards and Technology (NIST). It consists of the sum of the systematic error (B_1) plus a multiple of accuracy uncertainties, defined as follows.

$$U = \pm(B_1 + t_{95} S_1) \tag{B.2}$$

where S_1 is the mean standard deviation and t_{95} is the 95% t-Student distribution with *df* degrees of freedom. The calibration accuracy is determined by the following equation:

$$S_1 = \pm\sqrt{\frac{\sum_{n=1}^{N} s_i^2}{k}} \tag{B.3}$$

where k is the number of experimental data obtained from curve and s_i is the accuracy of each temperature defined as follows:

$$s_i = \pm\sqrt{\sum_{j=1}^{N} \frac{(Y_j - \overline{Y})^2}{N-1}} \tag{B.4}$$

where N is the number of calibration performed, Y_j are the values obtained from curves adjustment, and $\overline{Y}$ is the individual measurements mean of each individual measurement Y_k given by:

$$\overline{Y} = \frac{1}{N}\sum_{k=1}^{N} X_k \tag{B.5}$$

The average of multiple measurements reduces the random uncertainties. The freedom degrees for each temperature calibration is defined as follows:

$$df_i = N - 1 \tag{B.6}$$

The freedom degree for multiple samples is defined as follows:

$$df = \frac{(\sum_{n=1}^{N} s_i^2)_2}{\sum_{n=1}^{N} \frac{s_i^4}{df_i}} \tag{B.7}$$

B.4 Final adjustment of calibration data

Finally, to obtain the adjustment calibration curve for each channel, it is performed a linear regression with the data of all ten calibrations curves in order to obtain a function that correlates the actual temperature T_{real} to the temperature measured T_m by the channel, given as follows:

$$T_{real} = \frac{1}{m}T_m - \frac{b}{m} \tag{B.8}$$

APPENDIX C – MEASUREMENT UNCERTAINTIES AND ERROR PROPAGATION

The errors related to estimated parameters were evaluated based on the propagation of error according to the procedure suggested by Moffat (1988). Partial derivatives of R with respect to measurement X_i is the sensitivity coefficient for the results R with respect to the measurement X_i. When the results R depends on several independent variables measurements X_i, i.e. $R = f(X_1, X_2, ..., X_3)$, the individual terms are combined by a root-sum-square method, and the uncertainty of R is given as follows:

$$\delta R = \sqrt{\sum_{i=1}^{N} \left(\frac{\partial R}{\partial X_i} \delta X_i \right)^2} \tag{C.1}$$

The errors associated to heat flux and vapor quality were derived through the procedure suggested by Moffat (1988). The uncertainty related to the heat losses (Eq. 5.2) in heat section is given as follows:

$$\delta Q_{loss} = \left[\left(\frac{\partial Q_{loss}}{\partial \dot{m}_{water}} \delta \dot{m}_{water} \right)^2 + \left(\frac{\partial Q_{loss}}{\partial T_{hs_{out,water}}} \delta T_{hs_{out,water}} \right)^2 + \left(\frac{\partial Q_{loss}}{\partial T_{hs_{in,water}}} \delta T_{hs_{in,water}} \right)^2 + \left(\frac{\partial Q_{loss}}{\partial \dot{m}_{R134a}} \delta \dot{m}_{R134a} \right)^2 + \left(\frac{\partial Q_{loss}}{\partial T_{hs_{out,R134a}}} \delta T_{hs_{out,R134a}} \right)^2 + \left(\frac{\partial Q_{loss}}{\partial T_{hs_{in,water}}} \delta T_{hs_{in,water}} \right)^2 + \right]^{1/2} \tag{C.2}$$

The uncertainty of the heat losses from the heating section outlet to the test section inlet (Eq. 5.3) is given as follows:

$$\delta Q_{loss} = \left[\left(\frac{\partial Q_{loss}}{\partial \dot{m}_{R134a}} \delta \dot{m}_{R134a} \right)^2 + \left(\frac{\partial Q_{loss}}{\partial T_{ts_{in,R134a}}} \delta T_{ts_{in,R134a}} \right)^2 + \left(\frac{\partial Q_{loss}}{\partial T_{hs_{out,R134a}}} \delta T_{hs_{out,R134a}} \right)^2 \right]^{1/2} \tag{C.3}$$

According to the data reduction procedure adopted in the present work, the TXV outlet vapor quality uncertainty was estimated based on two different conditions according to the fluid inlet thermodynamic state. Under single-phase flow in the test section inlet, the outlet vapor quality uncertainty was directly estimated from the inlet fluid enthalpy and the outlet local pressure or temperature.

As described in Section 5.1, the inlet vapor quality was estimated based on the local pressure and enthalpy. The procedure suggested by Moffat (1988) requires an explicit expression

for determining the experimental errors, however, the data reduction procedure adopted in this work does not contemplate an analytical expression for determining the vapor quality at the test section inlet and outlet. Therefore, as an alternative approach, an analytic expression for estimating the vapor quality at the test section inlet was derived by employing energy conservation in a control volume from the heat section inlet to the test section inlet, given as follows:

$$x_{ts_{in,R134a}} = \frac{\dot{m}_{water} c_{p_{water}} \Delta T_{hs_{water}} - Q_{losses} - \dot{m}_{R134a} c_{p_{R134a}} \Delta T_{sub}}{\dot{m}_{R134a} i_{lv_{R134a}}} \tag{C.4}$$

where $\Delta T_{hs_{water}}$ is the water temperature difference between the heat section inlet and outlet, ΔT_{sub} is the subcooling temperature at the inlet of the heating section, c_p is the heat capacity at constant pressure, and i_{lv} is the enthalpy of vaporization. An analytical expression was derived from the experimental data to estimate the total heat losses (Q_{losses}) evaluated as the sum of the contribution of the heat losses in the heating section ($Q_{loss,1}$) and from the heat section outlet to the test section inlet ($Q_{loss,2}$), given as follows:

$$Q_{losses} = Q_{loss,1} + Q_{loss,2} \tag{C.5}$$

$$Q_{loss,1} = -1.34 + 1.44(\overline{T}_{R134a} - T_{room}) \tag{C.6}$$

$$Q_{loss,2} = -0.46 + 1.32(\overline{T}_{R134a} - T_{room}) \tag{C.7}$$

Therefore, the uncertainty related to the vapor quality at the test section inlet was estimated, as follows:

$$\delta x = \left[\left(\frac{\partial x}{\partial \dot{m}_{water}} \delta \dot{m}_{water} \right)^2 + \left(\frac{\partial x}{\partial \Delta T_{hs_{water}}} \delta \Delta T_{hs_{water}} \right)^2 + \left(\frac{\partial x}{\partial Q_{losses}} \delta Q_{losses} \right)^2 + \left(\frac{\partial x}{\partial \dot{m}_{R134a}} \delta \dot{m}_{R134a} \right)^2 + \left(\frac{\partial x}{\partial \Delta T_{sub}} \delta \Delta T_{sub} \right)^2 \right]^{1/2} \tag{C.8}$$

Table 15 summarizes the vapor quality uncertainties at the test section inlet (left) and the test section outlet (right). From this table, it is seen that the uncertainty of the vapor quality decreases as the vapor quality increases. Although the relative uncertainty for vapor qualities of 2 and 4% at the test section inlet are relative high, its absolute values is reduced. From this table, it is seen that the uncertainty of the vapor quality decreases as the vapor quality increases.

Table 15 – Experimental uncertainties for the vapor quality at the test section inlet (left) and outlet (right).

Inlet vapor quality	Relative uncertainty	Outlet vapor quality	Relative uncertainty
2%	25.0%	16%	6.8%
4%	18.3%	19%	4.9%
6%	13.3%	21%	4.2%
9%	8.8%	25%	3.7%
12%	6.7%	29%	2.8%
15%	5.3%	33%	2.4%